

# Intracellular protein conformation measured with coherent Raman microspectroscopy

by

Frederik Franz Georg Fleissner

DISSERTATION

MAX PLANCK INSTITUTE FOR POLYMER RESEARCH

JOHANNES GUTENBERG-UNIVERSITÄT MAINZ

MAX PLANCK GRADUATE CENTER

2018

---

Dissertation zur Erlangung des Grades eines doctor rerum naturalium (Dr. rer. nat.) der  
Fachbereiche

08 - Physik, Mathematik und Informatik,

09 - Chemie, Pharmazie und Geowissenschaften,

10 - Biologie und

Universitätsmedizin

der Johannes Gutenberg-Universität Mainz

### **Supervisors:**

Prof. Dr. Mischa Bonn, Max Planck Institute for Polymer Research

Prof. Dr. Dirk Schneider, Johannes Gutenberg-Universität Mainz

Dr. Sapun Parekh, Max Planck Institute for Polymer Research

### **Declaration**

I hereby declare that I wrote the dissertation submitted without any unauthorized external assistance and used only sources acknowledged in the work. All textual passages which are appropriated verbatim or paraphrased from published and unpublished texts as well as all information obtained from oral sources are duly indicated and listed in accordance with bibliographical rules. In carrying out this research, I complied with the rules of standard scientific practice as formulated in the statutes of Johannes Gutenberg University Mainz to insure standard scientific practice.

Frederik Fleissner

Copyright: Frederik Fleissner, 2018

Verlag Dietmar Fölbach, Koblenz

ISBN 978-3-95638-855-2

*About the cover:* The cover art shows the fluorescently labelled intermediate filament cytoskeleton of an adherent cell. Those filaments provide mechanical stability and help the cell to resist external forces.



---

## Publications covered in this thesis

### Chapter 3

Frederik Fleissner, Mischa Bonn and Sapun H. Parekh. *Microscale spatial heterogeneity of protein structural transitions in fibrin matrices*. Science Advances, 08 Jul 2016: Vol. 2, no. 7, e1501778. DOI: 10.1126/sciadv.1501778

### Chapter 4

Frederik Fleissner, Sabine Pütz, Mischa Schwendy, Mischa Bonn and Sapun H. Parekh. *Measuring intracellular secondary structure of a cell penetrating peptide in situ*, Analytical Chemistry, 2017, 89(21): 11310-112317. DOI: 10.1021/acs.analchem.7b01895.

### Chapter 5

Frederik Fleissner, Noreen Klein, Daniel Wirth, Ravi Dhiman, Sachin Kumar, Dirk Schneider, Mischa Bonn and Sapun H. Parekh. *Tension causes structural unfolding of intracellular intermediate filaments*. In preparation.

## Other publications

Nils Billecke, Madeleen Bosma, William Rock, Frederik Fleissner, Gerrit Best, Patrick Schrauwen, Sander Kersten, Mischa Bonn, Matthijs K. C. Hesselink and Sapun H. Parekh. *Perilipin 5 mediated lipid droplet remodelling revealed by coherent Raman imaging*. Integr Biol (Camb). 2015 Apr;7(4):467-76. DOI: 10.1039/c4ib00271g.

Frederik Fleissner and Sapun H. Parekh. *Imaging mechanotransduction: seeing forces from molecules to cells*. Current Opinion in Biomedical Engineering, 2018. DOI: 10.1016/j.cobme.2018.01.003

Zahra Rastian, Sabine Pütz, Yujen Wang, Sachin Kumar, Frederik Fleissner, Tobias Weidner, and Sapun H. Parekh. *Type I collagen from jellyfish *Catostylus mosaicus* for biomaterial applications*. ACS Biomater. Sci. Eng., Just Accepted Manuscript, 2018 DOI: 10.1021/acsbiomaterials.7b00979

# Contents

<b>1</b>	<b>Introduction</b>	<b>1</b>
1.1	Overview . . . . .	1
1.1.1	How to determine intracellular protein structure . . . . .	2
1.1.2	Structure of this thesis . . . . .	3
1.2	Proteins under mechanical load . . . . .	5
1.2.1	Protein secondary structure . . . . .	5
1.2.2	Mechanically induced unfolding of protein . . . . .	6
1.2.3	Measuring secondary structure with molecular spectroscopy . . . . .	10
1.3	Mechanobiology . . . . .	15
1.3.1	Mechanical forces in nature . . . . .	15
1.3.2	The cytoskeleton . . . . .	15
1.3.3	Mechanosensing in cells . . . . .	18
1.3.4	Probing cellular mechanics . . . . .	19
1.3.5	Mechanically induced structural transitions in biopolymers . . . . .	21
1.4	Coherent anti-Stokes Raman scattering . . . . .	24
1.4.1	Spontaneous Raman scattering . . . . .	24
1.4.2	Towards greater signal: CARS . . . . .	26
1.4.3	Broadband CARS . . . . .	30
<b>2</b>	<b>Experimental methods</b>	<b>33</b>
2.1	Rheology . . . . .	33
2.1.1	Basic concepts . . . . .	33
2.1.2	Tensile testing . . . . .	36
2.1.3	Shear rheology . . . . .	36
2.2	Broadband CARS microspectroscopy . . . . .	38
2.2.1	Technology . . . . .	38
2.2.2	Experimental setup for BCARS microspectroscopy . . . . .	39
2.2.3	Phase retrieval to obtain Raman-like spectra . . . . .	41
2.2.4	Multivariate curve resolution . . . . .	43
2.2.5	Decomposition of amide I band . . . . .	47
2.3	Fluorescence microscopy . . . . .	48
2.3.1	Wide-field microscopy . . . . .	48
2.3.2	Confocal microscopy . . . . .	50
2.4	Protein expression and purification of vimentin . . . . .	52
2.4.1	Preparation of chemically competent E.coli cells . . . . .	52
2.4.2	Transformation . . . . .	52
2.4.3	Expression of vimentin in LB medium . . . . .	52
2.4.4	Expression of vimentin in deuterated minimal medium . . . . .	52
2.4.5	Cell lysis . . . . .	53
2.4.6	Purification of vimentin by Ni-NTA . . . . .	53
2.4.7	Concentrating the protein . . . . .	54

2.4.8	Test for filament formation . . . . .	55
2.4.9	Appendix: Buffer and media used for protein production . . . . .	56
2.5	Creation of a GFP expressing HeLa strain . . . . .	56
<b>3</b>	<b>Microscale spatial heterogeneity of protein structural transitions in fibrin matrices</b>	<b>59</b>
3.1	Introduction . . . . .	60
3.2	Results . . . . .	61
3.3	Discussion . . . . .	67
3.4	Conclusion . . . . .	70
3.5	Methods . . . . .	70
3.6	Appendix I . . . . .	72
<b>4</b>	<b>Measuring intracellular secondary structure of a cell penetrating peptide <i>in situ</i></b>	<b>85</b>
4.1	Introduction . . . . .	86
4.2	Results . . . . .	87
4.3	Discussion . . . . .	92
4.4	Conclusions . . . . .	94
4.5	Methods . . . . .	95
4.6	Appendix II - Supplementary Information . . . . .	98
<b>5</b>	<b>Tension causes structural unfolding of intracellular intermediate filaments</b>	<b>113</b>
5.1	Introduction . . . . .	114
5.2	Results . . . . .	115
5.3	Discussion . . . . .	122
5.4	Conclusion . . . . .	123
5.5	Methods . . . . .	124
5.6	Appendix III - Supplementary Information . . . . .	127
<b>6</b>	<b>Outlook and Summary</b>	<b>137</b>
6.1	Future directions . . . . .	137
6.1.1	Local hydrogel deformation . . . . .	137
6.1.2	Design of a cell stretching device for large deformations . . . . .	138
6.1.3	Reconstructing the non-resonant CARS contribution with MCR-ALS	140
6.2	Summary . . . . .	143

# Chapter 1

## Introduction

### 1.1 Overview

Mechanical force is omnipresent in life and determines not only each step we go but also every sound we hear. For the macroscopic world, this is obvious as each of us feels and interacts physically. Yet, on the cellular scale scientists most often think only about chemical reactions, diffusion, or enzyme activity and ignore the physical forces that act upon molecules. In the doctoral thesis presented here, I investigated how mechanical forces affect proteins, the basic building blocks of life, in their structure. To do so, I studied how mechanical forces affect protein structure in a hydrogel model system as well as within cells and discuss what possible implications for mechanobiology could arise from these results.

All cellular functions depend on the structure and functionality of proteins. Those two properties are intrinsically coupled to each other - the geometric arrangement of the amino acid sequence defines the chemical and physical properties of a protein. The interplay with other molecules or forces can change the structure and thereby alter the protein functionality. Because of this varying functionality, the behavior of living cells is determined not only by the underlying composition of proteins but also their structure, and changes in protein conformation can lead to different reactions and behaviors of the entire cell.

Recent work has shown that not only biochemical pathways, but also mechanical, forces influence protein conformation and therefore cell function. For example, passive mechanical inputs such as substrate stiffness are capable of influencing cell behavior, like cell fate [1], multicellular tissue organization [2] and modulation of carcinoma metastatic potential [3]. It is now evident that mechanical factors can trigger fundamental changes in cells, but it is yet unknown how exactly the mechanical load is transformed into altered biochemical signaling - protein-based interactions - within cells. Several proteins, such as titin [4], vimentin [5] and keratin [6] were identified as 'mechanically active' and force-induced protein unfolding has been demonstrated *in vitro*. Nevertheless, it is unclear whether and how such changes occur in the complex cellular environment. Thus, to better understand the true relevance of force on protein structure in nature would require a direct structural determination of proteins within cells while the cell is exposed to external forces.

The overall topic of this PhD project was to determine the impact of mechanical loads on the secondary structure of mechanosensitive proteins that form intermediate filaments. Those proteins have previously been shown to bear loads and undergo structural changes in single molecule or non-cellular contexts. I describe a way to measure the structural motifs of mechanosensitive proteins under different states of tension using a vibrational

imaging technique called broadband coherent anti-Stokes Raman scattering microspectroscopy. Intermediate filaments form a filamentous network, which is part of the load-bearing cytoskeleton and which, as a result, is constantly exposed to varying tensile forces in an organism. The structure of intermediate filaments is predominately  $\alpha$ -helical and has been predicted to change under mechanical tension [6, 7]. However, this has never been observed directly *in situ*, and it is unclear if the range of deformations - and the cellular environment - support such structural transitions or not. In addition to this physical function, the expression pattern of IFs has been shown to change between epithelial and mesenchymal cell types. While an expression change alone can be used as a putative marker of metastatic cancer [5, 8], the impact of this change on the structural integrity of the IF protein network, if any, is unknown.

### 1.1.1 How to determine intracellular protein structure

The analysis of protein secondary structure in macroscopic amounts of sample is an established routine measurement with circular dichroism spectroscopy in biochemistry. Unfortunately, this method can not be used for a direct probing of proteins in the cellular environment and is thereby unsuited when it comes to *in situ* structure analysis.

An experimental approach that potentially allows intracellular imaging of protein-specific secondary structure with submicron spatial resolution is broadband coherent anti-Stokes Raman scattering (BCARS) microspectroscopy. Similar to spontaneous (often called 'normal' or 'linear') Raman spectroscopy, BCARS generates a spectrum of vibrational modes depicting the local chemical composition within focal volume of the excitation lasers. The fundamental problems of spontaneous Raman, its weak signal and large background fluorescence in biological samples, are avoided in CARS due to coherent driving of the molecular modes and coherent emission of the detected anti-Stokes light, respectively. To produce a hyperspectral image of the protein distribution and structure, the sample has to be raster-scanned where a BCARS spectrum is acquired for each position. In order to apply this approach to intracellular measurements, two model systems were examined in preceding projects before experiments with vimentin were undertaken:

First, hydrogels made out of the blood-clotting protein fibrin which are known to undergo load-induced structural changes [9] were investigated with BCARS spectroscopic imaging. In this simplified system, the mechanically-induced protein secondary structural changes were shown to be detectable by BCARS. Maps of the local contribution for each structural motif as a function of load were generated and the sensitivity of CARS microscopy to secondary structure changes was shown.

Second, the cell-penetrating peptide (CPP) Penetratin was used to demonstrate the feasibility of isotopic labelling to find a target protein in cells. Penetratin is a well-studied CPP capable of trafficking cargos into the cytosol [10, 11]. As the average amount of protein inside cells is more than 200 mg/ml [12], it was necessary to highlight the fingerprint of penetratin in the CARS spectrum. For this, an isotope-labeling approach was used where hydrogen in the attached glycine is replaced by deuterium - analogous that used for in-cell NMR [13, 14]. This shifts the  $\text{CH}_2$  resonance to a spectral region where no other intracellular molecules will interfere and enables the identification and localization of penetratin. The unique  $\text{CD}_2$  peak is then exploited to separate the spectral signal of the cell penetrating peptide from the remaining protein using multivariate analysis. In our study, we link a deuterated hexaglycine tag to the CPP to allow a spectral separation which is small compared to large DNA or proteins cargos shown previously [10, 11].

Based on these results and experimental experience, I developed an experimental approach to examine the structure of deuterated vimentin intermediate filaments *in vivo* under different tensed states. HeLa cells are known form an abundant network of intermediate

filaments including the protein vimentin [15], which, as mentioned above, is predicted to undergo an  $\alpha$ -helix to  $\beta$ -sheet transition during mechanical loading [6, 7]. Similar to experiments with penetratin, vimentin protein was isotopically labelled by  $^2\text{H}$  to locate it in cells via BCARS. Deuterated vimentin (d-Vim) was produced in a recombinant bacterial cell culture, purified, and microinjected into HeLa cells for subsequent incorporation of d-Vim into the native vimentin network. This technique has previously successfully been used for doping fluorescently labeled actin [16]. Such prepared cells were cultured on substrates of different stiffness or treated with chemical agents to release cellular tension. High substrate stiffness is known to lead to larger intracellular tension, and I found that these cells show more unfolded vimentin while the secondary structure of d-Vim in relaxed cells was closer to monomeric vimentin. Thereby, we showed that mechanical stimuli can indeed cause conformational changes of intermediate filaments within cells.

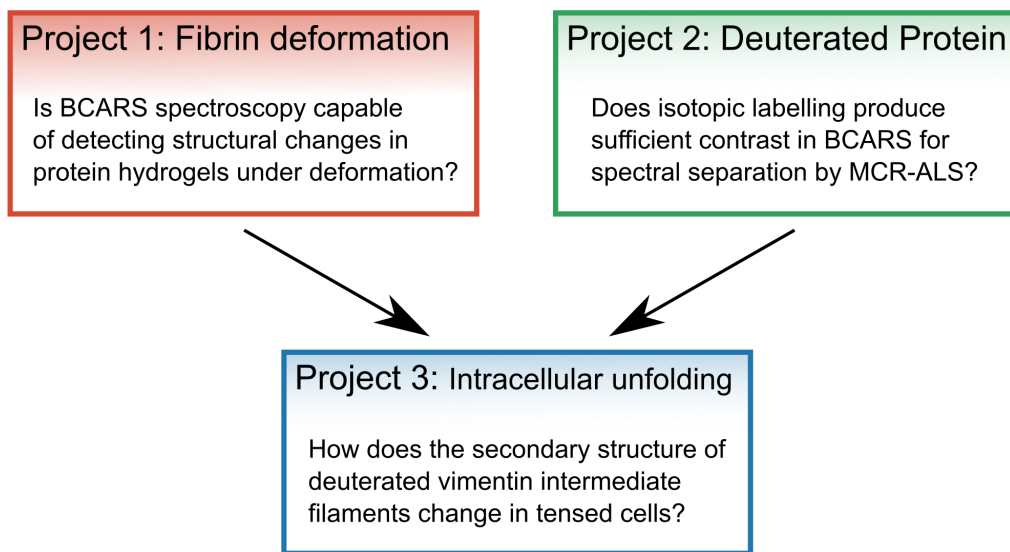


**Figure 1.1:** Structuring of the three projects covered in this thesis.

### 1.1.2 Structure of this thesis

This dissertation presents the results, and associated background information, from my PhD research on intracellular protein secondary structure under mechanical deformation. In two sub-projects, I demonstrate first that BCARS microspectroscopy is capable of measuring structural changes and second how to locate a specific protein by isotopic labelling. Based on these results, I analyzed deuterated vimentin intermediate filaments in adherent cells under different tensed states.

**Chapter 1** provides a theoretical background of the work. First, the fundamentals of secondary structure, the molecular response of proteins to mechanical forces and the spectroscopic background on how to characterize different structural motifs by Raman scattering are discussed. Then, an overview on mechanobiology of cells, explaining cytoskeletal networks and their interplay is given. The chapter closes with the derivation of signal generation in coherent anti-Stokes Raman scattering and the necessary processing to obtain a Raman-like spectrum from it.

In **Chapter 2** the experimental techniques used in this project are described: mechanical characterization by rheology, fluorescence-based and molecular vibrational imaging

and the subsequent data processing. Furthermore, multivariate curve resolution and its application to hyperspectral datasets are discussed. The biological methods for protein expression and purification as used for the production of deuterated vimentin are explained. **Chapter 3** focuses on how tensile strain changed the secondary structure in fibrin hydrogels. We employ spatial resolved broadband CARS to show conformational changes in fibrin under load, the different orientation of structural motifs and spatial heterogeneity of unfolding in deformed samples. (Paper 1, Fleissner *et al.*, 'Microscale spatial heterogeneity of protein structural transitions in fibrin matrices' [17]).

**Chapter 4** describes the usage of isotopically labelled amino acids as a marker in Raman spectroscopy. We observe the uptake of a deuterated cell penetrating peptide in adherent cells and separate its intracellular spectrum by sophisticated component analysis. This allows us to determine the peptide structure both in the cytosol and the nucleus which helps to illuminate its uptake mechanism. (Paper 2, Fleissner *et al.*, 'Measuring intracellular secondary structure of a cell penetrating peptide *in situ*' [18]).

**Chapter 5** combines those established methods and investigates deuterated vimentin within HeLa cells under different cellular tension. We show that in tensed cells grown on glass, vimentin IFs undergo a transition from  $\alpha$ -helix to  $\beta$ -sheet and that this effect is reduced in physically and chemically relaxed cells. This indicates that intracellular conformational changes in vimentin occur in tensed adherent cells. We hypothesize that unfolding might act as a local mechano sensor within the cytoskeleton and possibly triggers further mechanosresponse of cells. (Paper 3, in preparation, Fleissner *et al.*, Tension causes structural unfolding of intracellular intermediate filaments).

In **Chapter 6** the results from all three projects are summarized and an outlook for possible future directions is provided.

## 1.2 Proteins under mechanical load

### 1.2.1 Protein secondary structure

Proteins are (arguably) the building blocks of life, which fundamentally consists of polymerized amino acids in the form a polypeptide chain. Their biological function is based not only on the sequence of amino acids but also on their specific shape, which mediates the interaction of weak chemical forces to enable biochemical reactions [19]. Within the polypeptide chain, the amino acids usually align in a trans-configuration with the (bulky) side-chains being located in an alternating pattern. The rotation of each amide plane (the plane of the peptide bond) is constrained by repulsive forces from neighboring groups as well as the charge and size of its side-chain. These conditions lead to a most probable and stable configuration of dihedral angles  $\psi$  and  $\varphi$  between two amide planes and the  $\alpha$ -carbon in the center (see figure 1.2A). Because both angles only depend on the properties of the two amino acids that interact at the respective peptide bonds, the polypeptide chain folds into a shape that is determined by its sequence. The folding process then leads to a stable three-dimensional arrangement of the protein, named secondary structure, which then becomes stabilized by hydrogen bonds [19, 20]. Several structural patterns are universal in all proteins and it is useful to describe their common properties. The most abundant structural motifs are briefly introduced in the following section.

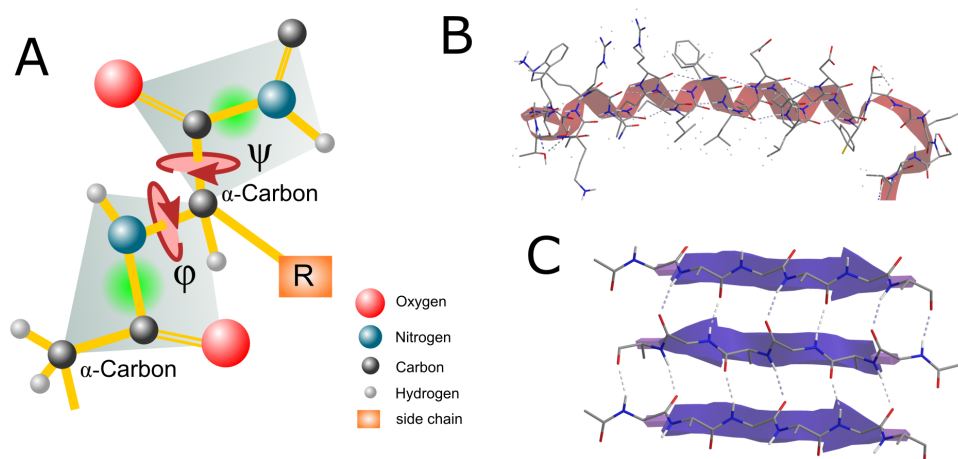


**Figure 1.2:** Basic peptide bond geometry illustrating the amide planes in grey (A). The spatial arrangement is depicted for  $\alpha$ -helix (B) and  $\beta$ -sheet (C) with hydrogen bonds being indicated by dotted lines.

#### $\alpha$ -helix

When several dihedral angles in a sequence of amino acids have values close to  $\psi = -40^\circ$  and  $\varphi = -60^\circ$  the chain folds into a rod-like helix structure (see figure 1.2B). In an  $\alpha$ -helix, the polypeptide chain winds into a counterclockwise spiral with the side-chains pointing outwards. On average, there are 3.6 amino acids per full turn. Hydrogen bonds form along the axis of the helix between partially negatively charged carbonyl groups and partially positively charged amino hydrogen four residues further along the polypeptide chain.

Two or more  $\alpha$ -helices can twist around each another to form a coiled coil structure if the sequence has an appropriate pattern of seven-residue repeats known as a heptad



and characterized by nonpolar residues present at position 1 and 4 forming an interior hydrophobic core [21]. The coiled coil superstructure is stabilized by hydrophobic interactions or disulfide bonds [20, 22]. Large  $\alpha$ -helical structures ( $> 22$  amino acids) have the ability to span lipid bilayers, which enables many functionalities with respect to the cell membrane [23].

### **$\beta$ -strand and sheet**

The  $\beta$ -strand structure is a polypeptide conformation where the protein backbone is fully extended [20] and dihedral angles become larger than for the  $\alpha$ -helix structure with values reaching  $\psi = -180^\circ$  and  $\varphi = 180^\circ$ . In this configuration, carbonyl oxygen and amino hydrogen are oriented in the same direction while the side chains point alternating up and down on the strand [19]. A solitary  $\beta$ -strand is sterically stable but rarely found [20]. Two or more  $\beta$ -strands can form a  $\beta$ -sheet structure as shown in Fig.1.2C, where hydrogen bonds form between the residues of adjacent strands to give stability to the structure. The hydrogen bonding pattern defines if the  $\beta$ -sheet is in a parallel or antiparallel configuration. For the parallel case, the neighboring polypeptide strands follow the same direction (from N- to C-terminal) and the stabilizing coupling occurs with an angle relative to the strand direction. On the contrary, the sheet is antiparallel if both strands run in opposite direction [19].

### **Random coils**

As the name suggests, protein segments that show no repetitive hydrogen bonding pattern are termed random coils or unstructured. The random coil state of a polypeptide indicates that there is no interaction between the side chains of residues [24] and that in each amino acid the values of the dihedral angles are independent from neighboring residues [25]. This rotational freedom adds local flexibility to the protein arrangement and lowers the threshold for conformational changes elsewhere in the polypeptide chain. Furthermore, as the random coil areas do not form hydrogen bonds within the protein, they are obvious interaction sites for ligands or other proteins [20].

## **1.2.2 Mechanically induced unfolding of protein**

Specific secondary structures are stabilized by hydrogen bonds ( $\sim 4$  kJ/mol) and therefore by energies only about twice as much as the thermal energy ( $\sim 2.5$  kJ/mol) at room temperature. These bonds can be broken easily by solvents, strong acids and bases or simply by heating [20]. In general, the loss of secondary structure is called denaturation and leads to unstructured proteins. Yet another process can cause the breaking of structural bonds, which is mechanical stress. A daily-life example is the beating of chicken egg white with a whisk to produce a stable foam that is used for cooking and baking. Here, the physical stress causes the egg protein to unfold and to form a mesh where air gets trapped in [20]. Such structural transitions of proteins under mechanical load are a core tenant of this thesis and will be discussed in the next section.

### **Bell's theory**

Rod-like proteins have the ability to unfold their  $\alpha$ -helical domains as well as the coiled-coil superstructure under tensile force. This gives rise to advantageous mechanical properties that would not be possible otherwise. Many load-bearing proteins such as myosin, keratin, vimentin, and fibrin follow the coiled-coil  $\alpha$ -helical blueprint, and they all show strain stiffening that only sets in after large extension of the molecule together with having large rupture strains [6, 21, 26–28]. The interplay of mechanical forces acting on individual

molecules can be described by a theoretical framework postulated first by Bell in 1978 [29]. Using the example of vimentin, an intermediate filament protein of interest in chapter 5, the theory from Bell was implemented in atomistic simulations to provide detailed insights in the molecular force response by Ackbarow and Buehler [30]. In the following section, I will summarize the central statements of this theory and what can be learned from it with respect to protein unfolding.

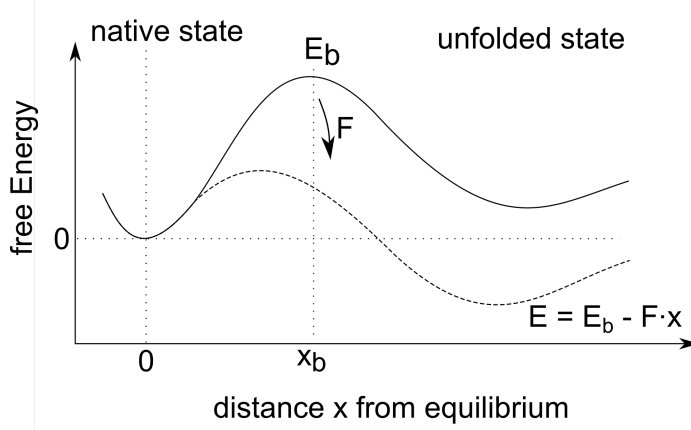


**Figure 1.3:** Plot of the free energy as a function of reaction coordinate (e.g. displacement).

Molecules form noncovalent linkages between each other based on van der Waals, electrostatic, or hydrogen bond interactions. The energies are small (relative to thermal energy), and therefore it is likely that such a bond might break after some time without the need of external forces. To allow molecular separation it usually is required to break multiple bonds simultaneously. Therefore, the lifetime of each single bond must be reduced drastically.

The free energy landscape of a molecular bond as a function of distance as depicted in Fig.1.3 shows the minimum at the equilibrium binding position. To transition from a native state to the unfolded state, the molecules has to overcome the energy barrier that is associated with interactions [29] stabilizing it in a potential well that characterizes the native state. By applying a force  $F$  on the molecules, the energy landscape can be tilted, and the transition barrier lowered. The separation force thereby provides energy  $E_1$  into the system:

$$E_1 = F \cdot x_b \quad (1.1)$$

where  $x_b$  is the separation distance. This adds energy to system in the native state as

$$E = E_0 + F \cdot x_b \quad (1.2)$$

which is conceptually similar to saying that it lowers the energy barrier into the transition state by  $E_1$ . The minimum force that will annihilate the energy barrier  $E_b$  and lead to a rapidly rupture of the bond follows as

$$f_0 = 1.6 \cdot 10^{-10} \frac{E_b}{x_b} \quad (1.3)$$

in Newton where the prefactor results from unit conversion when using  $E_b$  in electron volts and the separation distance  $x_b$  in nanometers. Some typical values occurring in biochemistry are given in table 1.1. The lifetime  $\tau$  of a bond can be described by the product of the reciprocal natural oscillation frequency of atoms in a solid  $\omega_0$  ( $\sim 10^{-13}s$ ) [29], and the exponential effect of the energy barrier modulation on the bond lifetime as [30]

$$\tau = \frac{1}{\omega_0} \exp \left( \frac{E_0 - F \cdot x_b}{k_b T} \right). \quad (1.4)$$

type	$E_0$ [eV]	$x_b$ [nm]	$F_0$ [N/bond]	reference
antigen-antibody	0.37	1	$6 \cdot 10^{-11}$	[29]
covalent bond	3	0.14	$3 \cdot 10^{-9}$	[29]
H-bond	0.22	0.1	$3.5 \cdot 10^{-10}$	[30]
unfolding of $\alpha$ -helix	0.65	0.1	$1.1 \cdot 10^{-9}$	[30]

**Table 1.1:** Typical forces required to break bonds in Bell’s theory.

Here,  $k_b$  is Boltzmann’s constant and  $T$  the temperature. A separation force thereby lowers the lifetime of a bond and makes a rupture event more likely.

### Structural transitions in coiled-coils and $\alpha$ -helix under load

The load-bearing proteins of interest in this study, fibrin and vimentin, form a coiled-coil structure where  $\alpha$ -helical domains are wrapped around each another. These coiled-coil domains define the mechanical properties of both proteins whereas additional terminal or central linking domains have only a minor structural role. Force spectroscopy, where single molecules or domains are pulled by an AFM cantilever (or equivalent setup), can be used to investigate the mechanical properties of proteins. The resistance to deformation of the sample (force) is recorded while the sample is deformed. This force-extension curve then provides insights on the mechanisms that are relevant for different amounts of strain [31]. For the coiled-coil domains of vimentin, such a curve was successfully modeled on basis of Bell’s theory [7, 32]. These *in silico* experiments revealed the structural transition from  $\alpha$ -helix to  $\beta$ -sheet under tensile load [7, 32], which is consistent with experimental data [6, 33]. Under tensile load, coiled-coils exhibit a characteristic response to mechanical strain consisting of three defined regimes (see Fig.1.4) that are described in the following:

#### 1: Stretching of hydrogen bonds

At low strain, the sample behavior is fully elastic, and the small deformation is distributed equally over the entire molecule. Individual hydrogen-bonds within the  $\alpha$ -helices are stretched but not disrupted.

#### 2: Unfolding of $\alpha$ -helices

When all available H-bonds are fully extended the sequential unfolding of  $\alpha$ -helical segments sets in. A second regime starts at a characteristic angular point (see Fig.1.4) where the linear increase of the force-strain curve ends and a force plateau sets in. The individual  $\alpha$ -helices are unfolded by force into  $\beta$ -strand structures and neighboring strands then form  $\beta$ -sheets. Furthermore, as the resistance strength of formed  $\beta$ -sheets is known to be significantly larger than for  $\alpha$ -helix [26, 34–36], firstly more helix residues will unfold. This transition from  $\alpha$ -helical into  $\beta$ -sheet structure either starts at the ends of the molecule [30] or a special ‘stutter region’ within the helix where the protein sequence folds into a discontinuity [37]. It continues as an unfolding wave that propagates through the entire protein where h-bond of all involved  $\alpha$ -helices are being ruptured in parallel. While in an  $\alpha$ -helix each residue provides about 0.15 nm in length, the unfolding to  $\beta$ -strand extends it to 0.32-0.34 nm per residue [35]. Thereby, conformational change results in an overall extension of the molecule that can reach more than three-fold the initial molecule length [38]. Remarkably, at low pulling speed ( $\sim 1m/s$  in simulations [7, 32],  $\sim 1\mu m/s$  in experiments [39]) the force response in the unfolding regime results is constant, while for faster deformation a linear increase in force is observed [30].

#### 3. Coiled-coil unwinding and stretching of covalent bonds

The plateau regime is followed by a non-linear strain-hardening caused by shearing of

$\beta$ -strands within their sheet-structure [36] and stretching of the protein backbone itself. This continues on until the entire molecule is fully extended and amide bonds fail [30].

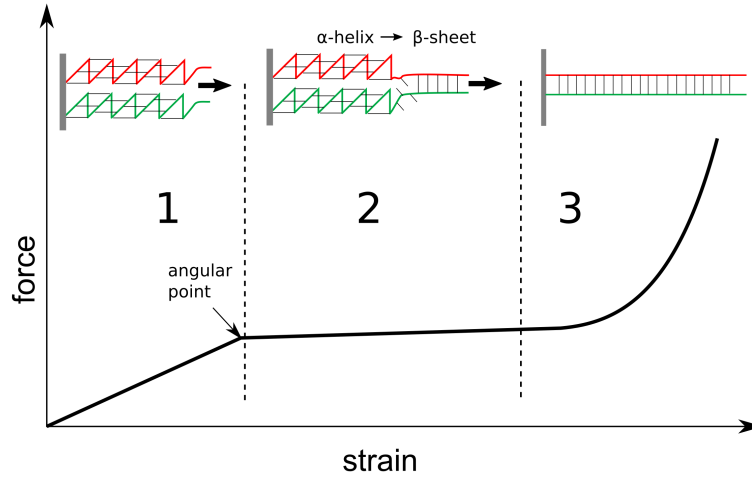


**Figure 1.4:** Schematic force-strain curve of a coiled-coil structure and the occurring structural changes. Adapted from [7, 30].

With respect to conformational changes in proteins, the energy that is required to break the stabilizing hydrogen bonds in an  $\alpha$ -helix structure, is of special interest. As discussed earlier, the unfolding of  $\alpha$ -helices starts at the angular point, where strain becomes large enough to cause failure of hydrogen bonds. The energy barrier for breaking a single hydrogen bond is known to be 5-6 kcal/mole (0.22 eV). However, in the coiled-coil configuration it was shown that under tensile force the rupture occurs for three neighboring H-bonds simultaneously. In consequence, a three-fold higher force is required to convert a segment of coiled-coil  $\alpha$ -helix into  $\beta$ -sheet structure [30].

### Transition of a single $\alpha$ -helix

For a single  $\alpha$ -helix domain it was found that the unfolding occurs in an unsystematic fashion where random H-bonds break at different locations. Nevertheless, the overall stress-response is comparable to the coiled-coil superstructure with small variations in the transition of the different regimes [30].

The transition from  $\alpha$ -helix to  $\beta$ -sheet is reversible for a single molecule assuming no irreversible damage. A protein will fold back into the more stable  $\alpha$ -helix structure and H-bonds again as soon as no tensile force is acting on the molecule [30]. Tensile experiments on myosin proteins, which contain a large coiled-coil domain, showed that the refolding occurs within less a second [26]. Infrared spectroscopy of fibrin samples under tensile load demonstrated that the  $\alpha$ -helical structure is partially recovered after relaxation [9] which is consistent with simulation data [35].

In most experimental work that investigates protein response to force, multiple additional factors affect the measured response from the sample. For example, macroscopic techniques have used gelatinized samples where a full three-dimensional protein network is formed. The mesh parameters like branch point density and filament thickness will influence the mechanical properties as well as additional cross-linking [40]. Furthermore, when deforming a macroscopic specimen, one has to consider local defects and the sliding of filaments. Taken together, those effects create a smoother stress-strain curve compared to single-molecule stretching where the different regimes are less pronounced [6, 40, 41].

### 1.2.3 Measuring secondary structure with molecular spectroscopy

The secondary structure of proteins can be measured by spectroscopy, where light interacts with molecular vibrations that are determined by structural motifs. In the following section, the theoretical background for this sensitivity, which is the foundation of experiments in the later chapters, is discussed.

#### Background on molecular spectroscopy

Atoms in a molecule oscillate along their bonds with a characteristic frequency given by the reduced mass and their bonding strength. In a 'simple' case this might be an isolated O-H stretching vibration in pure water while in complex molecules, such as proteins, a vibrational mode can be formed by the combined collective motion of several nuclei [42]. The mathematical description of a vibration along a single bond is that of a harmonic oscillator. The atoms are drawn together by their chemical bond(s) with a potential energy that depends quadratically on the nuclear displacement from the mean bond length. Such a system oscillates with a frequency  $\nu$  that is defined by the reduced mass of all involved atoms  $\mu$  and a force constant  $k$  representing the bond strength as follows:

$$\nu = \frac{1}{2\pi} \sqrt{\frac{k}{\mu}} \quad (1.5)$$

The total energy of a harmonic oscillator contains contributions from both kinetic and potential energy that reflect the atomic motion and the stiffness of the bond. Because of the quantum mechanical nature of molecular bonds, the change in energy is only permitted in discrete steps. This leads to separated energy levels  $E_n$  instead of a continuous energy range and can be written as

$$E = \left(n + \frac{1}{2}\right) h\nu \quad \text{with } n = 0, 1, 2 \dots \quad (1.6)$$

Here,  $h$  is Planck's constant,  $n$  the quantum number of the respective energy level and  $\nu$  the frequency of the harmonic oscillator. The ground state energy of the system is given by  $\frac{1}{2}h\nu$ . As a consequence of those discrete levels, the exchange of energy with a light field must be done in matching quanta of light, ergo energy packages [42].

A molecule has  $3N-6$  degrees of freedom that reflect either a change in length of the chemical bond or in the angles between bonds. The resulting harmonic oscillations are the so-called normal vibrational modes of the molecule where all involved atoms move with a defined phase relation and at a certain frequency as illustrated for the water molecule in Fig.1.5. The normal vibrations of a molecule oscillate at frequencies in the mid infra-red

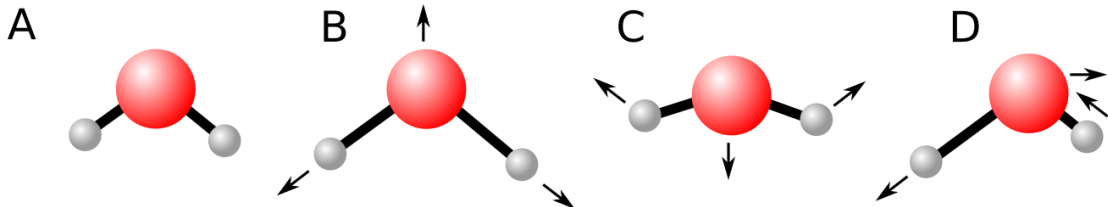


**Figure 1.5:** The water molecule has  $3N-6 = 3$  normal modes that oscillate with respect to the ground state (A): The symmetric stretch (B), the bending (C) and the asymmetric stretch vibration (D) [43].

(IR) region ( $2.5\text{-}50 \mu\text{m}$ , corresponding to  $200 \text{ cm}^{-1} - 5000 \text{ cm}^{-1}$ ) and therefore can be probed by either IR absorption or Raman scattering spectroscopy [42]. In IR absorption,

the exciting light becomes absorbed by the molecule if the photon energy matches the energy difference between two excited states or the ground state of a molecular vibration. Raman scattering on the other hand can be described as inelastic scattering of a photon. Here, an incident light field excites a mode into a short-living virtual state followed by immediate emission of a second photon. The energy difference between incident and emitted photon is transferred to a molecular vibration. Both IR and Raman can provide information about the energies of different vibrational modes in form of a spectrum, which gives the frequency-dependent intensity of the scattering or the absorption. Still, the underlying mechanisms differ fundamentally and lead to specific selection rules that define if a vibrational mode can be excited or not. A mode is active for IR absorption if the interaction leads to a change of its transition dipole moment and if the photon energy matches the required energy for the transition to a higher energy level. For Raman scattering, the selection rules state that the polarizability of the molecule has to change by the molecular displacement in addition to the matching in energy [42]. Thus, some (but not all) vibrational modes are only active in IR absorption while others only show up in Raman scattering [44]. The Raman process and the possibilities for its nonlinear enhancement will be discussed in more detail in section 1.4.

In general, the instrumentation for IR spectroscopy is more robust and has superior signal-to-noise ratios compared to Raman spectroscopy. However, the strong absorbance of water at IR energies but its poor Raman cross-section makes Raman spectroscopy the preferred method of choice when it comes to aqueous samples like most biological specimens [45]. The Raman scattering becomes especially strong for multiply bonded or electron-rich groups (e.g. C=O, C=N, C=C, S-S, S-C, S-H) while single bonded groups show less intense Raman bands [45]. In proteins, most Raman active modes are from molecular vibrations in the peptide backbone, aromatic chains (like in Phenylalanine), sulfur-rich side chains [45] and C-H oscillations. This results in a characteristic spectrum as shown in figure 1.6, which is dominated by an intense band between  $2800\text{ cm}^{-1}$  and  $3000\text{ cm}^{-1}$ , caused by  $\text{CH}_2$  and  $\text{CH}_3$  stretching vibrations, and an informative fingerprint region ( $500\text{-}1800\text{ cm}^{-1}$ ) where most other molecular vibrations can be found [46].

When taking a closer look at the fingerprint region of a protein spectrum, several prominent bands and peaks can be found (see also Fig.1.6). Starting at low wavenumbers, the first sharp peak at  $1004\text{ cm}^{-1}$  comes from the symmetric ring breathing mode from phenylalanine followed by several minor peaks C-C vibrations. The region from  $1200\text{-}1300\text{ cm}^{-1}$  represents the amide III modes caused by C-N stretching and N-H bending. A clear peak at  $1206\text{ cm}^{-1}$  represents contributions from phenylalanine and tyrosine. Next, a band from various  $\text{CH}_2$  twisting vibrations is located between  $1320\text{-}1340\text{ cm}^{-1}$  followed by a strong band from the  $\text{CH}_2$  deformation mode between  $1440\text{-}1460\text{ cm}^{-1}$ . The amide II band appears relatively weak at  $1550\text{ cm}^{-1}$  while the amide I gives high intensities around  $1650\text{ cm}^{-1}$  [46,47].

### The amide I band

Molecular vibrations in a protein are influenced by its secondary structure. Spectroscopy therefore can be used to measure those sensitive vibrational bands that reflect different structural motifs. The most important indicators in structure analysis are the amide modes that originate from the protein backbone. The intense band from  $1600\text{-}1690\text{ cm}^{-1}$  in the Raman spectrum is named amide I and arises predominantly from C=O stretching vibration of the peptide carbonyl groups and some minor contribution from the stretching and bending vibration of the C-N bond and N-H bond respectively (see Fig.1.7A) [48–50]. Going to lower wavenumbers, the amide II band is located at  $1480\text{-}1580\text{ cm}^{-1}$  followed by the amide III at  $1230\text{-}1300\text{ cm}^{-1}$  [46,51]. Those two spectral regions result from cou-

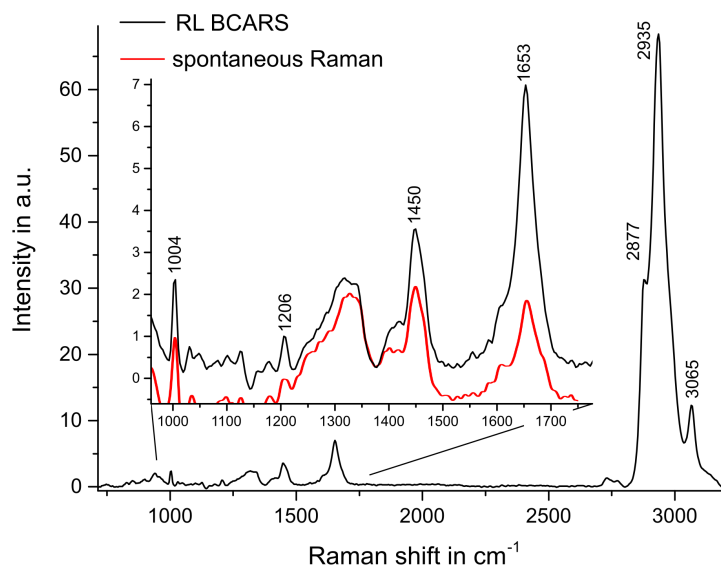


**Figure 1.6:** Representative Raman spectrum from protein. 200 mg/ml BSA in DI-water were measured with broadband CARS followed by phase-retrieval and error phase subtraction. A spontaneous Raman spectrum of BSA powder (red) shows similar peak positions. The intensity variation results from differently performed subtraction of the fluorescent background.

pled C-N stretching and N-H bending vibrations [52]. Several more amide bands exist at wavenumbers beyond  $800\text{ cm}^{-1}$  but can be neglected here due to their weak intensity [51]. Moreover, the amide vibrations are unimpaird from direct influence of the side groups and allow a somewhat universal analysis independent of the amino acid composition [51]. Hereafter, I focus on the amide I band for a more detailed discussion as this spectral region is used in the projects described in this thesis (chapter 3-5) to derive structural information.

The amide I band is the summed-up signal of multiple vibrational modes that each reflect different structural motifs. The vibrational energies of the amide modes change due to the secondary structures present in a protein sample. Because the Raman intensities are linearly dependent on the number of oscillators, the observed amide I band is the summed signal of each structural motif weighted by the respective contribution. In consequence, the amide band changes its maximum position and overall band shape due to the secondary structure present in the probed sample. As the individual peaks overlap to a large degree, the measured spectrum shows a broad band without clear features and, at first glance, appears to make a robust, quantitative analysis difficult [53–55]. The lower wavenumber side of the amide I band is flanked by further vibrations from aromatic side chains like in tyrosine, phenylalanine or tryptophan [55]. Depending on the amount of these amino acids in the polypeptide sequence, the additional peaks can affect the overall appearance of the amide I band. The side chain vibrations are located at  $1602\text{ cm}^{-1}$  (Phe),  $1607\text{ cm}^{-1}$  (Phe and Tyr ring vibration),  $1614\text{--}1620\text{ cm}^{-1}$  (Phe, Tyr and Trp) and  $1622\text{ cm}^{-1}$  (Trp) [46]. Furthermore, the amide I band spectrally overlaps with C=C stretch vibrations either from protein or lipids at  $1650\text{ cm}^{-1}$  and  $1670\text{ cm}^{-1}$  [46]. Those peaks are assumed to be weak enough to be neglected in the further data processing. Still, in cell or tissue samples the presence of lipid signal can disturb the amide I analysis. Thus, it can be summarized that the measured amide I band results from several slightly shifted peaks that are all from the C=O vibration and which each can be assigned to a structural motif or aromatic side chain vibrations. But why are these vibrations shifted?

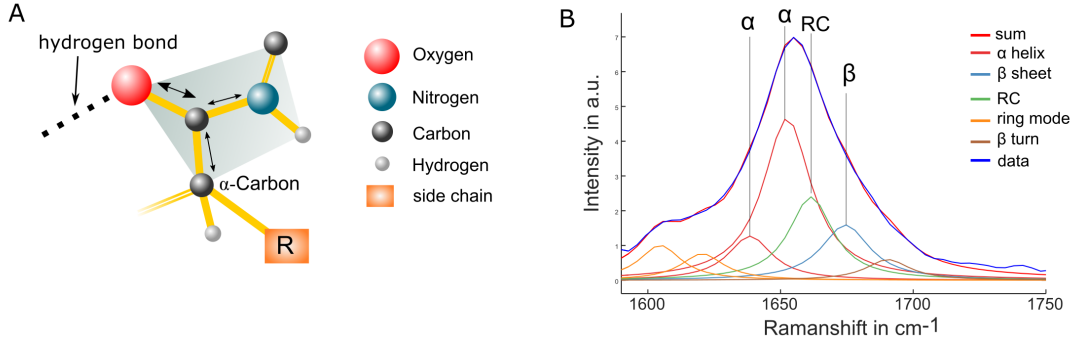


**Figure 1.7:** The amide I vibrations reflect the secondary structure of the sample. A) Molecular location of the Amide I mode in a polypeptide chain is highlighted by the shaded plane. B) Amide I band of bovine serum albumin (BSA) and its decomposition into Lorentzians for different structural elements

To understand the connection between secondary structure and vibrational energies, one has to consider how the single vibration becomes disturbed by its residues. In a polypeptide chain, the amide vibration of one group cannot be treated in isolation anymore as it is influenced by multiple local modes close by.

The interaction of two or more local modes depends on their spatial distance and their relative orientation. If the coupling is strong, the individual local vibrations become synchronized and form a delocalized state, a so called vibrational exciton [54]. In the transition dipole-dipole coupling model the coupling strength  $\beta$  is given by

$$\beta_{ij} = \frac{1}{4\pi\epsilon_0} \left[ \frac{\mu_i \cdot \mu_j}{r_{ij}^3} - 3 \frac{(r_{ij}\mu_i)(r_{ij}\mu_j)}{r_{ij}^5} \right] \quad (1.7)$$

where  $r_{ij}$  is the displacement vector between the two local modes  $i$  and  $j$  and  $\mu$  the respective transition dipole [54,56]. This coupling changes the mode energy with respect to the unperturbed vibration and thereby the resulting frequency as explained below.

### Amide I modes for $\alpha$ -helix structure

For a sufficiently long  $\alpha$ -helix, one can ignore the influence of the terminal groups when thinking about possible modes. Such a helix with 3.6 residues per turn is stabilized by intrachain hydrogen bonds. The  $\alpha$ -helix secondary structure must be treated as a 3D arrangement of local oscillators of each peptide unit  $j$  that interact along the chain but also with residues in the twists above and below [53,54]. Along the helical axis, an excitonic state  $A$  forms with an eigenstate energy of

$$E_A = h\nu_0 + 2 \sum_j \beta_j \quad (1.8)$$

Perpendicular to the helix axis (in  $z$ -direction), two weaker excitonic states can be found as whose transition dipoles are either in  $x$  or  $y$  direction and have a shifted energy of

$$E_A = h\nu_0 + 2 \sum_j \beta_j \cos\left(\frac{2\pi j}{3.6}\right) \quad (1.9)$$

The resulting local mode frequency is expected to be about  $1645 \text{ cm}^{-1}$  which is very similar to the calculated frequency for an unstructured polypeptide chain [54]. This weak peak shift might seem surprising as the modes become highly delocalized along the helix.



Yet, the competing couplings partially cancel themselves out as for the nearest neighbor  $\beta$  becomes large and positive but negative for all other couplings. Thus, the total shift in the amide I band in a  $\alpha$ -helix is only a few wavenumbers lower compared to random structure. In Raman scattering experiments on predominantly  $\alpha$ -helical proteins, the amide I band was found to be centered between 1640 to 1650  $\text{cm}^{-1}$  [55] which is consistent with those calculated frequencies.

### Amide I modes for $\beta$ -sheet structure

Different to the  $\alpha$ -helix, the  $\beta$ -sheet structure consists of several neighboring polypeptide chains that are coupled by interchain hydrogen bonds. The sheet-like arrangement is extended and can be assumed as a planar array of coupled oscillators [54,56]. The excitonic states can be found with energies that are affected by interchain coupling  $j$  as well as intrachain coupling  $i$  [53].

$$E_{ij} = h\nu_0 \pm \sum_{ij} \beta_{ij} \quad (1.10)$$

Sophisticated simulations of transition dipole coupling in anti-parallel and parallel  $\beta$ -sheets [54] found that only two out of many possible modes are observable by vibrational spectroscopy. The first one is caused by the interaction of transition dipoles orthogonal to the chain alignment and leads to a mode at 1620  $\text{cm}^{-1}$ . Yet this mode is only IR active and cannot be probed by Raman scattering. The second dominating mode comes from a transition dipole moment that lies perpendicular to the sheet plane [53,54]. While the local modes between adjacent strands are out of phase and thereby cancel their transition dipole out, the modes within a polypeptide chain are unison. This excitonic state is Raman active and causes a shift of the amide I band to 1670  $\text{cm}^{-1}$  [54]. Raman experiments on predominantly  $\beta$ -sheet structured proteins confirmed this second frequency for the amide I band [55].

## 1.3 Mechanobiology

The following section provides an overview on the mechanical properties of cells and how mechanical forces are recognized by cells.

### 1.3.1 Mechanical forces in nature

Cells are constantly exposed to external and internal forces. Every cell is subject to the pressure from blood flow, shear forces and pushing or pulling by neighboring cells. A cell is able to generate contractile forces by the actomyosin system [57] as well as protrusive pressure through actin polymerization [58]. This active mechanical role becomes obvious in migrating cells, where the cell's body is moving along a surface or through a 3D tissue matrix [57]. Moreover, the combined contraction of muscle cells creates the forces required for any physical work in living entity. The range of the resulting forces spans several orders of magnitude (see table 1.2), and cells must be sufficiently strong to sustain these loads. To do so, a complex system of intracellular polymer networks, named the cytoskeleton, that is linked to the plasma membrane, organelles, and, through specific anchorage points, to the external environment exists in each cell [59].

Type of force	Exerted stress	Reference
Shear stress due to blood flow	2.5 N/m <sup>2</sup>	[59]
Blood pressure	13 kN/m <sup>2</sup>	[59]
Muscle contraction	100 kN/m <sup>2</sup>	[59]
Bite (teeth) force, male human	> 3000 kN/m <sup>2</sup>	[60]

**Table 1.2:** Examples for biomechanical forces over a range of several orders of magnitude.

### 1.3.2 The cytoskeleton

Eukaryotic cells construct a cytoskeleton consisting of three separate protein networks as shown in figure 1.8: actin stress fibers, microtubule and intermediate filaments. Each element of the cytoskeleton has different mechanical properties and functional roles. Together, these structural networks resist deformation and maintain the cellular integrity [61]. The filamentous components are constantly adapted by the cells to compensate forces in the most effective way. To do so, new filaments are assembled from a soluble pool of monomers where needed while elsewhere structures are broken down and recycled [62]. There is no singular starting point for building up the cytoskeleton as '*cells form from other cells*' [62], but only continuous expanding and remodeling of existing structures. In the following section, I'll briefly characterize the three major components of the cytoskeleton followed by an introduction on the mechanical properties of the combined network structure.

#### Elements of the cytoskeleton

Stress fibers consist of multiple polymerized filaments formed from actin, a highly conserved and abundant globular protein [63]. Stress fibers are bundles of filamentous actin (F-actin), which itself forms thin filaments only  $\sim 5$  nm in diameter. They act as 'cables' for all kinds of pulling forces within the cell. Under mechanical load, they show (relatively) high stiffness of  $10^3$  kPa [64] followed by rupture at 20 % strain [65, 66]. In combination with myosin motor proteins and potentially other crosslinking proteins, actin filaments form stress fibers (so-called actomyosin filaments) that are able to generate tension. Myosin molecules link actin filaments and nearby stress fibers to translocate them

by a coordinated power stroke under consumption of adenosine triphosphate [57]. The contraction of actomyosin filaments is a potent force generating mechanism of all kind of cell motility (evident e.g. in muscle contraction) but also plays a pivotal role in setting the cytoskeleton under a prestress, which will be discussed in more detail later [57, 62]. Microtubules (MT) are tube-shaped polymers of 25 nm in diameter, which are assembled of  $\alpha$ - and  $\beta$ -tubulin dimers. They are the most rigid and stiff component in the cytoskeleton and have a persistence length of 1 mm [61, 67]. As a result, they can bear large compression forces and act as structural rods within the cytoskeleton. Microtubules grow from a central microtubule organizing center towards the periphery but single branches can break off and exist further as isolated components [62]. Besides their usual structural role, MT rearrange into the mitotic spindle that segregates chromosomes into two sets during mitosis [68]. The third cytoskeletal network is called intermediate filaments (IF). While the two other components of the cytoskeleton consist of limited number of isoforms, IF can be built from a variety of different proteins [38]. The most common IF proteins are vimentin, desmin and keratin for cytosolic IF as well as lamin for nuclear IF [38, 62]. Intermediate filaments are more flexible than f-actin or MT and can be extended to a multifold of its initial length [6, 69]. IF exhibit a multi-regime strain response that is caused by conformational changes followed by strain-hardening [6, 66]. These mechanical properties led to the suggestion that IF contribute to the cellular integrity predominantly under high-strain conditions where a cell is deformed far above its physiological range [70]. Yet, for many cell types a change in the orientation and density of the IF network can be observed when shear stress is applied [61, 71]. IF have been shown to be reinforced into thicker bundles when mechanical stress is applied and thereby make the cells more robust which indicates a mechanical role of IF also at relatively low mechanical stress [71]. The

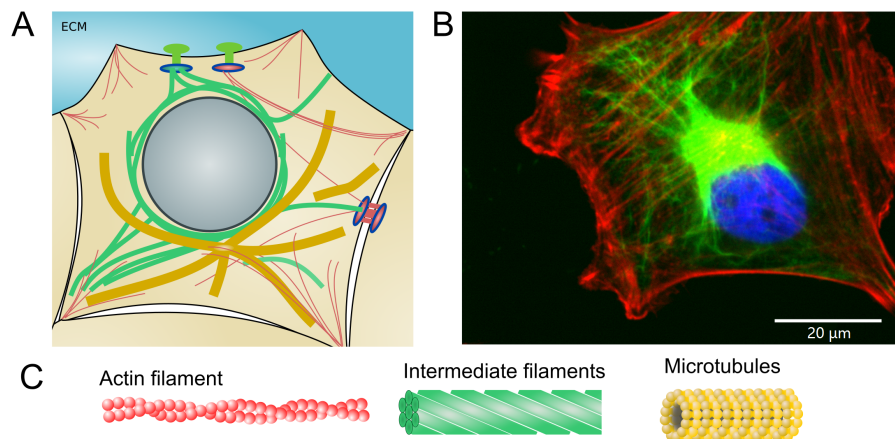


**Figure 1.8:** Elements of the cytoskeleton in adherent cells. A) Schematic of the actin stress fibers (red), intermediate filaments (green) and microtubules (yellow) in an epithelial cell. The cytoskeleton is connected by desmosomes to neighboring cells and to the ECM via focal adhesions. B) Cytoskeletal elements of a HeLa cell shown by fluorescently labelled actin stress fibers (phalloidin, red), vimentin IF (GFP, green) and nucleus (DAPI, blue). The scale bar represents 20  $\mu\text{m}$ . C) Molecular architecture of actin filaments, IF and MT.

cytoskeleton is physically connected to the cell's environment, ergo neighboring cells or the ECM, by special contact sites. Cells attach to the ECM using integrin receptors that span the cell membrane and bind to actin-binding proteins in the cytosol. These actin-binding proteins, such as talin, vinculin and paxillin, then provide the further linkage to the actin cytoskeleton [72, 73]. Multiple integrins form clusters called focal adhesions (FA), that locally anchor the cell to the ECM. These adhesions undergo a constant turnover and new FAs are formed at locations where mechanical force needs to be transmitted to the

surrounding while elsewhere existing connections are disassembled. The site-specific force sensing that allows such an adaptive assembly of FA is realized, at least in part, by conformational changes in vinculin [74]. In addition to FA, cells can form connections to adjacent cells, so called desmosomes, by transmembrane proteins of the cadherin family. The cytoplasmic part of cadherin proteins is linked to the actin network and the extra-cellular part binds with similar proteins from other cells. The inter-cellular linkage allows the force transmission between the cytoskeletons of different cells which has been shown to regulate the functional state of cells within tissue [75, 76].

	<b>Diameter</b> [ <i>nm</i> ]	<b>Persistence length</b> [ $\mu m$ ]	<b>Reference</b>
F-actin	5-10	10	[67]
IF	10	1	[6]
MT	25	$10^3$	[67]

**Table 1.3:** Mechanically relevant parameters of cytoskeletal elements

### Mechanics of the cytoskeleton

The different cytoskeletal networks are not isolated but rather interconnected by various proteins. For example, plectin acts as a universal linker protein that connects IF, MT and stress fibers to one another as well as towards focal adhesions, desmosomes and the nucleus [77]. Furthermore, stress fibers can be linked to IF and MT by multiple proteins of the plakin family [78]. As described above, each individual network possesses unique molecular qualities that result in distinct mechanical properties - linking structure with mechanics. While f-actin and IF withstand tensile forces, MT structures are built to resist compression forces. However, to understand how cells response to physical forces, a universal model that takes all three cytoskeletal elements and their interconnectivity into account is required.

First, consider the possible configuration of a self-assembled network of loose fibers (f-actin) connected to rods (MT). Such an arrangement would hardly be able sustain its shape against any disturbing force as its structural components are not fully constrained [79]. To avoid this freedom in motion, the entire system needs to be 'latched together' in some way. Such a so-called prestress to the cytoskeleton is provided by the contractile force generation by actomyosin. Neighboring actin fibers become cross-linked by multiple myosin motor proteins that pull on the fibers and thereby create tensile forces [57]. This leads to a contraction of stress fibers which then causes the entire network to become taut. As the stress fibers are connected to other components of the cytoskeleton, the prestress is transmitted across the entire interwoven system. Several elements can resist such a contraction: MT can bear compression and thereby give an internal counterpart to the cell membrane against tensile loads. Moreover, cells and thereby the cytoskeleton, are constrained in their surrounding by focal adhesion sites or cell-cell adhesion complexes that resist the cell-generated contraction. Taken together, this creates a prestressed or tensegrity system, where pulling forces from stress-fibers are in balance with compression resistance from MT and external anchorage points [62, 79]. This prestress is thereby maintained and effectively stabilizes the cytoskeleton against local mechanical disturbance [62]. This building principle is called 'cellular tensegrity' [80] and explains many observed mechanobiological phenomena in cells [62]. It was adapted from architecture, where the term tensegrity was firstly coined by the Buckminster Fuller, who described the interplay of tension bearing cables and rigid struts as an economic and structurally efficient way to construct buildings and structures [81]. An example how tensegrity gives stability to a large-scale work of art is shown in Fig.1.9.

Several experiments have demonstrated that the assumptions of tensegrity can be applied to cells. For instance, actin filament bundles in living cells were disrupted by laser nanoscissors and reacted immediately through contraction indicating their tensed state [82]. Brangwynne and coworkers demonstrated that microtubules bear large-scale compressive loads by applying compressive forces via microneedles on MT and thereby causing similar buckling as observed *in vivo* [83].

So far, the model of a prestressed cytoskeleton did not require the mechanical contribution of intermediate filaments. Stress fibers as cables and MT as rods should be sufficient to build a stable structure. Yet, computational modelling of a simple cytoskeleton in tensegrity architecture showed that the addition of IF influenced the time-dependent elasticity of the system and prevent peak values at specific frequencies [84]. From microrheological measurements of cell stiffness, it is known that IF contribute to the overall mechanical response and that the absence of vimentin IF caused a reduced proliferation rate in fibroblasts [70]. However, because IFs are soft at low strain, their contribution to cell elasticity is assumed to be only relevant for large deformations [62, 70] where strain stiffening sets in [66].

Indeed, tensegrity is able to describe many cellular phenomena but it is not a complete model. Multiple aspects of cell mechanics like the elastic properties of cytoskeletal components or the presence of multiple compressed MTs at nodes are not covered by tensegrity [85]. Some mechanical behavior can better be understood in model systems that assume cells as soft glassy material or the cytoskeleton as viscoelastic polymers [86, 87]. Each model thereby covers only parts of the whole system and should be considered as incomplete in describing cellular mechanics.



**Figure 1.9:** Tensegrity, the combination of tension and structural integrity, allows the *Needle tower* (by Kenneth Snelson, 1968) to stand up to 18 m without having a continuous rigid structure. Picture taken by the author outside the Hirshhorn Museum and Sculpture Garden in Washington, DC, United States.

### 1.3.3 Mechanosensing in cells

Cells are active objects which exert physical forces to their surrounding and can adapt their cytoskeleton in response to mechanical stimuli [88]. While most cellular processes, like enzyme activity, reaction rates and affinities are seen as pure chemistry, the influence of mechanical forces on cell behavior has become increasingly apparent [89]. This

mechanosensitivity is most obvious in the senses of hearing and touch, where pressure is converted into neural activity that leads to a signal and the body's perception [90]. However, already on the level of single cells (and even single enzymes) one can observe different reactions to physical forces that influence cell motility or even cell differentiation into specific lineages [1, 61, 91, 92].

Recent studies have shown that cells actively pull on their surroundings to probe its stiffness and then convert the obtained information into behavioral changes [93, 94]. Thereby, the matrix stiffness directly influences the cytoskeletal tension, amount of focal adhesions and adherens junctions, and is able to drive fibroblasts into a tumor phenotype [2].

In tissue, cells use mechanical clues to undergo mitosis in a favorable direction [95]. The forces between neighboring cells lead to a directed movement of the cell collective, which is required in morphogenesis [96] and tissue repair [97]. It was shown that these cell-cell interactions are not only chemical but also physical, and therefore require mechanical sensing. Moreover, a complex tug-of-war like interaction between leader cells at the leading edge and more remote cells have been found [98]. All those examples cannot be reduced to one single reaction pathway; instead, a variety of mechanosensitive proteins in different locations (and under different loads) must be invoked to explain those observed behaviors.

In general, the sensing process can be classified in three distinct steps: 1) force transmission, 2) transduction, and 3) response [88, 89]. First, mechanical forces from external sources like the ECM, neighboring cells or the substrate as well as internal pressure and tension are directed to mechanosensitive elements. Here, the force is converted (transduced) into chemical signals [89]. These cause the binding of molecules, start a polymerization or switch membrane channels [99] and finally even might change gene expression [61].

As an example, the pulling of nearby cell acts firstly on an adhesion protein like cadherin which is connected to the cytoskeleton. Next, the force is propagated by rigid proteins or long-range protein networks like the actin filaments or intermediate filaments to force sensitive proteins (e.g. talin) which respond by changing their conformation [89]. As a result, the altered protein offers new binding sites that allow reinforcing proteins (e.g. vinculin) to locally stabilize the cytoskeleton [100]. Taken together, the external tensile force is firstly passed on to a non-arbitrary intracellular site where sensing takes place and a response in form of additional binding is initiated [88]. An overview of various sensing mechanism is given in table 1.4. When investigating the effect of mechanical interference with cells, one has to consider the temporal component, too. Cyclic changing forces might result in different response than static ones or changed force rates. In addition, the overall duration of the applied force will cause further mid-term and long-term reactions like migration or apoptosis [61, 89]. At the heart of all those sensing processes stands a conformational change of the involved protein that triggers a desired response. In the research chapters of this thesis, I will investigate a variety of systems that show changes in secondary structure in response to mechanical forces or surrounding conditions.

### 1.3.4 Probing cellular mechanics

Several methods have been established to investigate the mechano-response of cells over the last years.

#### Active deformation

A first group of experiments uses direct physical probes to apply a local force to the specimens. In this way, the cellular elasticity can be quantitatively measured by nano-indentation with AFM [105], which provides information on the *in vivo* mechanical properties of cytoskeletal elements [106]. Optical tweezers, where the focus of an intense laser

Type	Description	Function	Reference
Ion-channel opening	The mechanosensitive channel of large conductance' opens its transmembrane barrel in response to increased lateral tension	Regulation of osmotic conditions	[99, 101]
Exposing cryptic binding sites	Talin-1 is bound to focal adhesions and possesses a tail rich in vinculin-binding sites. These are mostly inaccessible in the relaxed state but become exposed under force to allow vinculin recruitment.	Stabilization of connections between focal adhesions and the cytoskeleton	[100]
Exposing cryptic binding sites	Tensile load causes P130Cas substrate domain protein to extend. This results in higher levels of phosphorylation and initiates the RAP1 signaling pathway	Formation of cell adhesions, morphogenesis, cell growth	[102, 103]
conformational change in the filament	Actin filament bending affects the location of branch nucleation.	organizing the cytoskeleton in response to force	[104]

**Table 1.4:** Examples of mechanosensitive proteins.

beam creates a local dragging force, can be used to apply forces either by manipulating microbeads with linker molecules to the cell membrane [107–109] or by optically trapping and thereby squeezing the cell itself [110]. Similar experiments can be performed with super-paramagnetic beads that are bound to a cell. By applying a high magnetic field gradient on a metal needle mounted on a micromanipulator one can create precise displacements of the beads and thereby creating a well-defined local pulling force [111]. Another tool is micro aspiration, where a micropipette and negative pressure is used to locally suck in the cell surface. From observing how the leading edge moves into the glass tube one then can gain insights on the physical properties [112, 113].

Macroscopic stretching of elastic membranes can be utilized to deform cells that are grown on such a substrate. Flexible materials such as polydimethylsiloxane (PDMS) can be molded or spun into optical transparent and biologically inert thin films that are suitable for culturing cells [114, 115]. The deformation of such a membrane is almost homogenous over the entire area providing a precise local deformation of each cell [115]. As the samples are covered in medium during the entire time, those cell stretching devices allow long-term measurements to study oscillatory strain [114, 116, 117].

### Substrate stiffness

Besides those active methods, the substrate itself where cells are grown on top or inside can act as a mechanical inducement. Cells feel their environment and try to balance out the external stiffness with internal prestress of the cytoskeleton [62]. One therefore can vary the substrate stiffness or creep behavior to induce a specific response [1, 91, 118]. The elastic modulus in biological material spans several orders of magnitude from soft eukaryotic cells ( $1 - 10^3$  Pa), muscle cells ( $10^4$  Pa) tendon ( $10^7$  Pa) up to bone tissue ( $10^9$  Pa) [119]. This variability in stiffness is of special interest in the case of cancer mutations, where the cellular modulus is increased from  $\sim 170$  Pa for normal mammary

gland cells to 4000 Pa in tumor cells [2]. Substrates of different stiffness are used in a vast number of studies and led to striking insights on cell mechanics so far [92, 120]. Paszek and coworkers demonstrated that the matrix stiffness can regulate cytoskeletal tension and change the tissue phenotype [2]. By altering the collagen substrate stiffness between 170 Pa and 5000 Pa they found changes in single cell and cell colony morphology as well as upregulated actin, vinculin and focal adhesion kinases on stiff surfaces [2]. Even more pervasive response to substrate elasticity was shown for mesenchymal stem cells. These cells developed into specific lineages (neurons, muscle or bone cells) as predetermined by the respective matrix elasticity [1].

### Chemical agents

A more indirect yet powerful way to perturb the mechanical equilibrium of cells is by manipulating the cytoskeletal components with chemical agents. By selectively removing or deactivating elements of the cytoskeleton one can investigate its respective contribution to the global mechanical properties.

Stress fibers can be depolymerized by latrunculin-A, a marine toxin, without affecting the MT network [121, 122]. The loss of actin cables releases all intracellular prestress and leads to spherical cells. Another, more gentle way to reduce cellular tension is switching off the actomyosin system with the molecule blebbistatin, while f-actin stays structurally intact. Through the inhibition of adenosine triphosphates by blebbistatin, motor proteins like myosin get blocked which then prevents further f-actin contraction and therefore the generation of tension [123]. To disturb the microtubule structure, cells can be treated with colchicine, which binds to the tubulin heterodimers with high affinity and thereby suppresses the assembly of MT. This results in mostly depolymerized tubulin over time [124, 125]. Intermediate filaments can be specifically disrupted by the drug cycloheximide while the other cytoskeletal components remain unaffected. The disassembly is reversible and new IF were shown to form within several hours [126].

### 1.3.5 Mechanically induced structural transitions in biopolymers

In this thesis, the mechanical behavior of two loadbearing biopolymers is studied: fibrin in chapter 3 and vimentin intermediate filaments in chapter 5. Both proteins are shortly described in the following sections followed by a discussion of their common structural features.

#### Fibrin as extracellular loadbearing protein

The essential protein in blood clot formation is fibrin, which forms a mesh-like polymeric network together with platelets to stop bleeding [27, 41]. To form such a macroscopic plug, the protein gel must be able to withstand the pressure of blood flow as well as occurring deformations without failure. Therefore, the structure should be able to react elastically to allow flexible response for small displacements while becoming stiff and rigid for larger strains [27]. This is achieved by a multi-scale mechanical response that's based on several hierarchical acting mechanisms [40, 41].

Fibrin is polymerized through the activated protease thrombin from the monomer fibrinogen that circulates in the bloodstream [27, 128]. Figure 1.10 depicts the molecular structure of the precursor fibrinogen consisting of three chains ( $A\alpha, B\beta, \gamma$ ), two terminal D-regions and a central E-regions which are connected by coiled-coil segments. To initiate the polymerization, thrombin cleavage releases the fibrinopeptides FpA and FpB and thereby makes the knobs 'A' and 'B' accessible for binding.

In a first stage, fibrinogen assembles into protofibrils of half-staggered opposing molecules



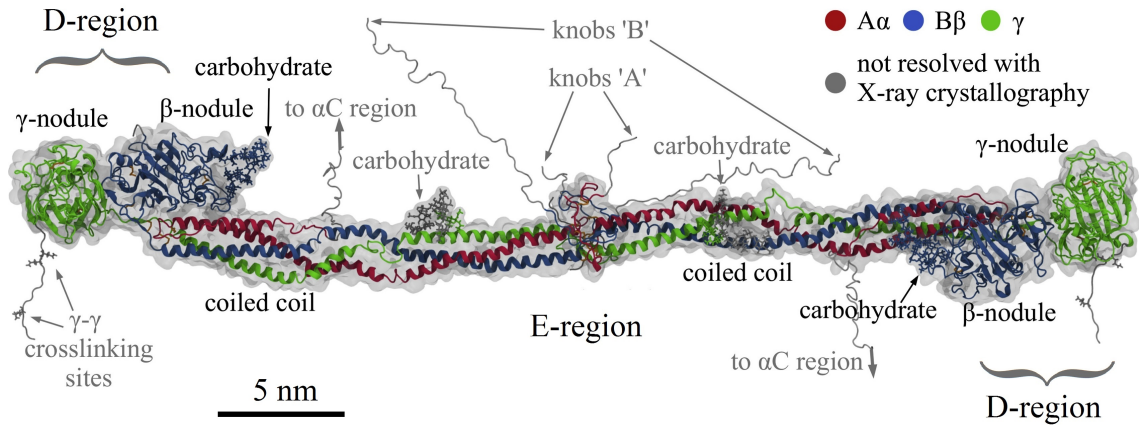


**Figure 1.10:** Structure of monomeric human fibrin. Figure adapted from [127] and based on PDB:3GHG

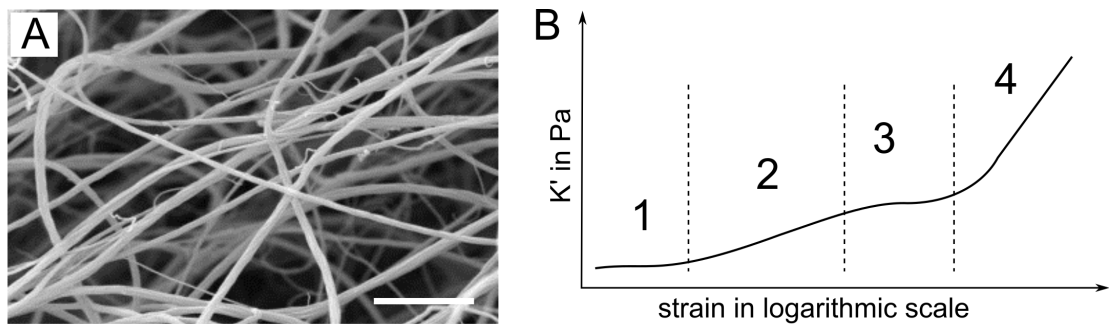


**Figure 1.11:** Fibrin structure and elastic properties. (A) Scanning electron microscopy image of a fibrin clot showing thick fibers with few branching points, reprinted from Weisel, 2004 [27]. The scale bar represents 5  $\mu\text{m}$ . (B) Schematic illustrating the different strain regimes of fibrin. At low strain the network stiffness is elastic and mainly caused by thermal fluctuations (1). Increasing strain leads to stiffening of the fibrin sample as the thermal slack from fibers segments is pulled out (2) followed by a plateau regime where fibers are stretched and undergo conformational changes (3). Final strain-stiffening sets in when all extendable domains are stretched (4) [40, 41].

followed by lateral connection of protofibrils into fibers. These fibers are non-covalently bound and equilateral branching takes place to create an interwoven three-dimensional network (see also Fig.1.11A) [27, 129]. This initial fibrin formation is followed with some delay by cross-linking by activated factor XIII [130] where the C-terminal  $\gamma$ -chains of adjacent fibrin molecules is linked by covalent isopeptide bridges [27].

A polymerized and cross-linked fibrin hydrogel shows viscoelastic properties that result from the consecutive responses that take place on the different hierarchical levels of the network as depicted in Fig.1.11 [27, 40, 41]. Most importantly, high strains are required to cause strain-stiffening. This offset between initial linear regime (2) and the nonlinear stiffening (4) is caused by the sequential unfolding of the  $\alpha$ -helical domains into  $\beta$ -sheet leading to a constant force that is necessary for further elongation of the material (regime 3 in Fig.1.11B) [9, 17, 41, 131].

### Vimentin intermediate filaments

Intermediate filaments are formed by a diverse group of proteins that share a similar structural design. A coarse classification distinguishes keratins, found in hair, nails and feathers, lamins that supports the nuclear envelope and vimentin-like cytoplasmic IF forming proteins [38]. The following section describes vimentin, the most abundant IF forming protein in mesenchymal cells, and how it assembles into intermediate filaments.

The vimentin monomer consists mainly of a  $\alpha$ -helical rod domain of  $\sim 45$  nm length and non-helical, flexible terminal domains (head and tail) [38, 132]. Its central rod domain is subdivided in three helices (coil1A, coil1B and coil2) that are connected by linker segments (L1 and L12) that act as hinges for the otherwise rigid helix domains as illustrated in figure 1.12A. The head domain is required for the assembly of higher-order structures but the exact molecular mechanism is still unknown [133, 134].

Two individual vimentin monomers form a dimer by curling into a coiled-coil formation, which is the basic building block for further assembly [38]. The dimers firstly form premature unit-length filaments (ULFs) consisting of the lateral grouping of typically eight antiparallel tetramers [38, 39]. Those ULFs then grow stepwise into micrometer-long filaments that form spread out networks *in vivo* [133]. While the exact process of branching and network formation within cells is still unknown [135], *in vitro* studies on hydrogel systems have shown that vimentin IF form networks of about  $1\ \mu\text{m}$  mesh size [136]. The mechanical properties of vimentin IF have been investigated experimentally in the form of hydrogels [66] and single filaments (figure 1.12B) [30, 39] as well as by MD simulations [7, 30, 137]. It was found that vimentin IF under tensile load exhibit distinct strain regimes that reflect different mechanisms. At low strain, the samples behave with linear elasticity followed by a plateau regime that continues until strain stiffening sets in for large deformation [7, 39]. The extensibility for Vimentin IF is many-fold larger than for actin or microtubule and can reach up to 350 % of the initial length before rupture [39, 66]. Similar to fibrin, the delayed stiffening results from the sequential unfolding of  $\alpha$ -helical structure to  $\beta$ -sheet structure and the associated gain in molecule length [7, 30]. This unfolding process is discussed in more detail in chapter 5.

### Coiled-coil as a fundamental motif in structural biomaterials

Fibrin and vimentin filaments share common features that can be seen as universal for structural biomaterials. Both proteins fold to a large degree into  $\alpha$ -helical domains that undergo structural transitions into  $\beta$ -sheets under extensional force. The fibrinogen monomer and the basic vimentin dimer form a coiled-coil motif where several  $\alpha$ -helical segments wrap around each other. This superstructure provides additional structural stability as the disruption of the coiled chains requires firstly helix unfolding followed by an unzipping

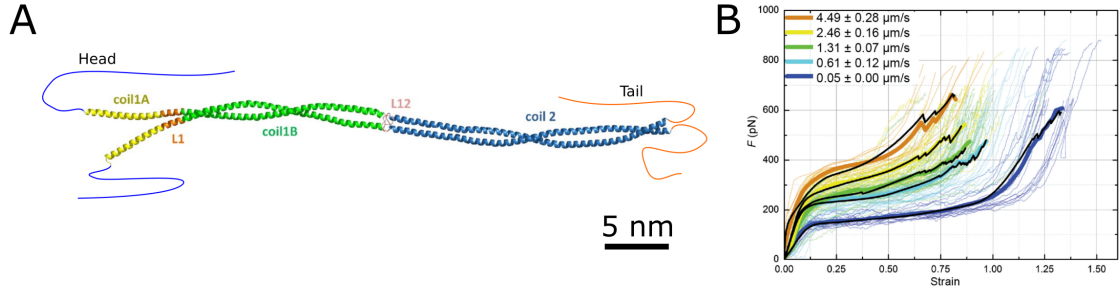


**Figure 1.12:** Vimentin structure and mechanical properties. (A) Structural model of human vimentin dimers based on crystallographic data, adapted from Chernyatina *et al.* [132]. (B) Force-strain curves of vimentin filaments at different loading rates, reproduced from Block *et al.* [39] under CC BY 3.0.

process. Taken together, this creates a high energy barrier that protects the protein's structural integrity against mechanical forces [21, 138]. At low strain vimentin IF [66] as well as fibrin [41] are very soft materials allowing for elastic response to small deformations. For both systems, the strain-hardening does not occur immediately (as for actin [139]) but for large deformation. Before reaching the nonlinear stiffening regime, energy is required to unfold the  $\alpha$ -helix segments into an extended form [6, 7, 9, 32]. Because of the similar secondary structural design, the mechanical behavior of both proteins under load is rather similar. While fibrin has to provide stability on the macroscopic scale of a blood clot, vimentin intermediate filaments have the comparable role of a 'safety belt' within a cell [140, 141].

## 1.4 Coherent anti-Stokes Raman scattering

The following chapter outlines the theoretical background for coherent anti-Stokes Raman scattering (CARS) spectroscopy as it is used for the experiments in this thesis. Starting from spontaneous Raman scattering, the basics of nonlinear Raman interaction are derived, followed by a detailed overview on broadband CARS and the required processing that result in a quantitative spectrum of the probed sample.

### 1.4.1 Spontaneous Raman scattering

Light can interact with matter by absorption or scattering. When a photon gets elastically scattered by a molecule the resulting photon contains the same energy as the incident one. This process is called Rayleigh scattering and no energy is transferred from the incident photon to the molecule. Thus, no information on the interaction partner can be obtained from this process when analyzing the (energy of) scattered light [43]. Spontaneous Raman scattering on the other hand results from inelastic light scattering, where the emitted photons either lose or gain energy with respect to the exciting ones. A photon with an initial energy of  $\hbar\omega_1$  might lose some energy when colliding with a molecule which then becomes excited into a higher energy level  $v$ . This surplus in energy is converted into vibrational, rotational or electronic energy of the molecule [43]. The resulting photon possesses a Stokes-shifted frequency  $\omega_s = \omega_1 - \omega_v$  reflecting its lower energy. But also the opposite situation is possible: If an initially excited molecule scatters a photon, it will be excited further into a virtual state, which is not necessary an eigenstate of the molecule [43], and immediately fall back to ground state while emitting a photon that obtains the entire energy difference. The frequency of such an anti-Stokes shifted photon is  $\omega_{as} = \omega_1 + \omega_v$ . All three processes are summarized in the level diagram in figure 1.13.

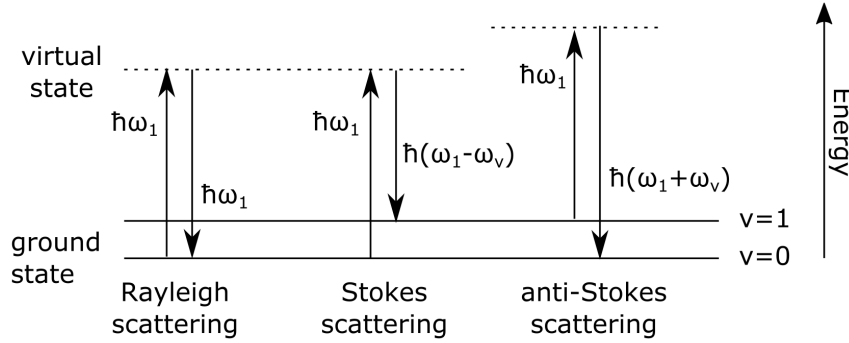


**Figure 1.13:** Jablonski diagram of Rayleigh scattering and the two types of spontaneous Raman scattering.

The scattering mechanism can be understood as a interaction of the oscillating electric field of a photon and the electron cloud of a molecule if both are brought in close proximity. The Coulomb force caused by the electric field drives the electrons, which follow the field instantaneously with the same frequency as the exciting light. Because the electrons are bound to nuclei, their oscillation is coupled to nuclear motion and energy transfer between both is possible.

In the non-resonant case, the electric dipole moment  $\mu$  is given by the product of polarizability  $\alpha(t)$  and the driving field, defined by its amplitude  $A$  and its frequency  $\omega_1$  as

$$\mu(t) = \alpha(t)E(t) = \alpha(t)Ae^{-i\omega_1 t}. \quad (1.11)$$

The optical polarizability of a molecule depends on the time-dependent internuclear separation  $Q(t)$  and can be written for small displacements in form of a Taylor series as

$$\alpha(t) = \alpha_0 + \left( \frac{\delta\alpha}{\delta Q} \right)_0 Q(t) + \dots \quad (1.12)$$

The nuclear motion  $Q(t)$  can be described as a classical harmonic oscillator that is fully defined by its amplitude  $Q_0$ , the nuclear resonance frequency  $\omega_\nu$  and the phase of the nuclear mode vibration  $\varphi$ . We therefore can write

$$Q(t) = Q_0 [e^{i\omega_\nu t + i\varphi} + e^{-i\omega_\nu t - i\varphi}]. \quad (1.13)$$

Using this definition in eq.1.12 gives the dipole moment  $\mu$  of a molecule in the expanded form of eq.1.11 as

$$\mu(t) = \alpha_0 A e^{-i\omega_1 t} + A \left( \frac{\delta\alpha}{\delta Q} \right)_0 Q_0 e^{-i(\omega_1 - \omega_\nu)t + i\phi} + A \left( \frac{\delta\alpha}{\delta Q} \right)_0 Q_0 e^{-i(\omega_1 + \omega_\nu)t - i\phi} \quad (1.14)$$

where  $\alpha_0$  is a constant polarizability,  $\delta\alpha/\delta Q$  the coupling strength between nuclear and electronic coordinates and  $\phi$  the phase of the nuclear vibration.

An oscillating dipole therefore emits new electric fields when being excited from an incident photon. By taking the frequencies appearing in each term into account, one can associate the first term to Rayleigh scattering while the two last terms describe Stokes- and anti-Stokes Raman scattered contributions which allow the direct measuring of the vibrational frequency of the dipole. Both Raman terms are direct proportional to the amplitude of the nuclear motion as well as to its influence on the polarizability. Furthermore,

the phase-shift  $\phi$  indicates that the Raman signal of a sample is incoherent because the phase shift is different for each dipole emitter while the Rayleigh scattering is independent from the nuclear vibration and therefore coherent.

Raman scattering spectroscopy is a useful and established tool but suffers from the low cross section of the Raman processes. The emitted intensities at the Stokes- and anti-Stokes frequency depend on the polarizability of the molecule and are therefore much weaker than Rayleigh scattering [142]. Thus, only about 1 out of  $10^8$  photons are Raman scattered [143] and one has to pay in long acquisition times or high excitation laser intensities to obtain a sufficient strong signal.

### 1.4.2 Towards greater signal: CARS

Various techniques have been developed to enhance the weak Raman signal and thereby increase its sensitivity as a spectroscopic tool. By tuning the excitation laser frequency close to the molecular vibration of interest, the scattering cross-section becomes enhanced by several orders of magnitude. Yet, this so-called resonance Raman scattering suffers in many cases from strong fluorescence and sample decomposition [143]. Another group of methods employs field-enhancement effects at metallic interfaces (lightning rod effect) to generate more Raman scattering. Those high local fields can be achieved by rough surfaces and close to metal nanoparticles (surface enhanced Raman scattering, SERS) [144] from where the tip of an AFM cantilever can be seen as the most well-defined one (tip-enhanced Raman scattering, TERS) [145]. A third approach takes advantage of the simultaneous interaction of multiple fields with the sample which will be discussed in more detail in the following.

In coherent Raman scattering, additional stimulating fields enhance the probability of emitting radiation at the Raman-shifted frequencies [42]. The two main optical techniques are stimulated Raman scattering (SRS) [146] and coherent anti-Stokes Raman scattering (CARS) [147], which both were firstly described in the 1960th but only became popular to study biological samples in the last two decades due to technological progress [148–151]. SRS differs from spontaneous Raman scattering in the way how individual modes are oscillating compared to each another. While in spontaneous Raman scattering the oscillations are incoherent they become synchronized and therefore coherent in SRS. This results in a coherent polarization in the samples and thereby an amplification of the scattering process itself [152]. However, the SRS signal spectrally overlaps with the excitation field signal and a sophisticated separation by lock-in amplifiers is required to obtain quantitative results [151, 153]. A detailed summary on SRS can be found in recent reviews from Prince [153] and Cheng [151].

The experiments described in this thesis are based on the CARS technique, which will be discussed in more detail in the following. To derive the main properties of coherent Raman scattering with a focus on the CARS process, I follow the line of arguments from Boyd [154] and Potma [155]. The central question to solve is how to get a stronger signal without increasing the average laser intensity.

A Raman signal becomes amplified when the interaction of the exciting field with the molecular vibration gets stronger, for example by driving the oscillator at its resonance frequency. This can be achieved by combining two incident fields with a frequency difference matching the resonance frequency of a vibrational mode. For a weak exciting electric field, the polarization depends linear on the field and can be written as:

$$P(t) = \epsilon_0 \chi E(t) \quad (1.15)$$

If the incident field becomes large, the electron cloud is no longer able follow the driving field in a linear fashion and the interaction becomes nonlinear. For such a nonlinear case,

the induced polarization can be described by expanding eq.1.15 into a power series as followed:

$$P(t) = \epsilon_0 \left[ \chi^{(1)} \mathbf{E}(t) + \chi^{(2)} \mathbf{E}^2(t) + \chi^{(3)} \mathbf{E}^3(t) + \dots \right] \quad (1.16)$$

where  $\chi^{(n)}$  is the  $n^{th}$  order susceptibility.

In coherent Raman scattering two optical fields oscillating at frequencies  $\omega_1$  and  $\omega_2$  are employed to drive a molecular vibration of a molecule. For  $\omega_1 > \omega_2$  the combined fields cause a nonlinear electron motion at the (difference) beat frequency  $\Omega$  given by

$$\Omega = \omega_1 - \omega_2. \quad (1.17)$$

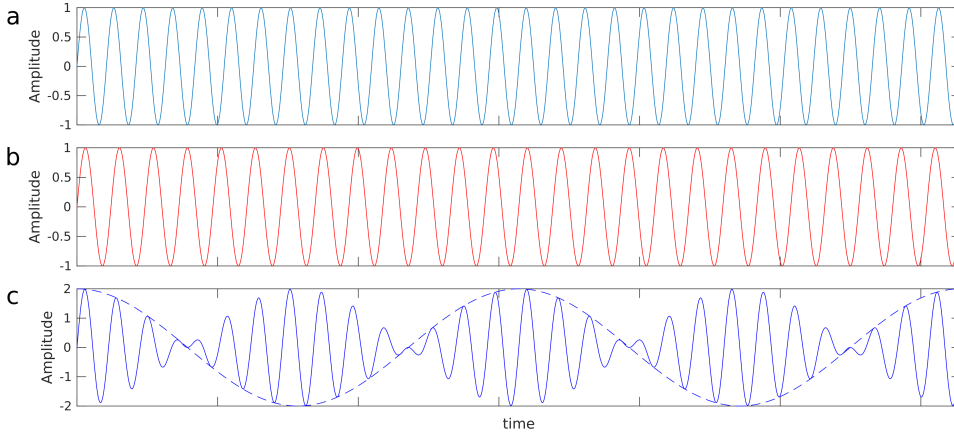


**Figure 1.14:** Interference of two oscillations at different frequencies (panel a and b) resulting in oscillation at the beat frequency (c). When the oscillation of both fields are in phase, their summed amplitude becomes maximal while both oscillations annihilate for a phase difference of  $\pi$ . The perceived oscillation is indicated by the the envelope of the beat pattern (dotted line in c).

The interference of two fields and the resulting acting field is illustrated in figure 1.14. While the independent fields are oscillating too fast for the inert nuclear vibration to follow, the beat frequency is not and thereby capable to act upon the molecule. The resulting interaction of both fields with a molecule induces a time-dependent force  $F$  on the molecule given by

$$F(t) = \left( \frac{\delta\alpha}{\delta Q} \right)_0 \left[ A_1 A_2^* e^{-i(\Omega)t} + c.c. \right] \quad (1.18)$$

For the coherent case, we refine our assumptions by a radiative energy loss that dampens the molecular oscillation and thereby determines the Lorentzian line profile of the Raman transition [43]. Then, the damped harmonic oscillation of the nuclear displacement, that is driven by the force  $F(t)$ , satisfies the following differential equation:

$$\frac{d^2 Q(t)}{dt^2} + 2\gamma \frac{dQ(t)}{dt} + \omega_v = \frac{F(t)}{m} \quad (1.19)$$

where  $m$  is the reduced mass of the oscillator and  $\omega_v$  is the resonance frequency. Like in eq.1.13, the nuclear displacement for such an oscillating system is found by

$$Q(t) = Q(\Omega) e^{-i\Omega t} + c.c. \quad (1.20)$$

The dependence of  $Q$  with respect to the resonance frequency can be analyzed by looking at the harmonic oscillator in frequency domain. By applying the inverse Fourier transform on eq.1.19 one can describe the damped harmonic oscillator as

$$\left( \frac{d^2}{dt^2} + 2\gamma \frac{d}{dt} + \omega_v \right) \int_{-\infty}^{+\infty} Q(\omega) e^{i\omega t} d\omega = \frac{1}{m} \int_{-\infty}^{+\infty} f(\omega) e^{i\omega t} d\omega \quad (1.21)$$

$$\int_{-\infty}^{+\infty} \left( \frac{d^2}{dt^2} + 2\gamma \frac{d}{dt} + \omega_v \right) Q(\omega) e^{i\omega t} d\omega = \frac{1}{m} \int_{-\infty}^{+\infty} f(\omega) e^{i\omega t} d\omega \quad (1.22)$$

and after another transformation this results in

$$\int_{-\infty}^{+\infty} (-\omega^2 + 2i\gamma\omega + \omega_v) Q(\omega) e^{i\omega t} d\omega = \frac{1}{m} \int_{-\infty}^{+\infty} f(\omega) e^{i\omega t} d\omega \quad (1.23)$$

which can be integrated to obtain the algebraic form

$$(-\omega^2 + 2i\gamma\omega + \omega_v) Q(\omega) = \frac{f(\omega)}{m} \quad (1.24)$$

By inserting the Fourier transformed eq.1.18 in eq.1.24, one finds the amplitude of the nuclear displacement as a function of the resonance frequency by

$$Q(\omega_v) = \frac{1}{m} \left( \frac{\delta\alpha}{\delta Q} \right)_0 \frac{A_1 A_2^*}{\omega_v^2 - \Omega^2 - 2i\Omega\gamma} \quad (1.25)$$

which becomes maximum when  $\Omega$  matches the resonance frequency  $\omega_v$ . Furthermore, it scales with the amplitudes  $A_1$  and  $A_2$  of the incident fields and the strength of coupling between the nuclear and electronic coordinates. The interaction between the two incoming fields and the molecule therefore grows rapidly when  $\Omega$  approaches a resonance of the nuclear mode.

So far, we have described a way to drive a strong molecular vibration by excitation of a molecule with two well-defined electric fields (which are completely in phase). But what are the implications of such a driven mode? The oscillating molecule alters the refractive index in its surrounding and thereby enhances its electronic polarizability. In consequence, the molecule's Raman scattering cross section is enhanced, too. A third electric field - the so-called probe field - will be strongly Raman scattered by such a molecule and generate new Stokes- and anti-Stokes shifted fields.

For simplicity, we can suppose a probing field of similar frequency of either  $\omega_1$  or  $\omega_2$ , which will then give the Stokes shifted contribution as

$$\omega_s = 2\omega_2 - \omega_1 \quad (1.26)$$

and the anti-Stokes shifted frequency as

$$\omega_{as} = 2\omega_1 - \omega_2. \quad (1.27)$$

The corresponding energy diagrams are shown in figure 1.15.

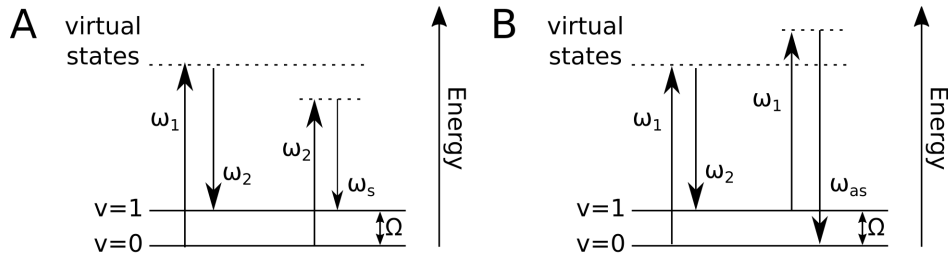


**Figure 1.15:** Jablonski diagram illustrating the four-wave process of (A) coherent Stokes Raman scattering and (B) coherent anti-Stokes Raman scattering.

The intensity of such a scattering process depends on the coherent oscillating polarization of the involved driven molecules. For an ensemble of  $N$  molecules, we find the macroscopic polarization to be

$$P(t) = N \left[ \alpha_0 + \left( \frac{\delta\alpha}{\delta Q} \right)_0 Q(t) \right] \{ A_1 e^{-i\omega_1 t} + A_2 e^{-i\omega_2 t} \} \quad (1.28)$$

More specifically, when looking only at the contribution that is oscillating at the anti-Stokes frequency and therefore ignoring  $\alpha_0$  as well as the term for  $E_2$ , we find by using eq.1.25 the amplitude of the polarization in the frequency domain to be

$$P(\omega_{as}) = \frac{N}{m} \left( \frac{\delta\alpha}{\delta Q} \right)_0^2 \frac{1}{\omega_v^2 - \Omega^2 - 2i\Omega\gamma} A_1^2 A_2^* \quad (1.29)$$

The essence of this equation is pooled as the nonlinear susceptibility  $\chi_{NL}$ :

$$\chi_{NL}(\Omega) = \frac{N}{6m\epsilon_0} \left( \frac{\delta\alpha}{\delta Q} \right)_0^2 \frac{1}{\omega_v^2 - \Omega^2 - 2i\Omega\gamma} \quad (1.30)$$

Here, the numerical factor 6 originates from total number of contributing permutations of the field frequencies (3!) [154] and  $\epsilon_0$  is the vacuum permittivity. For CARS, the third-order nonlinear susceptibility  $\chi^{(3)}$  consists of a non-resonant, frequency-independent contribution  $\chi_{NR}^{(3)}$  originating from electronic resonances, and a resonant part  $\chi_R^{(3)}$  from the vibrational resonances.

$$\chi^{(3)} = \chi_{NR}^{(3)} + \chi_R^{(3)} \quad (1.31)$$

From eq.1.29 one can see that the polarization is comprised of a real and an imaginary part and the susceptibility can be expanded to:

$$\chi^{(3)} = \chi_{NR}^{(3)} + \left( \chi_{R'}^{(3)} + i\chi_{R''}^{(3)} \right) \quad (1.32)$$

As shown earlier, the induced polarization then can be written as

$$P^{(3)}(\omega_{as}) = \chi^{(3)} \times E_1^2 * E_2. \quad (1.33)$$

The intensity of the emitted CARS signal at the anti-Stokes frequency is thereby proportional to the modulus of the polarization

$$I_{CARS} \propto |P^{(3)}|^2 \quad (1.34)$$

This raw CARS signal is perturbed relative to the spontaneous Raman spectrum because of the mixing of non-resonant and resonant contributions resulting in the relation

$$I_{CARS} \propto |P_{NR}^{(3)}|^2 + 2P_{NR}^{(3)} \cdot P_R^{(3)} + |P_R^{(3)}|^2 \quad (1.35)$$

and is proportional to the nonlinear susceptibility as follows [150]:

$$I_{CARS} \propto |\chi_R(\omega)|^2 + 2\Re\{\chi_R^*(\omega)\chi_{NR}(\omega)\} + |\chi_{NR}|^2 \quad (1.36)$$

Here, the spectral information about the sample is given by the phase function and thereby the imaginary part of  $\chi_R$ .



### 1.4.3 Broadband CARS

So far, CARS was treated as a four-wave mixing process resulting in an anti-Stokes signal at a well-defined frequency. However, this approach only would involve a single molecular vibration as set by the tuning of pump and Stokes frequency and result in the intensity information for a single mode.

To obtain 'chemical information' of a sample, it is desirable to probe several modes simultaneously and modified CARS setups have been designed to achieve this goal. The state-of-the-art experiments employ a spectrally broadened Stokes beam to excite all Raman-active molecular vibrations simultaneously and collect a CARS spectrum covering several thousand wavenumbers within milliseconds acquisition time [150]. These methods are termed differently depending on the spectral bandwidth they provide as multiplex CARS (from 300-1500  $\text{cm}^{-1}$ ) or broadband CARS (BCARS, 500-3000  $\text{cm}^{-1}$ ) [156]. Because a full spectrum is acquired, a more subtle analysis of the chemical composition is possible [156, 157]. In this work, BCARS is used as it acquires signal from both the fingerprint region (800-1800  $\text{cm}^{-1}$ ) and the CH-stretch region (2840-3000  $\text{cm}^{-1}$ ) of the spectrum and therefore gives a comprehensive insight to biological specimens.

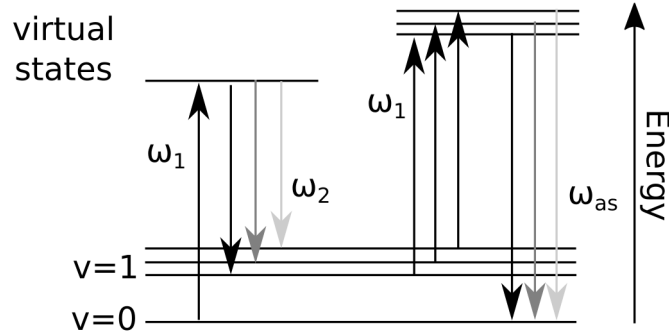


**Figure 1.16:** Jablonski diagram for broadband CARS. A spectrally broad Stokes field ( $\omega_2$ ) is employed to excite multiple modes simultaneously (instead of a defined Stokes field as shown in figure 1.15) resulting in CARS signal ( $\omega_{as}$ ) containing the spectral information of the involved molecular vibrations.

### Phase retrieval and background correction

As derived earlier (see equation eq.1.36), the detected CARS signal consists of a non-resonant and a resonant contribution from which only the imaginary part contains information on the Raman line shape [158]. Furthermore,  $\chi^{(3)}$  depends linearly on the molecular concentration. The spectral phase of the CARS signal is necessary to extract the  $\Im(\chi^{(3)})$  features, and this signal can be retrieved quantitatively by two functionally equivalent approaches [159]: a method employing the maximum entropy [158, 160] and a method that exploits the Kramers-Kronig (KK) relation in the time domain [161].

In this work, the Kramers-Kronig method is used to isolate the imaginary component of the resonant CARS signal from the non-resonant background (NRB), which will be explained briefly in the following section.

The Kramers-Kronig relation connects the phase information of a complex signal to its modulus by integrating over the entire frequency space:

$$\varphi(\omega) = -\frac{P}{\pi} \int_{-\infty}^{+\infty} \frac{\ln|\chi(\omega'')|}{\omega'' - \omega} d\omega'' \quad (1.37)$$

Here,  $P$  represents the Cauchy principal value to circumvent an otherwise improper integral.

However, this expression is problematic in nonlinear spectroscopy as the  $\ln(\varphi)$  diverges to  $-\infty$  when  $\varphi$  approaches zero and the experimental data only covers a finite frequency range. Furthermore, the non-resonant background signal contributes only a real component which causes the total CARS signal to be unequal in its complex amplitudes which violates the assumption of strict causality for the KK relation [150].

To avoid these difficulties, the KK relation is performed in the time domain instead of frequency domain. To do so, the raw CARS signal and the NRB are Fourier-transformed (FT) for further usage. Next, the envelope and phase of the NRB needs to be subtracted from the raw CARS signal to obtain the spectral phase. This can be achieved by replacing the amplitude of the FT CARS amplitude with the FT NRB amplitude for the negative-time range. After a subsequent back-transformation into frequency domain, the spectral phase can be calculated. Mathematically, the process are described by the following steps: The phase of the CARS signal  $|\chi(\omega)|$  can be written as a function of the detected CARS signal modulus by expanding the Kramers-Kronig relation.

$$\varphi(\omega) = 2\Im \left\{ \psi(\ln |\chi(\omega)|) - \frac{1}{2} \ln |\chi(\omega)| \right\} \quad (1.38)$$

Here,  $\psi$  indicates an transformation operator defined as

$$\psi(f(\omega)) = F[u(t) \star F^{-1}(f(\omega))], \quad (1.39)$$

where  $F$  and  $F^{-1}$  represent the Fourier transform and inverse Fourier transform respectively and  $u(t)$  the Heaviside function.

Because a frequency-dependent, non-flat NRB would result in a symmetric function in time space centred at time zero, the step function is insufficient to describe this behavior [162]. A more accurate representation is found by assuming that the negative-time component arises only from the NRB while for the positive-time both NRB and resonant component contribute. Thus, we can replace the product of the Heaviside function  $u(t) \star F^{-1}(f(\omega))$  from eq.1.39 by the stepwise defined function

$$\eta(t : f(\omega)) \begin{cases} F[F^{-1}[f(\omega)]] & t \geq 0 \\ F[F^{-1}[f_{NR}(\omega)]] & t < 0. \end{cases} \quad (1.40)$$

where  $f_{NR}$  represents the non-resonant signal.

The phase  $\varphi(\omega)$  can be retrieved from the known modulus by employing the Kramers-Kronig relation eq.1.37 and by combining eq.1.40 one gets

$$\varphi = 2\Im \left\{ \eta(\ln |\chi(\omega)|) - \frac{1}{2} \ln |\chi(\omega)| \right\} \quad (1.41)$$

The third-order susceptibility, as described earlier, can be rewritten as a complex number

$$\chi(\omega) = |\chi(\omega)| \exp[i\varphi(\omega)] \quad (1.42)$$

from which the imaginary part follows as

$$\Im \{\chi(\omega)\} = |\chi(\omega)| \sin[\varphi(\omega)]. \quad (1.43)$$

The Raman-like response can therefore be calculated from the measured signal modulus  $|\chi(\omega)|$  when the modulus of the non-resonant component is known, as required in eq.1.40.

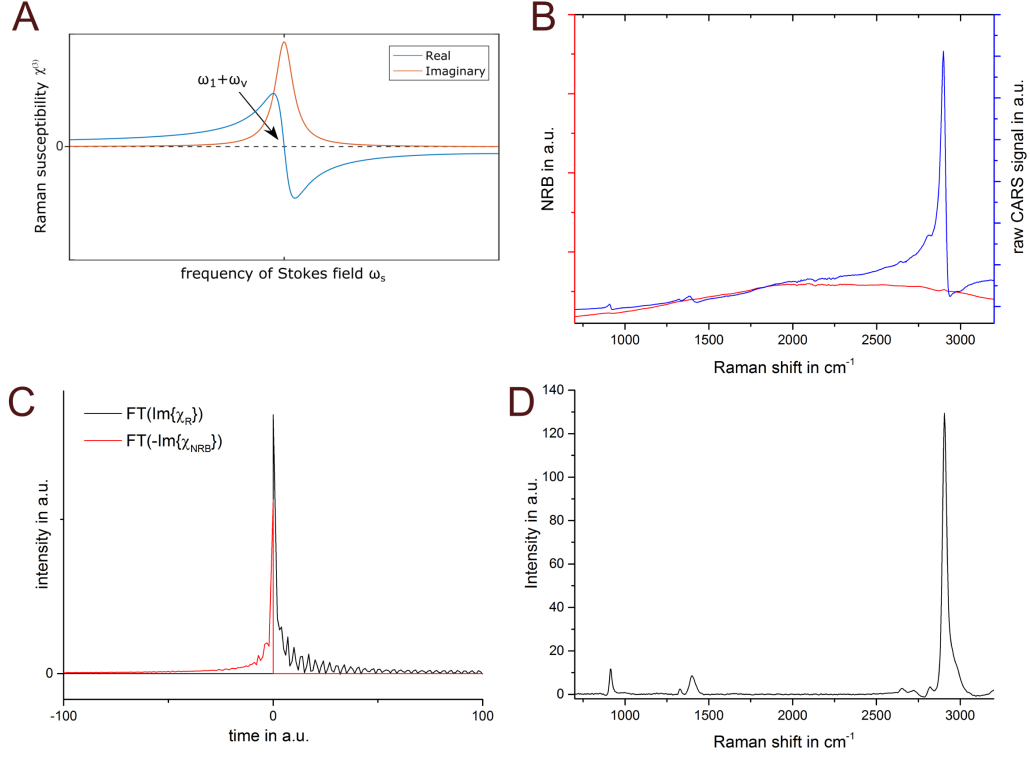


**Figure 1.17:** Data processing to obtain a Raman-like spectrum out of the raw CARS data of sodium acetate. A) Raw CARS signal and measured non-resonant background. The peaks of the raw spectrum are distorted and not quantitative. B) Signal of the Fourier-transformed NRB and CARS in the time domain. C) Resulting imaginary part of  $\chi(\omega)$  and Savitzky-Golay-fit to subtract background. D) Final Raman-like spectrum showing the correct peak shape and positions.

An experimental way to obtain the NRB signal is by taking a measurement from a reference material (e.g. the glass coverslip or water). This method is valid if the reference does not create a significant Raman signal in the spectral region of interest [150, 156, 163]. However, such an empirically obtained NRB is only an approximation of the true non-resonant component and is affected by numerous errors. Obviously, the NRB might vary to some degree between different materials and the exact beam aberration depends on the spatial position. Furthermore, when obtaining hyperspectral images and a heterogeneous sample is raster-scanned to take CARS spectra for multiple laterally shifted pixel, the local NRB will differ [150]. Luckily, these distortions of the local NRB with respect to the measured component can be assumed to vary only slowly in the spectral dimension and can be represented by a smooth spectral function [156, 161]. The retrieved Raman-like signal together with a disturbing varying baseline is shown in figure 1.17c. To obtain a spectrum that represents the molecular vibrations correctly, this background needs to be subtracted from the intermediate spectrum. As the baseline varies only slowly compared to the relevant spectral signals, it can be approximated by a higher-order polynomial function or an iterative non model-based Savitzky-Golay filtered spectrum with a window size larger than the Raman peaks of interest. Such a background subtraction then results in a Raman-like quantitative spectrum as shown in figure 1.17d. One has to keep in mind, that this method is only valid under ideal conditions like a constant stimulation profile and an undistorted phase. A copious analysis of arising errors when dealing with real-world experimental data and how to compensate for them is beyond the scope of my thesis and can be found elsewhere [150].

## Chapter 2

# Experimental methods

In this chapter, I describe the essential experimental methods used for my research. First, the rheology measurements to probe material properties of protein samples are illustrated. Thereafter, the broadband CARS setup and data processing of the obtained spectra are explained. As most samples at some time were analyzed by fluorescence microscopy, I will outline the basic concepts of fluorescent labeling and microscopy techniques. This is followed by the biochemical work that was done to produce deuterated vimentin for the experiments of chapter 5. Finally, I outline the creation of a GFP-vimentin expressing HeLa cell line.

### 2.1 Rheology

#### 2.1.1 Basic concepts

The mechanical response of a material to deformation contains plenty of information about its molecular and structural properties. Rheology is the study of material response with respect to an applied force. It uses deformation experiments to probe the material which then allows conclusions to be drawn about the intrinsic properties of the specimen. A sample can be deformed in two different ways: 1) in shear, where the acting force is parallel to the surface that experiences deformation or 2) in tension, where the force acts perpendicular to it (see also 2.1).

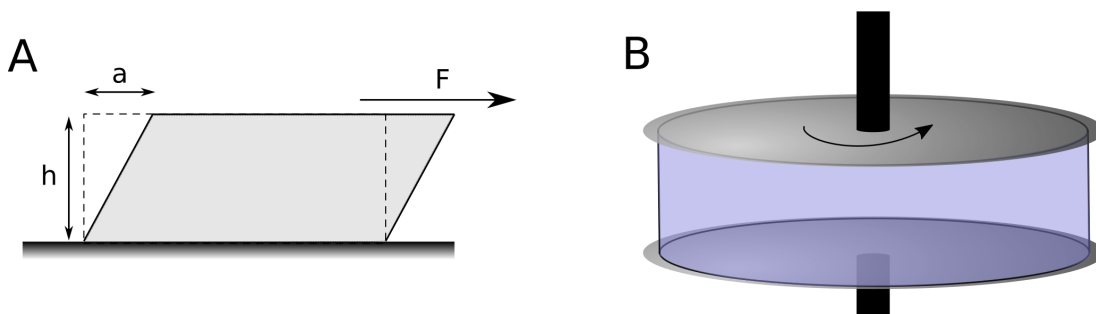


**Figure 2.1:** Geometries in shear rheology (A) and typical plate-plate configuration with a fix bottom plate and a rotating top plate.

The fibrin and vimentin hydrogel samples studied in this thesis are treated as nonlinear viscoelastic materials [66,164]. Mechanically, the elastic and viscous behavior of a material can be described by the combination of two simple elements: the spring and the oil-filled

dashpot. Hooke's law describes a mechanical spring with the linear relation between force and deformation as

$$\tau = G \cdot \gamma \quad (2.1)$$

The stress  $\tau$  is equal to the product of a proportionality constant  $G$  and the strain  $\gamma$  that represents the relative change in length.  $G$  is called the elastic modulus and indicates how soft or stiff a material is. Thus, to cause a certain strain one has to apply higher stress when  $G$  is increased.

A dashpot model can be seen as a piston that is moved within a cup filled with Newtonian oil. The stress for this element depends on the viscosity of the oil as well as the speed by which the piston is moved. We therefore can write

$$\tau = \nu \cdot \dot{\gamma} \quad (2.2)$$

where  $\dot{\gamma}$  is the time derivative of the strain.

Both elements can be arranged in series, in parallel or combinations of both to model the rheological profile of the sample [165, 166]. For the simple serial case one therefore can describe a viscoelastic sample by

$$\tau = G \cdot \gamma + \nu \cdot \dot{\gamma} \quad (2.3)$$

A convenient way to probe the rheological properties is by using oscillating stress or strain and performing analysis in the frequency domain. Here, either the frequency  $\omega$  or the amplitude can be swept to obtain a response that is defined by an amplitude and phase  $\delta$  as illustrated for different cases in figure 2.2. Oscillatory stress of frequency  $\omega$  is described by

$$\tau(t) = \tau e^{i\omega t - \delta} \quad (2.4)$$

resulting in a strain of

$$\gamma(t) = \gamma e^{i\omega t - \delta} \quad (2.5)$$

The ratio of strain per stress then gives the complex in the frequency domain, give frequency dependent dynamic modulus  $G^*$  [164]

$$G^* = \frac{\tau}{\gamma} \quad (2.6)$$

which can contain a complex contribution and therefore may be written as

$$G^*(\omega) = G'(\omega) + iG''(\omega) \quad (2.7)$$

Here, the real term is called storage modulus  $G'(\omega)$  and the imaginary contribution  $G''(\omega)$  the loss modulus. A physical interpretation is that the storage modulus represents the stored (elastic) energy in the system during the deformation while the loss modulus describes the (viscous) dissipation of energy [165]. Biopolymer networks are known to creep under deformation, especially when not cross-linked. This behavior leads to a discrepancy in the measured linear and nonlinear response of the system with respect to the actual material properties when measured with traditional strain sweep methods where the amplitude increased with time (see Fig.2.3A). Another experimental problem caused by large deformation amplitudes is that the response signal will be distorted by higher harmonics. To avoid these issues, a prestress method was developed [164, 167, 168] where a baseline prestress is continually increased on the sample upon which a small oscillatory stress is applied. Even at high prestress, this small signal analysis allows the assumption of quasi-linear behavior in the force response and thereby the higher harmonics can be neglected. The applied strain profiles for the traditional method of ramped strain amplitude and with prestress are shown in Fig.2.3B. Especially in the high strain regime the prestress

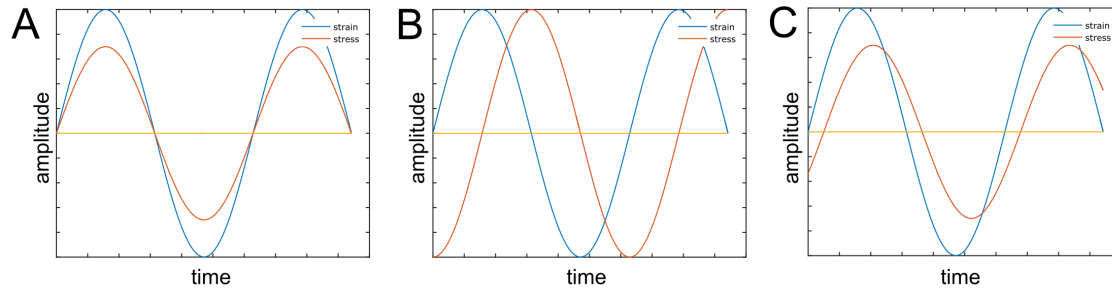


**Figure 2.2:** Oscillatory stress response as a function of oscillatory strain. Panel (A) shows the response of a perfect elastic sample where the in-phase stress is modulated only in amplitude. For a perfect viscous (Newtonian) sample, the amplitude is equal but phase-shifted by  $\pi/2$  with respect to strain (B). A real sample (C) has both viscous and elastic components and thereby a phase- and amplitude changed stress.

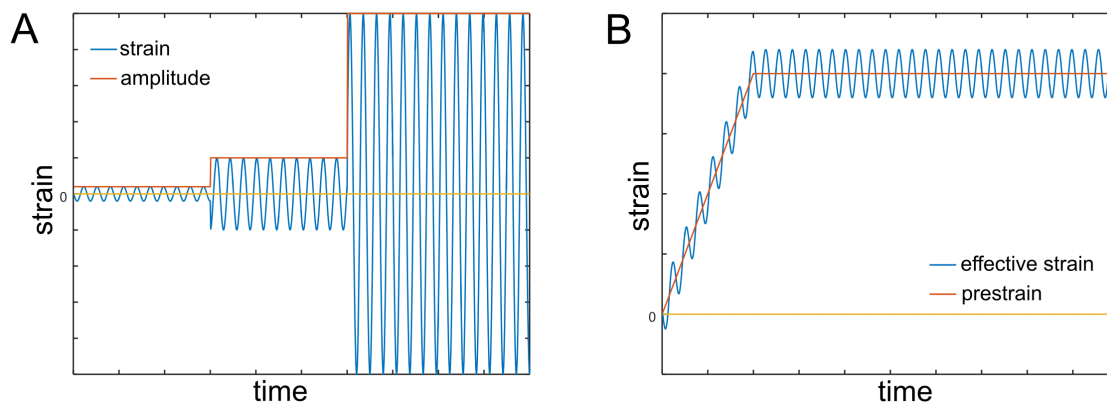


**Figure 2.3:** Types of oscillatory strain profiles in shear rheology. (A) Step-wise increase of the amplitude results in higher strains. (B) A ramped and then constant prestress that is superimposed by a small oscillatory stress probes similar stress rates but without the high oscillatory amplitudes.

approach provides consistent results that are insensitive to creep [164]. Because of the frequency dependence in such an experiment, the complex tangent differential modulus is used to describe the material properties here, given by

$$K = \frac{\partial \tau}{\partial \gamma} \quad (2.8)$$

This tangent differential modulus can be obtained as numerical derivative of the experimentally obtained stress-strain curve.

### 2.1.2 Tensile testing

In a tensile test configuration, the sample gets pulled apart in the direction of load as illustrated in figure 2.4. Thereby, the initial length  $l_1$  gets extended to  $l_2$  and the engineering strain  $\epsilon$  results as

$$\epsilon = \frac{l_2 - l_1}{l_1} \quad (2.9)$$

During the deformation, the force response of the sample is recorded. To determine the engineering stress, one needs to know the cross-sectional area of the sample. However, in soft hydrogel samples it was not possible to monitor the sample geometry (especially the diameter) during the deformation with the available testing devices. Thus, only the normalized force response with respect to strain is used to describe the tensile properties of the samples [165].

A tensile testing device (Z005, TestXpert II, ZwickRoell) with a mounted load cell (Z6FD1, HBM) was used for tensile measurements. The samples were clamped by two grips connected with the load cell (bottom) and a moveable holder (top). Then the sample was pulled apart with constant speed (usually 10 mm/min) and the force was recorded.

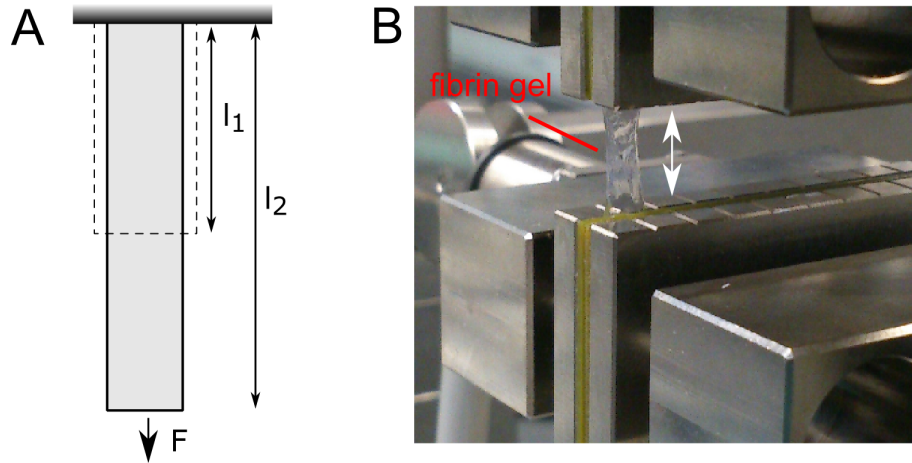


**Figure 2.4:** Experimental geometry of a tensile test. (A) A force  $F$  is applied to a sample of initial length  $l_1$  which then becomes extended to  $l_2$  along the direction of load. (B) Picture of a clamped fibrin hydrogel in the tensile testing device. The initial sample dimensions of the relaxed gel were approximately 20 mm x 0.2 mm x 5 mm (LxWxH) and direction of deformation is indicated by an arrow.

### 2.1.3 Shear rheology

Shear rheology probes the mechanical properties of a sample with respect to parallel deformation as shown in Fig.2.1A. In a typical setup the sample is placed between a fixed

bottom plate and a top plate that can be rotated by a motor with a specific frequency and amplitude (see Fig.2.1B). The sample has contact to the plates over the entire upper and lower interface. Torque forces that occur for a given rotation are recorded and converted into shear stress. As described earlier, the nonlinear response of soft hydrogel samples can be investigated with the prestress method. In shear rheometry this can be achieved by rotating the movable plate by a calculated angle and then adding an oscillation of small amplitude. Shear strain is defined by the lateral displacement  $a$  caused by a shear force  $F$  divided by the sample thickness  $h$  as depicted in Fig.2.1A:

$$\gamma = \frac{a}{h} \quad (2.10)$$

The response of viscoelastic samples varies with the applied deformation and often different characteristic regimes (like linear or nonlinear increase) occur in the stress-strain curves. From the analysis of such patterns and their turning points one can obtain insights into the underlying material mechanisms that cause the sample stiffness. Experimentally, those strain-dependent regimens are probed by a rheological prestrain sweep measurement superposed by a small oscillatory strain where the frequency is fixed (usually at 1 Hz) and the complex moduli are measured as a function of strain amplitude [169].

A sample is not required to support itself in the shear geometry (see Fig.2.1B) which enables experiments on highly viscous materials. For example, the gel formation of fibrin or vimentin could be observed over time where the initially liquid protein solution was polymerized into hydrogels. For this thesis, experiments were performed on a commercial shear rheometer (ARES, Rheometric Scientific) and data acquisition was done in TA Orchestrator software. Stainless steel plates of 25 mm diameter were used with a plate separation of several hundred  $\mu\text{m}$ . Evaporation of water at the outer edge during the experiments was prevented by sealing the samples with silicon oil (Baysilone Fluid, Bayer).



## 2.2 Broadband CARS microspectroscopy

### 2.2.1 Technology

As described in the theory section above, the CARS process involves four electromagnetic fields: the pump-, Stokes- and probe-field are required for the coherent excitation that causes the emission of an anti-Stokes field. In an experimental setup, the pump- and probe-fields can be provided by the same laser beam without disadvantages. For the simultaneous excitation of multiple molecular vibrations as illustrated in figure 1.16, the Stokes-field has to provide a range of different energies. This is achieved by a spectrally broadened laser beam that contains many frequencies.

Two technological findings stimulated the further spreading of CARS microspectroscopy [170] since 1999, when Zumbusch and coworkers demonstrated an experimental setup for vibrational imaging [149]. By using objective lenses with high numerical aperture (NA) both pump/probe- and Stokes-beam can be tightly focused so that the phase-matching conditions are relaxed. The high NA generates a large cone of wave vectors that allows phase-matching of the collinear beams to generate the anti-Stokes signal [149, 171]. Furthermore, because the CARS process scales quadratic to the concentration of vibrational modes, most signal is produced in the small focal volume where the locally strong CARS signal can overwhelm the incoherent background of linear intensity dependence [149].

In addition to tight focusing, the performance can be optimized by choosing the laser range in the near IR region. Even so this is contradictory to the fact that Raman scattering scales with  $\lambda^{-4}$  [172], (e.g. excitation by 488 nm would generate  $\sim 23$  times more Raman signal than 1064 nm), the lower cross section for non-resonant contributions makes the usage of near IR lasers favorable [149]. The usage of lasers in the visible wavelength range resulted in CARS spectra that were dominated by the non-resonant background signal [170]. Near-IR excitation on the other hand does not excite electronic transitions in the sample and thereby significantly reduces the NRB. Also, laser sources in the NIR minimize two-photon interactions that can give rise of further non-resonant signal [148]. Finally, because of the lower scattering cross section at higher wavelength, the Rayleigh scattering in the sample, especially tissue, is also reduced. This makes larger penetration depths and thereby three-dimensional imaging inside a specimen possible [148, 149].

The CARS signal depends quadratically on  $\chi^{(3)}$ , and therefore the concentration of the analyte, and cubic on laser power (see eq.1.34) whereas spontaneous Raman scattering has a linear dependence on both variables [173]. Indeed, for samples of low concentration and at low laser power, the spontaneous scattering process will provide more sensitivity than coherent methods. Only when both the concentration and laser power are above a certain threshold, the CARS process will offer a massively enhanced signal [173, 174]. By taking the heterodyne mixing contribution into account (second term in 1.36 containing both non-resonant and resonant signal) the CARS sensitivity can be increased for low concentrations as this term is linear dependent on concentration [156]. In summary, it can be ascertained that for similar laser powers and sufficient high local concentrations, CARS provides a stronger signal than spontaneous Raman scattering and thereby allows faster acquisition rates for a spectrum of equal signal-to-noise ratio.

This gain in speed makes spatial resolved spectroscopy possible, where a sample is raster-scanned, and a full CARS spectrum is collected for each pixel [148]. The microspectroscopy approach thereby collects datasets where the spatial dimensions are expanded by a spectral one - e.g. a two-dimensional scan of a sample results in a three-dimensional data cube with the third dimension being spanned by the wavenumber axis.

### 2.2.2 Experimental setup for BCARS microspectroscopy

The broadband CARS setup used in this work is based on a nanosecond-laser that provides the two required laser fields as spectrally narrow pump/probe beam and white-light Stokes beam. First experiments of multiplex CARS were built for this laser source by the Hamaguchi group [175, 176].

The setup design of the current BCARS setup is depicted in figure 2.5 and figure 2.7 and shown in 2.6. The laser beams are generated by a dual-output compact laser source (CARS-SM-30, Leukos) where a passively Q-switched microchip laser emits spectrally narrow sub-nanosecond pulses at  $\lambda = 1064$  nm and 30 kHz repetition rate. Those initial pulses are equally divided into the pump/probe-beam and Stokes-beam. While the pump/probe-beam is directly passed on to the optical setup, the Stokes-beam is coupled into a photonic crystal fiber (PCF). Here, the monochromatic pulse is broadened in spectral space by strong third-order nonlinear effects along the propagation in the fiber [176] to obtain a white-light supercontinuum in the range of 0.4 to 2.4  $\mu\text{m}$ . The output power from the laser source was measured as 101 mW for the pump/probe beam and 120 mW for the Stokes beam with a spectral power density of  $\sim 100 \mu\text{Wnm}^{-1}$ .

After leaving the PCF, the Stokes beam is spectrally clipped to a range of 1100-1600 nm by two filters (LP700nm, LP830nm) and linearly polarized by a Glan-Thompson polarizer. The pump/probe beam is slightly divergent from the laser source. It is therefore collimated by a telescope configuration of two plano-convex lenses (L1,  $f=50$  mm and L2,  $f=100$  mm). To compensate the temporal delay of the Stokes-pulse (which has to propagate through the PCF first), a delay line extends the optical path by several meters length. Hereafter the beams polarization is rotated by a  $\lambda/2$  plate (1064nm) and spectrally filtered (FL1064-10 notch filter).

Both beams are superimposed by a dichroic mirror that reflects for 1064 nm and introduced via a periscope into the inverted microscopy (Eclipse Ti-U, Nikon). An objective lens (60x/NA:1.2 NIR water immersion, Olympus or 100x, NA:0.85 air, Zeiss) is used to tightly focus the beams in the sample plane. The total average laser power in the focal volume is  $\sim 30$  mW. For spectral imaging, the sample stage is mounted on a xyz piezo stage (Nano-PDQ 375 HS, Mad City Labs) for small area ( $75 \times 75 \times 50 \mu\text{m}$ ) raster scanning and a motor driven micro stage for coarse sample movement (Micro-Drive, Mad City Labs). CARS signal that is generated in the sample is collected by a second objective lens (10x, NA:0.25, Zeiss) and guided to the spectrograph. As only the anti-Stokes shifted signal is of interest for the further analysis, the pump/probe and Stokes beams are blocked by a notch filter (NF03-532/1064E-25, Semrock) and a short-pass filter (FES1000, Thorlabs), respectively before entering the spectrometer (Shamrock 303i, Andor). Here, the remaining signal is spatially separated by a diffraction grating and the spectral intensity is analyzed with an attached cooled CCD camera (Newport DU920P-BR-DD, Andor). This results in a spectral range from  $500 \text{ cm}^{-1}$  to  $4000 \text{ cm}^{-1}$  with a spectral pitch of  $\sim 4 \text{ cm}^{-1}$  and thereby covering the fingerprint and  $\text{CH}_2/\text{CH}_3$  region of the Raman spectrum. The setup is controlled by a graphical user interface written in LabView (National Instruments).

In addition to the BCARS features, the setup also allows to view the sample in normal bright field microscopy mode. Therefore, the gold mirror in the microscope turret is rotated out the optical path and the sample image is captured by a CCD camera (EXI-blue, Chromaphor) that is mounted to the side port. The live images are displayed in the  $\mu\text{manager}$  software package (Open Imaging) for ImageJ [177].

In its current configuration, the setup provides a S/N that requires acquisition times of 100-500 milliseconds per spectrum to obtain valuable spectral data in the fingerprint region for biological sample such as adherent cells or protein gels. The imaging capability is thereby limited to frame rates of several minutes and small images (usually  $81 \times 81$  pixel). Compared to confocal laser scanning microscopy [178] or single line CARS [151], the col-

lection time per pixel is long. However, in broadband CARS a full Raman spectrum is obtained instead of only an intensity value for a given wavenumber at every position. This makes a detailed chemical analysis of the sample possible. One therefore trades spatial-temporal resolution versus spectral information.

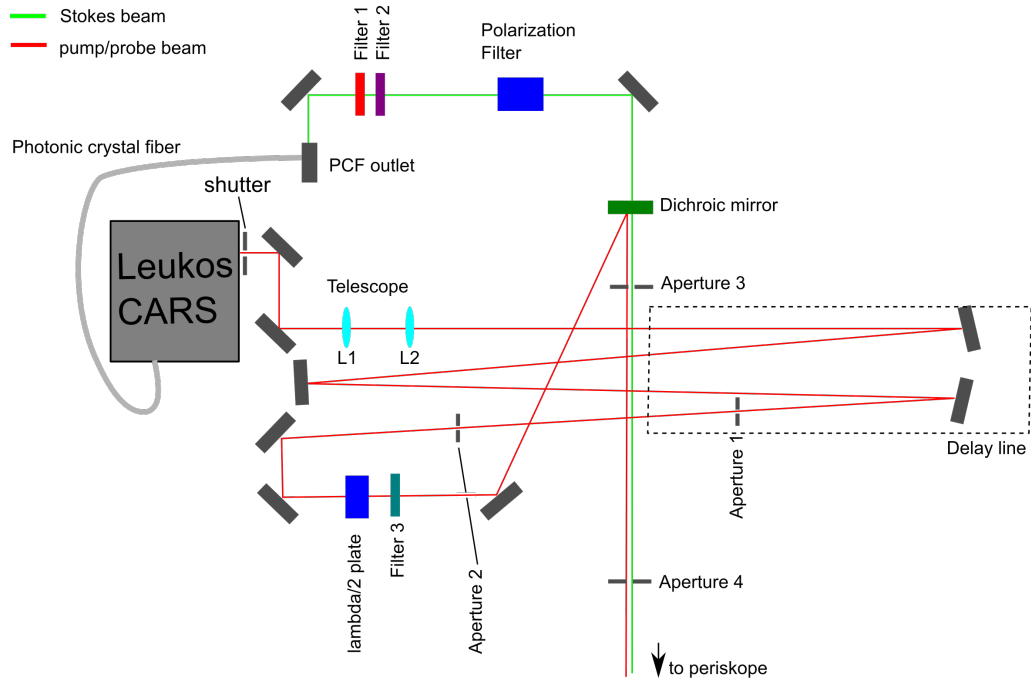


**Figure 2.5:** Schematic of the BCARS setup: part 1: 'on the table'. The two beams have to match in space, ergo in the sample, and in time. Thus, the pump/probe beam are directed through a delay line that adds more optical path length and thereby run time for each pulse. Filters, mirrors and lenses are used to define the wavelength range, beam shape, polarization and direction of both beams.

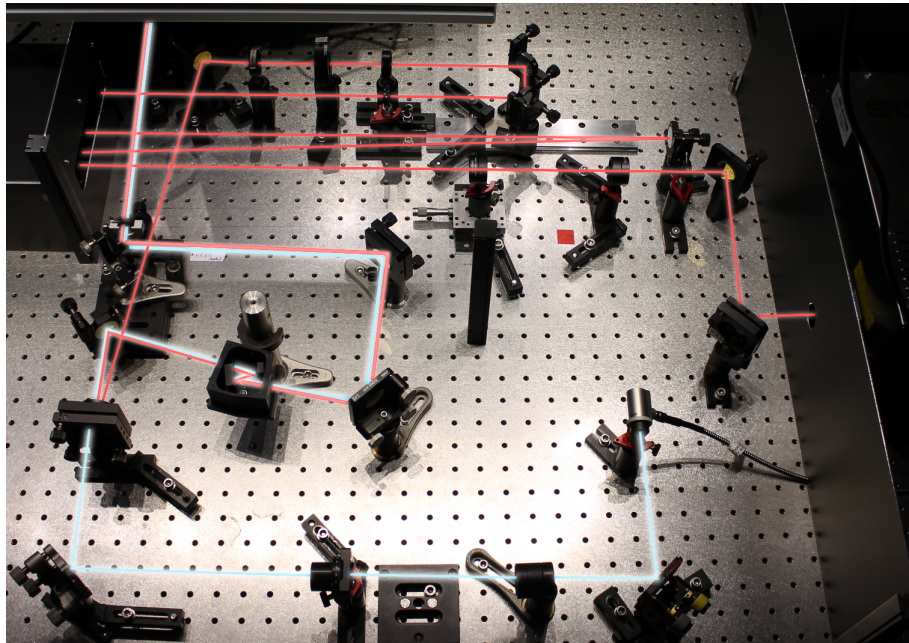


**Figure 2.6:** Photo taken from the current BCARS setup where the optical pathway of both (invisible) beams is indicated by an artistic representation (Stokes beam in blue and pump/probe beam in red).

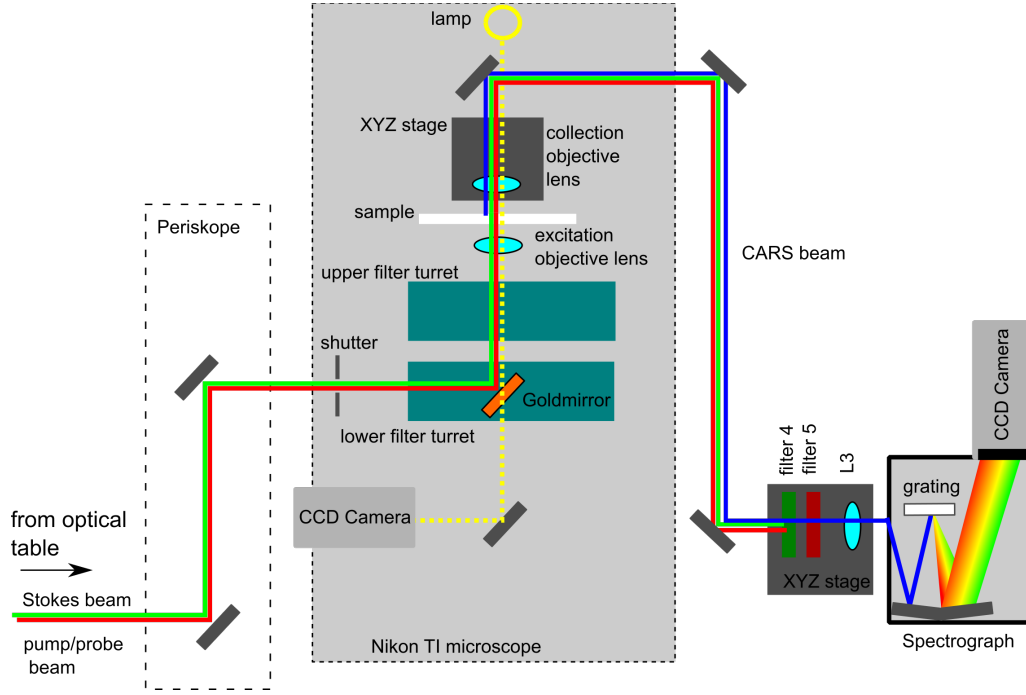


**Figure 2.7:** Schematic for the BCARS setup, part 2: 'BCARS microscope'.

### 2.2.3 Phase retrieval to obtain Raman-like spectra

The acquired raw BCARS spectra need to be processed further to obtain quantitative data that is comparable to spectra from spontaneous Raman spectroscopy. This step is done in a semi-automated way by multiple scripts in IgorPro. A schematic flow chart of the different processing steps is shown in Fig.2.8.

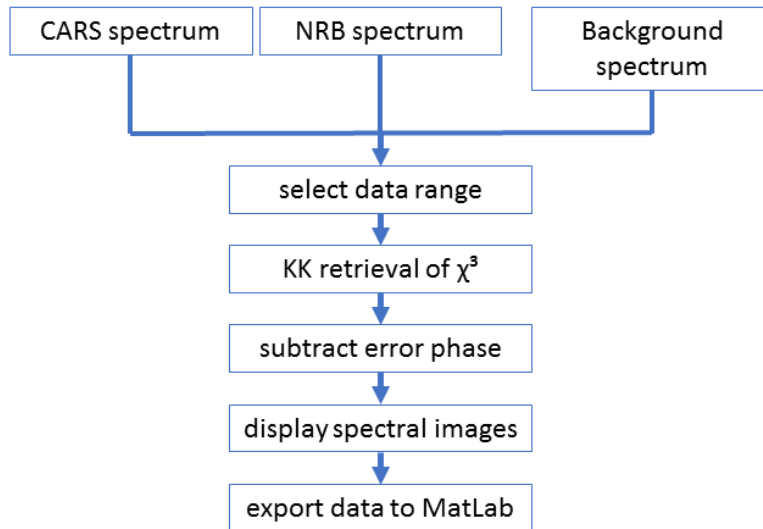


**Figure 2.8:** Flowchart for BCARS data processing in Igor. The  $\chi^{(3)}$  component is retrieved from the raw CARS data and prepared into a Raman-like spectrum.

Besides the raw BCARS data, a spectrum of the background (ambient light, detector noise) and a spectrum of the non-resonant background are required for the processing. Usually, the NRB spectrum is taken either inside the glass slide of the sample or in the

water/buffer solution next to a specimen. This method assumes that no resonant signal is generated in the reference medium and potential resonant peaks collected with the NRB spectrum will be eliminated during the processing [150,161]. For the background spectrum, the microscope shutter is closed to block the laser beams. Otherwise, both supplementary spectra are recorded under the same conditions as the actual dataset. The current processing assumes a constant NRB and background for all positions which can lead to artifacts in heterogeneous samples. To filter out any signal not related with the CARS process, the background spectrum is subtracted from all raw CARS spectra as well as from the NRB spectrum.

The further processing, as described in the previous theory chapter, is done sequentially for all collected pixels of the spectral dataset. In an optional step, the data range can be clipped to a spectral range of interest (e.g. the fingerprint or the CH region only) to avoid edge effects during error phase subtraction.

First, the Fourier transform of the NRB spectrum and the raw CARS spectrum is calculated. The negative time component of the FT CARS spectrum is replaced by the negative FT NRB spectrum (compare to eq.1.40). Thereafter, the complex susceptibility  $\chi^{(3)}$  and the phase angle  $\phi$  are determined by exploiting the Kramers-Kronig relation (see eq.1.37). Finally, the Raman like response is calculated by taking the imaginary part of the multiplied  $\chi^{(3)}$  and the sine of the phase angle (eq.1.43).

The retrieved CARS spectrum is perturbed by an error phase that is slowly varying over the entire spectrum. It is removed by an asymmetric, iterative Savitzky-Golay filter procedure where a filtered version of the spectrum is subtracted and negative values are set to zero until an optimum is found. This is functionally similar to asymmetric least squares as implemented by others in Raman scattering [179].

After all pixels are processed, the now Raman-like dataset can be analyzed for specific spectral features. By integrating a spectral range of choice an intensity map can be created to show the spatial distribution of the feature.

The data set or single spectra can be exported as ASCII text where the three-dimensional data is unfolded into a linear number sequence.

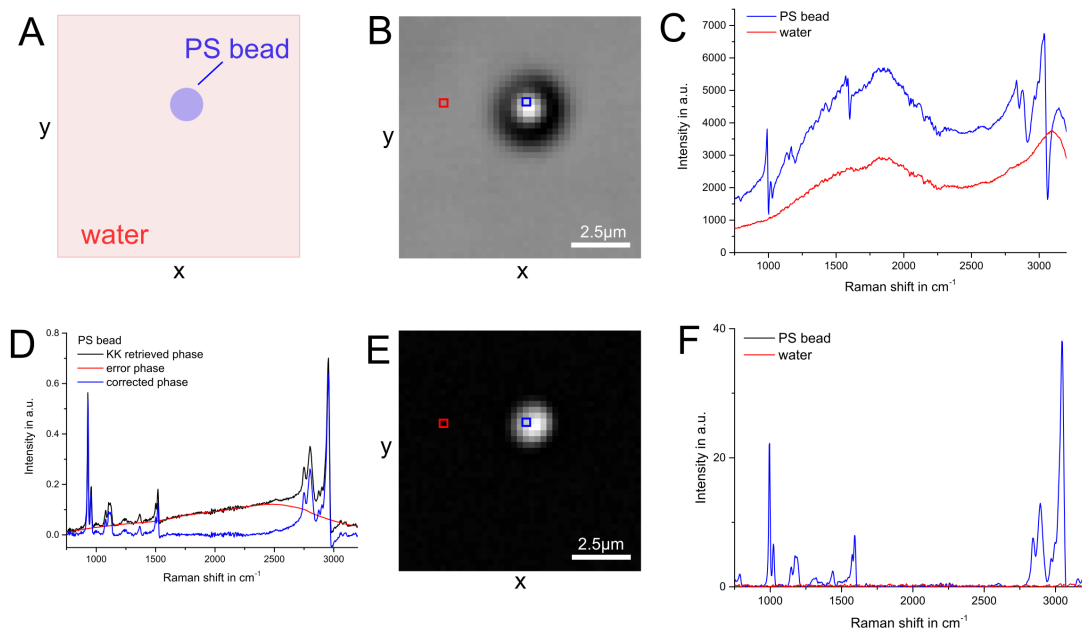


**Figure 2.9:** Example for BCARS microspectroscopy of a polystyrene bead in water. (A) Schematic of the sample arrangement where a polystyrene (PS) bead of  $2\ \mu\text{m}$  diameter is placed on a glass surface and is surrounded by water. (B) The sample is raster-scanned in  $250\ \text{nm}$  step size in  $x$  and  $y$  to obtain a hyperspectral data set from which an image is calculated where the brightness indicates the integrated intensity in the range of  $995\text{--}1005\ \text{cm}^{-1}$  (ring breathing mode [180]). (C) Raw CARS spectra from a location in the PS bead (blue box) and from nearby in the water (red) as acquired in the experiment. The water spectrum consists mostly of NRB contribution and a broad band of the OH-vibrations from  $3000\text{--}3700\ \text{cm}^{-1}$  (partially clipped) [181]. Polystyrene shows multiple strong CARS peaks with a dispersive line-shape (see also Fig.1.17). (D) Background correction to remove the slowly varying error phase from the retrieved phase. (E) Spectral image of the corrected, Raman-like data and same spectral range as in (B). (F) Final, Raman-like spectra of polystyrene showing Lorentzian shaped peaks at the expected positions [180]. As the water was used as NRB, all its peaks are eliminated in the retrieved spectrum.

### 2.2.4 Multivariate curve resolution

Multivariate curve resolution (MCR) is a chemometric method to resolve a dataset of mixtures into its pure components without having prior information or training. It is applied for separating the spectral components from BCARS hyperspectral images via a MatLab toolbox (MCR-ALS GUI 2.0) in chapter 4 and 5. In the following, the basic concepts of MCR and chemometric data processing are described.

The aim of MCR in this work is to represent hyperspectral image data that consists of many spectra, by a simplified version that is defined by a set of pure components weighted by their local concentrations. This idea is comparable to digital images, where an object is represented by three basic colors for each pixel (see Fig.2.10).

There are some very basic prerequisites to consider for the MCR processing: what actually represents the spectrum? How can different chemical species be distinguished? How many input spectra are required?

A pure spectrum, i.e. from a single substance, usually consists of multiple peaks originating from different vibrational modes of the sample molecule(s). For the MCR analysis, the ratio between those peaks is assumed to be constant and independent of a changing environment. The spectral pattern of each pure component is conserved throughout the entire data set and the individual values for each wavenumber are highly correlated to



**Figure 2.10:** Representation of a colored image by the basic colors red, green and blue and their local weighing. Image taken from [https://commons.wikimedia.org/wiki/File:Oak\\_tree\\_with\\_moon\\_and\\_wildflowers.jpg](https://commons.wikimedia.org/wiki/File:Oak_tree_with_moon_and_wildflowers.jpg), under creative commons CC BY-SA 3.0 by Matthew Roth.

each another. A component must have a dominant presence in the entire data, hence having distinguishable spectral features and a sufficient intensity in multiple spectra, to be recognized by the algorithm. Furthermore, the spectral shape must be assumed to change linearly with concentration for constant experimental conditions (laser power, acquisition time) [182]. Having this last assumption in mind it is clear that the raw CARS data does not fulfill these requirements and the phase retrieval is necessary to obtain RL data for the later processing.

In the projects of this thesis, the secondary structure of a target protein or peptide is changing with different treatments. This also results in a change of the spectral shape in the amide regions and therefore a reference spectrum taken from a pure sample will not help for separating the component of interest. The experimental trick we use is to introduce an additional peak from isotopic labelled amino acids [183,184] that allows separating the target protein from all other protein signal.

The number of required input spectra depends highly on how spectrally different the individual components are and how many components are assumed. Theoretically  $(2 \cdot n + 1)$  spectra should be sufficient to obtain an over-determined system of  $n$  components. However, the real data often varies only little at certain vibrational frequencies and always includes noise and artifacts. Thus, as a rule of thumb a 10fold number of input spectra as components will provide reasonable results from the MCR-ALS algorithm and more initial data will lead to more accurate component spectra.

Based on those considerations a sufficient large data set can be processed to obtain the purest components. Mathematically, a system of multiple independent (here: from different spatial positions) spectra can be expressed by a system of linear equations which is solvable when the number of equations is larger than the one of variables. Then, the given data Matrix  $\mathbf{D}$  can be represented by the sum of  $i$  different chemical species as follows

$$\mathbf{D} = \sum_i \mathbf{C}_i \mathbf{S}_i + \mathbf{E} \quad (2.11)$$

where  $\mathbf{C}$  is the component intensity matrix ('loadings') and  $\mathbf{S}$  the pure spectra matrix. Here,  $\mathbf{E}$  represents an error term that is independent of the chemical species in which all unexplained variance as well as noise is binned. The MCR method assumes that every chemical species has a unique spectrum and that the components can be mixed in bilinear fashion [185]. A single spectrum in the initial data set is thereby reproduced through the summation of a given number of weighted pure component spectra.



MCR shares some concepts with principal component analysis (PCA) [182,186]. While in PCA the data is decomposed in orthonormal components that strictly maximize the explained variance [187], the constraints in MCR represent an additional framework for the components. This results in MCR components that may not explain the variance in the data optimal but follow the given physical meaningful constraints. Furthermore, the obtained pure component profiles have chemical meaning, and the 'scores maps' can be interpreted as local concentration and spectra, respectively [186].

The adequate application of constraints determines if the MCR method provides useful results. Possible constraints are [185,188]

- Unimodality: each loading profile must have a unimodal peak
- Non-negativity of the loadings
- Non-negativity of the spectra
- Closure: the sum of all component loadings always must be 1.

These constraints introduce basic physical assumptions to the model. For the spectroscopic data used in this work, the two non-negativity constraints were applied as one can assume that both the pure spectrum and the local concentration must be zero or positive.

An established method to solve the fundamental equation (eq.2.11) of MCR is by Alternating Least Squares (ALS) as proposed by Tauler [185]. Beforehand, the number of pure species that shall be included in the model must be determined. This can be done either manually or by a chemical rank analysis where the possible components are sorted by their eigenvalues and thereby their contribution to the whole data set [189,190]. As usually no *a priori* information on the components is known (e.g. how the pure spectrum looks like), an initial estimate of the concentration profile of the data or the spectra is done by evolving factor analysis [191] or singular value decomposition [192]. Next, the alternating least square method [192] is used to optimize the initial estimations in eq.2.11 [193]. After each iterative step, a new estimation of the C and S matrix is found which replaces the previous values in case of a more optimal result or is discarded if not. The algorithm is repeated until a sufficient good combination is found or a limit of allowed steps is reached [185,186]. As a result, the MCR-ALS algorithm presents an optimal set of pure component spectra S together with a loading vector **C** for each component. The individual steps of the procedure are shown in Fig.2.11.

A critical step during a MCR analysis is to decide on the number of allowed components. If all components in the experiment are known, e.g. in a defined mixing series, the number of pure species is obvious. However, in complex systems such as hyperspectral data of cells, this is not trivial anymore. The state-of-the-art solution for this problem as described in a recent review is a "trial-and-error approach based on different rank estimations" [186]. One therefore has to figure out first, how heterogeneous the input data is and how dominant occurring artifacts, especially from e.g. spectroscopic etaloning or sample drifting, are. The number of components then can be set as the different chemical distinguishable species plus one component where non-random disturbing signals, e.g. from etaloning, is gathered up.

Another problem of multivariate data analysis is rotational ambiguity which must be seen as an intrinsic theoretical limitation of the method [194]. The relation given by eq.2.11 that connects the experimental data to the matrices of loadings and pure spectra does not provide a unique solution [185]. Instead, it only might result in one of multiple feasible solutions for the given data and constraints [194]. An indicator for possible rotational ambiguity is given by the error estimation from the MCR-ALS algorithm as well as by the percentage of data represented by the results [194,195].



To close this section I would like to add some comments about the data processing with the MCR-ALS Matlab GUI.

- The toolbox limits the allowed size for the input data matrix to 10000 in both spectral dimension and number of different spectra. This can be overridden in the code without severe consequences besides longer calculation times.
- Often it is useful to clip the input spectra to regions of interest. For example, the  $\text{CH}_2$  region shows high variability for data obtained from cells which might overrule the more subtle changes in the fingerprint region.
- The background subtraction during the CARS processing often creates nonlinear trends close to the range limits. Those are avoided by selective clipping, too.
- Assuming more than three components might slow down the processing a lot.
- The required time scales with the number of input spectra and their vector size even if empty. Eliminating empty rows and columns therefore speeds up the procedure, too.
- If etaloning or gradual trends, which are both not random noise, occur in the data, one might consider including more components to dump those disturbing patterns and to clean up the remaining pure spectra.
- Finally, one should check the loading distribution over the data. Single pixel can disturb the whole dataset if their values are extreme outlier for example from cospics or saturated pixels in the raw CARS spectrum.

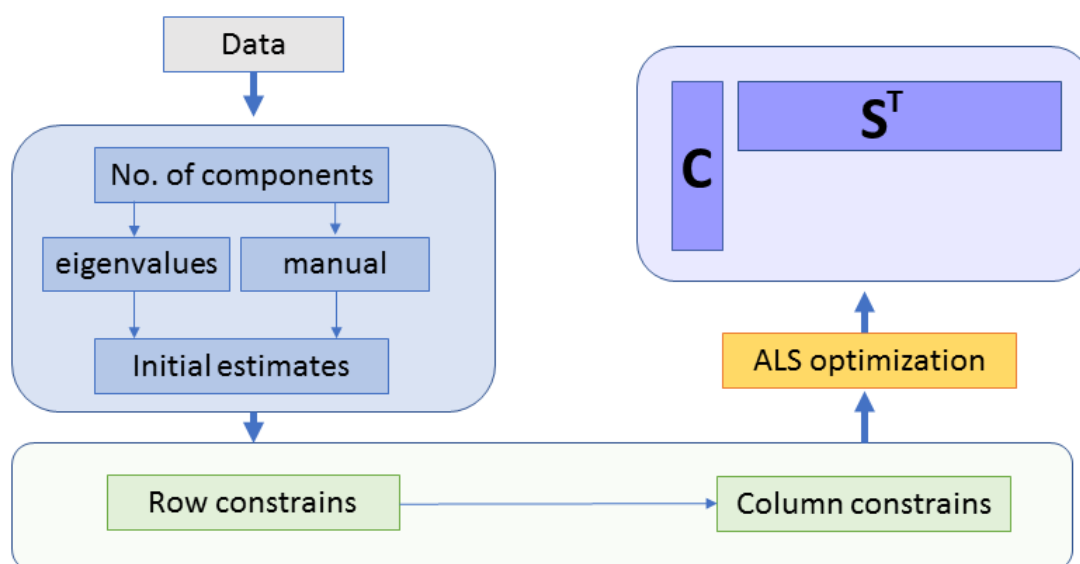


**Figure 2.11:** Flowchart of the analysis using the Matlab toolbox MCR-ALS GUI 2.0 [195].

### 2.2.5 Decomposition of amide I band

The amide I band in Raman spectroscopy consists of several underlying peaks that are assigned to different structural motifs. Peak center positions are known from literature [46, 55] and can be exploited to decompose the experimentally obtained BCARS spectra into contributions from different secondary structure. In chapters 3-5 of this thesis, this method is used multiple times to analyze the structural compositions in fibrin gels, *in vivo* structure of a cell penetrating peptide called Penetratin, and *in vivo* vimentin IF.

A fitting procedure was written in Matlab featuring the in-build nonlinear least-squares solver 'lsqcurvefit', based on the Levenberg-Marquardt algorithm. The first step was to clip the spectrum of interest to a spectral range from 1585  $\text{cm}^{-1}$  to 1723  $\text{cm}^{-1}$ , and a linear background was subtracted. The prepared spectrum is then fitted by a user-defined function given in eq.2.12 consisting of the sum of seven Lorentzian peaks and a constant baseline ( $y_0$ ).

$$\begin{aligned}
 p = y_0 &+ A_1 \frac{0.5 \cdot WL_1}{(x - X_{c1})^2 + (0.5 \cdot WL_1)^2} + A_2 \frac{0.5 \cdot WL_2}{(x - X_{c2})^2 + (0.5 \cdot WL_2)^2} \\
 &+ A_3 \frac{0.5 \cdot WL_3}{(x - X_{c3})^2 + (0.5 \cdot WL_3)^2} + A_4 \frac{0.5 \cdot WL_4}{(x - X_{c4})^2 + (0.5 \cdot WL_4)^2} \\
 &+ A_5 \frac{0.5 \cdot WL_5}{(x - X_{c5})^2 + (0.5 \cdot WL_5)^2} + A_6 \frac{0.5 \cdot WL_6}{(x - X_{c6})^2 + (0.5 \cdot WL_6)^2} \\
 &+ A_7 \frac{0.5 \cdot WL_7}{(x - X_{c7})^2 + (0.5 \cdot WL_7)^2}
 \end{aligned} \tag{2.12}$$

Each peak is defined by a center wavelength and width that are allowed to vary within some upper and lower boundaries as stated in table 2.1 and shown in Fig.2.12. The resulting

Peak #	center [ $\text{cm}^{-1}$ ]	FWHM [ $\text{cm}^{-1}$ ]	structure
1	1640	14-16	$\alpha$ -helix
2	1650	18-22	$\alpha$ -helix
3	1660	18-22	Unstructured
4	1674	18-22	$\beta$ -sheet
5	1693	8-12	Unstructured
6	1600	8-12	Tryptophan
7	1612	8-12	Tyrosine

**Table 2.1:** Parameters for amide I fitting.

peak parameters are used to integrate the individual peak area. Peak 1-5 are assigned to secondary structure and their summed up peak area is set as 100% of structural content while peak 6 and 7 result from side chains and are ignored in the secondary structure percentage calculations. Peak 1 and 2 together represent the amount of  $\alpha$ -helix, peak 3 and 5 contribute for random coil structure and peak 4 is assigned to  $\beta$ -sheet structure. The peak areas are normalized to the total peak area resulting from secondary structure motifs and converted into percentage of structural contribution.

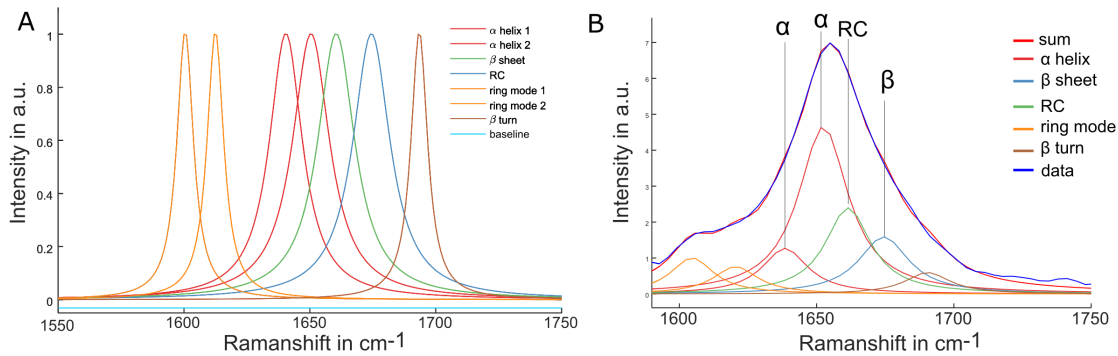


**Figure 2.12:** Decomposition of the amide I mode in Matlab. (A) Center position and FWHM for seven Lorentzian peaks and a constant baseline as given in eq.2.12. (B) A Raman-like CARS spectrum from BSA is fitted with the given function indicating a predominantly  $\alpha$ -helical structure.

## 2.3 Fluorescence microscopy

Light microscopy is the omnipresent tool in biology to visualize structures and processes that occur on sub-micron scales. As a frame of reference, epithelial cells typically have dimensions of several dozens of micrometers whereas organelles and other intracellular structures often scale on the lower limit of optical methods at only several hundreds of nanometers [43, 196]. While simple bright field microscopy creates contrast from absorption, scattering, or phase shifts when passing through a specimen, the method of fluorescence microscopy utilizes the luminescent emission of fluorophores as a signal [197].

Fluorescence describes absorption of light of a certain wavelength followed by the emission of photons at longer wavelength. The fluorescence signal is therefore Stokes-shifted with respect to the excitation light. Figure 2.13 shows the absorption and emission spectra of typical fluorophores used in following projects. Depending on the molecular structure, the different fluorophores molecules can be excited in a specific wavelength range with the emitted photons being about 50 nm red-shifted [197]. The physical theory for the fluorescence process can be found elsewhere [198]. Fluorescent molecules can be used to selectively examine single cellular components of interest. This can be realized by staining with

- Small molecule fluorophores (e.g. DAPI, Rhodamine 123, Phalloidin) that partition into certain compartments or bind to certain proteins
- Immunofluorescence, in which fluorophores are covalently linked to a protein - most often a primary or secondary antibody (e.g. AlexaFluor and Anti-vimentin) that binds to a target in the cell or
- Cellular expression of fluorescent proteins (e.g. GFP, YFP, etc.) with a target protein [199, 200].

### 2.3.1 Wide-field microscopy

In conventional light microscopy, a sample is homogeneously illuminated by a white light source and a magnified image is produced by an objective lens. The image then can be acquired by a camera or viewed through an eyepiece. For epi-fluorescence microscopy, a standard light microscope is equipped with set of filters together with a dichroic mirror to illuminate the sample with the excitation wavelength, and the same objective is used for

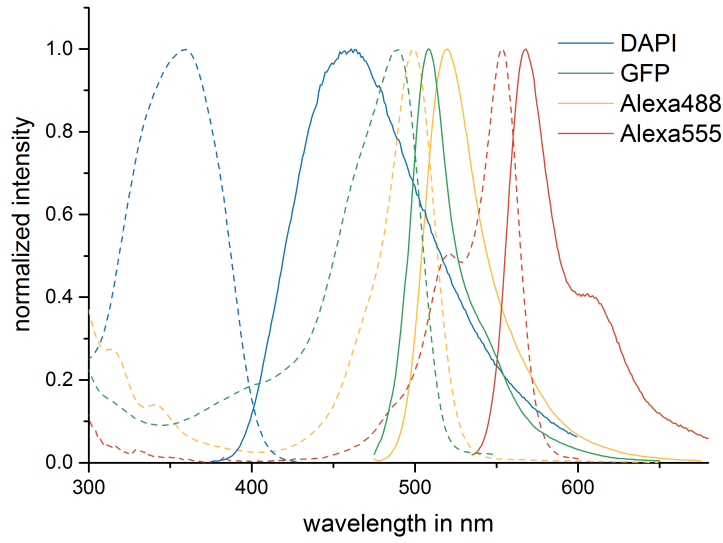


**Figure 2.13:** Absorption and emission spectra of common fluorophores. Spectral data was taken with permission from the fluorophore database from [www.chroma.com](http://www.chroma.com).

illumination. As the light illuminates a wide field-of-view, e.g. the entire specimen, this mode is also called 'wide-field fluorescence'.

The schematic illumination path for a wide-field fluorescence microscope is shown in Fig.2.14. To excite the fluorescently labelled sample, a high-power light source (typically an arc lamp or LED source) with a quasi-white spectrum in the visible range is used. The light passes a short-pass filter to limit the spectrum to the excitation range of the chosen fluorophore. Subsequently, the light is reflected towards the sample by a dichroic mirror that shows high reflectance only for the required excitation wavelength. The light is then delivered to the sample by the objective lens. The light is absorbed by fluorophores that label the target structure, and thereby create the red-shifted fluorescence photons. They are collected in epi-direction by the same objective lens, this time passing through the dichroic mirror and a longpass-filter right behind that blocks scattered excitation light. The fluorescently generated light is imaged onto a CCD-camera where an intensity image of the fluorophore distribution against a black background is formed [197].

Wide-field microscopy provides a lateral resolution that is a function of the numerical aperture (NA) of the used objective lens. The resolution for a self-luminous object, such as a fluorescently labelled specimen [201], is according to the Rayleigh criterion given by

$$R_{xy} \approx \frac{0.61 \cdot \lambda}{NA} \quad (2.13)$$

where  $R_{xy}$  is the lateral resolvable feature radius and  $\lambda$  the wavelength of the image creating light [196,199]. It states the minimal distance between two infinitesimally small point sources such that they are resolvable from one another is where the first minimum in the diffraction (Airy) pattern of point A coincides with the maximum of the nearby point B [196]. The Abbe limit provides a similar, slightly more restricted definition for the resolution based on considerations about the diffractive orders from an illuminated scattering object [201]. Along the z-axis (optical axis) the focal volume is more extended than in lateral dimensions and the focus extends over a range  $R_z$  given by

$$R_z \approx \frac{2 \cdot \lambda \cdot n}{NA^2} \quad (2.14)$$

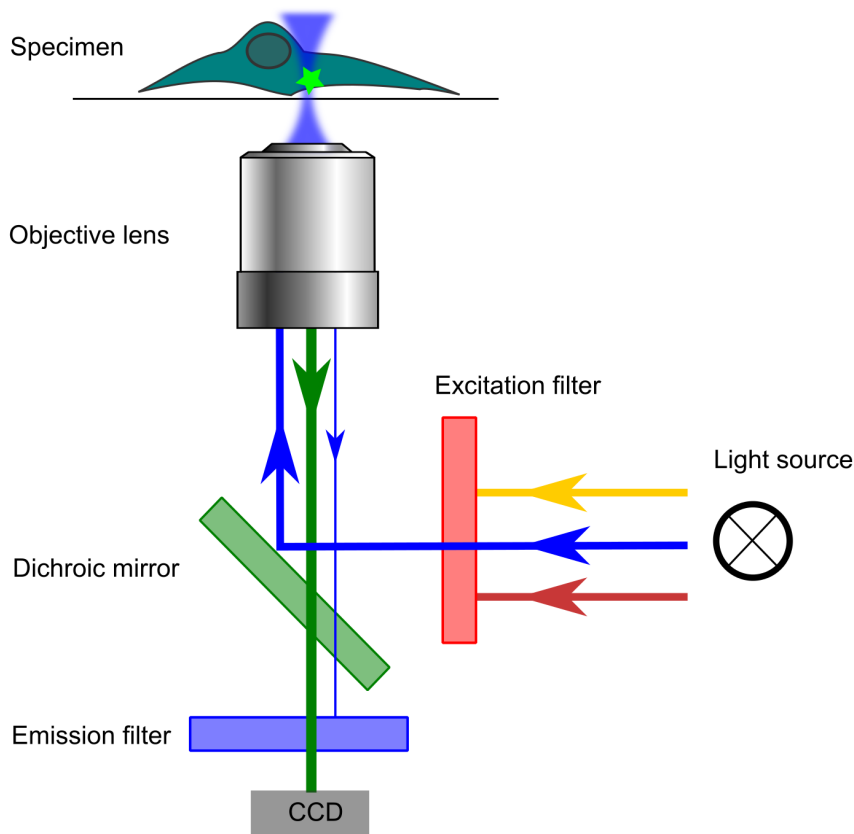


**Figure 2.14:** Basic setup design in an wide-field fluorescence microscope

where  $n$  is the refractive index of the mounting medium [196,199]. Therefore, the optical resolution is worse in depth, and the  $z$ -position of a fluorophore is less precise than for  $x$  and  $y$ .

Experiments in this thesis were performed on an Olympus IX-81 inverted microscope (Olympus), and images were acquired with a F-View II CCD camera (Olympus). Fluorescent illumination was provided by a X-cite 120PCQ excitation lamp (Excelitas technologies) with filter sets covering the range from  $\sim 300$ -650 nm.

### 2.3.2 Confocal microscopy

A more advanced imaging technique is confocal microscopy. Here, only light from within the focal volume is collected by a detector while out-of-focus light is physically blocked by a pinhole.

The experimental configuration for optical sectioning by a confocal pinhole is shown in Fig.2.15A. Monochromatic light (usually from a laser source) is directed by scanning mirrors through an objective lens where it is focused in a defined spot. The size of the focal volume is defined by the NA of the lens and the refractive index of the medium between objective lens and specimen. In the sample, fluorescent molecules are excited by the illuminating laser, and a fluorescence signal is generated. Linear fluorescence excites fluorophores along the entire optical path of the beam in the sample, not just the focus. All the created fluorescent signal is collected and passed through a dichroic mirror and further filters. To filter out all unwanted signal from out-of-focus events, a pinhole is positioned in the conjugate image plane to the focal point in the sample. In this way, fluorescent light that is produced in a different focal plane is defocused on the pinhole and will be mostly blocked. Only signal that arises from the focal volume will pass the pinhole and create an

intensity signal at the detector (usually a photomultiplier tube) for the selected position in the sample. By raster-scanning the focus through the sample and measuring the light intensity at each position a three-dimensional image of the fluorophore distribution can be obtained [199].

The size of the pinhole defines how much light can reach the detector and how strong the depth discrimination is [202]. While increasing the excitation laser power will result in more fluorescence it also will bleach the fluorophore and might damage the sample. Optimal imaging conditions therefore depend strongly on the stability of the sample and the fluorophore.

This superficial explanation gives only an overall idea of confocal microscopy. A more detailed theoretical analysis of the image formation process reveals further benefits such as an axial and spatial resolution that is improved by  $\sim \sqrt{2}$  compared to conventional light microscopy [202].

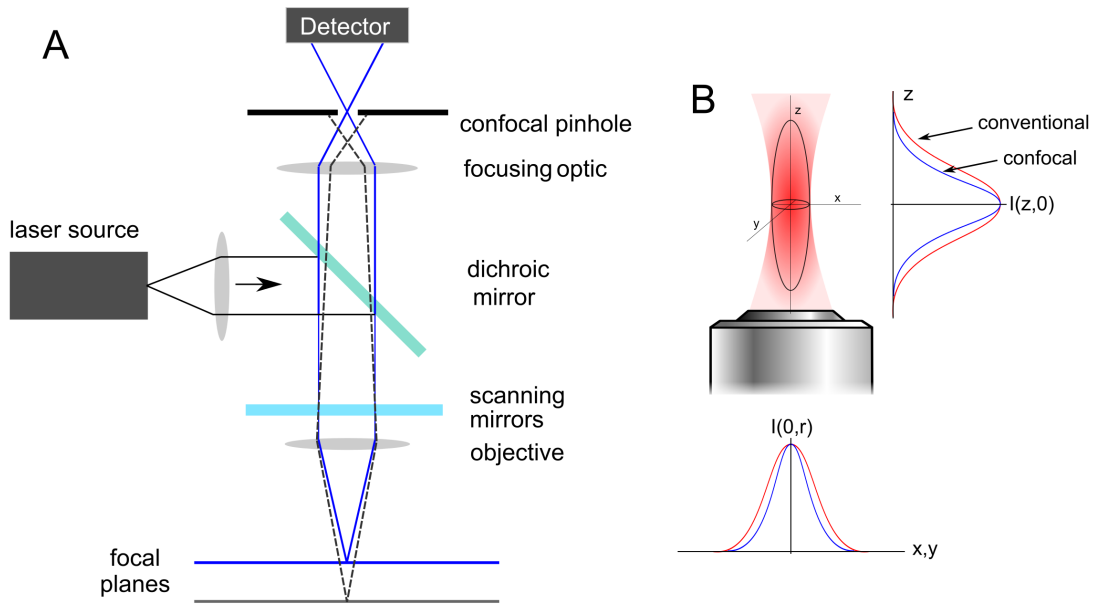


**Figure 2.15:** Schematic of a confocal microscope and the focal volume. (A) Only light from the selected focal plane (here indicated in blue) is able to pass through a confocal pinhole before the detector. Fluorescence signal from different focal planes in the samples (red) will be filtered out by the pinhole positioned in confocal configuration in front of a detector. (B) The focal volume describes the volume where the light intensity profile decays to  $1/e$  [196]. It forms a spheroid extended along the optical axis resulting in an improved lateral resolution. In confocal microscopy, the probed focal volume can be shrunk with respect to the usual wide-field microscopy.

Confocal microscopy experiments were performed in this work on Leica TCP SP5 confocal microscopes (Leica microsystems) in epi mode. The detailed experimental parameters varied with the different types of samples. Measurements were done, depending on the available laser sources, either at MPIP or at the IMB microscopy core facility. The obtained images were processed in the FIJI software package [203], which is an open-source package initially developed by the National Institutes of Health. If not stated otherwise, a constant background intensity taken from a specimen-free region was subtracted from all raw images.

## 2.4 Protein expression and purification of vimentin

For experiments on intermediate filaments described below in this thesis the protein vimentin and deuterated vimentin are used. Therefore, protein was expressed with normal and semi-deuterated medium in *E.coli* followed by purification via nickel-NTA affinity chromatography. This project was done in collaboration with the research group of Prof. Dr. Dirk Schneider at the Institute of Pharmacy and Biochemistry, Johannes Gutenberg-University Mainz. The following protocols were tested for high yields and protein functionality by Dr. Noreen Klein and Daniel Wirth and later further adapted by me.

### 2.4.1 Preparation of chemically competent *E.coli* cells

*E.coli* cells were made chemically competent for subsequent transformation as described in the following. The bacterial strain *E.coli* BL 21 (DE3)-Gold was used in all processes. A starter culture of *E.coli* cells were inoculated and grown over night in 3 mL LB (Luria-Bertani) medium (without antibiotics), under shaking and at 37°C. The next day the starting culture was diluted 1:100 to 50 ml fresh LB medium and grown further as before until an optical density of 0.5 at 600 nm absorption (OD600) was reached. Afterwards, the culture was centrifuged (3220g, 4°C, 10 min) to collect bacteria pellet from the medium. The obtained pellet was resuspended in 5 mL ice-cold Tryptic Soy Broth (TSB)-medium. After 10 minutes of incubation on ice the suspension was aliquoted in 100  $\mu$ L batches and flash frozen in liquid nitrogen, thereafter aliquots were stored at -80°C until further usage.

### 2.4.2 Transformation

For the expression of His-tagged vimentin, the genetic information must be introduced into the bacteria. To do so, a plasmid for human vimentin containing a C-terminal His-tag and ampicillin resistance was purchased (EX-D0114-B31, tebu-bio, Germany) and transformed into chemical competent *E. coli* BL21 (DE3)-Gold cells following the method from Chung and Miller [204] using 1  $\mu$ L plasmid DNA and 100  $\mu$ L suspension of BL21-Gold competent cells. The mixture was incubated on ice for 30 min and heated in a thermomixer for 45 s at 43°C. Afterwards, 400  $\mu$ L of LB-media were added to the solution and placed in a shaker at 200 rpm for 45 min at 37 °C. The solution was centrifuged (1 min, 13000 rpm), and the pellet was resuspended in 150  $\mu$ L of the supernatant. The transformed cells 'B21-Vim' were plated on ampicillin containing (100  $\mu$ g/mL) LB-agar and incubated overnight at 37°C to check for colonies.

### 2.4.3 Expression of vimentin in LB medium

LB medium (50 mL) containing 50  $\mu$ L ampicillin (100  $\mu$ g/mL) was inoculated with a single colony of BL21-Vim picked from an agar-plate. The pre-cultures were agitated at 200 rpm and grown at 37°C overnight. Subsequently, 2 1-L flasks filled with LB-medium supplemented with 2 mL ampicillin (100  $\mu$ g/mL) were inoculated with 50 ml of the overnight culture (1:40) and shaken at 37 °C, 150 rpm until an optical density of approximately 0.6 at 600 nm was reached. Protein expression was induced by adding 1 mL 1 M IPTG (final concentration 500  $\mu$ M). 6 h after IPTG induction the cells were harvested by centrifugation (6000 g, 10 min, 4 °C). The pellet resulting from 1-L expression culture was resuspended in 40 mL phosphate buffer and stored at -20 °C.

### 2.4.4 Expression of vimentin in deuterated minimal medium

Isotopic labelled vimentin, where hydrogen atoms are replaced by deuterium, was produced as it provides spectral contrast in BCARS imaging without the need of fluorophores. This

was achieved by growing E.coli in minimal medium and only a deuterated carbon source available which leads to the biosynthesis of deuterated protein. However, the final product was only partially labelled as H<sub>2</sub>O was used as solvent in all experimental steps and thereby exchange back to hydrogen occurred.

A pre-culture of BL21-Vim cells was picked from a single colony and grown in ampicillin (100 µg/mL) containing LB-medium agitated and at 37°C over night. Before inoculation of the expression culture, the cells were centrifuged (10 min, 3220 g) and the supernatant was removed to deplete available 'normal' carbon sources. Cells were then resuspended in M9 medium without acetate, and the centrifugation was repeated once. Afterwards, M9 medium was added to the previous volume, and the expression culture in M9 medium containing deuterated acetate and ampicillin (100 µg/mL) was inoculated in a ratio of 1:40. The culture was agitated at 200 rpm and grown at 37°C until an optical density of 0.6 at 600 nm was reached. Expression of vimentin was induced by the addition of 500 µM IPTG, and the antibiotic protection was refreshed by adding further 100 µg/mL ampicillin to the medium. Thereafter, the bacteria were grown over night agitated and at 37°C. Cells were harvested by centrifugation (1700 g, 10 min, 4°C), and the resulting pellet was resuspended in phosphate buffer (40 mL buffer per 1 L initial culture volume). If not used immediately afterwards, the cell suspension was stored at -20°C until further usage.

Deuterated sodium acetate-d<sub>3</sub> (C<sub>2</sub>D<sub>3</sub>NaO<sub>2</sub>, Sigma-Aldrich) was chosen as carbon source for bacteria growth (based on the work by Paliy *et al.* [205]) as it showed the best protein-for-money ratio in pre-tests. For the later upscaling of the production of deuterated vimentin a cost efficient process was essential.

#### 2.4.5 Cell lysis

To break up the cell membranes and thereby make the expressed protein, present in inclusion bodies, available solution of vimentin expressed bacteria was treated with ultrasonication. Cell lysis was performed on a Omnisonic Ruptor400 sonicator for 12 in (40% power, 50% duty time) and the solution being cooled by ice. Afterwards the inclusion bodies were sedimented by centrifugation at 6000 g, 4°C for 30 minutes. The obtained pellet was solubilized at room temperature by adding 600 µL urea buffer for 2-3 h. Before usage the Ni-NTA spin columns were equilibrated two time in 10 mL di-water followed by 3 x in 10 mL urea buffer per column. Solutions were run through the columns with help of vacuum suction.

#### 2.4.6 Purification of vimentin by Ni-NTA

Recombinant produced protein containing the His-tag (6x His) was purified by nickel-charged nitrilotriacetic acid (Ni-NTA) resin. Small spin columns filled with Ni-NTA (Qiagen, Ni-NTA Superflow 1.5 mL) were used for purification and one column was sufficient for 50 mL expression culture.

The cell lysate was added to the Ni-NTA column and passed through the column by help of vacuum suction. The flow-through was pipetted again on the column and passed a second time at similar conditions. During the slow centrifugation, the His-tag of the target protein is supposed to bind to the Ni-NTA. To remove unbound protein and cell fragments, the columns were washed in a subsequent step by 2x 5 mL rinsing buffer with increasing imidazole concentrations (0, 5, 10, 15 mM).

The protein bound to the Ni-NTA was eluted by rinsing with increased imidazole concentrations. Imidazole competes with the His-Tag for binding to the Ni-NTA and thereby displaces the formerly immobilized protein. For elution, 5 mL rinsing buffer containing imidazole (100 mM, 200 mM and 400 mM) were pipetted on the column and run by vac-



uum suction. This step was done twice per imidazole concentration and each eluate was stored separately. Thereafter, the protein concentration was measured by light absorption at 280 nm ( $\epsilon_{280} : 26360 M^{-1} cm^{-1}$ , calculated by the software tool ExPASy ProtParam using the sequence for vimentin). SDS-PAGE of the different elution fractions showed a majority of vimentin being in the 400 mM imidazole rinsing fraction (see Fig.2.16).

The protein containing fractions from the elution step were unified and imidazole was removed from the solution by dialysis. Therefore, the protein solutions were filled into an equilibrated dialysis membrane (MWCO 12-14 kDa) and incubated in dialysis buffer of decreasing urea concentrations (6 M, 4 M, 2 M urea for 1 h and 0 M urea overnight). A 100-fold excess in buffer was used and dialysis took place while stirring the buffer at 4°C.

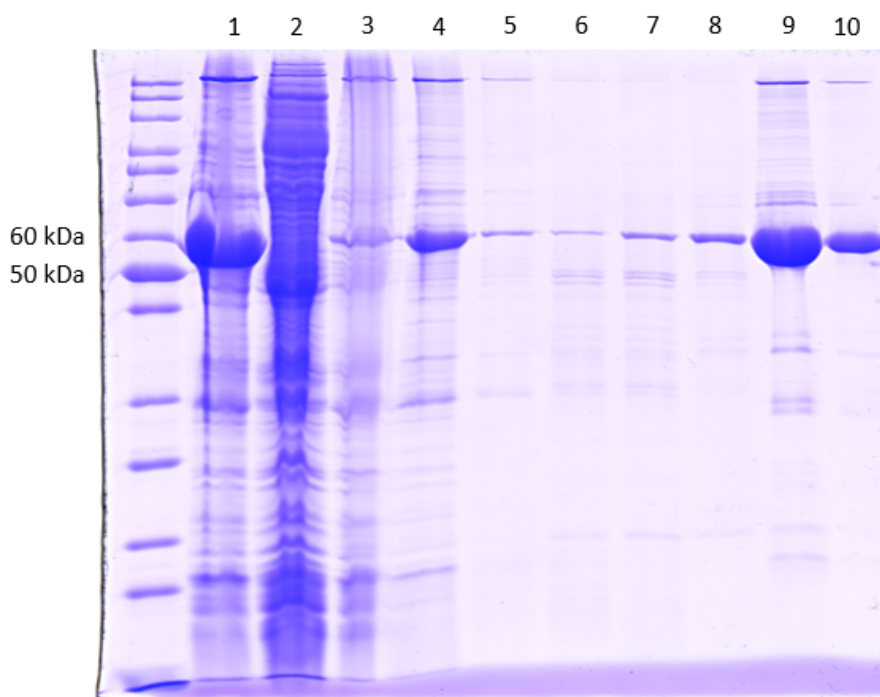


**Figure 2.16:** SDS-PAGE analysis of the Vimentin (54.880 Da) purification process. A 10% SDS-PAGE gel was loaded with the different fraction from purification and proteins were separated by their electrophoretic mobility. In a subsequent step, the protein position was made visible by staining with Coomassie Brilliant Blue. The lanes are assigned as follows: Left lane is the protein marker, (1) pellet of inclusion bodies after centrifugation, (2) supernatant of first centrifugation. (3) pellet and (4) supernatant after solubilization in urea buffer, (5) - (8) washing steps with increasing imidazole concentration and (9), (10) elution steps with 400 mM imidazole. The shown gel analysis was prepared by Dr. Noreen Schneider and Daniel Wirth.

#### 2.4.7 Concentrating the protein

Following the dialysis, the protein was concentrated to final concentrations of 1.6 - 2 mg/ml. First, aggregated protein was removed by sedimentation (15 min at 13000 rpm and 4°C). Thereafter, the supernatant containing the monomeric vimentin was concentrated in Centricons (Vivaspin 6, MWCO 30 kDa), and the protein concentration was checked by light absorption at 280 nm. The final protein stock was flash frozen in liquid nitrogen and stored aliquoted at -80°C.

### 2.4.8 Test for filament formation

The functionality of the produced vimentin was tested by its ability to form filaments. As described by Perez-Sala and coworkers, monomeric vimentin in salt-free buffer can be polymerized by the addition of sodium chloride to a final concentration of 340 mM. Vimentin samples at 1.6 mg/ml concentration were polymerized at 37°C for 30 min and samples were checked in light microscopy subsequently. Figure 2.17 shows representative microscopy images of intermediate filaments from non-deuterated vimentin that were formed *in vitro*. The filamentous structure is clearly visible at large magnification. ULF filaments and aggregated vimentin were observed in some samples. A similar filament formation was successfully shown for deuterated vimentin. The mechanical properties and further test assays of the produced vimentin were done by Daniel Wirth and are covered in his bachelor thesis [206].

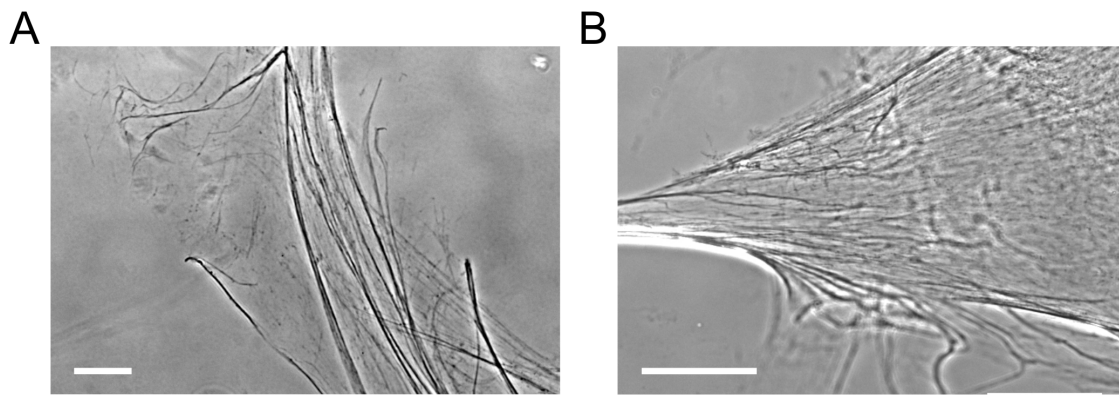


**Figure 2.17:** Phase contrast microscopy images of polymerized vimentin filaments with error bars representing 50  $\mu\text{m}$ .

#### 2.4.9 Appendix: Buffer and media used for protein production

Material	Description
Luria-Bertani (LB)-agar	1 % (w/v) Tryptone, 0.5 % (w/v) yeast extract, 1 % (w/v) NaCl, 1.5 % (w/v) Agarose, autoclave and add antibiotics after cooling below 50°C
LB-Medium	1 % (w/v) Tryptone, 0.5 % (w/v) yeast extract, 1 % (w/v) NaCl, autoclave and add antibiotics after cooling below 50°C
Tryptic Soy Broth-Medium (TSB)	10% (w/v) PEG 4000, 5 % (v/v) DMSO, 2 % (v/v) 1 M $MgCl_2$ , 1 % (w/v) Tryptone, 0.5 % (w/v) yeast extract, 0.5 % (w/v) NaCl, sterile filter final solution
Phosphate buffer (PB)	50 mM Phosphate, pH 8.0 (43 mM $Na_2HPO_4 \cdot 7H_2O$ and 7 mM $Na_2H_2PO_4 \cdot H_2O$ ), 300 mM NaCl, 10% (v/v) Glycerol, DI-water
Urea buffer	100 mM $NaH_2PO_4$ , 10 mM Tris-HCl, 150 mM NaCl, 8 M Urea, DI-water, pH 8.0
Rinsing buffer	100 mM $NaH_2PO_4$ , 10 mM Tris-HCl, 150 mM NaCl, 8 M Urea, 0, 5, 10, 15 mM Imidazol, DI-water, pH 8.0
Elution buffer	100 mM $NaH_2PO_4$ , 10 mM Tris-HCl, 150 mM NaCl, 8 M Urea, 200 mM, 400 mM Imidazol, DI-water, pH 8.0
Dialysis buffer	0/2/4/6 M Urea, 5 mM Tris-HCl, 5 mM DTT, DI-water, pH 7.0
M9 salt solution	800 mL DI-water, 64 g $Na_2HPO_4-7H_2O$ , 15 g $KH_2PO_4$ , 2.5 g NaCl, 5.0 g $NH_4Cl$ , Stir until dissolved, then adjust to 1000 ml with distilled H <sub>2</sub> O. Sterilize by autoclaving
Minimal medium	700 mL DI-water, 200 mL M9 salt solution, 2 mL 1 M $MgSO_4$ (sterile), 20 mL of 20% sodium acetate-d <sub>3</sub> ( $C_2D_3NaO_2$ ), 100 $\mu$ l of 1M $CaCl_2$ (sterile). Adjust to 1000 mL with DI-water.

**Table 2.2:** Buffer and media used for protein production

## 2.5 Creation of a GFP expressing HeLa strain

A stable cell line HeLa GFP-Vim was established to investigate vimentin intermediate filaments without the need of immunostaining. Commercially available lentiviral particles (LentiBrite, EMD Millipore) were used to introduce genes for vimentin and GFP into HeLa cells [207] resulting in the expression GFP-labelled vimentin IF. By this, a continuous live cell observation of the IF morphology under different drug treatments was possible.

Before transduction, the Multiplicity of Infection (MOI) was determined from viral titer ( $2.01 \times 10^9$  IFU/ml) indicated on the vial as infectious units (IFU). HeLa cells were seeded onto a 6-well plate in filtered DMEM culture media containing 10 % fetal calve serum

(FCS) without antibiotics ~12 h prior to transduction. The seeding density was chosen as  $10^5$  cells/well in a seeding volume of 2 mL, so that cells become ~60 to 70% confluent at the time of transduction.

The stock solution containing the lentiviral particles was diluted in 1 ml serum-free DMEM to the desired MOI and then added to the cells. In order to optimize the transduction, the MOI can be varied (10, 20 and 40) between different wells. Next, cells were incubated to allow viral uptake. The viral genome will be integrated into the host cell genome after 24-48 h post transduction. A successful transduction results in the expression of green fluorescent protein (GFP), which is fluorescent when excited at a wavelength of 483 nm. After 48 h, cells were washed three times in PBS to remove remaining lentiviral particles followed by normal incubation in DMEM + 10% FCS. The rate of transduced cells was found to be 10-20 % of all cells as measured by counting GFP-expressing cells in fluorescence microscopy.

To increase the percentage of GFP-Vim expressing cells, the transduced cells were sorted by fluorescence-activated cell scanning (FACS). Cell sorting was done in collaboration with the Core facility for Flow Cytometry at the Institute for Molecular Biology, Mainz, and excellent help from Mrs. Ina Schaäfer. As cell sorting required partial non-sterile conditions, the addition of antibiotics (penicillin and streptomycin) is necessary for further culturing of the cell strain. The sorted cells were re-planted in T75 flasks, grown to 70% confluency and then frozen as cryo stocks. HeLa GFP-Vim cells were shown to have stable GFP-vimentin expression over at least 30 passages.

Gene	Donating organism	Description
TagGFP2	<i>Aequorea macrodactyla</i>	Optimized version of TagGFP, a mutant of the GFP-like protein [208] showing fluorescence when excited at 483 nm.
Vim	<i>human</i>	Vimentin, class-III intermediate filament forming protein
EF-1	<i>human</i>	Human elongation factor-1 alpha (EF-1 alpha), Promoter for Gene-expression in <i>in vitro</i> and <i>in vivo</i> -applications

**Table 2.3:** Transgenes used in Lentibrite-Vimentin particles

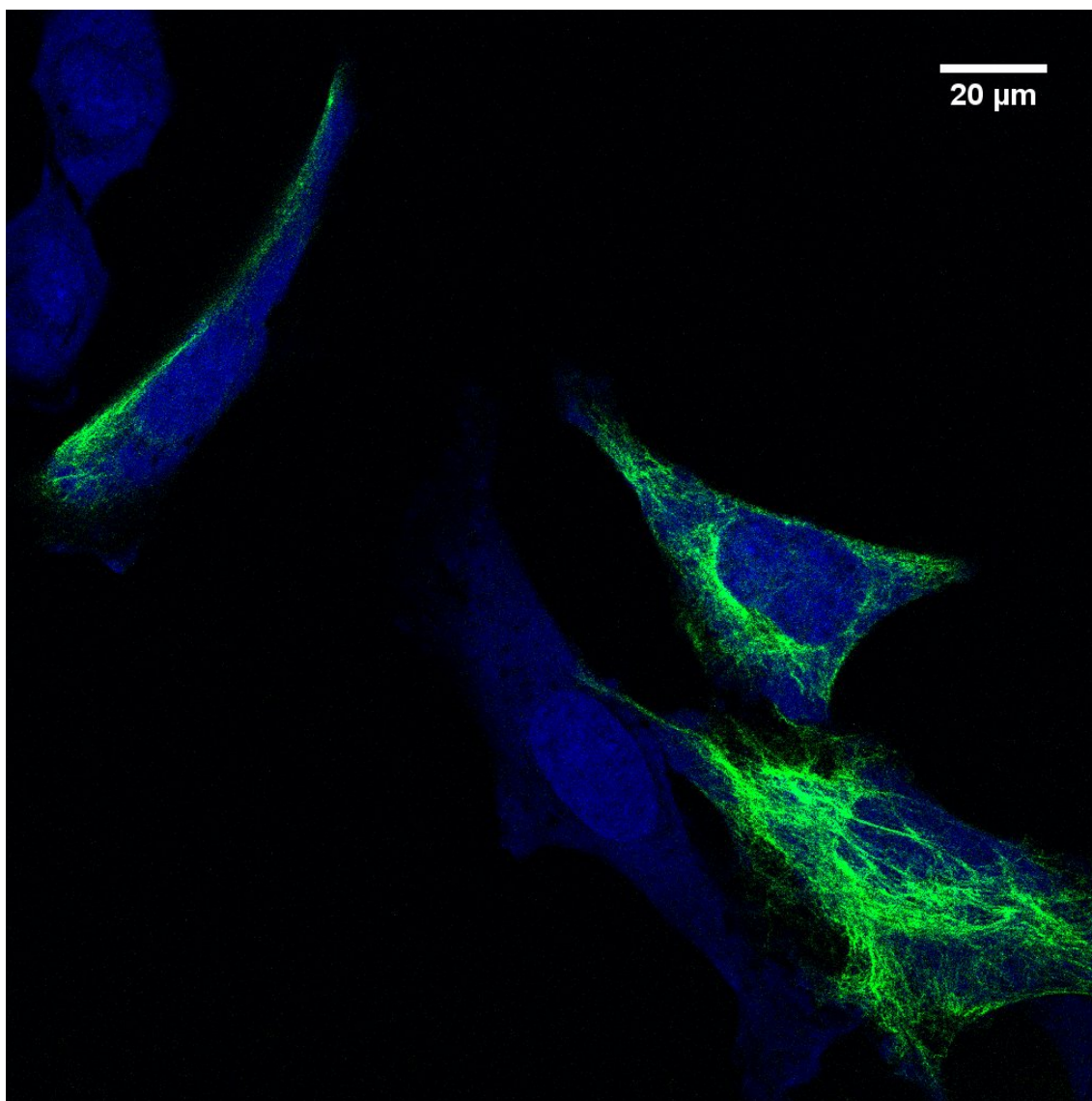


**Figure 2.18:** Lentiviral transduced HeLa cells expressing GFP-vimentin. Merged images from confocal microscopy showing unspecific staining of the cytosol by DRAQ5 in blue and GFP-vimentin in green with the scale bar indicating 20  $\mu\text{m}$ . Cells were incubated for 48 h to reach a high percentage of GFP-expressing cells. The filamentous IF network spreading in the cytosol and forming a cage-like shell around the nucleus is visible.

## Chapter 3

# Microscale spatial heterogeneity of protein structural transitions in fibrin matrices

Reprint from the article ‘Microscale spatial heterogeneity of protein structural transitions in fibrin matrices’ by Frederik Fleissner, Mischa Bonn and Sapun H. Parekh in Science Advances, 08 Jul 2016, Vol. 2, no. 7, e1501778, DOI: 10.1126/sciadv.1501778

This work is licensed under CC BY-NC (<http://creativecommons.org/licenses/by-nc/4.0>).  
©2016, The Authors.

## Abstract

Following an injury, a blood clot must form at the wound site to stop bleeding before skin repair can occur. Blood clots must satisfy a unique set of material requirements; they need to be sufficiently strong to resist pressure from the arterial blood flow but must be highly flexible to support large strains associated with tissue movement around the wound. These combined properties are enabled by a fibrous matrix consisting of the protein fibrin. Fibrin hydrogels can support large macroscopic strains owing to the unfolding transition of  $\alpha$ -helical fibril structures to  $\beta$ -sheets at the molecular level, among other reasons. Imaging protein secondary structure on the submicrometer length scale, we reveal that another length scale is relevant for fibrin function. We observe that the protein polymorphism in the gel becomes spatially heterogeneous on a micrometer length scale with increasing tensile strain, directly showing load-bearing inhomogeneity and nonaffinity. Supramolecular structural features in the hydrogel observed under strain indicate that a uniform fibrin hydrogel develops a composite-like microstructure in tension, even in the absence of cellular inclusions.

## 3.1 Introduction

Fibrin is the primary filamentous protein component in blood clots during hemostasis. Blood clots need to be sufficiently strong to prevent further bleeding, while also being sufficiently flexible to support large strains [209]. Under shear strains of more than  $\sim 20\%$ , clots exhibit nonlinear elasticity - an increase in elasticity with strain amplitude, known as strain hardening. This mechanism allows a blood clot to be flexible when relaxed and to become robust and resistant under large external forces [40, 209]. Following hemostasis, fibrin degradation occurs as the skin is rebuilt toward the end of wound healing. Interestingly, it has been shown that fibrin degradation is significantly slower (more than 10-fold) in 'tight' clots and fibrin under tensile strain [210]. Fibrin monomers have a coiled-coil structure consisting of six  $\alpha$ -helices. To form the hydrogel, fibrin monomers self-assemble resulting in double-stranded protofibrils with monomers staggered relative to one another by roughly half a protein length (45 nm) [211]. Multiple protofibrils further assemble into larger fibers with a final thickness in the range from 50 to 200 nm and fiber length from 0.3 to 4.8  $\mu\text{m}$  [40, 130]. These fibers are the primary structural unit of fibrin hydrogels. At an even larger scale, fibers form branches and entanglements between each other until a three-dimensional network is established with a mesh size of order 1  $\mu\text{m}$  [27, 129]. This hierarchical and complex structure of fibrin networks gives it unique mechanical properties, with the network responding to strain on several length scales. At the molecular level, the  $\alpha$ -helices can be unfolded into  $\beta$ -sheets under tensile force, which has been shown in both single molecule experiments [212] and in strained fibrin networks. Small angle x-ray scattering (SAXS) has revealed that structural transitions of the coiled-coil  $\alpha$ -helices in fibrin monomers must play a role in the elongation of a fibrin starting at 15 % tensile strain [41]. Recently, attenuated total internal reflection Fourier transform infrared (ATR-FTIR) spectroscopy on fibrin clots directly showed that secondary structure content of fibrin clots was altered under compression and tension [9]. Spectral analysis of the amide I and amide III vibrational bands revealed that relaxed human fibrin gels contained 31 %  $\alpha$ -helix, 37 %  $\beta$ -sheet, and 32 % turns, loops and random coils, which changed to 16 %  $\alpha$ -helices and 52 % of  $\beta$ -sheet structures under large (400%) extensional strain [9, 213]. Combined with previous rheological studies, a physical-chemical description of fibrin at the molecular (from spectroscopy and scattering) and macroscopic (from rheology) scale in response to strain is becoming clear. However, a description that spans the molecular- to micro-scale of fibrin is comparatively absent. Since fibrin clots contain

micron-sized platelet inclusions that exert contractile forces, a description of load bearing and structure on micron length scales is highly relevant to understanding the underlying physics governing stress distribution in the material. A microscopic mechanical description of collagen recently showed rich mechanical properties not observable (or explainable) from continuum theories using holographic optical tweezers, which highlights importance of measuring local mechanics in protein hydrogel materials [214]. Morphological evidence of spatially heterogeneous strain is clear from ultrastructural images and confocal fluorescence of fibrin networks [9, 41, 215]; however, these images do not provide any evidence of local force distribution in the network, which (as mentioned above) is related to fibrin protein structure. Therefore, by measuring spatially-resolved fibrin protein structure within the hydrogel, it would be possible to visualize the local load distribution directly. This would allow identification of rich local mechanical properties in fibrin, similar to those recently discovered in collagen. Observation of spatially heterogeneous protein structure as a function of load requires measuring protein structure at the sub-micrometer scale (ideally on the fiber length scale,  $\sim 100 - 300nm$ ) combined with defined mechanical deformations. Raman spectroscopy is ideally suited for this purpose as it is capable of probing amide I and III molecular vibrations similar to FTIR, yet possesses much better ( $\sim 400nm$ ) spatial resolution, and does not suffer from the intense water absorption in aqueous samples that can mask amide vibrations [216]. Indeed, spontaneous Raman spectroscopy has been used to quantify secondary structure in various biopolymers, including whelk egg capsules [217]), keratin [218], and collagen fibers [219]; however, not as a function of external strain. Unfortunately, the signal intensity in spontaneous Raman is limited as only 1 out of  $10^{10}$  photons is inelastically Raman scattered [216, 220]. Thus, it is challenging to perform spectral imaging without excessively long measurement times that could complicate interpretation for even slightly viscoelastic materials. One route to overcome the limitations of spontaneous Raman is nonlinear Raman scattering such as coherent anti-Stokes Raman scattering (CARS). Here, the Raman signal is generated in a four-wave mixing process where the signal strength is resonantly enhanced by up to 6 orders of magnitude [216]. This is realized by spatial and temporal overlap of two laser beams where the energy difference between the two lasers defines the Raman frequency that is probed. Quantitative band analysis of broadband CARS spectra is possible with established routines, and thus CARS provides Raman-like vibrational spectra at increased speed [221]. In this study, we employ hyperspectral broadband coherent anti-Stokes Raman scattering (BCARS) [156, 176, 222, 223] - in which an entire vibrational spectrum ( $800 - 4000\text{ cm}^{-1}$ ) is acquired in a single acquisition at each spatial location - to determine spatially-resolved secondary structure in fibrin hydrogels. We combine the BCARS approach with tensile measurements of fibrin gels to quantify mechanically-induced secondary structural changes at sub-micron spatial length scales. Our results show that the secondary structure in fibrin becomes increasingly heterogeneous with increasing tensile load with micron-sized regions showing primarily  $\alpha$ -helix next to similarly sized  $\beta$ -sheet regions.

## 3.2 Results

### Fibrin networks strain-stiffen both in shear and tension

Before investigating structural properties of fibrin hydrogels using BCARS, we measured the viscoelastic properties of our hydrogels with shear rheometry and tensile testing. Pre-strain sweeps on both partially cross-linked - defined here as fibrin gels polymerized from as-received fibrinogen - and FXIIIa-cross-linked fibrin samples - defined here as fibrin cross-linked with saturating FXIIIa - were conducted to measure the so-called differential shear modulus,  $K$ , of the materials [40, 167, 224]. It should be noted that our partially



cross-linked fibrin samples have trace amounts of FXIII as it co-purifies with fibrinogen but still less than in cross-linked samples (Fig.3.6) [225]. Figure 3.1A shows prestrain sweeps in shear for both types of gels and shows a characteristic plateau storage modulus  $K'$  at low strains of 320 Pa and 420 Pa for the partially cross-linked and cross-linked samples, respectively. The plateau modulus for our fibrin gels was comparable to that observed in other studies [40, 226], and prestrain sweeps of fibrin hydrogels with  $c_{fibrin} = 15\text{mg/mL}$  show the characteristic increase in  $K' \propto c_{fibrin}^{11/5}$  as well as  $K'$  convergence at large prestrains (Fig.3.7). The onset of nonlinear elasticity in shear occurred at a strain of  $\sim 40\%$  for partially cross-linked and  $50\%$  for cross-linked samples, respectively as judged by the intersection of linear fits to the high and low strain region for each curve. We performed additional shear creep recovery experiments for both partially cross-linked and fully cross-linked hydrogels (Fig.3.8). These measurements show that additional FXIII led to a decreased dissipative response and faster response dynamics to steady mechanical perturbation compared to partially cross-linked fibrin. As an additional mechanical characterization, we also performed tensile tests on the hydrogels. From this data, we see a critical strain of  $\sim 35\%$  extension where the normalized force vs. strain curve changes from a shallow slope at low strain to a large slope at high strain (Fig.3.1B). However, these measurements do not show substantial differences between partially cross-linked fibrin and cross-linked fibrin hydrogels. Taken together, the shear and tensile measurements do not show substantial differences in the nonlinear mechanics of the fibrin hydrogels. Nevertheless, the shear measurements - both rheology and creep recovery - show a clear increase in the linear differential modulus and reduced dissipative response, as is expected with additional cross-linking of fibrin [225, 227, 228].

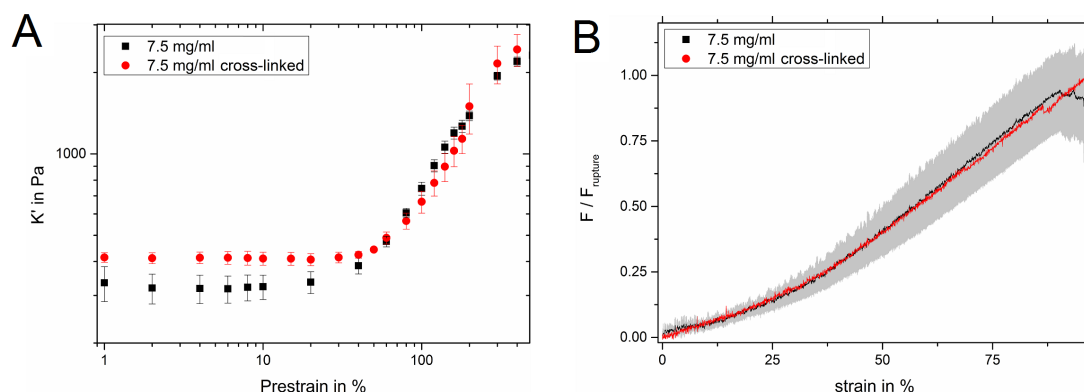


**Figure 3.1: Strain-dependent elasticity fibrin hydrogels.** A) Shear rheology of partially cross-linked and cross-linked 7.5 mg/mL fibrin. Three hydrogel samples were averaged per strain point, error bars are SEM. B) Tensile tests for the same types of samples. Force-strain curves were normalized to the rupture force. The average (black and red) represents 5 measurements from independent samples; SEM is depicted as gray area.

### Helix and sheet structures are orthogonal under tensile strain

In our BCARS measurements of protein structure, we apply uniaxial tension to fibrin hydrogels, which defines a clear anisotropy in the material along the loading direction. Fibrin fibers are known to align under increasing strain, which should occur prior to any tension-based protein unfolding [41]. Previous molecular dynamics simulations have shown that the orientation of the coiled-coil helices (present at low strains) and sheet structures (present only at large strain) are organized such that their stabilizing hydrogen bonds are orthogonal to each other. Thus, we initially focus on identifying the orientation of the  $\beta$ -sheet with respect to the uniaxial load to maximize our sensitivity for strain-induced

$\beta$ -sheets. To determine secondary structure in fibrin gels *in situ*, we acquire hyperspectral BCARS datasets of fibrin (one spectrum at each spatial position) and decompose the vibrational amide I spectra ( $1570 - 1700 \text{ cm}^{-1}$ ) from each resonantly retrieved Raman-like spectrum to determine the contribution of  $\alpha$ -helix,  $\beta$ -sheet, and random coils structure in each spectrum (see CARS data processing in Methods). The amide I vibration (corresponding to the NH-coupled C=O vibration) is present in any protein; however, because of the local hydrogen bonding that stabilizes  $\alpha$ -helices and  $\beta$ -sheets, the amide I vibrational resonance shape is distinct for each secondary structure:  $\alpha$ -helices have a peak at  $1640 \text{ cm}^{-1}$  while  $\beta$ -sheets have a peak at  $1667 \text{ cm}^{-1}$ . In an  $\alpha$ -helix, the C=O group in one peptide is hydrogen bonded to secondary amines of another peptide bond in a direction that is parallel to the helical axis. Corresponding hydrogen bonds that stabilize  $\beta$ -sheets are formed orthogonal to each  $\beta$  strand [229]. The characteristic spectra of these structures, an additional mode from random coils, and two tyrosine ring breathing mode vibrations [46] were used to fit the amide I region of each spectrum. Prior to decomposition, spectra were normalized by the amount of protein in each spectrum as given by the  $\text{CH}_3$  vibration ( $2934 \text{ cm}^{-1}$ ) that arises from protein side chains [46]. After spectral decomposition, the fractional area of each component relative to the total area was quantified to determine the percentage contribution of each structural motif in every spectrum (Fig.3.2A and 3.2B). Similar decomposition of Raman spectra has been shown to correspond better than 95 % with structural percentages determined by X-ray diffraction [55]. By scanning the sample, we can measure the relative contribution of particular secondary structural motifs within  $0.5 \times 0.5 \times 3.5 \text{ }\mu\text{m}^3$  voxels in native, unlabeled samples. Since the amide I vibrational line

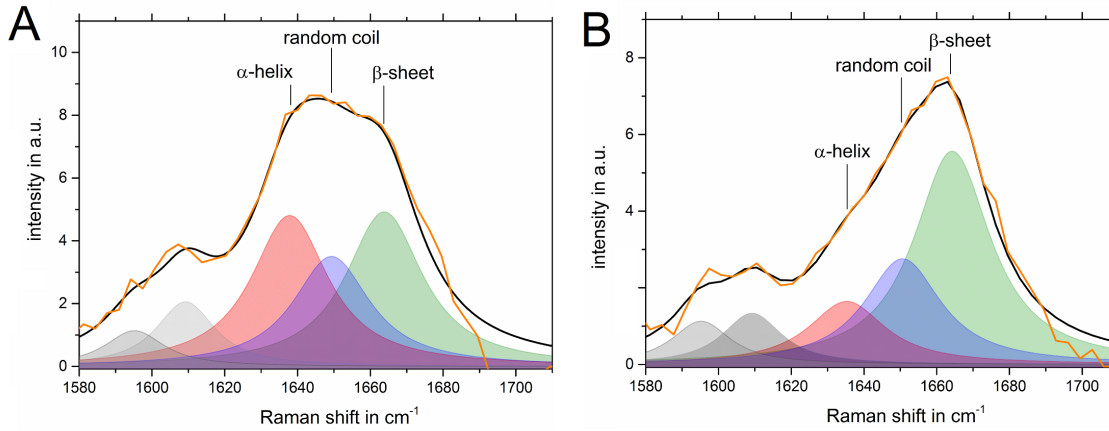


**Figure 3.2: Phase-retrieved and  $\text{CH}_3$ -normalized B-CARS spectrum of fibrin.** (A) Never loaded and (B) 80% strained fibrin hydrogel. The amide I band was decomposed with a sum of five Lorentzians: green, blue and red peaks that represent structural species indicated as well as two smaller ring modes depicted in grey related to tyrosine rings. The contribution of each species to the amide I band was determined by the fractional area under each component. Black is the raw data and orange lines are the Lorentzian fits.

shapes of  $\beta$ -sheet and  $\alpha$ -helix motifs are different due to the stabilizing hydrogen bonds within each structure, it is possible to investigate the orientation of these structures by determining the angular dependence of the amide I resonance for each structural motif. The orientation of sheet and helix motifs in partially cross-linked fibrin hydrogels ( $c_{\text{fibrin}} = 7.5 \text{ mg/mL}$ ) was measured by rotating the sample relative to the microscope (and lasers) and measuring BCARS hyperspectral datasets at each rotation angle in both never loaded and strained fibrin. At each angular position, a hyperspectral map of  $5 \times 5 \text{ }\mu\text{m}^2$  (11 x 11 pixels) was acquired, and the 30 pixels with the highest protein content, as judged by the value of  $\text{CH}_3$  vibration, were selected for quantification of secondary structure. The

structural content, % contribution of each structural motif to the total amide I band area, was averaged for these 30 pixels. We found that including the 30 pixels with the highest protein content was an acceptable number to represent the hydrogel average behavior while allowing for automated, unsupervised analysis. Including additional pixels in the analysis did not change the results significantly (Fig.3.9). In the case of the never loaded fibrin we observe an angularly isotropic Raman contribution for both  $\alpha$ -helix and  $\beta$ -sheet peaks, as indicated by observing nearly circular shapes in polar plots (Fig.3.3A). When stretching the sample to 60 % strain, we observe a change in the spectral shape (Fig.3.2) and opposing trends for the two peaks with respect to sample rotation angle (Fig.3.3B). The polar plot of the peak related to  $\beta$ -sheets shows an elliptic orientation with a major axis nearly orthogonal to the laser axis. The second peak, indicative of  $\alpha$ -helices, shows an ellipticity with a major axis parallel to the laser polarization. Figure 3.3B shows that the contribution of  $\beta$ -sheet structures to the amide I vibration is maximized when the loading axis and laser polarization are nearly orthogonal (angle  $\sim 80^\circ$ ) while for  $\alpha$ -helices the contribution is maximized when the laser and loading axes are parallel. This can be generalized to note that the stabilizing hydrogen bonds within the  $\beta$ -sheet and  $\alpha$ -helices in fibrin are orthogonal to one another under load, which is consistent with the  $\alpha$ -helix and  $\beta$ -strand elements lying along the loading direction, as previously postulated [35]. Furthermore, the angle-integrated (total) contribution for  $\alpha$ -helix decreases by 11 % under strain while for  $\beta$ -sheet it increases by 19 %, showing that the amount of  $\beta$ -sheet increases under tension and assumes a preferential orientation.

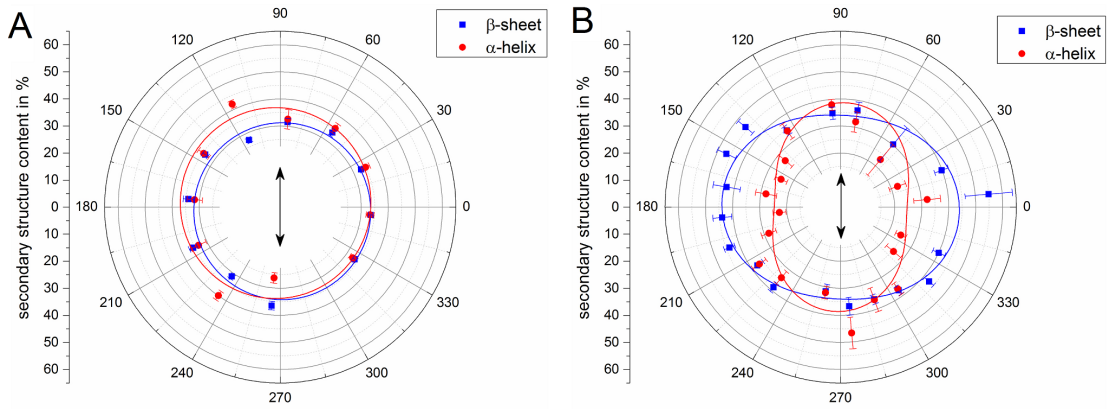


**Figure 3.3: Polar plots show the orientation of the different secondary structure motifs in a never loaded and strained fibrin gel.** 30 spectra from a single gel (at rest, then strained) with the most intense  $\text{CH}_3$  peak ( $2934 \text{ cm}^{-1}$ ) were averaged to generate each point in these plots. Error bars are SEM. (a) At 0 % strain, both motifs show an isotropic distribution, as expected. (B) At 60 % strain, the two motifs exhibit elliptical shapes indicating a preferred direction of the load with respect to the laser polarization (double headed arrow). The  $\alpha$ -helix peak shows a maximum intensity when the load aligned to the polarization of the lasers, indicated by the arrow, whereas the  $\beta$ -sheet peak maximum is rotated  $80^\circ$  with respect to the  $\alpha$ -helix. Lines show fits to a sine function,  $y = y_0 + A \cdot \sin\left(\frac{\pi(x-x_c)}{90^\circ}\right)$ . For each secondary structure motif, the contribution to the amide I spectrum was calculated by integrating the fit function over the entire polar range. (C) Example schematic of  $\alpha$ -helix (structure from PDB: 2MJ2) and (D) antiparallel  $\beta$ -sheet (structure from PDB: 1SLK) under load (indicated by the arrow) similar to secondary structures present in fibrin fibers. Hydrogen bonds are shown as dotted lines.

### Strain-induced increase in $\beta$ -sheet content is more pronounced in cross-linked hydrogels

Following identification of the  $\beta$ -sheet motif orientation relative to the loading direction, we measured the secondary structural changes as a function of increasing tensile strain in both cross-linked and partially cross-linked fibrin. In the following measurements, the laser polarization was fixed nearly perpendicular to the loading direction, which was chosen to maximize the sensitivity to new  $\beta$ -sheets formed with increasing strain (indicated by the angle between the major axis in the polar plot relative to the laser in Fig.3.3B (red)). We stretched gels from initial length to 110 % strain. For larger strains, many of the gels broke or started to slide; however, all gels withstood 110 % strain without failure. The contribution of  $\alpha$ -helix and  $\beta$ -sheet structures are plotted against the local strain, by averaging over the 30 most protein-rich spatial pixels in a  $5 \times 5 \mu m^2$  field-of-view (Fig.3.4). Because all spectra were normalized to protein concentration, we combined the spectra from five independent hydrogel samples and binned the measurements along the strain axis into 20 % increments, starting from 10 %. The local strain in the sample was quantified by measuring the displacement of polystyrene beads in the field-of-view from bright field images (see Methods). The local strain, calculated from different pairs of polystyrene bead displacements in the field-of-view, varied by less than 5 %. Therefore, the strain was assumed to be applied uniformly over the sample. As the tensile load stretches the gel relative to the fixed mounting point, the field-of-view, and hence the analyzed collection of pixels included in our calculation for secondary structure, are not the same for each strain level. Consistent with previous results by Brown *et al.* [41], showing water expulsion with tensile strain, we observe increased fibrin concentration (inferred from an increased CH intensity) with increasing strain on fibrin hydrogel samples (Fig.3.10). The contribution of the peak centered at  $1667 \text{ cm}^{-1}$ , representative of  $\beta$ -sheet structures [55], increased for both hydrogel samples starting at  $\sim 30$  % strain - excluding the initial jump from 0 - 10 % strain that arises from sample handling, as will be explained below. We observed that partially cross-linked hydrogels yielded a lower amount of  $\beta$ -sheet over the entire range of strains compared to additionally FXIIIa-cross-linked fibrin. Looking at each of the curves in figure 3.4A, the amount of  $\beta$ -sheet sharply increases from 30-90 % strain (more so for FXIIIa-cross-linked samples) and flattens out by 90 % strain in both samples. The standard error of the mean increases under load relative the 'true' 0 % measurement. From decomposition of the amide I band, we determine the amount of  $\beta$ -sheet increased to a final content of 42 % for partially cross-linked gels and 52 % for cross-linked gels. The contribution of the peak centered at  $1640 \text{ cm}^{-1}$ , representative of  $\alpha$ -helical structures [46], decreased with increasing deformation for both samples (Fig.3.4B). Coincident with a strong increase in  $\beta$ -sheet content at 30 % strain, a decrease in  $\alpha$ -helix content was seen starting at the same strain (neglecting the small decrease from 0-10 % strain). The  $\alpha$ -helix content in the partially cross-linked gel seems to stabilize at 25 % whereas the cross-linked does not stabilize by 110 % strain. The measured contribution from random coils, represented by a peak centered at  $1650 \text{ cm}^{-1}$ , remained largely constant at all strains (Fig.3.11), consistent with previous IR data [9]. As a 'true' 0 % strain measurement, BCARS hyperspectral maps of fibrin directly formed between two coverslips were acquired and processed for both partially cross-linked and FXIIIa-cross-linked hydrogels, which are shown at 0% in both plots of figure 3.4. The 'true' 0 % measurement shows the largest contribution for  $\alpha$ -helices and smallest contribution of  $\beta$ -sheets. Therefore, we surmise that the initial change in secondary structure seen from 0-10 % strain contains effects from sample handling, which is unavoidable in our experiment. Minimal deformations of fibrin hydrogels have been shown to cause both rearrangement of fibers along the loading axis of the samples [40], and even minimal tensile strains ( $\sim 15$  %) in handling could lead to unfolding of fibrin [41]. Both of these effects would lead to

an increase in  $\beta$ -sheet content at 10 % strain in our measurements compared to the 'true 0 %' measurement where no handling occurs. For both  $\alpha$ -helix and  $\beta$ -sheet structures, it is clear that the absolute change in each secondary structure motif is smaller at all strains for partially cross-linked fibrin compared to the FXIIIa-cross-linked gel. Another noticeable trend is the larger error bars at larger strains in both motifs, in both types of gels. Since the data for figure 3.4 were determined by pooling all spectra from partially cross-linked or cross-linked samples at each strain, it is challenging to determine whether the fibrin gel exhibits more structural (and therefore load-bearing) heterogeneity at larger strains or if the larger scatter comes from increased measurement noise. We note that the spread of values of the  $\text{CH}_3$  vibration relative to the mean at each strain - indicative of protein concentration heterogeneity - at low and high strain for both gels changes only slightly (in the cross-linked gel) and not at all in the partially cross-linked gels (Fig.3.12). Furthermore, the uncorrelated spatial features between protein content and  $\beta$ -sheet when never loaded (Fig.3.13), strongly suggest structural heterogeneity develops in the gel due to increasing load that is independent of any measurement uncertainty.

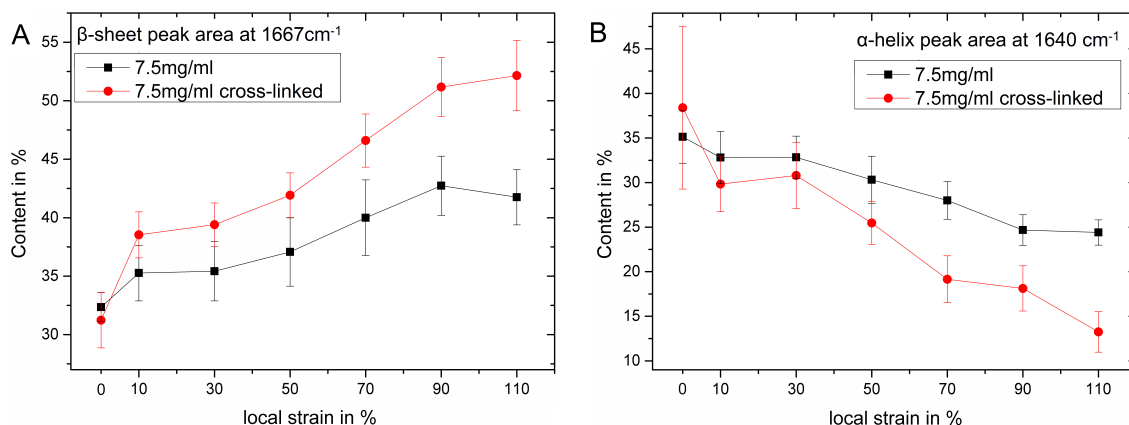


**Figure 3.4: Secondary structure content for increasing strain in partially cross-linked and cross-linked hydrogels.** A) % contribution of  $\beta$ -sheets and B) % contribution of  $\alpha$ -helices to the amide I band at increasing strain. Each data point represents the average of 150 spectra (top 30 from five independent experiments) with SEM as error bars.

### Tensile strain increases structural heterogeneity

To examine if the spatial distribution of secondary structure in fibrin hydrogels becomes more heterogeneous under strain, we acquired hyperspectral data from  $20 \times 20 \mu\text{m}^2$  regions ( $41 \times 41$  pixels) to create images depicting the contribution of  $\beta$ -sheet,  $\alpha$ -helix and random coil structural elements in both gel formulations. The spatial pixel spacing in each image is  $0.5 \mu\text{m}$ , which is roughly the same size as the largest fiber diameters in the gel. We note that all gray pixels in the maps are fluid or polystyrene pixels that do not contain any detectable protein signature (based on absence of  $\text{CH}_3$  vibration). The image of  $\beta$ -sheet content - related to the distribution of local force - in a never loaded partially cross-linked gel (0 % strain) is somewhat homogeneous with  $\sim 37$  %  $\beta$ -sheet content on average (Fig.3.5A). The  $\alpha$ -helix and random coil content look equally homogeneous (Fig.3.14 and Fig.3.15). Figure 3.5B shows the corresponding histogram of  $\beta$ -sheet contribution for all spatial pixels in the map. This histogram depicts the relative spatial homogeneity with a mean ( $\mu$ ) of 37.2 % and standard deviation ( $\sigma$ ) of 2.8 % when fit with a Gaussian distribution. By stretching the hydrogel to 50 % local strain, more  $\beta$ -sheet content appears on average, as expected. Interestingly, the  $\beta$ -sheet map (Fig.3.5C) now shows more heterogeneity. The histogram of all the protein-containing pixels demonstrates

that the distribution of  $\beta$ -sheet has broadened when compared to the never loaded case,  $\mu = 38.0$  and  $\sigma = 3.2$  (Fig.3.5D). For 100 % local strain, the  $\beta$ -sheet heterogeneity is even more pronounced (Fig.3.5E) as quantified by the increasing standard deviation in the Gaussian fit of the histogram ( $\mu = 43.2$ ,  $\sigma = 6.6\%$ , Fig.3.5F). Coupled with the similar decreasing heterogeneity in the spatial distribution of  $\alpha$ -helix content and increasing heterogeneity in the random coil structure with increasing strain (Fig.3.14 and Fig.3.15), these data demonstrate that fibrin structural heterogeneity increases under load in a non-trivial manner. Looking closely at the high strain  $\beta$ -sheet maps, for multiple experiments we observe that a supramolecular structure with  $\sim 4\text{-}6\ \mu\text{m}$  scale appears (Fig.3.16). The random coil and  $\alpha$ -helix contributions seem to be complementary to the  $\beta$ -sheet. We note that similar results to figure 3.5 were obtained with cross-linked gels (Fig.3.17). This indicates that fibrin possesses a structural (and load-bearing) disorder on the micron-scale that becomes apparent under uniform strain and is not present when never loaded.

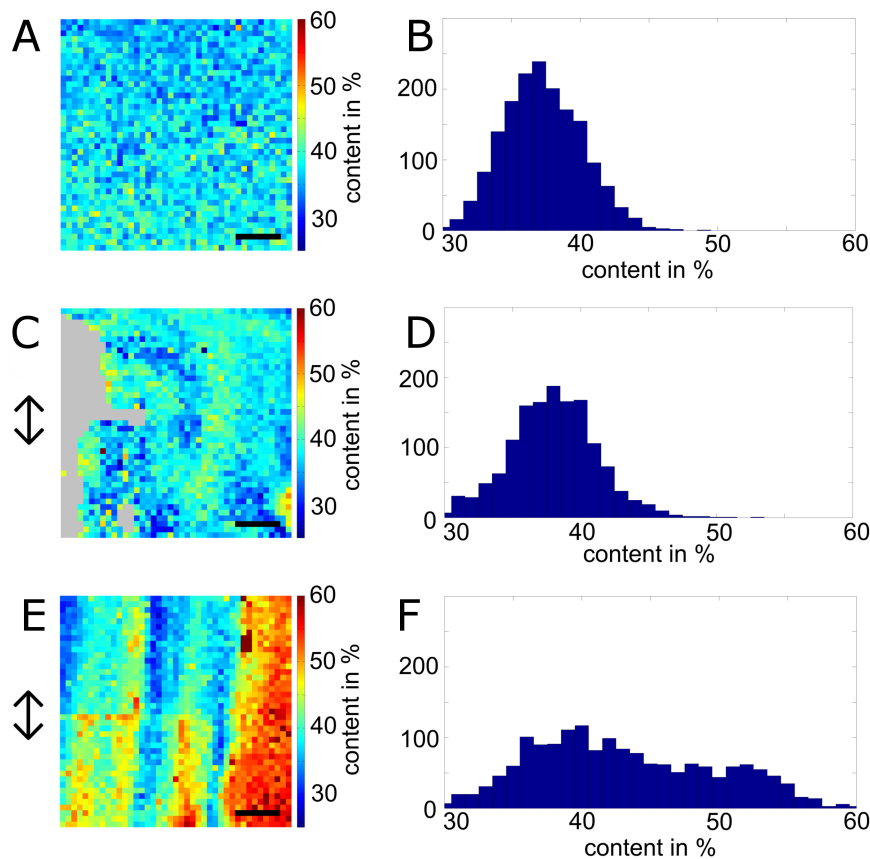


**Figure 3.5: Images and histogram plots showing the  $\beta$ -sheet contribution as % content in partially cross-linked fibrin gels at different strains:** never loaded (A, B), 56 % vertical strain (C, D), and 100 % vertical strain (E, F). The direction of load is indicated by the arrow. Pixels with  $\text{CH}_3$  values below threshold as well as pixels that showed polystyrene signal were excluded from further analysis and are shown in gray. Scale bars represent  $4\ \mu\text{m}$ . Histogram plots of all three samples had a bin size of 1 %.

### 3.3 Discussion

All tested fibrin hydrogels strain-stiffened in shear rheology measurements (Fig.3.1). The cross-linked network had a 30 % larger plateau shear modulus than the partially cross-linked network while the nonlinear elasticity (both onset and moduli) was very similar



for both samples, which is consistent with previous measurements [225, 227]. Though the nonlinear elasticity was similar for the two networks, additional FXIIIa cross-linking resulted in substantially increased tension-induced  $\beta$ -sheet content in the gel (Fig.3.4), similar to that seen previously by Brown *et al.* [230]. The  $\beta$ -sheet content for gels was  $\sim 30$  % when never loaded and increased to 42 % and 52 % at high tensile strain for partially cross-linked and FXIIIa-cross-linked gels, respectively. The results for secondary structural content of the partially cross-linked gel at high strain are nearly identical to those obtained using ATR-FTIR by Litvinov *et al.* on 'naturally' cross-linked fibrin gels at 100 % extensional strain, which also contain trace amounts of FXIII [9]. It is well known that CARS (and generally all vibrational) signal strength depends both on the orientation of the molecular vibration (axis of polarizability) with respect to the laser polarizations as well as on the concentration of vibrational oscillators in the focal volume [157, 173]. Our results from Fig.3.3 demonstrate that rotating the fibrin gel sample relative to a constant laser polarization reveals the specific orientation of the  $\alpha$ -helical and  $\beta$ -sheet motifs in the gel under strain. Fibrin(ogen) proteins contain multiple  $\alpha$ -helices, specifically between the two D domains and E domain of the protein. These helices have been shown to lie along the long axis of the protein [27]. Therefore, a strongly directional amide I contribution for the  $\alpha$ -helices, with a maximum signal when the loading direction is parallel to the laser polarization, is consistent with the helical axis being parallel to the protofibrils (and fibers) and with the alignment of fibrin fibers under uniaxial tension. The  $\sim 80^\circ$  rotation of the  $\beta$ -sheet major axis confirms the prediction that the  $\beta$ -strands of the  $\beta$ -sheets are nearly parallel to the long axis of the protein as this would result in hydrogen bonded C=O vibration nearly orthogonal to the  $\beta$  strands [35]. From previous knowledge about the hierarchical assembly of fibrin molecules into protofibrils, fibers, and entangled gels, and the semiflexible nature of fibrin gel elasticity [40], we expect that protofibers will align to a unidirectional load [217]. Therefore, it is possible that the Raman signal in the amide I region is affected by two coupled effects: 1) reorientation of fibrin fibers (and constituent proteins) leading to reorientation of secondary structural elements and corresponding reorientation of the hydrogen bonded C=O moieties in the proteins and 2) structural transitions from  $\alpha$ -helix to  $\beta$ -sheet with increasing load. From integrating the polar plot traces in figure 3.3B over all angles, it is evident that the total  $\beta$ -sheet contribution to the amide I spectrum increases by 19 % when the network was strained by 60 % compared to the never loaded network while the total  $\alpha$ -helix contribution decreased by 11 %. The loading axis was fixed at  $80^\circ$  relative to the laser polarization for measuring force-induced structural transitions and spatial heterogeneity. At this orientation, an increase from 32 % to 42 %  $\beta$ -sheet contribution was observed under 60 % tensile strain (Fig.3.3). If one only accounts for new  $\beta$ -sheet formation (on average a 19 % increase), the signal at  $80^\circ$  orientation would have increased from 32 % to 38 %, meaning that the remaining 4 % comes from reorientation of existing  $\beta$ -strands. Indeed, the native fibrinogen molecule is known to contain trifle disordered  $\beta$ -strand structures in the outer D domains, which assume no particular orientation with respect to the long axis of the protein and may potentially reorient under load [231, 232]. Nevertheless, the majority of the additional  $\beta$ -sheet signal at the  $80^\circ$  orientation comes from new  $\beta$ -strands created by strain-induced transitions from  $\alpha$ -helices to  $\beta$ -sheet. Looking at the trends in structural changes from our BCARS measurements, we observe that cross-linked gels exhibit greater increase in  $\beta$ -sheet (and greater decrease in  $\alpha$ -helix) content. It is known that FXIII addition leads to formation of more tightly coupled protofibrils, which increases the bending rigidity of fibers, leading to a larger plateau modulus (as indeed observed in figure 3.1) [40, 225]. The gel nonlinear elasticity is believed to originate from the resistance to extension of protofibrils themselves in the following way. First, the  $\alpha$ C-domains in fibrin monomers that connect protofibrils can be elongated. Second, forced unfolding of the coiled-coils

( $\alpha \rightarrow \beta$ ) within the monomers is possible [40,41]. Covalent bonds catalyzed by FXIIIa enhance the  $\gamma$ -chain connections as well as the  $\alpha$ -chain linkage [233]. Helms *et al.* proposed that  $\gamma - \gamma$  cross-linking might change the pattern of stress propagation from a dominating  $\alpha$ C-domain deformation towards an unfolding mechanism. Instead of routing the stress back and forth via  $\alpha$ C-domain connections, the strong  $\gamma - \gamma$  linking in FXIII-cross-linked gels channels the stress through the coiled-coil region of monomers in protofibrils. This pathway would result in enhanced unfolding of coiled-coil  $\alpha$ -helices that connect the D- and E-domains into  $\beta$ -sheets [227,234]. Our data supports this hypothesis as additional FXIIIa cross-linking increases the strain-induced changes in secondary structure compared to the partially cross-linked gels. Interestingly, we observe similar changes in secondary structure with strain in samples with reduced mesh size (partially cross-linked 15 mg/mL fibrin gels) as those in 7.5 mg/mL cross-linked samples (Fig.3.18 and Fig.3.19). This indicates that decreasing the mesh size also results in greater structural transitions at a given tensile strain in partially cross-linked fibrin. BCARS imaging of secondary structure directly showed increasing  $\beta$ -sheet content and substantial spatial-structural heterogeneity in strained samples when compared to never loaded samples. From our structural images over  $20 \times 20 \mu m^2$  regions, we observed that discrete sections of the fibrin mesh exhibit large  $\beta$ -sheet content under uniaxial strain while others show very little  $\beta$ -sheet content. Complimentary heterogeneity was found in the random coil and  $\alpha$ -helix structural content (Fig.3.14 and Fig.3.15). Considering previous electron micrographs of fibrin gels under 400 % tensile strain [9], as well as confocal micrographs of fluorescently labeled fibrin under shear strain [235], it is clear that not all fibers align to the load. Correspondingly, a unidirectional deformation will cause only parts of the gel to unfold while other may stay relaxed. Thus, it is plausible that some fibers will not actively resist the load. Based on autocorrelation of multiple  $\beta$ -sheet structural images at greater than 85 % strain, our data reveals that  $\beta$ -sheet bands, separated by  $\sim 4-6 \mu m$ , occur within strained fibrin gels (Fig.3.16). These  $\beta$ -sheet bands are orthogonal to the loading direction and identify regions that bear larger forces compared to neighboring helix-dominated regions. This length scale is  $\sim 5$ -fold larger than the largest fiber diameters reported to date and shows that fibrin cannot be considered an isotropic bulk, even at the micron scale, but is rather a reticulated material that shows non-affine behavior structurally, as well as morphologically. This strongly suggests that fibrin is itself becomes a composite at increasing strain and this non-uniformity must be accounted for in theoretical descriptions in order to accurately describe the mechanics of fibrin-based materials. Fibrin composites - fibrin plus red blood cells and platelets - are one of the most important biocomposite materials. Interestingly, the spatial structure observed in the  $\beta$ -sheet map shows that an initially uniform fibrin gel becomes a structured material on the micron-scale under external tensile strain. With conflicting reports in the literature about the reversibility of secondary structural changes, future experiments are aimed at determining if these structural transitions and heterogeneity observed in this work are reversible after removing all strain [40,130,236,237]. A possible physiological implication of the structural heterogeneity under tension is in regulating fibrin degradation within the blood clot environment. It has been shown that, in addition to pore size and fiber density [238], stretching fibrin reduces the rate of fibrin lysis by plasminogen [210,239]. The suggested mechanism assumes that fibrin unfolding leads to a loss of binding sites for tissue plasminogen activator due to exposed hydrophobic regions of fibrin and expulsion of water [41,238,239]. Following this logic, the structural heterogeneity observed in our experiments strongly suggests that fibrin degradation occurs in a similar spatially heterogeneous pattern. External loads, as well as contraction of platelets, may cause parts of the fibrin network (that are load bearing) to unfold and thus become more resistant to lysis. Consequently, only regions that are not load bearing - those in the native conformation - would be removed in the beginning of fibrinolysis. This would be an



intrinsic mechanism to regulate degradation of the entire fibrin mesh as it would maintain clot stability during clot turnover and skin rebuilding.

### 3.4 Conclusion

BCARS microscopy of fibrin hydrogels was used to determine mechanically-induced changes of secondary structure. The identification of orthogonal  $\alpha$ -helix and  $\beta$ -sheet hydrogen bonds experimentally confirms the proposed geometry of these structures in previous work [35]. Spectra of FXIIIa-cross-linked fibrin under load showed a reduced amount of  $\alpha$ -helix, as well as increased  $\beta$ -sheet content, compared to partially cross-linked gels. From structural maps, we directly observe the heterogeneity of secondary structure in the hydrogel under unidirectional tensile loads, which shows clear non-uniform force distribution. The combination of structural transitions and heterogeneity in the fibrin structure under load give additional insight into the fundamental mechanisms of elasticity of fibrin gels and how fibrin local structure helps to maintain stability throughout wound healing.

### 3.5 Methods

#### Hydrogel preparation

Fibrin hydrogels were prepared as described by Piechocka *et al.* [40]. Human fibrinogen monomers (FIB 3), human thrombin (HT 1002a) and human fibrin stabilizing factor (HFXIII) were obtained from Enzyme Research Laboratories (Swansea, UK). Fibrinogen was diluted in 20 mM Hepes and 150 mM NaCl at pH 7.4. To promote cleavage by thrombin, 5 mM  $CaCl_2$  was added to the buffer to ensure thrombin activation. Hydrogels were mixed to achieve final concentrations of 7.5 mg/mL fibrinogen and 1.05 U/mL thrombin. This protocol resulted in full polymerization of fibrin as judged by SDS-PAGE (Fig.3.20). For additional cross-linked gel, FXIII was activated by thrombin at the same unit concentration to form FXIIIa. The solution was kept at 37°C for 10 minutes before further usage to allow complete cleavage of FXIII. To form stabilized fibrin hydrogel, FXIIIa was added with a final concentration of 8 U/mL to a gel with 7.5 mg/mL fibrinogen [227,240]. For all gel solutions (partially cross-linked or cross-linked), 3  $\mu$ m diameter polystyrene microspheres (Polyscience GmbH) were doped at low concentration. In an area of 50  $\times$  50  $\mu$ m, typically  $\sim$ 25 beads could be found. This allowed post-processing calculation of the local gel deformation in the hydrogels under load. The final mixture was pipetted into glass molds of 150  $\mu$ m thickness and allowed to polymerize in an incubator (100 % humidity, 37°C, 5 % CO<sub>2</sub>) for at least 2 h.

#### Rheology and tension

Shear rheology of hydrogels was performed on a commercial shear rheometer (ARES, Rheometric Scientific) with the parallel plate geometry. Data acquisition was done in TA Orchestrator software (TA Instruments). Fibrin hydrogels were prepared by polymerizing 150  $\mu$ m fibrin solution between two circular cover glasses (d = 24 mm, Menzel) and sealed by silicon oil (Baysilone medium viscosity, Bayer) to prevent drying of the gel. The two cover glasses were fixed to the steel plates of the rheometer with double sided adhesive tape (Tesa SE). A normal contact force of 0.1 N was applied to the sample, which resulted in a gap spacing of approximately 175  $\mu$ m between the plates. Prestrain sweeps were executed by changing the prestrain from 1 % to 500 % superposed by an oscillating strain with amplitude smaller than 10 % of the prestrain value. For tensile tests of fibrin gels a material testing machine (Z005, TestXpert 2.0, Zwick Roell) equipped with a load cell (Z6FD1, HBM) was used. The initial sample geometry was approximately 5 mm x 20

mm  $\times$  0.2 mm. Fibrin gels were physically clamped and stretched at a constant rate of 10 mm/min until samples broke.

### BCARS microspectroscopy

We used a nanosecond-based BCARS system for microspectroscopy of fibrin hydrogels as depicted in figure 3.21. The details of this setup have been described extensively elsewhere [241] and additional details are provided in the supplemental information.

### Sample handling and strain application to fibrin hydrogels

A small piece of polymerized fibrin ( $\sim 0.5$  mm  $\times$  5 mm  $\times$  150  $\mu$ m) was cut by a scalpel from the mold, carefully picked with a precision tweezer and placed on two coverslips such that the two ends of the gel could be fixed on the coverslips with super glue (Loctite 454, Henkel). Care was taken to ensure that no glue was in the center of the gel where the measurements took place and. After gluing, the sample was sandwiched between two additional cover slips and surrounded by buffer solution to ensure the sample was fully hydrated throughout the measurement. The sandwich was transported to the microscope and mounted as shown in the zoomed image in figure 3.21. Fibrin samples were raster-scanned in plane with a step size of 0.5  $\mu$ m. For most data presented in this study, an area of 5  $\times$  5  $\mu$ m was scanned to acquire 121 spectra for statistical evaluation and mapping. The exposure time for each spectrum was set to 1 s to acquire sufficient signal-to-noise. Uniaxial strain was applied by translating one coverslip, to which the gel was glued, with respect to the fixed coverslip, by a known amount relative to the original length of the gel (Fig.3.16). The local displacement in the hydrogel where the BCARS spectra were acquired was determined by quantifying embedded microsphere displacement in bright-field images at each strain. Bead tracking was done using ImageJ (National Institutes of Health).

### CARS data processing

Because raw BCARS contains both resonant and non-resonant component, recorded spectra must be processed into Raman-like spectra to allow quantitative analysis [221]. To extract the resonant, Raman-like, component from the CARS spectra a Kramers-Kronig transform that included a causality constraint was employed using Igor Pro 6.3 (WaveMetrics) as described in [156,242]). Further data processing to determine secondary structure was done in Matlab (R2012a, MathWorks). To account for variations in hydrogel thickness and non-systematic variations in the experimental setup, all spectra were normalized by the peak value of the CH<sub>3</sub>-stretching mode at 2934  $\text{cm}^{-1}$ , which is proportional to the amount of protein in the focus. The intensity of Raman signal related to  $\alpha$ -helices,  $\beta$ -sheet and random coil secondary structure was found by decomposition of the amide I band. We found that five different peaks were necessary to fit the amide I region between 1570  $\text{cm}^{-1}$  and 1730  $\text{cm}^{-1}$ : 1640  $\text{cm}^{-1}$  for  $\alpha$ -helices, 1650  $\text{cm}^{-1}$  for random coil, 1667  $\text{cm}^{-1}$  for  $\beta$ -sheet and two minor peaks at 1612  $\text{cm}^{-1}$  and 1600  $\text{cm}^{-1}$  for tyrosine ring modes [46]. Each peak was defined as a Lorentzian function with given line width, constrained (but floating) center frequency and floating (but positively constrained) amplitude. The fitting was executed on the normalized spectra using least-squares with a Levenberg-Marquardt algorithm. To identify polystyrene containing pixels, we searched spectra for strong peaks at 998  $\text{cm}^{-1}$  (ring breathing phenyl ring), 1029  $\text{cm}^{-1}$  (CH in-plane bending mode) and 1597  $\text{cm}^{-1}$  (ring breathing phenyl ring) [46]. Any spectra that showed spectral features from polystyrene microspheres were excluded from further processing.

### Data and materials availability:

All data needed to evaluate the conclusions in the paper are present in the paper and/or the Supplementary Materials. Additional data related to this paper may be requested from the authors.

## 3.6 Appendix I

### Supplementary Data

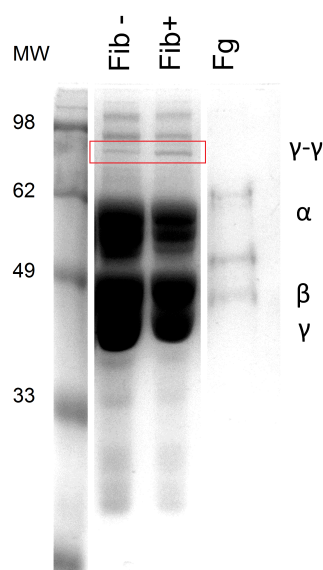


**Figure 3.6:** SDS-PAGE of reduced fibrin gels without (Fib-) and with additional cross-linking by FXIIIa (Fib+). Samples were polymerized, washed 3x in buffer and prepared with SDS sample buffer containing 500 mM  $\beta$ -mercaptoethanol. The gel was loaded with  $8\mu g$  fibrin for the gels and  $1\mu g$  fibrinogen (Fg) for comparison. The  $\gamma - \gamma$  segment is visible in both fibrin samples but more pronounced for the FXIIIa sample.

### Creep recovery experiments

In addition to viscoelastic measurements of the elastic modulus in shear and tension we performed creep recovery experiments as described earlier for fibrin [228]. This allows additional quantitative mechanical characterization of our samples in addition to the biochemical differences shown by SDS-PAGE (Fig.3.6). Under a constant shear stress  $\sigma$ , the sample reacts with an initial strain  $\gamma_1$ , which increases until an equilibrium is reached at a final strain  $\gamma'_1$ . The recovery is characterized by the relaxation time from the initial strain  $\gamma_s$  and  $\gamma'_s$  after removing the stress. Similar to Nelb *et al.* we use the ratio of  $\gamma_1/\gamma'_1$  to represent the amount of creep and the fractional recovery  $(\gamma'_1 - \gamma'_s)/\gamma'_1$  to measure the creep recovery of both types of fibrin gels (see Table 3.1). Fibrin without additional FXIII needs a longer time to reach a steady strain level in creep as well as in recovery compared to fully cross-linked fibrin as shown in figure 3.7 (reproduced below). Furthermore, fully cross-linked fibrin recovers to a higher degree while fibrin without external FXIII recovers to a lesser degree. These results demonstrate that external FXIII ligates fibrin fibers and further prevents network sliding under steady shear stress. This behavior is consistent

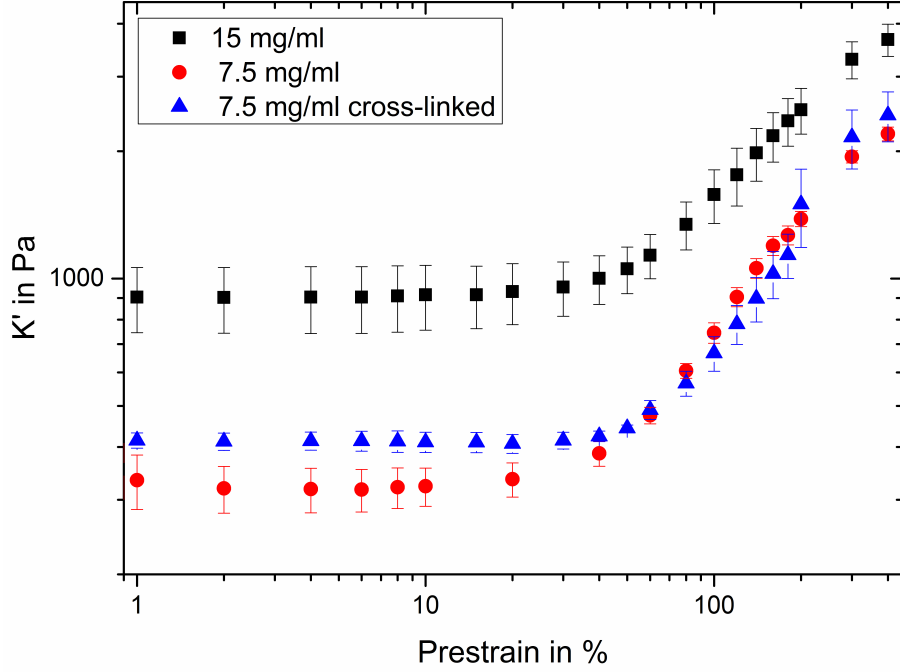


**Figure 3.7:** Differential storage modulus measured as a function of pre-strain for three different mixtures of fibrin hydrogels. Three separate hydrogels averaged per data point. Error bars are SEM.

	partially cross-linked fibrin	cross-linked fibrin	Unligated fibrin from [228]	Ligated fibrin from [228]
$\gamma_1/\gamma'_1$	0.84	0.96	0.55	0.92
$(\gamma'_1 - \gamma'_s)/\gamma'_1$	0.41	0.79	0.68	0.81

**Table 3.1:** Results from creep recovery experiments for partially cross-linked and fully cross-linked fibrin.

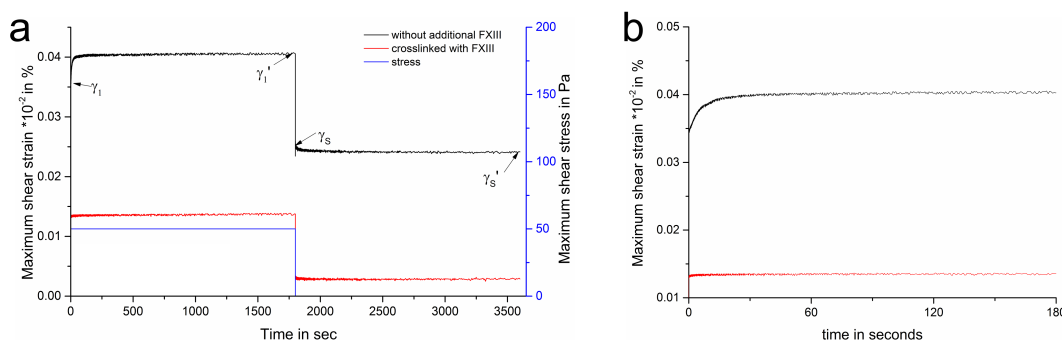


**Figure 3.8:** Creep recovery tests of partially cross-linked and fully cross-linked Fibrin gels. a) Temporal shear strain changes over time for both gels. b) Zoom-in of the first 180 seconds.

with results from Nelb *et al.*, for uncross-linked and cross-linked fibrin and indicate that our partially cross-linked gels are likely somewhat ligated.

### Representing average fibrin behavior by a subset of pixels

It was necessary to ensure that we are analyzing only protein, and therefore have to discard areas of the image that contained microbeads and those pixels in the data with prohibitively low protein concentration such that the spectral decomposition became unreliable. Neither of these effects was a constant number of pixels from image to image. Using the 30 pixels with highest protein concentration was done to ensure a consistent number of spatial pixels for analysis of datasets where average structure content was calculated (Fig.3.3, 3.4 and 3.11). Thus, pixels with polystyrene signatures in the BCARS data were initially removed, and then the top 30 pixels in protein concentration from the remaining pixels were used as representative pixels for calculating the average secondary structure within the hydrogel. While, indeed, the number 30 is somewhat ambiguous, and we could have selected more or less pixels, we empirically found 30 to be an appropriate number to include a reasonable proportion of the total area, ensure that the spectral decomposition would not fail for unsupervised data processing, and ensure that all calculations for figures 3.3, 3.4, and 3.11 had the same number of data points for each experiment and each strain level. We are aware that this selection biases our analysis to regions of the sample with larger fibrin concentration; however, including additional pixels with lower protein concentration changes the derived secondary structures by less than 2 % as shown in figure 3.9 below.

### Influence of mesh size to the change of secondary structure

To briefly explore the influence of higher fibrinogen concentration, and therefore a smaller mesh size in fibrin hydrogels, on changes in secondary structure with tensile load, we repeated the tensile deformation experiments for partially cross-linked fibrin of 15 mg/mL fibrinogen concentration. Multiple studies have shown that an increased concentration of protein leads to a smaller mesh size and more branching points in the hydrogel [40, 130, 239, 240]. Estimations of the mesh size from confocal microscopy images showed a decrease of the mesh size  $\xi$  with the relation  $\xi \sim c - 0.5$  to the fibrinogen concentration [40]. In agreement with these observations, our resulting gels showed a denser network with a higher number of branching points as can be seen by representative confocal images (see Fig.3.18). Both images shown were acquired 20  $\mu\text{m}$  above the coverslip to ensure that the bulk properties are measured. To investigate the mechanical properties of the high-concentration gel, we used shear rheometry as described in the methods section.

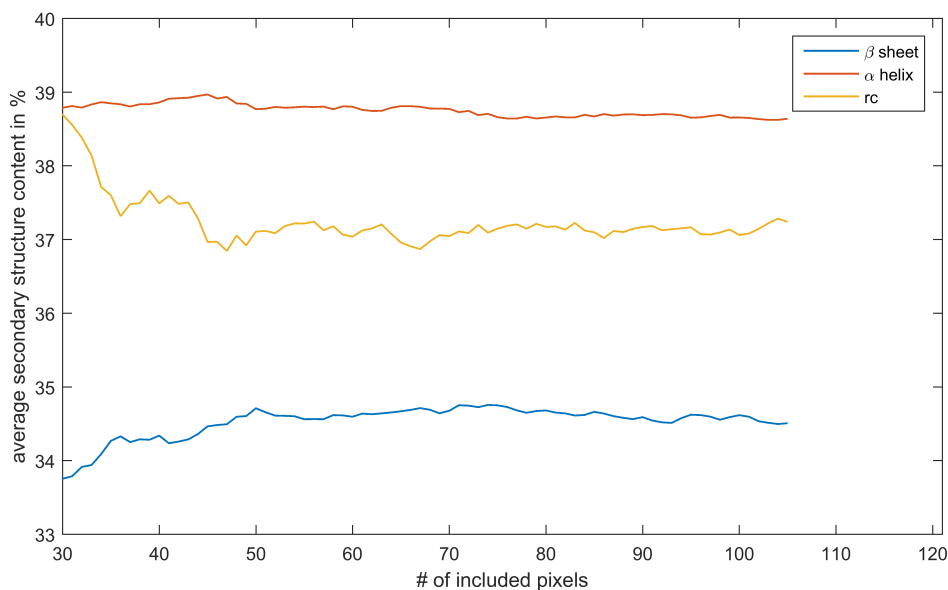


**Figure 3.9:** Curves showing average  $\alpha$ -helix,  $\beta$ -sheet, and random coil content of a typical relaxed hydrogel as a function of number of pixels included in the calculation, sorted from maximum protein content (CH value) to minimum protein content. The total number of pixels is 121. In this example, 15 pixels were automatically excluded and set to zero because either of too low CH signal or the appearance of spectral features indicating the presence of a polystyrene bead.

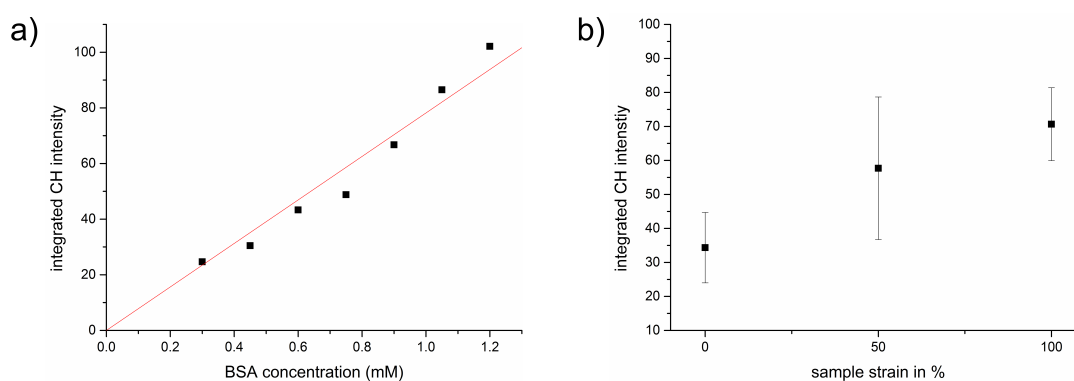


**Figure 3.10:** a) Integrated CH intensities of a BSA dilution series demonstrates the proportionality between this quantity and protein concentration over the values measured in fibrin gels. b) Integrated CH intensity from phase-retrieved CARS data (proportional to protein concentration) for 3 different sample strains from the same sample position (to within  $\sim 10\mu m$ ). Error bars are the standard deviation from all pixels over an  $81 \times 81$  pixel area.

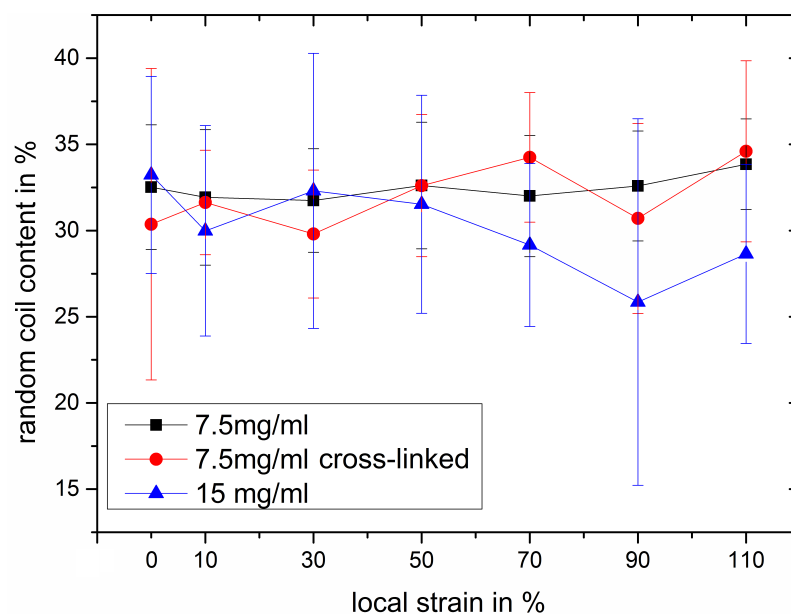


**Figure 3.11:** Random coil content for increasing strain in three different hydrogels. Each data point represents the average of 150 spectra (top 30 of five experiments) with SEM as error bars.

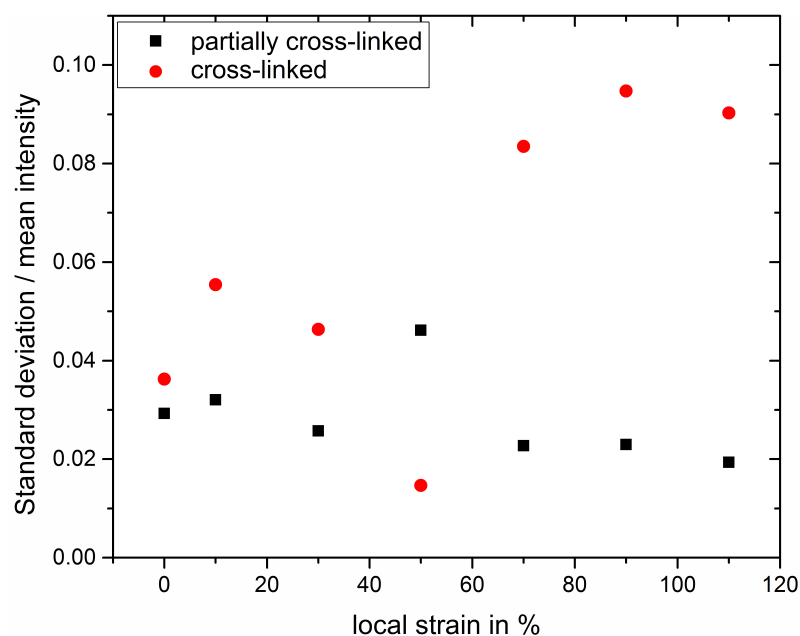


**Figure 3.12:** Standard deviation of  $\text{CH}_3$  intensity ( $2930\text{ cm}^{-1}$ ) within the top 30 highest protein signal pixels normalized to the average  $\text{CH}_3$  intensity of the experiment. The data points show the mean of 5 experiments taken per strain.

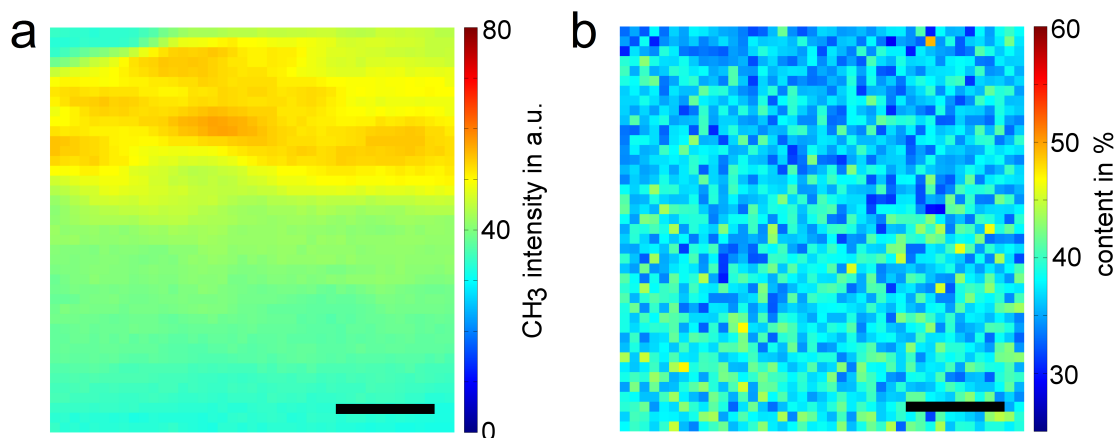


**Figure 3.13:** Spectral maps for never loaded partially cross-linked 7.5 mg/mL hydrogel showing the CH<sub>3</sub> (2930 cm<sup>-1</sup>) from the Raman-like spectra (a), and decomposed  $\beta$ -sheet content (b). Scale bars are 5  $\mu$ m.

The 15 mg/mL fibrin had a higher K' in the linear regime compared to the 7.5 mg/mL fibrin (Fig.3.7). The onset of the linear regime was earlier than for the low concentration gels. Similar measurements were previously performed for a broad range of concentrations from Piechocka *et al.* [40]. Our experimental results on changes in secondary structure with tensile strain show that the low protein concentration (7.5 mg/mL) gels showed less pronounced changes in the secondary structure (Fig.3.19) than gels of high concentration (15 mg/mL). Interestingly, the changes in secondary structure appear very similar to that observed in fully cross-linked 7.5 mg/mL hydrogels. In such a denser fibrin network, tensile forces are distributed amongst more entangled structural components. Apparently, this results in increased force transmission within the network fibers and more protein unfolding as opposed to sliding of fibers.

## Supplementary Methods

### Broadband CARS microspectroscopy

A spectrally narrow pump beam ( $\lambda = 1064\text{nm}$ ) and a spectrally broad Stokes beam ( $\lambda = 400 - 2400\text{nm}$ ) are provided from a commercial source (Leukos-CARS, Leukos). The Stokes beam is filtered to produce a final bandwidth from 1100-1600 nm with a spectral power density of more than 100  $\mu\text{Wnm}^{-1}$ . The beams are sent to an inverted microscope (Eclipse Ti-U, Nikon) where they are focused into the sample via a water immersion objective (60x IR, 1.2 NA, water-immersion, Olympus). At the sample the total average laser power is 16 mW. The sample is mounted on a xyz piezo stage (Nano-PDQ 375 HS, Mad City Labs) to raster-scan with a step size of 0.5  $\mu$ m. CARS signal is collected in the forward direction by a second objective (63x IR-VIS, 1.0 NA, water-immersion, Zeiss), and the pump and Stokes beams are removed by a notch (NF03-532/1064E-25, Semrock) and a short-pass filter (FES1000, Thorlabs), respectively. The CARS light is then dispersed in a spectrometer (Shamrock 303i, Andor) and analyzed by a cooled CCD camera (Newton DU920P-BR-DD, Andor) (Fig.3.21). The grating and focusing into the spectrometer resulted in a spectral range from 500 cm<sup>-1</sup> to 4000 cm<sup>-1</sup> with a spectral pitch of  $\sim 4\text{cm}^{-1}$ . The instrument is controlled with software written in LabView (National Instruments).



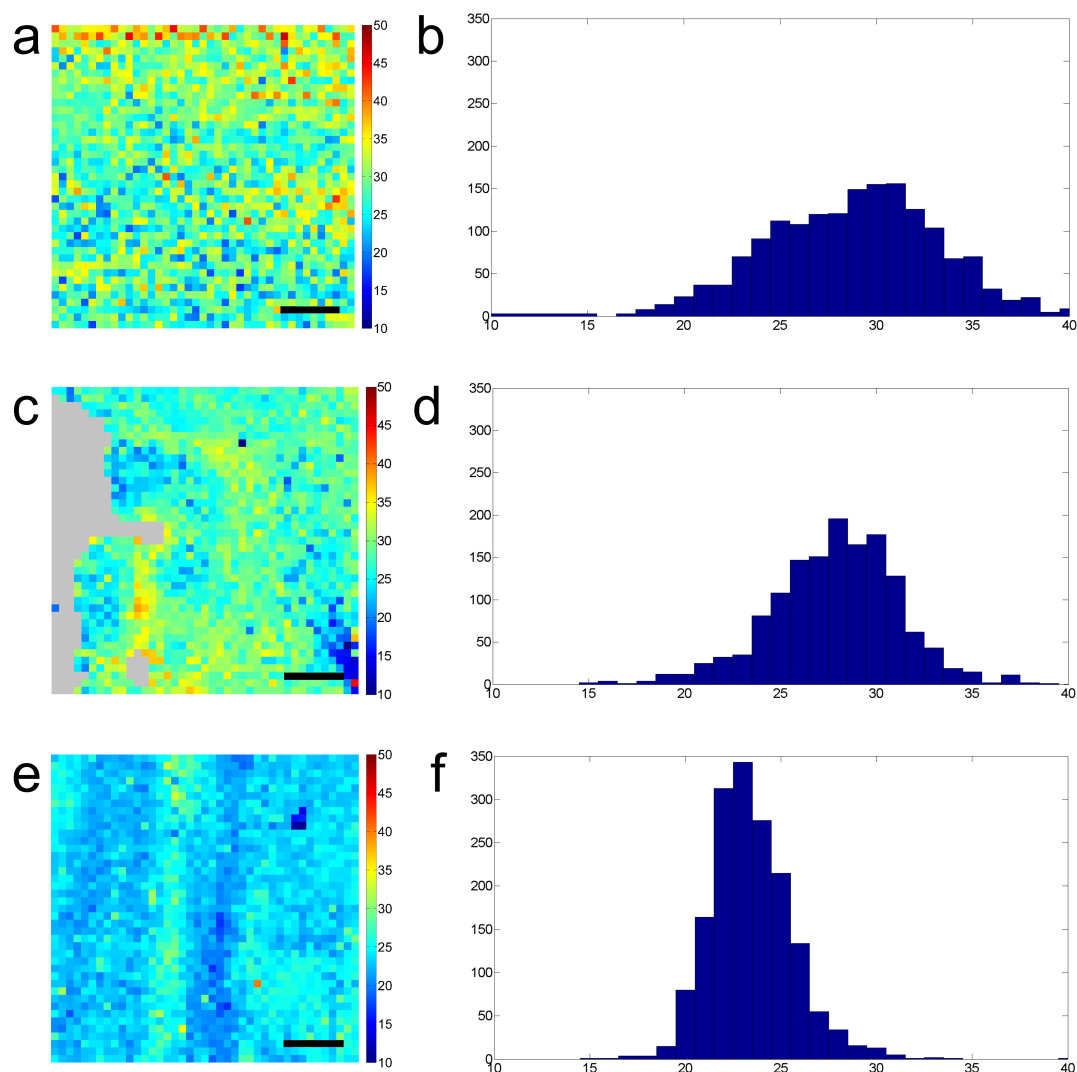


**Figure 3.14:** Images and histogram plots showing the  $\alpha$ -helix peak contribution as % content within partially cross-linked fibrin gels at different strains: relaxed (a, b), 56 % vertical strain (c, d) and 100% vertical strain (e, f). Pixels with  $\text{CH}_3$  intensity below threshold as well as pixels that showed polystyrene signal were excluded from further analysis and are shown in gray. Scale bars represent  $4\ \mu\text{m}$ . The load was applied vertically. Histogram plots of all three samples had a bin size of 1 %. Gels had a protein concentration of  $7.5\ \text{mg/mL}$ .

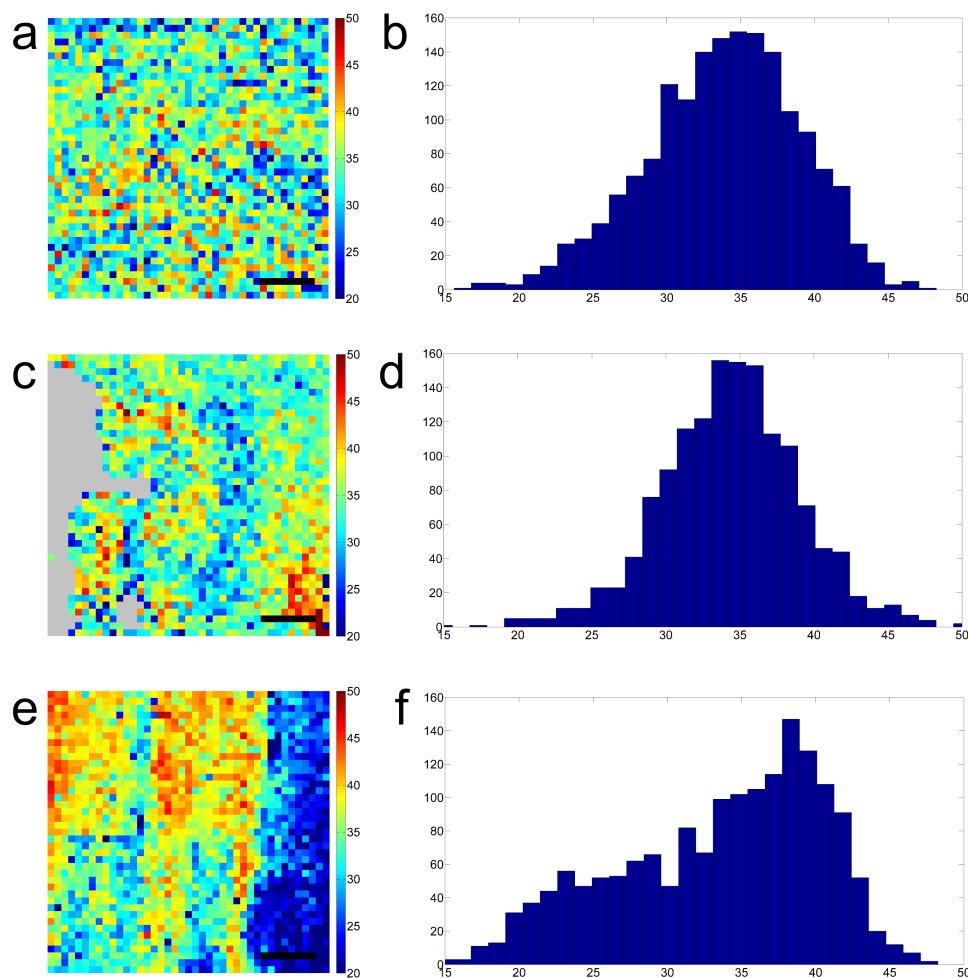


**Figure 3.15:** Images and histogram plots showing the random coil peak contribution as % content within partially cross-linked fibrin gels at different strains: relaxed (a, b), 56 % vertical strain (c, d) and 100 % vertical strain (e, f). Pixels with CH3 intensity below threshold as well as pixels that showed polystyrene signal were excluded from further analysis and are shown in gray. Scale bars represent 4  $\mu m$ . The load was applied vertically. Histogram plots of all three samples had a bin size of 1 %. Gels had a protein concentration of 7.5 mg/mL.

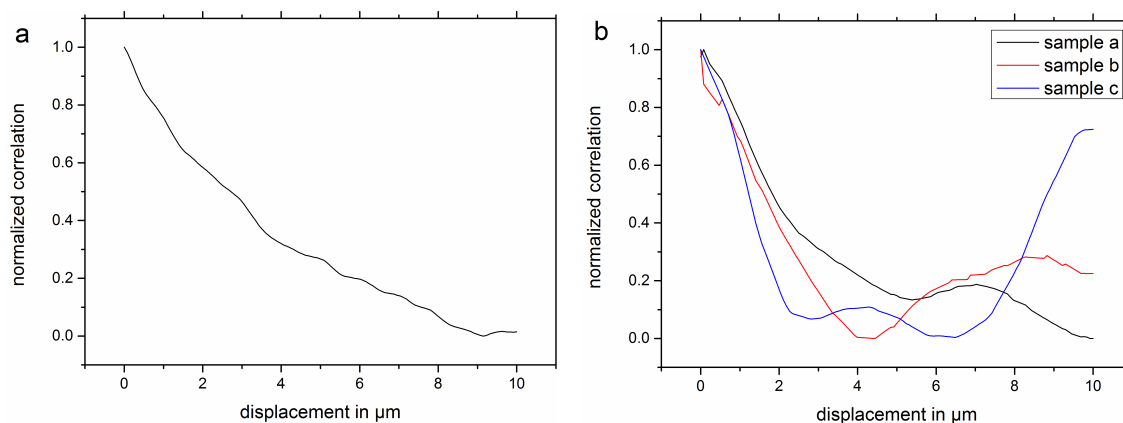


**Figure 3.16:** Normalized autocorrelation of spectral maps of the  $\beta$ -sheet content from a) relaxed and b) strained fibrin gels. The full-width half maximum of the central lobe is  $1.4 \pm 0.25 \mu\text{m}$  in deformed samples and side maxima displaced by  $5.4 \pm 1.4 \mu\text{m}$  to the zero position are seen. Autocorrelation by conjugate multiplication in the frequency domain was performed in ImageJ.

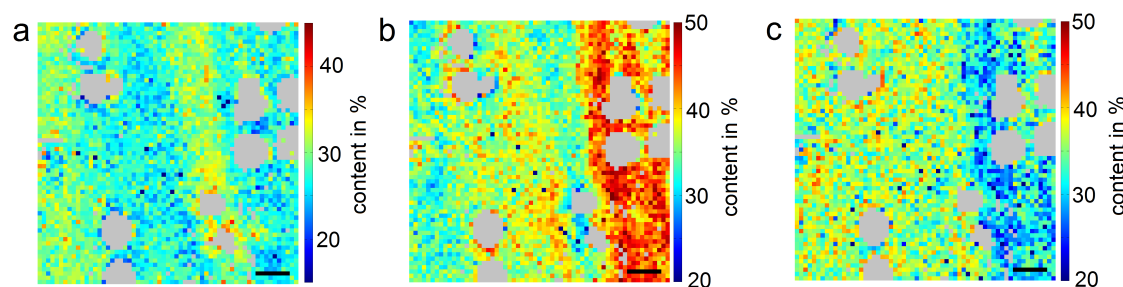


**Figure 3.17:** Spectral maps for 85 % vertical strained cross-linked hydrogel showing the decomposed  $\alpha$ -helix content (a),  $\beta$ -sheet content (b) and the random coil content (b). Pixels with  $\text{CH}_3$  intensity below threshold or one that showed spectral features of polystyrene microbeads are shown in gray. Scale bars represent  $4 \mu\text{m}$ .

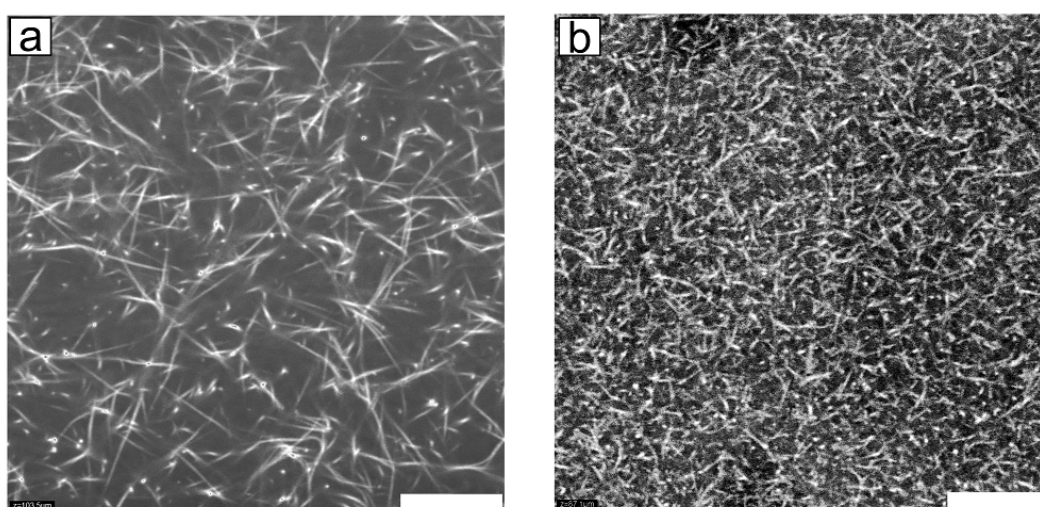


**Figure 3.18:** Confocal fluorescence microscopy of fibrin gels of different fibrinogen concentrations (total field of view:  $48 \times 48 \mu\text{m}^2$ ). a) partially cross-linked 7.5 mg/mL hydrogel shows a large mesh size and low number of branching points. b) partially cross-linked 15 mg/mL fibrin sample is much denser and has a smaller mesh size. The scale bars represent  $10 \mu\text{m}$ .

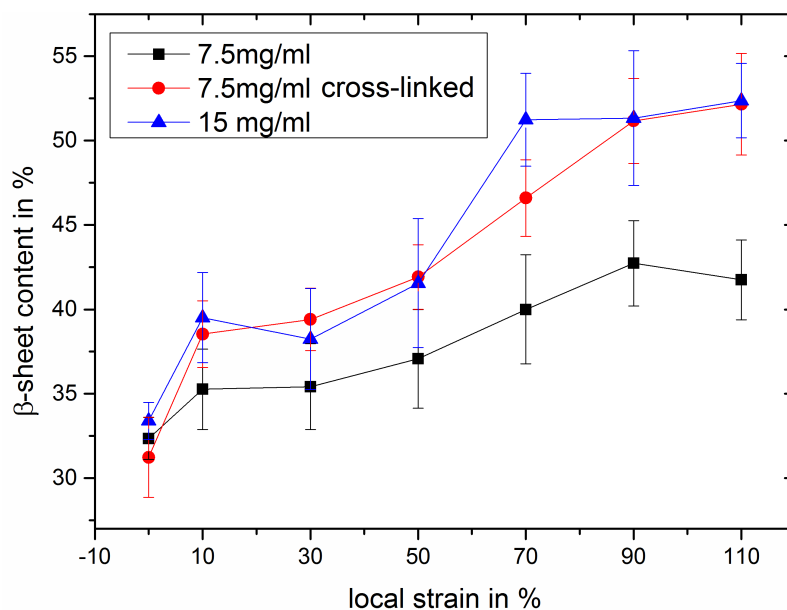


**Figure 3.19:** Contribution of  $\beta$ -sheets to the amide I band for increasing strain in low and high concentration fibrin. Each data point represents the average of 150 spectra (top 30 from five independent experiments) with SEM as error bars.

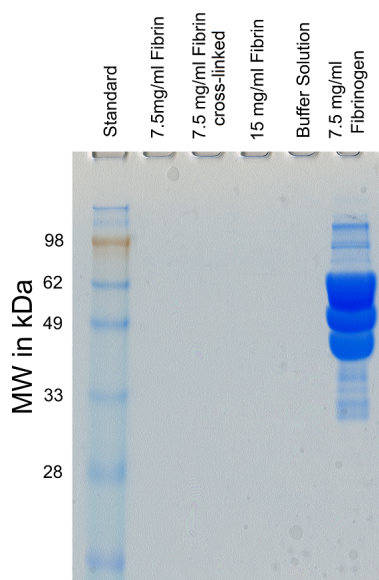


**Figure 3.20:** SDS-PAGE of the supernatant from different hydrogels to check the complete polymerization of fibrinogen monomer.

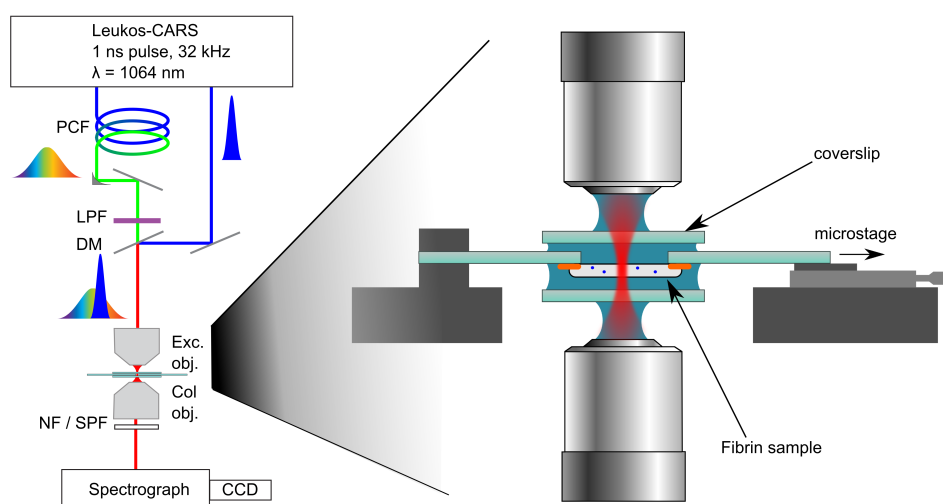


**Figure 3.21:** Schematic of the B-CARS microscope setup. Pump and probe beam are generated at  $\lambda = 1064\text{nm}$ . A photonic crystal fiber (PCF) broadens the Stokes laser spectrum, which is then spectrally filtered (LPF) to a range of  $\lambda = 1100 - 1600\text{nm}$ . Both beams are combined by a dichroitic mirror (DM) and directed to an inverted microscope. The beams are focused into the sample excitation objective (Exc. Obj.), and the created forward CARS signal is collected by the collection objective (Col. Obj.). Two water immersion objectives are used to reduce losses due to reflection and to obtain a tighter focus in the hydrogel sample. The pump and probe beam are filtered (NF/SPF) and the CARS signal is spectrally analyzed by a spectrograph with an attached CCD camera. The zoomed drawing depicts the geometry of the objectives and hydrogel sample. The fibrin hydrogel is glued to two cover slides, one that is fixed and the other that is moveable and mounted to a translation stage. To perform B-CARS raster scanning, the entire device is mounted on a xyz piezo-stage.

### **Confocal microscopy**

Fibrinogen from human plasma conjugated with Alexa Fluor 488 (#F13191, Thermo Fisher Scientific) was mixed with unlabeled fibrinogen in a ratio of 1:10 and let polymerized as described in the methods section. To analyze the mesh size samples were then imaged on a TCS SP5 confocal microscope (Leica) equipped with a HCX PL APO CS 63.0x 1.20 WATER UV objective (Leica). Scanning was done with a step size of 48 nm along x and y and 125 nm along the z axis. Confocal images were deconvolved with the Huygens software package (Scientific Volume Imaging) and contrast adjusted in ImageJ.

### **Shear rheology for creep recovery tests**

Creep recovery experiments were performed on a stress controlled Gemini 200 shear rheometer (Bohlin Instruments) with parallel plate geometry at room temperature and 100 % humidity. The samples had a thickness was 250  $\mu m$  and a diameter of 25 mm. Fibrin samples were polymerized in the rheometer for 2h and sealed with silicon oil after polymerization to prevent drying of the samples.



## Chapter 4

# Measuring intracellular secondary structure of a cell penetrating peptide *in situ*

Reprinted with permission from the article 'Measuring intracellular secondary structure of a cell penetrating peptide *in situ*' by Frederik Fleissner, Sabine Pütz, Mischa Schwendy, Mischa Bonn, and Sapun H. Parekh in *Analytical Chemistry*, 2017, 89, 11310-11317. DOI:10.1021/acs.analchem.7b01895

©2017, American Chemical Society.



## Abstract

Cell penetrating peptides (CPPs) are short peptide sequences that can translocate across cellular plasma membranes and are thus potential delivery vectors for diagnostic and therapeutic applications. Many CPPs exhibit some sort structural polymorphism, where the secondary structure of the peptide is altered strongly by its local environment, which is believed to facilitate membrane translocation. However, the fate and structure of CPPs within cells is much less known due to measurement difficulty. Here we employ isotopic labelling combined with hyperspectral, quantitative coherent-Raman vibrational microscopy to localize a model CPP - deuterated Penetratin (d-Pen) - and determine its secondary structure in different cellular compartments. Our results show d-Pen is more  $\alpha$ -helical in the cytosol and acquires a more  $\beta$ -sheet and random coil character in the nucleus. The increased helicity in the cytosol is similar to that in previous studies with model lipid membranes, suggesting that the peptide is associated to membranes in, e.g. endosomes (or lysosomes) in the cytosol. The ability to both localize and determine the secondary structure of a CPP within cells is critical for clarifying the mechanism of peptide-mediated translocation and delivery of cargo molecules to specific cellular destinations.

## 4.1 Introduction

Cell penetrating peptides (CPP) are small peptides that are able to translocate across cellular plasma membranes, and in some cases nuclear membranes. The wide range of possible bioactive loadings, such as drugs, peptides or nucleic acids, and their biomimetic nature makes them promising candidates as delivery vectors for diagnostics and therapeutics [243,244]. One such well-studied CPP is Penetratin, which is derived from the third helix of the Antennapedia homeodomain [245]. Penetratin has been shown to undergo internalization into cells via both endocytosis and direct translocation and has been successfully conjugated to various cargo complexes for delivery of these cargos into the cytosol [243,246,247]. Penetratin has been found in the cytosol of HeLa and other cell lines within the first 30 minutes after its addition to the medium (and as fast as 10 minutes) [183,248–250]. Thereafter, it was primarily localized in or near lipid environments [249]. Finally, after extended incubation periods, Penetratin can enter the nucleus, where it accumulates and binds to the negatively charged DNA and RNA [248,249,251].

As a CPP, the ability of Penetratin to achieve direct translocation through the plasma membrane, maintain a non-aggregated state in the cytosol, and translocate into the nucleus is undoubtedly related to its structural polymorphism [252,253]. Instead of a well-defined secondary structure, Penetratin exhibits a secondary structure that varies strongly based on its local environment. Several studies have shown that Penetratin's secondary structure, like other CPPs, is sensitive to the nature of the solvent, peptide concentration and membrane composition [252,253]. Penetratin has been shown to exist both as mostly unstructured (largely as a so-called random coil) in aqueous buffer solutions near physiological pH 9, [254–257]. A conformational transition to a primarily  $\alpha$ -helix structure was observed upon interaction with nominally neutral phosphatidylethanolamine vesicles, while similarly neutral phosphatidylcholine vesicles induced a Penetratin structure having different amounts of  $\alpha$ -helix,  $\beta$ -sheet, and random coil depending the exact lipid composition and lipid:peptide ratio [254,255,257–260]. Moreover, the formation of  $\beta$ -aggregates following a favorable helical conformation during the initial binding to lipid interfaces was observed by X-ray diffraction and circular dichroism spectroscopy for high lipid:peptide ratios [261]. Similar helical  $\beta$ -strand transitions were observed with increasing charge density of the lipid interface [254].

As is evident from these examples, many experiments have focused on clarifying the structure of Penetratin have by studying lipid-Penetratin interaction, despite the fact that Penetratin is found both in the nucleus and in the cytosol in affected cells as well as in the extracellular space. Works by Bechara and coworkers have demonstrated the influence of glycosaminoglycans on Penetratin structure [245,262]. However, only one recent study by Ye *et al.* has attempted to resolve the structure of Penetratin within cells using vibrational spectroscopy [183], but the ability to spatially localize Penetratin throughout cells was limited.

To study Penetratin (or any CPP) in terms of its structure during trafficking, the most direct and informative measurement is to localize the CPP molecules and measure their structure in cells *in situ*. Fluorescence imaging of labeled Penetratin has been used to localize uptake Penetratin alone [246] and uptake with attached cargo [248,249,263,264]. Another fluorescence strategy is immunohistochemical staining where the protein of interest is located via antibodies or affinity tags. This approach has been widely used for localization of Penetratin within the cell cytosol [265]. Unfortunately, it is very challenging - if not impossible - to determine the secondary structure of any protein that is visualized with fluorescence alone.

An alternative approach to localize and determine secondary structure of Penetratin simultaneously *in situ* is Raman microspectroscopy. In this method, contrast is derived from the inherent chemistry (vibrations of chemically-bonded nuclei) within the excitation volume and a full Raman (vibrational) spectrum is acquired at each spatial location in the sample. Raman scattering is well established as a method to quantify secondary structure of a proteins based on the spectral shape of the so-called Amide I vibrational mode (NH-C=O) [55,266,267] and was recently used to study Penetratin within human metastatic melanoma cells [183]. By applying advanced nonlinear variants of spontaneous Raman like stimulated Raman scattering (SRS) or coherent anti-Stokes Raman scattering (CARS), quantitative spectral imaging with sufficiently low integration times is now possible [150,151,156,221,268] such that it is possible to spatially map the location and secondary structure of proteins within a sample. This method was recently used, for example, to image secondary structure of proteins in hydrogels [17] and human hair [269].

In this study, we employ broadband CARS (BCARS) microspectroscopy to investigate the uptake, intracellular distribution, and secondary structure of isotopically-labelled Penetratin. By combining hyperspectral BCARS imaging with multivariate data analysis, we reconstructed the intracellular Penetratin spectra in several regions of interest and quantified its secondary structure by spectral decomposition. We measure the secondary structure in proximity to intracellular lipids, in the cytosol and in the nucleus, which provides a detailed picture of structural transitions of Penetratin at different stages of intracellular trafficking.

## 4.2 Results

### Cellular uptake and localization of d-Penetratin with BCARS imaging

In order to measure specific protein vibrational spectra in cells, we require a method to retrieve the vibrational spectrum of only Penetratin within the cellular milieu, which has an average protein concentration of 200 mg/ml [12]. Since all proteins have numerous Amide I vibrations (peptide bonds), a powerful and minimally perturbative method to investigate specific molecules in complex environments, which is well-established in nuclear magnetic resonance and vibrational spectroscopy, is stable isotope labelling. Chemical imaging us-

ing vibrational spectroscopy combined with isotopic labelling was previously done by van Manen *et al.* and Ye *et al.* for cellular imaging of protein metabolism (via  $^2\text{H}$  amino acid incorporation) [270] and Penetratin (via  $^{13}\text{C}$  and  $^{15}\text{N}$  substitution for phenylalanine), respectively [183]. We produced a Penetratin peptide with an N-terminal hexaglycine 'cargo' where deuterated glycines (d-Pen), instead of hydrogenated glycines were used. The isotope substitution allowed for straightforward spectroscopic identification of d-Pen relative to all other cellular proteins since deuterium is naturally very rare. D-Pen has red-shifted carbon-deuterium (CD) vibrations into the so-called quiescent region of the vibrational spectrum ( $1800 - 2600 \text{ cm}^{-1}$ , Fig.4.1) relative to typical carbon-hydrogen (CH) vibrations, which can be used as a spectroscopic marker for detection within the cell. As an independent method to localize d-Pen, we additionally added a C-terminal biotin that allowed for traditional immunohistochemistry staining. The resulting sequence for d-Pen was G'G'G'G'G'G'-RQIKIWFQNRRMKWKK-K(biotinyl), where G' is deuterated glycine. We verified the functionality of d-Pen as a CPP in C2C12 myoblast cells by incubation with  $50 \mu\text{M}$  d-Pen in media and found its secondary structure to be similar to standard Penetratin (Supplementary Data 4.5 and 4.6). Phase contrast microscopy showed that approximately one third of all cells showed a pronounced nucleus with brighter appearance within 10 minutes of incubation (Supplementary Data 4.5), consistent with descriptions for Penetratin entry into cells from earlier reports [183]. Further imaging of the uptake process was done with confocal imaging (Supplementary Data 4.7, 4.8, 4.9 and 4.10). Control experiments with a scrambled peptide (d-Random) at the same concentration showed only minimal changes in cell morphology, even for overnight incubations (see Supplementary Data 4.11 and 4.12). Additional washing with heparin and trypsin did not reduce the signal from fluorescently labelled intracellular d-Pen and thereby indicated that the majority of peptide is indeed intracellular (see Supplementary Data 4.13 and 4.14).

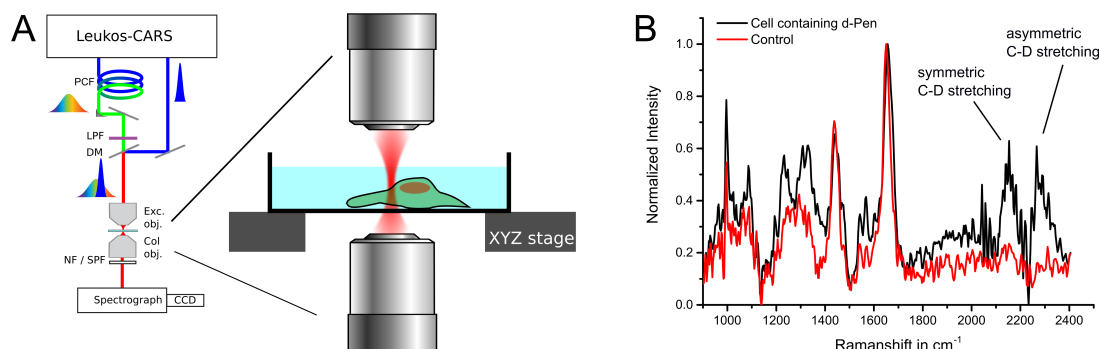


**Figure 4.1:** A) Schematic of the BCARS microspectroscopy setup. B) Raman-like spectra from a cell containing d-Pen and a control cell both normalized to their respective Amide I peaks. The quiescent region ( $1800\text{-}2600 \text{ cm}^{-1}$ ) shows characteristic peaks of the  $\text{CD}_2$  vibration at  $2165 \text{ cm}^{-1}$  and  $2240 \text{ cm}^{-1}$  for the d-Pen containing cell.

To demonstrate the ability to localize d-Pen using vibrational microscopy and determine its secondary structure in cells, hyperspectral imaging of C2C12 cells was performed by raster-scanning the sample and acquiring a BCARS spectrum at each location (see Fig.4.1A). Each spectrum is computationally processed to produce a Raman-like (RL) spectrum that is linear in concentration and contains information about the local chemical composition, which is nearly identical to a spontaneous Raman spectrum (see Methods) [158, 159, 161, 221, 271].

RL spectra from BCARS imaging of C2C12 cells that were incubated with d-Pen, clearly

show the characteristic Raman peaks assigned to the modes for symmetric ( $2165\text{cm}^{-1}$ ) and asymmetric ( $2240\text{ cm}^{-1}$ )  $\text{CD}_2$  stretching vibrations (Fig.4.1B) as well as the Amide I band ( $1600\text{-}1680\text{ cm}^{-1}$ ) - where spectral shape strongly depends on protein secondary structure [55, 266, 267, 269]. From these spectra, images of particular vibrations were created by plotting the integrated signal over a frequency window, e.g. the  $\text{CD}_2$  vibration from  $2150\text{-}2250\text{ cm}^{-1}$  (Fig.4.2A). These images show linear, quantitative data representing the concentration of  $\text{CD}_2$  at each spatial location.

To ensure that BCARS imaging depicts the true location of d-Pen in cells, we compared the fluorescence distribution of d-Pen from immunohistochemistry with that observed in  $\text{CD}_2$  images (see Fig.4.2). In these samples, C2C12 cells were incubated with d-Pen for 2 h to maximize the probability of uptake before immunohistochemically staining prior to fluorescence or BCARS imaging (for more details on the cellular uptake see Supplementary Information figures 4.7, 4.8, 4.9, 4.10, 4.11, 4.12). Figure 4.2 exhibits a distribution of d-Pen over the cytosol visible in both BCARS (Fig.4.2A, green channel) and confocal microscopy (Fig.4.2B, green channel). Co-localization in between the fluorescence and BCARS images is clear, but we also observe a sparser signal in the BCARS, likely related to the reduced sensitivity compared to fluorescence. Neither confocal nor BCARS microscopy showed a substantial d-Pen signal in the nucleus. As a complementary image, figure 4.2C shows the distribution of all proteins from BCARS within the cell by plotting the integration over the Amide I band, which appears as a spatially largely homogeneous signal over the entire cell.

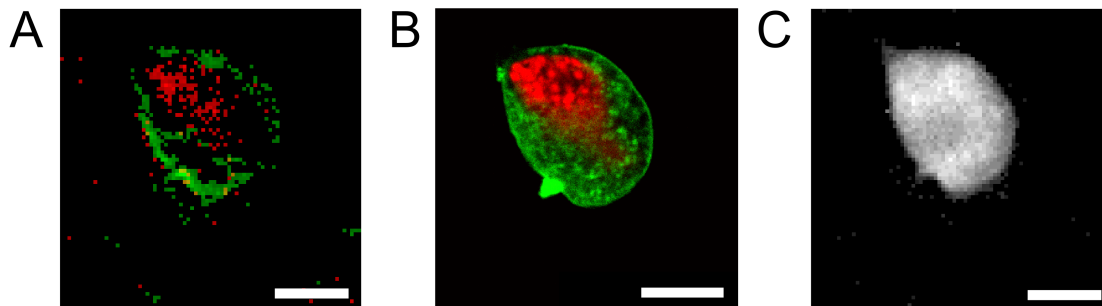


**Figure 4.2:** Co-localization of images from BCARS microspectroscopy and confocal microscopy of cells treated with d-Pen. Cells were incubated for 2 h with  $50\text{ }\mu\text{M}$  d-Pen, then fixed and stained with DAPI for DNA and Alexa555-Streptavidin for d-Pen. (A) BCARS image depicting the intensity of the  $\text{CD}_2$  vibration green (integrated RL intensity from  $2150\text{-}2250\text{ cm}^{-1}$ ) and DNA (calculated by the difference in RL intensity at  $3003\text{ cm}^{-1}$  minus  $2853\text{ cm}^{-1}$  as shown by Parekh *et al.*28) in red. (B) Confocal microscopy image of the same cell in (A) showing the nucleus in red and streptavidin-labelled d-Pen in green. (C) Total protein distribution in the cell shown by integrating the Amide I peak ( $1600\text{-}1680\text{ cm}^{-1}$ ) in the RL spectra. Scale bars in all images are  $10\text{ }\mu\text{m}$ .

### Isolation and quantification of d-Penetratin secondary structure in complex protein mixtures using multivariate curve resolution

As seen by the difference between figures 4.2A and 4.2C, cells incubated with d-Pen contain a plethora of proteins with Amide I vibrations, only a select few of which are associated with the d-Pen molecule. Therefore, the spectral information of d-Pen is mixed with Raman signals from all other proteins in the probing volume of each pixel. To obtain information about the secondary structure of only d-Pen within the cellular environment, we need to spectroscopically isolate not only the unique d-Pen signals ( $\text{CD}_2$  vibrations),

but also the critical Amide I features, which reflect secondary structure information. A convenient methodology to demix a dataset containing several spectral components of interest is multivariate curve resolution by alternating least squares (MCR-ALS) [186,195]. This method is essentially a matrix-based global fit with non-negativity constraints that is used to optimize both the spectral shape and concentration of different components quasi-simultaneously [272]. In order to demonstrate the capability of this method to quantitatively extract concentration and structural information of a deuterium-labeled peptide from an impure mixture, RL spectra from a dilution series of d-Pen and BSA in PBS were collected and separated back into the reconstructed 'pure' components. Five ratios of d-Pen:BSA (1:5, 1:4, 1:1, 4:1, 5:1), in addition to the pure solutions, were measured with BCARS, and the spectra of all mixtures were bundled into one data set matrix and processed with MCR-ALS to globally identify the best two component spectra that represent the data. The results from this decomposition are shown in figure 4.3. The component spectra of both d-Pen and BSA produced from MCR-ALS match the spectra from pure solutions with near perfect agreement (Fig.4.3A and B). The reconstructed and the original solution spectra clearly show the CD vibrations around  $2150\text{ cm}^{-1}$ . Importantly, the Amide I band, which is different for d-Pen and BSA, were faithfully reproduced, with near identical shape compared to the pure (100 %) d-Pen and BSA spectra. While for BSA the Amide I band shows its maximum at  $1653\text{ cm}^{-1}$ , indicating a substantial  $\alpha$ -helical structure, it is shifted to higher wavenumbers ( $1660\text{ cm}^{-1}$ ) in case of d-Pen reflecting the primarily unstructured peptide secondary structure in PBS. Because MCR-ALS finds only essential, non-random, spectral attributes, it is possible to reduce correlated noise in all spectra, which results in partial noise-suppression in the reconstructed component compared to the measured input spectra. The concentrations of the reconstructed components found by MCR-ALS were averaged and normalized to add up to one within each mixture. The resulting, decomposed concentrations for d-Pen and BSA are in good agreement with the known mixing ratios (Fig.4.3C and D). We find that for the given spectral data the MCR-ALS method is able to reproduce the variance to 92 % from the calculated components.

## Reconstruction of intracellular d-Penetratin spectra

To obtain information exclusively about the secondary structure of d-Pen in cells, we used MCR-ALS to isolate its spectral contributions from the cellular background after incubation with  $50\text{ }\mu\text{M}$  d-Pen for 120 minutes at  $37^\circ\text{C}$ . Similar to disentangling the different contributions from d-Pen and BSA in figure 4.3, we separated the d-Pen signal from other protein components based on the distinctive features provided by the  $\text{CD}_2$  vibrations. In this case, spatial pixels containing a  $\text{CD}_2$  signal were identified and used as input into the MCR-ALS algorithm to produce two components, a cell background and d-Pen component. We calculated the d-Pen secondary structure by analyzing the shape of the Amide I band in the d-Pen component using multi-peak fitting to established Raman secondary structures modes [55,267,272]. The spectral decomposition of the Amide I band into secondary structures was benchmarked by measurements of various other proteins of known structure against circular dichroism spectroscopy or published crystal structures (see supplementary data 4.17, 4.18 and 4.2). Furthermore, the Amide I analysis of secondary structure for pure d-Pen in PBS from our data was almost identical with analysis of circular dichroism spectroscopy of d-Pen at the same pH (see Supplementary Data 4.15, and 4.16) and previous reports from literature [183,254–257], showing 46 % unstructured, 23 %  $\alpha$ -helical, and 31 %  $\beta$ -sheet structure.

Moving forward, we quantified the secondary structure of d-Pen after 2 hours of d-Pen incubation with C2C12 cells. Each sample was scanned by  $81 \times 81$  pixels with  $0.5\text{ }\mu\text{m}$  step

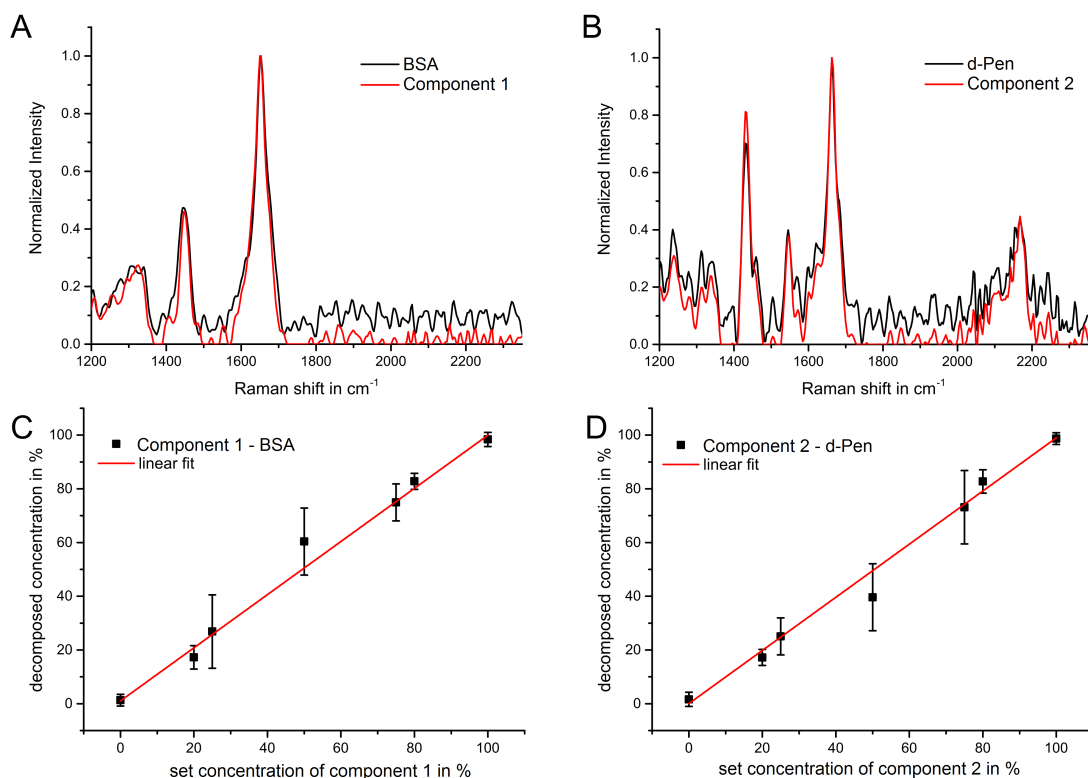


**Figure 4.3:** Demixing of d-Pen and BSA solutions with MCR into two components and their concentrations. The reconstructed component spectra from mixture solutions show similar spectral features like the RL spectra of the pure solutions for BSA (A) and d-Pen (B). For both components, the calculated average contributions correspond to the input concentrations (C and D). The error bars represent the standard deviation calculated for 484 spectra from four independent samples per data point.

size resulting in 6561 spectra from which  $\sim 50\text{--}80\%$  contained signal from the specimen as judged by the presence of CH signal. We stratified the intracellular space into cytosolic, lipid droplets, and nuclear compartments, and six different cells were analyzed, each showing at least 20 spatial pixels of detectable d-Pen ( $\text{CD}_2$ ) signal in the RL data in each compartment. A mask was created for pixels showing  $\text{CD}_2$  signal, and these pixels were then grouped based on whether they were located near lipid droplets, in the nucleus, or in the rest of the cell - here called the cytosol region (see Methods for detailed explanation of segmenting). These compartmentally segmented,  $\text{CD}_2$ -containing RL spectra were fed into the MCR-ALS algorithm to extract the spectral component associated with the  $\text{CD}_2$  vibration and fitted with our model for the Amide I band to obtain the secondary structure. The structural analysis was averaged over all cells to calculate a secondary structure for d-Pen in different cellular compartments as shown in figure 4.4. Plots of the complete spectral range and component spectra representing the cellular background are available in the supplementary data 4.19 and 4.20.

The component spectra obtained from the MCR-ALS processing showed an altered secondary structure of d-Pen anywhere within cells (Fig.4.4B and C) compared to in PBS (Fig.4.4A). While the random coil and  $\beta$ -turn content decreased with respect to the PBS sample, the  $\alpha$ -helical peaks centered at  $1652\text{ cm}^{-1}$  and  $1638\text{ cm}^{-1}$  became more pronounced. D-Pen containing pixels in the cytosol showed an increased  $\alpha$ -helical conformation (53 %) while the content of  $\beta$ -sheet (19 %) and unstructured peptide (28 %) were reduced when compared to the PBS sample (Fig.4.4B). Within the nucleus and near lipid droplets (Fig.4.4D), the % of each secondary structural motif were very similar, but col-

lectively exhibited statistically significant differences from the secondary structure in the cytosol. Compared to the cytosol, lower amounts of  $\alpha$ -helical structure (38 %) and a more pronounced contribution from  $\beta$ -sheet (27 %) and random coil structure (35 %) were observed (Fig.4.4C) in the nucleus and near lipid droplets. Regardless of location, the d-Pen component spectrum showed only weak contributions from the sidechain peaks.

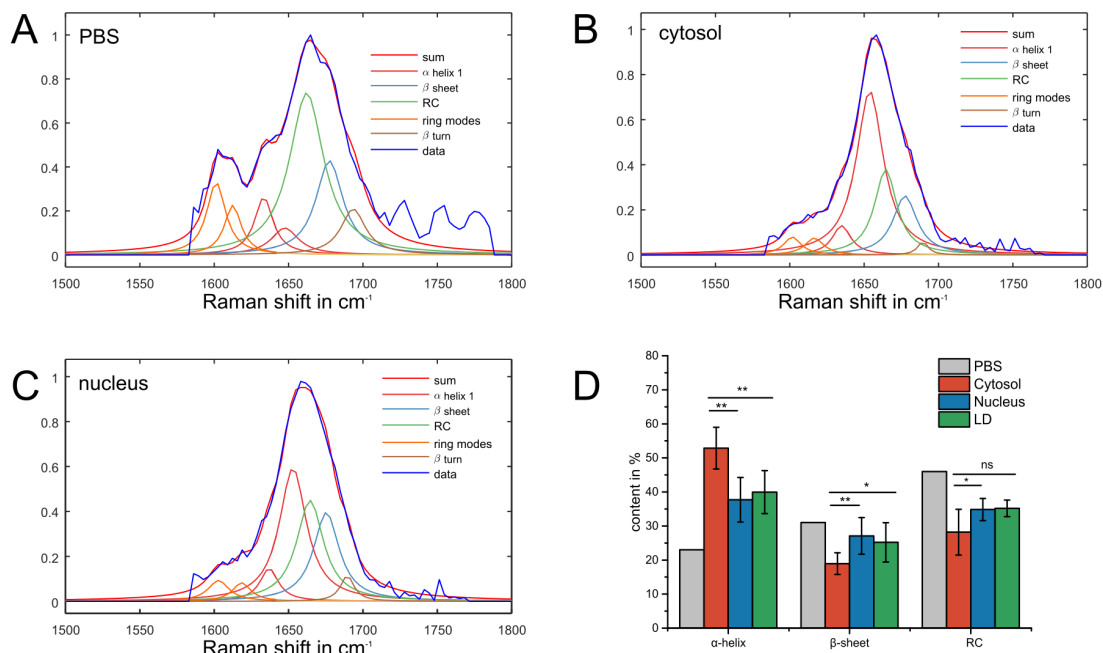


**Figure 4.4:** Secondary structure of d-Pen for different cellular locations. (A) RL spectrum of d-Pen in PBS at 0.25 M concentration appears mostly unstructured (RC = random coil). (B) The average MCR resolved spectrum for d-Pen from the cytosol shows a strong  $\alpha$ -helical contribution while the relative  $\beta$ -sheet and RC content are decreased compared to in PBS. (C) The average MCR resolved spectrum for d-Pen from the nucleus shows less  $\alpha$ -helical and more  $\beta$ -sheet and RC content compared to the cytosol. D-Pen in lipid droplets is structurally very similar to the nucleus (spectrum not shown). (D) Comparison of secondary structures from the band decomposition in different cellular compartments. The content is given as % of the summed secondary structure with error bars showing the standard deviation of 6 samples. For each structural motif, the statistically significant differences between the group from cytosol and the group from nucleus (or lipid droplets) was determined by one-way ANOVA and significance level are indicated as ns for  $P > 0.05$ , \* for  $P \leq 0.05$  and \*\* for  $P \leq 0.01$ .

### 4.3 Discussion

Attaching a six deuterated amino acid cargo to Penetratin introduced additional peaks in the BCARS spectrum of the target peptide. The new  $\text{CD}_2$  vibrations between 2150 and 2250  $\text{cm}^{-1}$  allowed direct visualization of d-Pen in cells with a similar distribution as the d-Pen distribution from fluorescence staining in the same cell (Fig.4.2). Importantly, constitution of the peptide did not alter its uptake propensity, specificity (D-Random was not taken up), and structure (circular dichroism was identical to native Penetratin in buffer, 4.5). However, BCARS was much less sensitive and requires a high local peptide concentration to detect specific vibrations, which is somewhat expected since Raman cross sections are typically  $10^8$ - $10^9$  fold smaller than effective fluorescence cross sections [220]. Accordingly, regions with small amounts of peptide (see 4.8 in Supplementary Data) show up in fluorescence staining but do not show above-threshold signal in BCARS. The unique CD vibrations of d-Pen provided sufficiently strong spectral features to allow a faithful

separation and reconstruction of d-Pen spectra from non-deuterated protein in solution mixtures. Using MCR-ALS on RL data of mixtures containing d-Pen and BSA, we were able to reproduce the spectral features of both components to a high degree. Most importantly, the shape of the Amide I band - when compared to a pure solution of BSA and d-Pen - was reproduced correctly by the algorithm. Building on the ability to isolate d-Pen spectra from non-deuterated protein spectra in solutions, we used the CD fingerprint as a threshold and binned different spatial pixels into groups based on their location in the cell, e.g. cytosol, lipid droplets, or nucleus. For these subsets MCR-ALS was used to calculate the corresponding average spectrum of d-Pen. By analyzing these spectra via spectral decomposition, we found that d-Pen in different cellular compartments adopted different secondary structures, which reflect the local environment around the peptide.

Our experimental parameters of high CPP concentration and incubation conditions ( $37^{\circ}\text{C}$ , 120 minutes) will tend to favor endocytic uptake over translocation [247, 273]. The increased  $\alpha$ -helical content in the cytosol suggests that d-Pen in the cytosol is likely associated to or within vesicular compartments as numerous studies have shown increased helicity of Penetratin when incubated with vesicles [254, 259, 260, 273]. Indeed our own circular dichroism experiments of d-Pen (and Pen) with small unilamellar vesicles show a modest growth of helical structure at pH 7 (4.6), supporting the idea that cytosolic d-Pen is somehow in contact with vesicular membranes.

We observed that the d-Pen structure within the cell, regardless of position, is considerably more  $\alpha$ -helical when compared to the structure in PBS. The study of Ye and coworkers found the secondary structure of Penetratin to be mainly random coil and  $\beta$ -strand in the cytosol, never showing a dominant  $\alpha$ -helical signature [183]. This discrepancy possibly arises due to the following three reasons: 1) Ye *et al.* studied Penetratin uptake at room temperature, where uptake tends (more) towards passive translocation compared to our studies where the cells were incubated at  $37^{\circ}\text{C}$  and only very short treatment times for the cytosol measurements of 2-40 min, while in the present study cells were incubated at  $37^{\circ}\text{C}$  and 2 h resulting in an overall faster metabolism and intracellular processing; 2) Principal component analysis (PCA) did not fully reconstruct the labelled peptide Amide I spectrum but only weak spectral features in the Amide I region in addition to the clear isotopically shifted phenylalanine peaks. The resulting penetratin structure was then assigned based purely on peak locations rather than on quantitative fitting. It is clear that the location and widths of the different peaks in the Amide I will influence any derived structural characterization from vibrational spectra, and the highly overlapping peaks for  $\alpha$ -helical and unstructured conformation give room for ambiguity. We confirmed the accuracy of our peak analysis method by measurements of various other proteins of known structure benchmarked against circular dichroism spectroscopy or published crystal structures (see supplementary data 4.17, 4.18 and 4.2). 3) The cytosolic data likely included spectra from lipid droplets (while here a preselection was performed), and PCA possibly allocated  $\alpha$ -helical amide signal into the lipid component as stated by Ye *et al.*

We found the  $\beta$ -sheet and random coil content to be on average 43 % and 16 % higher, respectively, in the nucleus than in the cytosol, with a corresponding reduction of 30 % helical content in the nucleus compared to the cytosol; however, the helical content was still well above that in PBS, and the  $\beta$ -sheet content was almost identical to that in PBS. The changes in secondary structural elements observed in the nucleus compared to the cytosol are consistent with previous studies showing that Penetratin interacting with high charge density molecules such as DNA or similar highly charged lipids (shown to compete for Penetratin) compared to less charged lipids [254, 273].



Interestingly, the structure of d-Pen associated with lipid droplets - harboring neutral lipids - was almost identical to what was observed in the nucleus. Lipid droplet cores exhibit a fairly hydrophobic environment for which Penetratin was shown to fold into helix structure by solution experiments in trifluoroethanol/water mixtures [183,248,256]. Even though we cannot state if the CPP stays at the surface or is incorporated in the lipid droplet, this conformational change towards  $\alpha$ -helical structure is therefore plausible. The similarity between d-Pen secondary structures in the nucleus and that associated with lipid droplets suggests that both highly charged and hydrophobic environments lead to similar structural manifestation of Penetratin though likely for different reasons. While, to the best of our knowledge, this is the first demonstration to use MCR-ALS analysis to accurately retrieve a specific protein spectrum within a protein-rich cell, our method has certain shortcomings. The method as implemented here inherently calculates average secondary structures both spatially and chemically as explained in the following. It was not possible to calculate secondary structure of d-Pen on a pixel-by-pixel basis due to the necessity of an overdetermined system to calculate pure components by MCR-ALS.

Nevertheless, when compared to the method of Ye *et al.*, which attempted a similar analysis using PCA, our method is benchmarked against a mixture of deuterated/non-deuterated protein and clearly produces chemical spectra that isolate the contribution of d-Pen relative to cellular background. In the MCR-ALS optimization, we used boundary conditions and physically rational constraints to find components that can be interpreted as chemical meaningful spectra. While a PCA analysis (as used by Ye *et al.* [183]) strictly maximizes the explained variance, MCR identified only a d-Pen component in a way that an average chemical fingerprint (spectrum) minimizes the error in the optimization [158]. Moreover, the method use here is more robust compared to 'cellular background subtraction' that can be ill-behaved due to unknown amount of and possibly time-dependent cellular background in each pixel. Taken together, the evidence provided here supports the idea that coherent Raman imaging with MCR-ALS and stable isotope exchange is a promising platform for localizing proteins within cells and determining their structure in a reliable way *in situ*.

## 4.4 Conclusions

Quantitative vibrational microscopy combined with isotopic exchange and multivariate data analysis was used to localize a deuterated CPP, Penetratin, in cells and to isolate its vibrational spectrum from the cellular background *in situ* in a label-free manner. From the derived spectra of Penetratin, the secondary structure in different cellular compartments was calculated, showing that Penetratin is substantially more helical in cells, regardless of location, than in solution. We further found that Penetratin in the cytosol is highly  $\alpha$ -helical, resembling the structure of Penetratin interacting with low and moderately charged lipid membranes, whereas it was more unfolded and sheet-like in the nucleus and near lipids. The vibrational imaging and spectral unmixing method presented here provides a framework for localizing and quantifying the secondary structure of arbitrary proteins within distinct cellular compartments.

## 4.5 Methods

### Synthesis of deuterated Penetratin (d-Pen)

Penetratin with an isotopic cargo of six deuterated glycine (G') and biotinylated lysine was synthesized on a peptide synthesizer (Liberty, CEM, USA) using solid phase peptide synthesis and standard Fmoc chemistry. The full sequence is G'G'G'G'G'G'-RQIKIWFQNRRMKWKK-K(biotinyl)-NH<sub>2</sub> for d-Pen and G'G'G'G'G'G'-RRIFNKMQUIWRWQKK-K(biotinyl)-NH<sub>2</sub> for the scrambled peptide d-Random. Amino acids and biotinylated lysine were purchased from Novabiochem (Merck, Germany) and deuterated Glycine (2,2-D<sub>2</sub>, 98 %) from Cambridge Isotope Laboratories. Further details can be found in the SI.

### Cell culture fixation and staining

C2C12 cells were grown in collagen coated glass bottom dishes (MatTek) and normal culture medium (Dulbecco's Modified Eagle's Medium + 10% fetal calf serum, Dulbecco). Cells were used from passage 4 to 20 and not synchronized. Before incubation with d-Pen, the medium was changed to serum free medium to prevent immediate degradation [274] [275]. Next, d-Pen was added to a final concentration of 50  $\mu$ M and incubated at 37°C, 100 % relative humidity and 5 % CO<sub>2</sub> for the specified time. Fixation and staining described below procedures were performed at room temperature. Incubation with d-Pen was stopped by washing with PBS and fixation for 30 min (4 % Paraformaldehyde in PBS, pH 7.4). Samples were washed three times for 5 min in PBS and permeabilized by incubation for 10 min with 0.1 % Triton X-100 and 0.025 % CHAPS (3-[(3-Cholamidopropyl)-dimethylammonio]-1-propane sulfonate) in PBS. For immunohistochemistry, cells were labelled with Alexa555 streptavidin (for d-Pen) and DAPI or DRAQ5 (for nuclei) - all from Molecular Probes - and subsequently washed three times in PBS. Fixed and stained specimens were stored in PBS at 4°C and analyzed within 3 days. For comparison of CARS and immunofluorescence, a confocal z-stack was acquired for each individual cell, and the slice with the closest similarity was compared against the distribution from BCARS. See SI for details of confocal imaging.

### BCARS phase retrieval into Raman-like spectra

BCARS microspectroscopy data was acquired by raster scanning a region of interest, normally covering a single cell, and recording an entire BCARS spectrum for each pixel. Details of our acquisition system can be found in the Supporting Methods. A recorded BCARS spectrum represent the sum of a resonant and a non-resonant component, which needs to be processed into Raman-like spectra for quantitative analysis [221]. Therefore, self-written scripts in Igor Pro 6.34 (WaveMetrics) were used to perform the following steps: First, a Kramers-Kronig transformation, which included a causality constraint, was used to separate the resonant component as described in by Liu *et al.* [156] [161]. Next, the error from the phase retrieval was corrected and normalized to the non-resonant background following the method from Camp *et al.* [268].

### Multivariate curve resolution on solution spectra

RL data of mixtures containing BSA and d-Pen was bundled into one data matrix and processed further in Matlab (R2015, MathWorks). For each mixing ratio, the analysis covered 484 spectra from four independent samples. To extract the pure d-Pen component, we employed multivariate curve resolution using an alternating least squares algorithm (MCR-ALS) [186] as provided in a Matlab toolbox (MCR-ALS GUI 2.0) from Tauler, de

name	spectral range	purpose
amide I	1600 - 1680 $\text{cm}^{-1}$	total protein concentration [46]
CD	2150-2250 $\text{cm}^{-1}$	signature of deuterated glycine originated from d-Pen
LD	2865 - 2880 $\text{cm}^{-1}$	lipid droplets [241]
nucleus	manually defined mask on data set	nuclear region
cytosol	mask(amideI)- mask(nucleus)- mask(LD)	cell region which is not nuclear region or LD region

**Table 4.1:** Overview of masks used to filter the initial BCARS data

Juan and Jaumot [195]. The data set  $\mathbf{D}$  was assumed to be constructed from a linear combination of two pure components  $\mathbf{S}$  - representing BSA (I) and d-Pen (II) - and their local concentration  $\mathbf{C}$ . An error term  $\mathbf{E}$ , which covers noise and uncorrelated spectral features, is also included.

$$\mathbf{D} = \mathbf{C} \cdot \mathbf{S} + \mathbf{E} \quad (4.1)$$

This system of linear equations is solvable for an overdetermined system, which requires more individual spectra than allowed components. The optimization was constrained to non-negativity of spectra and concentrations. Furthermore, component spectra were normalized to the Euclidean norm.

### MCR unmixing of the intracellular d-Pen component

The variation in spectral features is high when taking into account an entire cell. A MCR decomposition, as described earlier, of a full data set found besides an average protein component only more dominating features like DNA or lipids. Therefore, to enable the MCR algorithm to judge contributions of different components with regards to d-Pen, it was necessary to limit the data set down to relevant pixels (see also supplementary data 4.21). Only spectra showing the  $\text{CD}_2$  vibration, indicating the presence of d-Pen to some extent, were used for the component separation. From the given spectral data we created spatial (binary) masks assigned to total protein concentration and lipid droplets (see 4.1). Furthermore, data was categorized to either the cytosol or the nucleus by manual masking based on bright field images.

From logical conjunctions of these masks we created subsets for  $\text{LD} \wedge \text{CD}$ ,  $\text{Nucleus} \wedge \text{CD}$  and  $\text{Cytosol} \wedge \text{CD}$  allowing a separated analysis of d-Pen signal close to lipid droplets, within the cytosol and the nucleus. For each subset, the two most influential component spectra based on their eigenvalue rank were calculated by the MCR algorithm. By limiting the number of allowed individual components to two, only the dominant 'd-Pen' and average 'cell background' components were obtained, and less prominent spectral features were ignored. The obtained component spectrum for d-Pen (the one that has the CD peaks) is taken as the spectrum of the peptide for each cellular compartment.

### Calculation of local secondary structure

Both averaged RL spectra and component spectra from MCR analysis were quantified with respect to their secondary structure. The contribution of different structural motifs was calculated by decomposition of the amide I band (1570 - 1730  $\text{cm}^{-1}$ ) via least square peak

fitting with a Levenberg-Marquard algorithm in Matlab (R2015, MathWorks). Thereby, the amide I region was decomposed into Lorentzians, which are designated to structural motives and the resulting peak areas were normalized to the total secondary structure. The algorithm was terminated when the results were stable within a tolerance of  $10^{-6}$  in peak area deviation.

In contrast to our previous publication, the peak fitting procedure was refined to cover the more diverse spectra obtained from cell samples [17]. As described by Berjot *et al.* we included two peaks for  $\alpha$ -helix at 1635 and 1647  $\text{cm}^{-1}$ , 1660  $\text{cm}^{-1}$  for random coils, 1667  $\text{cm}^{-1}$  for  $\beta$ -sheets, 1693  $\text{cm}^{-1}$  for  $\beta$ -turn and two minor peaks at 1612 and 1600  $\text{cm}^{-1}$  for tyrosine, tryptophane and phenylalanine ring modes to fit the Amide I band [55] [46]. All peaks were defined as Lorentzian functions, where linewidth and center frequency were floating within a defined range and positive floating amplitude.

### Supporting Information Available

A comparison of d-Pen and standard Penetratin, details on cellular d-Pen uptake, high quality fluorescence images of intracellular d-Pen distribution, additional experiments on surface-bound peptide, circular dichroism and BCARS data used for peak deconvolution, additional data on MCR components and further method descriptions are provided in Appendix II.

## 4.6 Appendix II - Supplementary Information

### Supplementary Data

#### Comparison of d-Pen and standard Penetratin

To test if the additional glycine and K(biotinyl) affect the conformation of d-Pen with respect to standard Penetratin (RQIKIWFQNRRMKWKK-NH, purchased from Bachem, Switzerland), we performed circular dichroism spectroscopy of both peptides. Circular dichroism spectroscopy of 50  $\mu$ M peptide in salt free phosphate buffer at pH 7 and at room temperature was performed as described in the methods section. Figure 4.5 shows that the circular dichroism spectra of d-Pen and Penetratin are identical and indicate mostly unstructured peptide under these conditions. The cargo attached to d-Pen therefore has no significant effect on the secondary structure of the peptide.

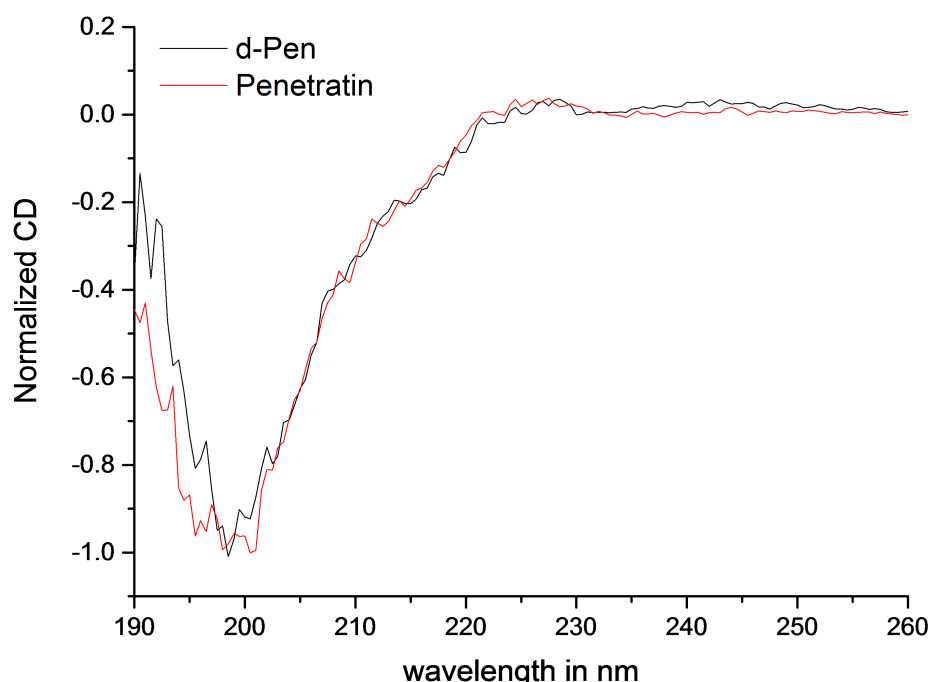


**Figure 4.5:** Circular dichroism spectra of d-Pen and commercially obtained Penetratin at pH 7. Both spectra show characteristic minima at 200 nm indicating mostly unstructured conformation under these conditions.

#### Penetratin and d-Pen interaction with lipids

The interaction with small unilamellar vesicles (SUV) was tested in circular dichroism spectroscopy for d-Pen and Penetratin. 1,2-Dioleoyl-sn-glycero-3-phosphocholine (DOPC, Sigma Aldrich) and 1,2-dioleoyl-sn-glycero-3-phospho-(1'-rac-glycerol) (DOPG, Avanti Lipids) were first dissolved in chloroform and mixed in molar ratio of 4:1. The mixture was then dried by evaporating the chloroform under a nitrogen stream followed by placing the lipids in vacuum for 15 minutes. The lipid film was then re-suspended in NaCl free 50 mM phosphate buffer, pH 7, and 1 mM lipid concentration and vortex for 5 minutes to obtain multi-lamellar vesicles. SUVs were then formed by lipid extrusion (Mini-Extruder, Avanti Lipids) where the lipid solution was repeatedly forced through a polycarbonate filter (Nuclepore 0.05, Whatman) with 50 nm pore size. This resulted in a transparent

solution with sufficient low scattering in circular dichroism spectroscopy.

For circular dichroism spectroscopy, 50  $\mu\text{M}$  peptide was added to 0.5 mM SUVs all in buffer solution at pH 7, incubated for 15 min at RT and spectra were acquired at RT as described in the methods section. As reference, either Penetratin or d-Pen in the same buffer and 50  $\mu\text{M}$  final concentrations were measured. Addition of SUV to the peptide solution induces slight helical formation for both d-Pen and Penetratin as can be seen in the reduced circular dichroism values from 215-230 nm as shown in figure 4.6A and B. A predominantly  $\alpha$ -helical sample would result two minima at 208 nm and 220 nm as shown in Fig 4.16B for BSA and Fig.4.17A and B for vimentin and fibrinogen, respectively. We note that the spectra for SUV containing samples become noisy below 200 nm due scattering, which leads to a saturation of the detector. The  $\alpha$ -helix formation in presence of moderately charged SUVs agrees well with reported results in literature [255] [259] [260]. In conclusion, these measurements show that d-Pen and Penetratin behave nearly identical alone in solution and both show a small conformational change towards  $\alpha$ -helical structure (indicated by the arrows) in the presence of lipid membranes.

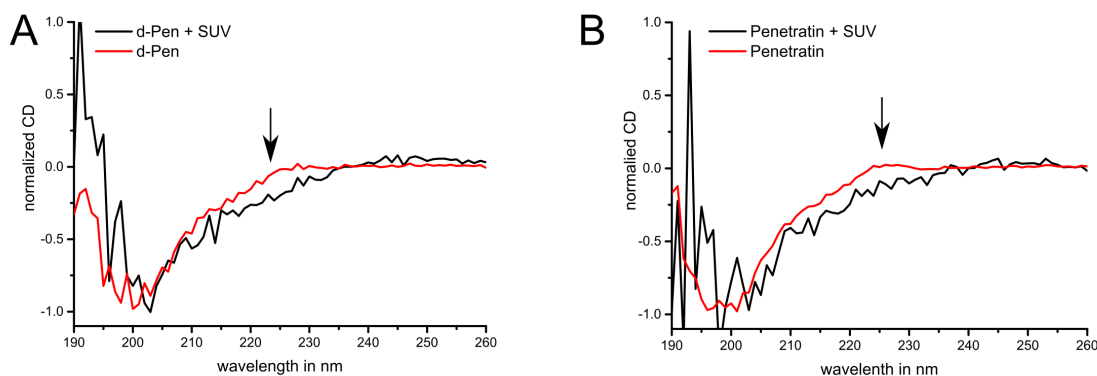


**Figure 4.6:** Circular dichroism spectra showing the interaction of d-Pen (A) and Penetratin (B) with DOPG/DOPC SUV at pH 7. The arrows indicate regions of reduced circular dichroism upon addition of SUVs.

## Cellular penetration of d-Pen and d-Random

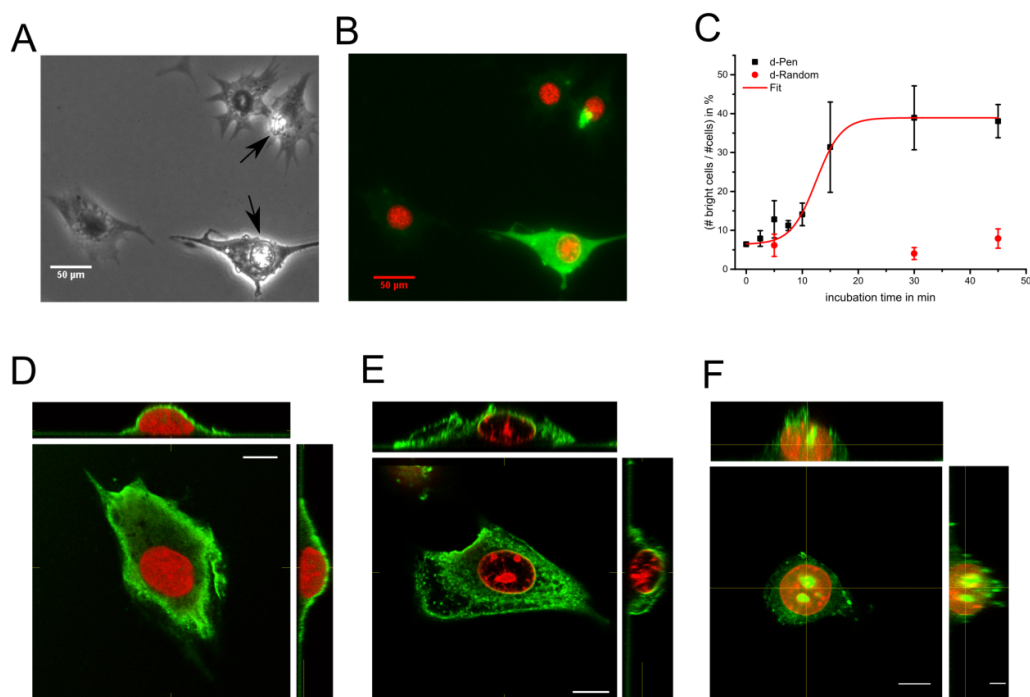


**Figure 4.7:** Different stages of d-Pen uptake in adherent cells. A) phase contrast image after 10 minutes incubation. The cells indicated by arrows show the characteristic brightening of the nucleus. B) Corresponding fluorescence image with d-Pen labelled in green (Streptavidin-Alexa555) and DNA in red (DAPI). C) Percentage of affected cells for different incubation times in d-Pen and d-Random, error bars indicate standard deviation. D) Confocal microscopy image after 5 minutes incubation time. Most fluorescence intensity is located still in the membrane region. E) Confocal microscopy image after 45 minutes incubation time. d-Pen fluorescence can be found all over the cytosol. Furthermore, a shell around the nuclear envelope has formed. The DNA has condensed to small clumps. F) Confocal microscopy image after 120 min incubation time. Aggregates of d-Pen have formed in the nucleus as well as in the cytosol. The scale bars in D-F are 10  $\mu\text{m}$ . High-resolution images of D-F can be found in the supplementary data 4.8, 4.9 and 4.10.

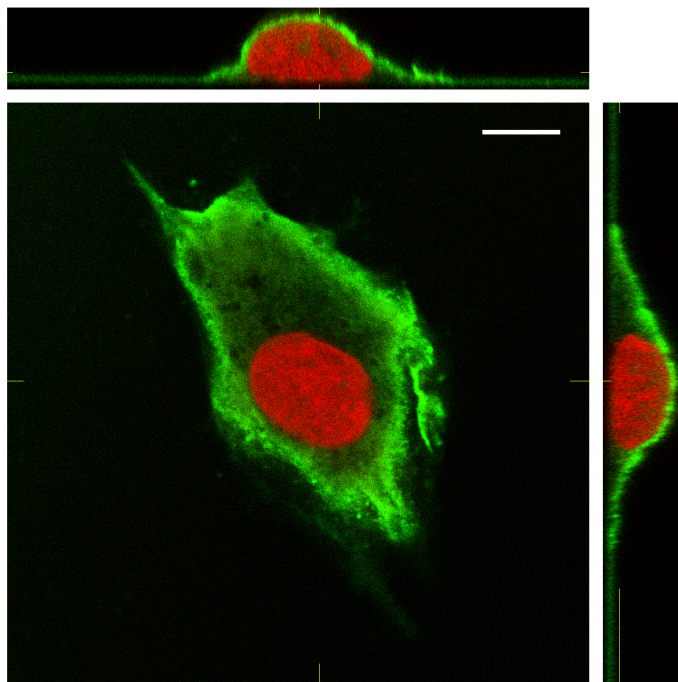


**Figure 4.8:** High-resolution confocal microscopy image after 5 minutes incubation time (Fig.4.7D). The scale bar represents 10  $\mu\text{m}$  and the yellow cross-hair indicates the section planes for XZ and YZ.

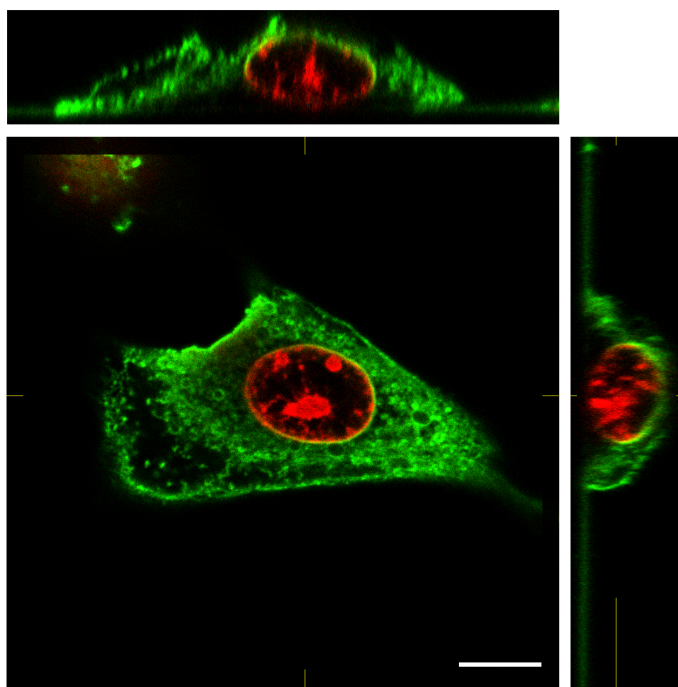


**Figure 4.9:** High-resolution confocal microscopy image after 45 minutes incubation time (Fig.4.7E). The scale bar represents 10  $\mu\text{m}$  and the yellow cross-hair indicates the section planes for XZ and YZ.



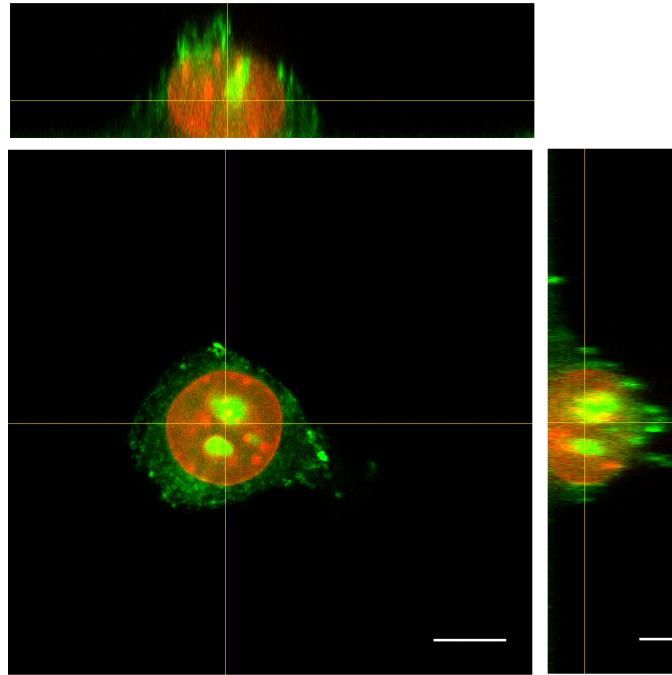


**Figure 4.10:** High-resolution confocal microscopy image after 120 minutes incubation time (Fig.4.7F). The scale bar represents 10  $\mu\text{m}$  and the yellow cross-hair indicates the section planes for XZ and YZ.

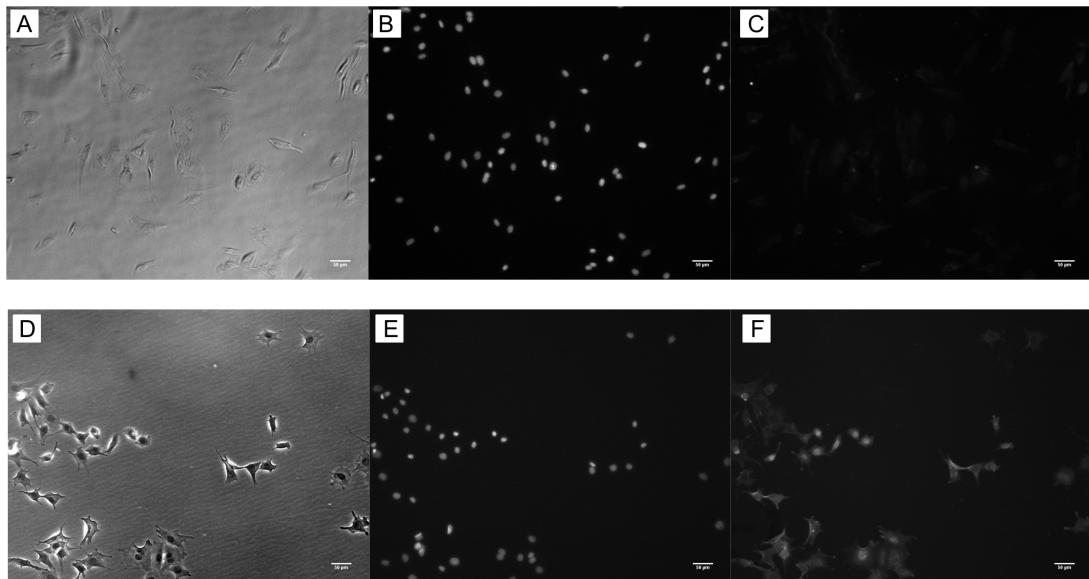


**Figure 4.11:** Microscopy images of C2C12 cells after 5 min incubation with 50  $\mu\text{M}$  d-Random (top row) and d-Pen (bottom row). Cells are shown in phase-contrast (A,D), DAPI staining (B,E) and streptavidin-Alexa 555 (C,F). All scale bars represent 50  $\mu\text{m}$  and imaging conditions were similar to figure 4.7A and B.

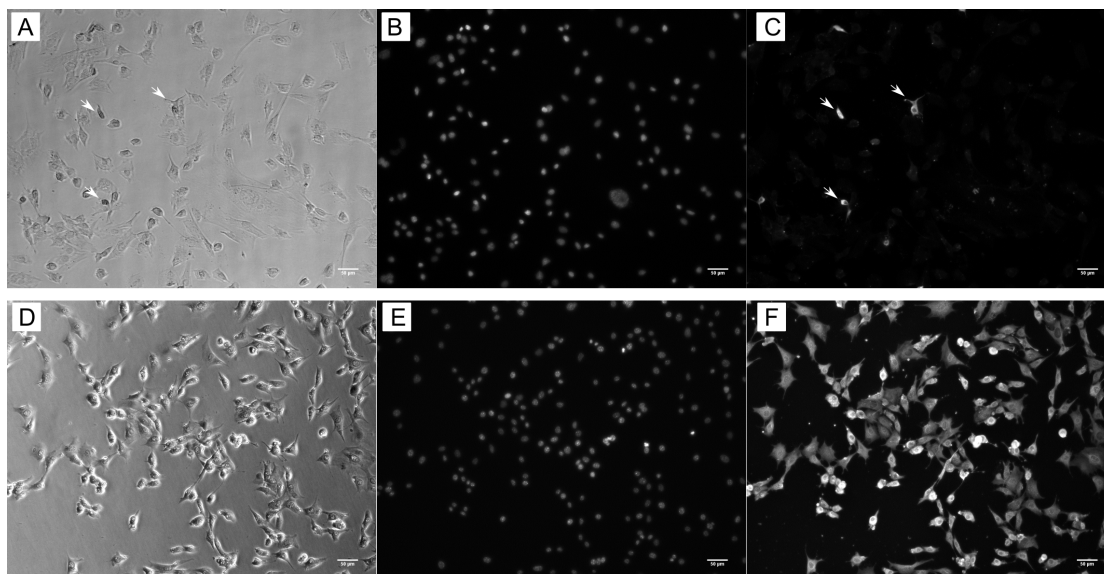
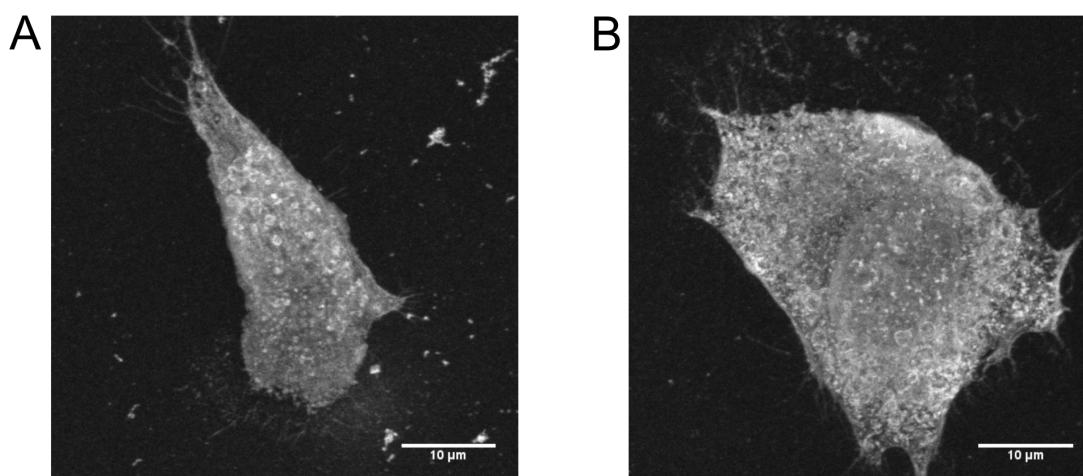


**Figure 4.12:** Microscopy images of C2C12 cells after 2 h incubation with 50  $\mu$ M d-Random (top row) and d-Pen (bottom row). Cells are shown in phase-contrast (A, D), DAPI staining (B, E) and streptavidin-Alexa 555 (C, F). All scale bars represent 50  $\mu$ m and imaging conditions were similar to figure 4.7A and B. As indicated by arrows in (C), only few cells show fluorescence signal in the d-Random group.

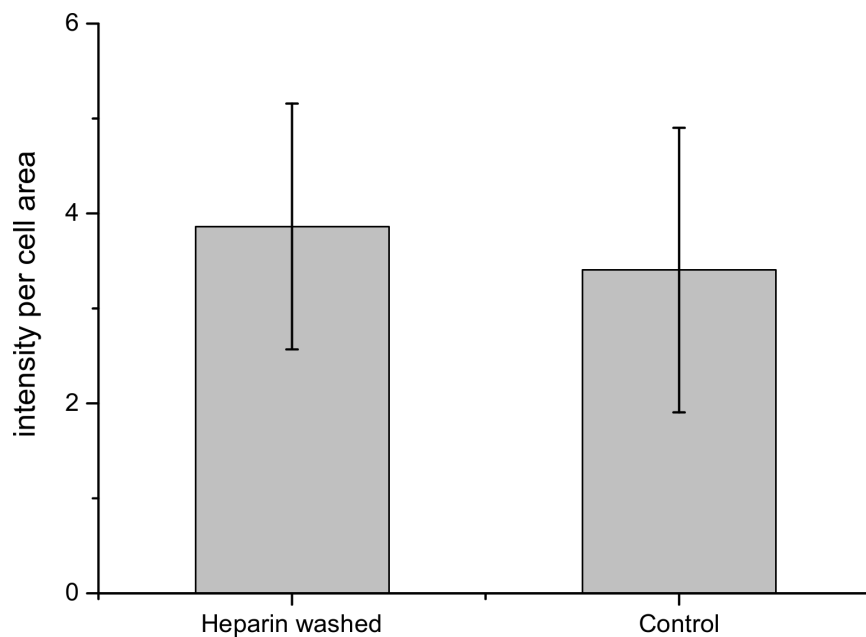
### Quantification of internalized versus membrane-bound d-Pen

To test if the plasma membrane-bound peptide is the dominant species in our experiments, C2C12 cells were incubated together with 50  $\mu$ M d-Pen for 2 h at 37°C exactly as described in the methods section for BCARS experiments, after which additional washing steps were performed to remove the membrane-bound fraction. Cells were washed by mild trypsinization (0.5 % trypsin in PBS) for 2 minutes followed by heparin treatment (0.5 mg/ml in PBS) for 5 min as described by Kaplan and coworkers [276]. Cells were then fluorescently labelled for d-Pen with a streptavidin conjugated fluorophore as described in the methods section (of the main text) and fluorescence images were acquired (see Fig.4.13).

Confocal microscopy images were processed on a single-cell basis to calculate the fluorescence intensity per cell. Cells were detected in a z-projected fluorescent signal image and mean gray values of the images were used for thresholding. Because of strong contrast between cellular fluorescence against background signals, mean value thresholding resulted in a binary mask of single cell bodies only, which was used for automated cell selection. Via reversed selection of non-cellular parts of the image, we quantified the mean fluorescence value of the background for each stack. This mean background intensity was used in turn to normalize the respective fluorescence signal from labelled penetratin and to compensate possible laser intensity heterogeneities between the experiments. With the cell selection and the value for normalization at hand, we then quantified fluorescence within the cell frame on the original z-stack on a per slice basis and summed the value before normalizing by the projected cell area. Values for the cells within each group (washed vs. non-washed) were averaged and compared as shown in Fig.4.14. From these experiments we do not find a significant reduction in d-Pen intensity caused by the additional washing with trypsin and heparin. Thus, we conclude that the d-Pen quantified with BCARS imaging after 2 h of incubation is predominantly internalized, and the membrane-bound peptide can be neglected for the interpretation of the results presented in our study.

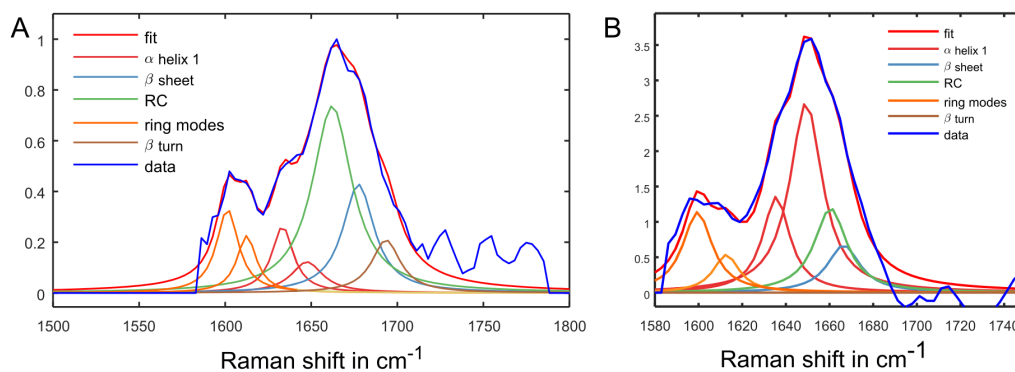


**Figure 4.13:** Z-projected confocal images of fluorescently labelled d-Pen in C2C12 cells without (A) and with heparin/trypsin washing (B). The acquisition parameters (time, laser intensity, detector voltage) were kept the same for all experiments. Scale bars represent 10  $\mu$ m.



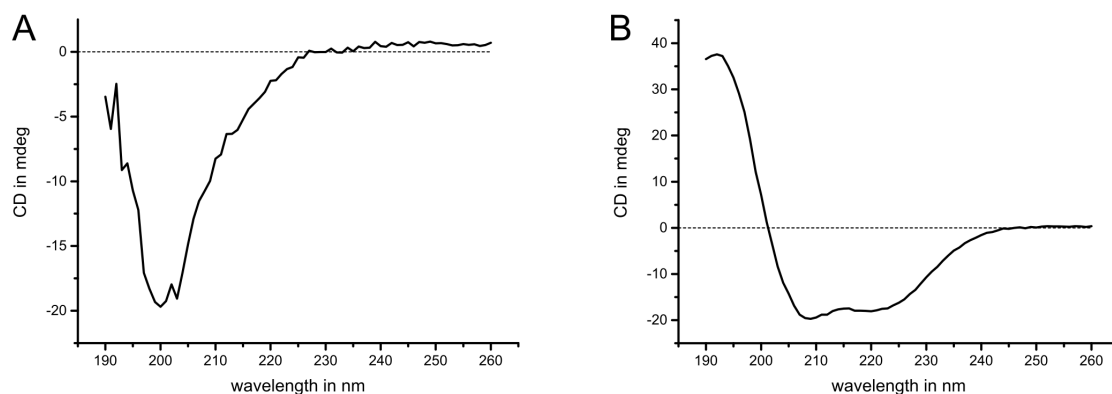
**Figure 4.14:** Comparison of fluorescence intensity normalized to the cell area for cells treated with heparin/trypsin washing steps (n=6) and the untreated control group (n=4). Error bars are standard deviation.

### Structural comparison between d-Pen and d-Random

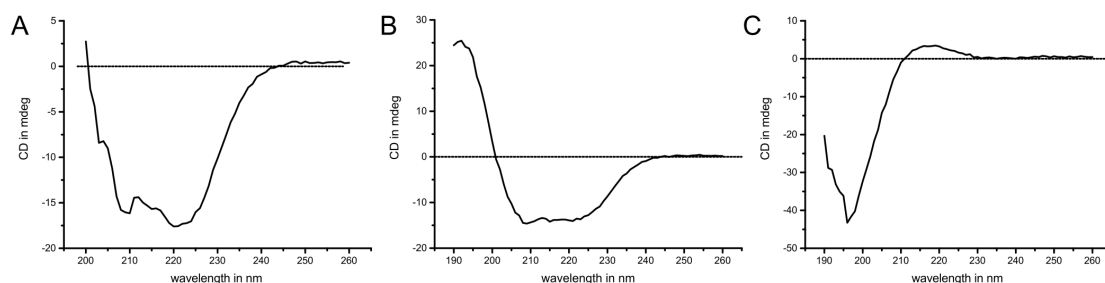


**Figure 4.15:** Peak deconvolution of RL spectra of d-Pen (A) and d-Random (B) in phosphate buffer at pH 7.4. The peptide secondary structure was found to be 23 %  $\alpha$ -helical, 31 %  $\beta$ -sheet and 46 % RC for d-Pen and 72 %  $\alpha$ -helical, 4 %  $\beta$ -sheet and 25 % RC for d-Random at pH 7.4.

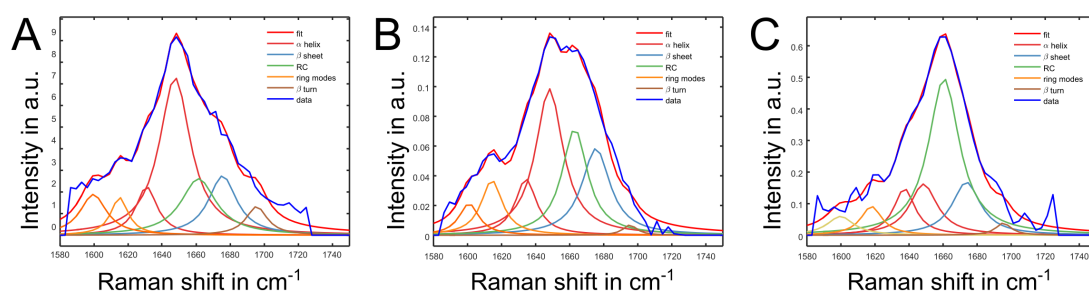
## Comparison of BCARS secondary structure determination with circular dichroism spectroscopy



**Figure 4.16:** Circular dichroism spectroscopy of d-Pen (A) and BSA (B) in phosphate buffer at pH 7.4. The spectrum for d-Pen shows a mixed contribution of mainly random structure (minimum at 195 nm) and some  $\beta$ -sheet structure (maximum at 196 nm) resulting in a shifted peak at 200 nm. BSA shows the peaks related to  $\alpha$ -helix at 222 nm and 208 nm [277].



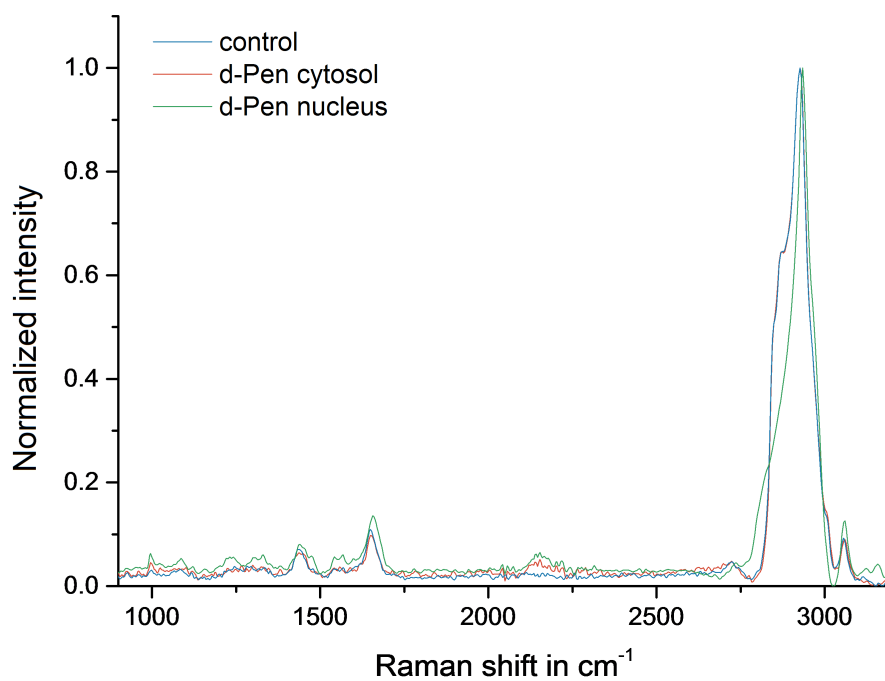
**Figure 4.17:** Circular dichroism spectroscopy of Vimentin monomers (A), Fibrinogen (B) and poly-L-lysine (C) in phosphate buffer at pH 7.4.



**Figure 4.18:** Peak decomposition of the amide I band from CARS spectroscopy of Vimentin monomers (A), Fibrinogen (B) and poly-L-lysine (C) in phosphate buffer at pH 7.4.

Protein	Method	$\alpha$ -helix [%]	$\beta$ -sheet [%]	RC [%]
BSA	Circular dichroism spectroscopy	76	9	15
	CARS	83	6	12
	$\Delta$ (Circular dichroism -CARS)	-7	3	3
Vimentin	Circular dichroism spectroscopy	60	18	22
	CARS	58	16	25
	$\Delta$ (Circular dichroism -CARS)	2	2	-3
Fibrinogen	Circular dichroism spectroscopy	61	11	27
	CARS	50	23	27
	$\Delta$ (Circular dichroism -CARS)	11	-12	0
Poly-L-Lysine	Circular dichroism spectroscopy	11	19	74
	CARS	25	12	63
	$\Delta$ (Circular dichroism -CARS)	-14	7	11
d-Pen	Circular dichroism spectroscopy	20	36	44
	CARS	23	31	46
	$\Delta$ (Circular dichroism -CARS)	-3	5	-2

**Table 4.2:** Secondary structure estimation for different proteins at pH 7.4 based on circular dichroism spectroscopy and BCARS data shown in 4.11, 4.12, 4.13, 4.14 and 4.15. The secondary structure for d-Pen is in good agreement to the values found by Ye *et al.* for fh-Penetratin in water (24 %  $\alpha$ -helix, 33 %  $\beta$ -sheet and 43 % RC) from spontaneous Raman spectroscopy [278] [183].

**Exemplary BCARS spectra from cells for data downstream data processing**

**Figure 4.19:** Raman-like spectra obtained from fixed C2C12 cell samples showing the spectral quality that was used for in further data processing.

## MCR-ALS extracted d-Pen and cell background components from different compartments

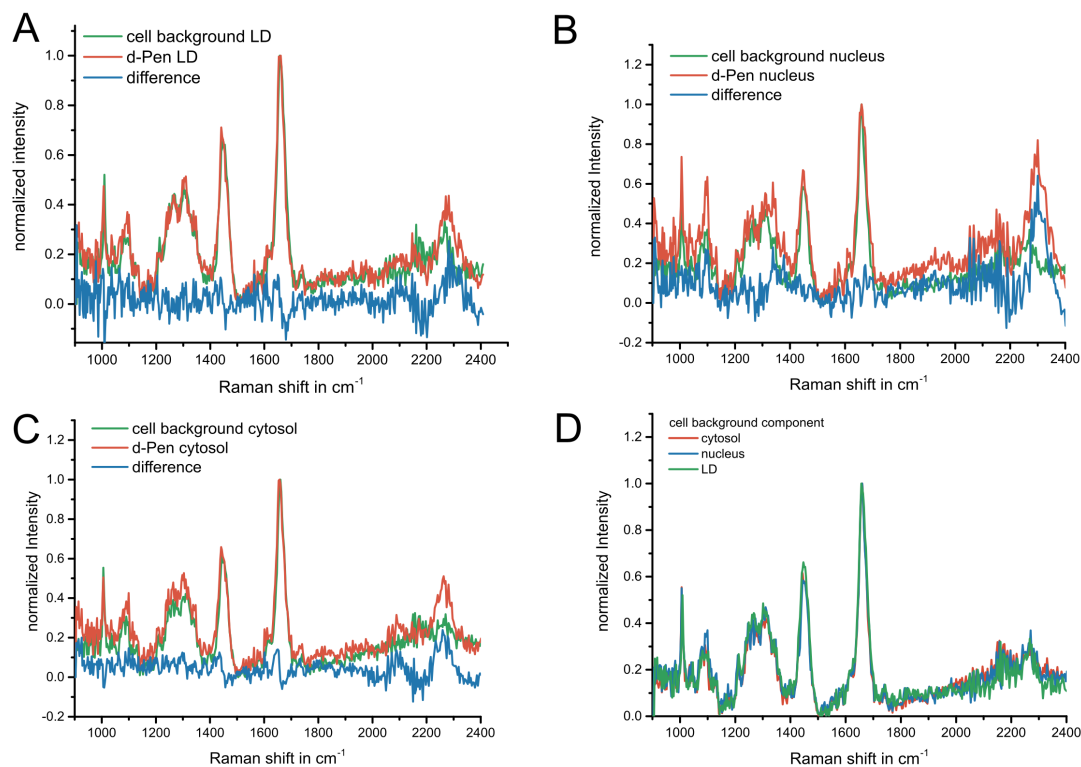


**Figure 4.20:** Average MCR derived component spectra for the cell background component and the d-Pen component for the different groups (A-C) as used in Fig.4.4 D). Comparison of the cell background component for all three groups showing only minor spectral differences due to the presence of lipids at  $1440 \text{ cm}^{-1}$  or phosphate (nucleus,  $1095 \text{ cm}^{-1}$ ) with the amide I band being unchanged. From these spectra, the difference between the d-Pen and cell background components always shows a CD vibrational peak; however, we acknowledge it is less clear for LDs. The background peaks have similar amide I shapes in all locations.



### Analytical workflow for secondary structure calculation of d-Pen within cellular compartments

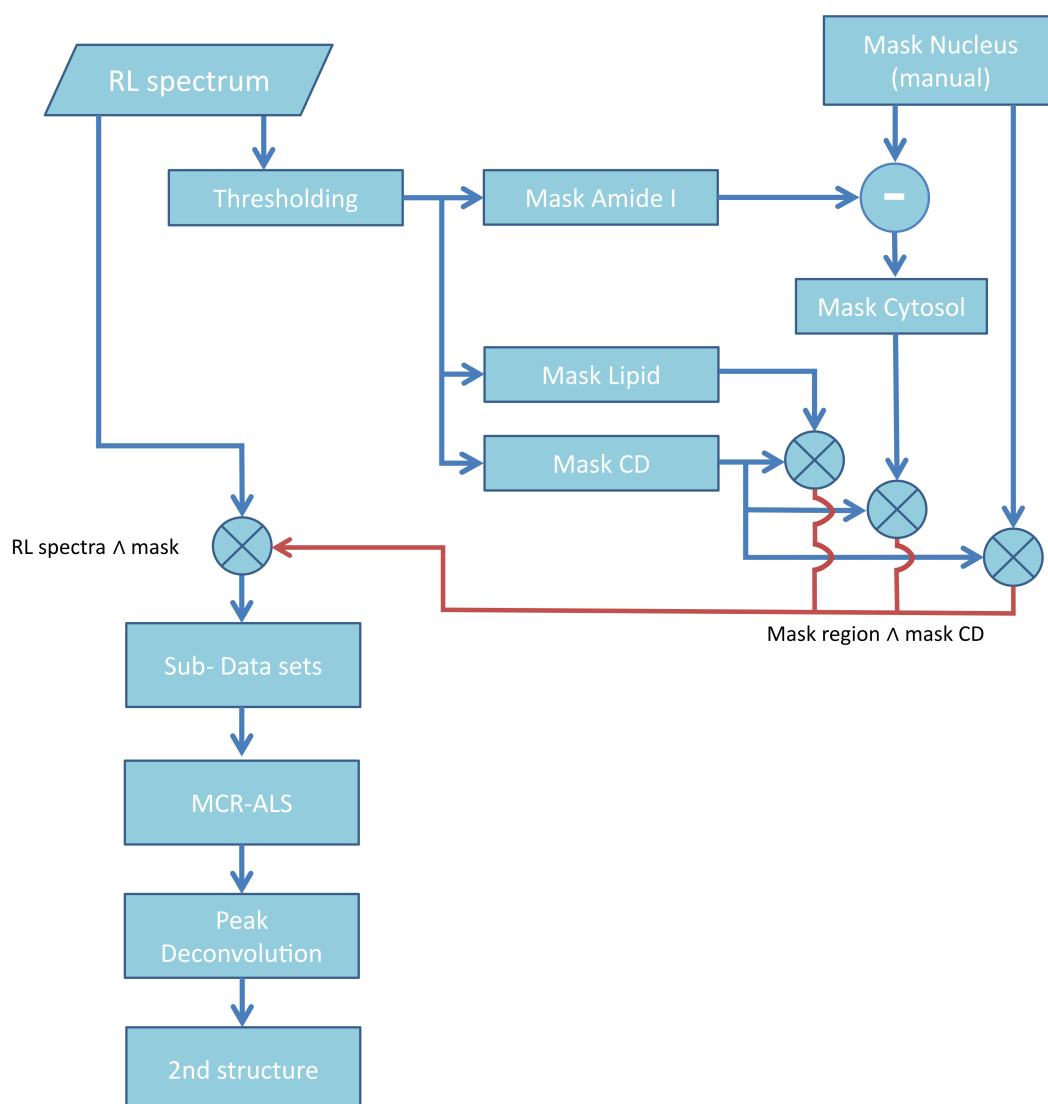


**Figure 4.21:** Flowchart of the data analysis to obtain regional secondary structure. The initial dataset containing the full RL hyperspectral data is used to calculate binary masks based on thresholding against peak intensities for protein, lipid droplets, and d-Pen as well as manual selection of the nucleus area. The reduced (sub) datasets are produced by multiplying the RL dataset with the respective mask. The d-Pen spectral component is derived using the MCR-ALS algorithm on the reduced datasets resulting in component spectra for different cellular regions. These components show the characteristic CD vibrations and are analyzed by peak decomposition to calculate the contribution of different structural motifs.

## Supplementary Methods

### Confocal microscopy

Confocal microscopy was used to acquire a more precise spatial distribution of intracellular d-Pen. Measurements were performed on a TCS SP5 confocal microscope (Leica, Germany) with laser excitation at 405 nm (DAPI) and 561 nm (Alexa555) and a 63x, 1.2 NA water immersion objective lens. DAPI was preferred over Draq5 as a nuclear stain to prevent possible Förster resonance energy transfer. The image contrast was adjusted in ImageJ with no further processing.

### CARS microspectroscopy

Broadband CARS was used for microspectroscopy of cells as depicted in figure 4.2A. A commercial laser source (Leukos-CARS, Leukos) provides a spectrally narrow pump/probe beam ( $\lambda = 1064$  nm) and a spectrally broad Stokes beam via a photonic crystal fiber ( $\lambda = 400$ -2400 nm). The Stokes beam is filtered by a short pass filter and a Glan-Thompson polarizer to produce a bandwidth from 1100-1600 nm. The linear polarized beam had a final spectral power density of more than  $100 \mu\text{W nm}^{-1}$ . By using near-IR laser light, the potential laser damage is reduced to a level, where we do not observe behavioral changes of the specimens [269] [150]. Both beams are combined and directed to an inverted microscope (Eclipse Ti-U, Nikon) where they are focused into the sample with an objective lens (100x, NA:0.85, Zeiss) resulting in a total average laser power of 30 mW. To allow raster scanning, the sample is mounted on a xyz piezo stage (Nano-PDQ 375 HS, Mad City Labs). The created CARS signal is collected in forward direction with a second objective lens (10x, NA: 0.25, Zeiss) and the pump/probe and Stokes beams are removed by a notch (NF03-532/1064E-25, Semrock) and a short-pass filter (FES1000, Thorlabs), respectively. The CARS signal is spectrally analyzed by a spectrometer (Shamrock 303i, Andor) with attached cooled CCD camera (Newport DU920P-BR-DD, Andor) resulting in a spectral range from  $500 \text{ cm}^{-1}$  to  $4000 \text{ cm}^{-1}$  with a spectral pitch of  $\sim 4 \text{ cm}^{-1}$ . The entire setup is controlled with software written in LabView (National Instruments). Further details of this setup can be found elsewhere [241].

### Circular Dichroism Spectroscopy

Secondary structure of d-Pen was analyzed with circular dichroism spectroscopy in the range from 190 to 260 nm. Experiments were performed on a J-815 spectrometer (JASCO Inc, Easton, USA) under nitrogen atmosphere. Proteins were dissolved in phosphate buffer at pH 7.4 with 1.25 mM final concentration. For each sample, 5 spectra were taken and averaged. The secondary structure was calculated by reconstructing the data with the CDSSTR method 11 and reference dataset 7 on Dicroweb [279].

### Widefield fluorescence microscopy

To determine the course of peptide uptake, fixed adherent cells were investigated by fluorescence microscopy of fluorescently labelled d-Pen as well as DNA. Measurements were done on an Olympus Ti-81 microscope with 20x magnification.

### Synthesis of deuterated Penetratin (d-Pen)

Biotinylated lysine was bond to NovaPEG Rink Amide resin (Merck, Germany) with an initial load of 0.45 mmol/g using 20% piperidine in dimethylformamide for deprotection and 1-[Bis(dimethylamino)methylene]-1H-1,2,3-triazolo[4,5-b]pyridinium 3-oxide hexafluorophosphate (HATU) and diisopropylethylamine (DIPEA) in N-Methyl-2-pyrrolidone

(NMP) as activators. The amino acids were used with an excess of 5 in the synthesizer. To reduce the consumption of G', it was coupled manually in 3.5-fold molar excess. The final product was cleaved from the resin using a mixture of triisopropylsilane/water/trifluoroacetic acid in a ratio of (2.5/2.5/95) for 3 h. Cleavage solution was extracted with diethyl-ether prior to purification. Reversed-phase high-performance liquid chromatography (RP-HPLC) purification was performed on a Rainin Autoprep System (METTLER TOLEDO) with a Vydac 218TP152022 C18 column (15-20  $\mu\text{m}$  particle size, 300 Å pore size, 250 x 22 mm) at a flow rate of 10 ml/min. Eluates were (a) 0.1 % trifluoroacetic acid (TFA) in water or (b) 0.1 % TFA in acetonitrile. The elution gradient was successively increased every 5 minutes from 0 to 90 %. Fractions were detected using absorbance measurements at  $\lambda = 220$  nm. For further analysis the fractions were analyzed by matrix assisted laser desorption/ionization time-of-flight mass spectrometry (MALDI-TOF MS) and by analytical RP-HPLC. MALDI-TOF MS was performed on a Bruker Time-of-flight MS Reflex III mass spectrometer with  $\alpha$ -cyano-4-hydroxycinnamic acid as matrix. The mass value of the peptide was determined to 2954.9 Da (2955.6 theoretical). Analytical RP-HPLC was performed on a Hewlett-Packard 1100 liquid chromatograph equipped with a Vydac 218TP5415 C18 RP column (5  $\mu\text{m}$  particle size, 300 Å pore size, 150 x 4.6 mm). Eluents were 0.1 % TFA in water (a) or 0.1 % TFA in acetonitrile (b). The elution gradient was 0-100 % (b) in 20 min with a flow rate of 1.0 ml/min and absorbance was detected at  $\lambda = 220$  nm. Peptide stocks were made up as 20 mM solutions in water (pH 7) and kept at 4°C. Stock concentrations were determined from absorbance measurements at  $\lambda = 280$  nm ( $\epsilon_{280} = 11000 \text{ M}^{-1} \text{ cm}^{-1}$ ). For control experiments, a random peptide sequence consisting of similar amino acids as d-Pen, d-Random, including a group six jasoned deuterated glycine was synthesized in a similar way.

## Chapter 5

# Tension causes structural unfolding of intracellular intermediate filaments

by Frederik Fleissner, Noreen Klein, Daniel Wirth, Ravi Dhiman, Sachin Kumar, Dirk Schneider, Mischa Bonn and Sapun H. Parekh

*In Preparation.*

## Abstract

Intermediate filaments (IF) proteins are a class of proteins that constitute different filamentous structures in mammalian cells, including being part of the load-bearing cytoskeleton and supporting the nuclear envelope. IF proteins have been predicted to undergo secondary structural changes to compensate mechanical loads via molecular dynamics simulations, which has been confirmed by experimental *in vitro* studies. However, the response of intracellular IF secondary structure to mechanical load has yet to be elucidated. Here, we use in situ nonlinear Raman imaging combined with multivariate data analysis to quantify the intracellular secondary structure of the IF cytoskeletal protein vimentin under different states of cellular tension. We find that cells under high tension contain more unfolded vimentin IFs than chemically or physically relaxed specimens. This demonstrates that forced unfolding of IF proteins occurs intracellularly, in addition to extracellularly, and supports the notion that IF structure possibly acts as a local force sensor in the cell to mark (and sense) mechanical tension.

## 5.1 Introduction

Cell shape and structure result from a well-orchestrated balance of forces acting between the cytoskeleton, extracellular adhesions, and membrane tension [61, 280]. In mammalian cells, the cytoskeleton is the primary load-bearing unit, and it consists of the three filamentous protein networks: actin filaments, microtubuli (MT), and intermediate filaments (IFs). While the roles of actin-based networks and MT in cell mechanics and cell function have been extensively studied (reviewed in [61, 62]), the contribution of IF to cell mechanics is still relatively opaque beyond their function in bearing large tensile forces. Of the cytoskeletal networks, IF constituent proteins have the unique feature of undergoing molecular structural changes in response to external loads, as shown by single molecule experiments and molecular dynamics simulations [7, 32, 33, 39]. This structural polymorphism has led to the hypothesis that IFs may play a role in intracellular mechanotransduction - relaying information about the cell's mechanical state into biochemical changes that influence cell shape [8, 38, 281] and phenotype [282]. IF proteins are 45 nm long [283], and crystal structure analysis show that they consist of more than 60%  $\alpha$ -helical secondary structure [137, 284]. They self-assemble into hierarchical networks with fibers consisting of apolar filaments, and they form quite diverse networks that have location-specific architectures and composition in cells [38]. Vimentin is one IF protein that forms cytoplasmic IF networks and is a particularly interesting because of its important role in cell adhesion, mechanics [70, 122, 285] migration and signaling in mesenchymal cells [38, 286]. Moreover, vimentin has been established as a marker of epithelial to mesenchymal transitions (EMT) in embryogenesis and in tumor metastasis as the cytoplasmic IF network in epithelial cells consists of mostly keratin that is converted to a vimentin-rich IF network during EMT [5, 8, 287, 288]. Studies of IFs mechanics have revealed a complex multi-regime response to deformation, which has been extensively studied in simulation [7, 30, 37] and experimentally *in vitro* [33, 39]. By simulating the vimentin central coiled-coil domain under tensile load, a hierarchical strain response was found. The coiled-coil is initially linear elastic, as only hydrogen bonds are stretched, until the strain exceeds a critical range. For higher strains, hydrogen bonds break and a sequential unfolding from the coiled-coil  $\alpha$ -helical structure into anti-parallel beta-strand structure occurs, where the strands arrange along the axis of the molecule [7]. Via this mechanism, each molecule can extend to a multiple of its initial length without breaking. Finally, when no further structural transition is possible to compensate for the load, strain hardening sets in caused by stretching of covalent peptide bonds together with uncoiling of the coiled-coils [7, 30]. Studies by

Fudge *et al.* [6] and Pinto *et al.* [289] on hagfish slime, which consists of keratin IFs, used X-ray diffraction and WAXS to show that indeed additional  $\beta$ -sheet signatures appeared in tensed samples. Infrared spectroscopy on horse hair, again consisting of mostly keratin IF, also showed an increased contribution from  $\beta$ -sheets under tensile strain [290]. While these studies clearly showed molecular structural transitions of IF proteins under tension *in vitro*, it is unclear if such transitions occur within the cellular IF network where the cellular environment can clearly modify cytoskeletal mechanics [291]. Few experimental methods are available that allow the analysis of intracellular protein structure. Forster Resonance Energy Transfer (FRET) sensors can be used to selectively measure intramolecular distances that can then be correlated to tension acting on the target protein [89, 292]. However, this approach is difficult to realize in bundle-forming filaments where cross-talk between neighboring dye molecules is possible [293, 294]. Cys-shotgun labelling of exposed cysteines is another method, introduced by Discher and colleagues, to show that IF proteins undergo conformational changes in response to cell tension by exposure of otherwise buried cysteines [295, 296]. However, both FRET and Cys-shotgun labeling methods are unable to probe a protein's secondary structure, which is necessary to rationalize if the *in vitro* load bearing mechanism involving structural transitions is relevant for intracellular IF networks. Protein secondary structure can be probed by in a noninvasive way using vibrational spectroscopy such as infrared or Raman spectroscopy [56]. Depending on the local hydrogen-bonding pattern (i.e. secondary structure), the atoms in the protein backbone (C=O vibrations in peptide bonds) show molecular vibrations at different vibrational frequencies, resulting in shifted Raman peaks in the Amide I region of the vibrational spectrum [55, 266, 297, 298]. This link between protein structure and spectral response can be exploited to determine the average secondary structural composition within the probed volume with high accuracy using quantitative spectral decomposition [55]. In this work, we use a nonlinear spectroscopic imaging method called broadband coherent anti-Stokes Raman scattering (BCARS) microscopy, a nonlinear analogue of Raman spectroscopy, taking advantage of the improved acquisition speed and reduced out-of-focus signal contribution. BCARS spectra can be converted into Raman-like (RL) spectra that reflect the same underlying information as a linear Raman spectrum [298], particularly as related to protein secondary structure determination [18, 269]. In this study, we investigated if tension-induced secondary structural transitions of vimentin IF occurs in adherent cells using hyperspectral vibrational microscopy with sub-micrometer spatial resolution. BCARS microscopy combined with isotope-substitution and a multivariate analysis protocol was used to resolve protein secondary structure from vimentin within cells. By exploiting the unique spectral features from isotopically-labelled vimentin to distinguish the vimentin Raman signal from the cellular background, we isolated the spectral fingerprint of deuterated vimentin in cells and calculate its secondary structure for cells in different tensile states. Our results show that cellular tension is sufficient to alter the secondary structure of intracellular vimentin IFs, resulting in more  $\beta$ -sheet content with increasing tension, consistent with previous *in vitro* observations and computational predictions.

## 5.2 Results

Since mechanical deformation has previously been shown to cause structural transitions in IF-composed structures (hagfish slime and hair) *in vitro* with X-ray scattering and infrared spectroscopy [6, 290], we initially tested how mechanical deformation affects the secondary structure of vimentin IFs when it is polymerized *in vitro*. Using a micromanipulator on our nonlinear Raman (BCARS) microscope (see methods for details), we acquired BCARS spectra from relaxed and physically tensed vimentin fibers (Fig.5.1A and B). Upon visual inspection of the Amide I region of the RL-spectra (Fig.5.1C), which is sensitive

to secondary structural motifs, clear spectral changes are observed between the relaxed and tensed vimentin IF bundles (Fig.5.1C). Spectral decomposition of the Amide I region using known peak shapes and locations for  $\alpha$ -helices,  $\beta$ -sheets and random coil (rc) motifs allow calculation of the average secondary structure [55, 267]. The relaxed vimentin IF bundles - with a sharp peak at  $\sim 1650\text{ cm}^{-1}$  - show predominantly  $\alpha$ -helical structure (64 %  $\alpha$ -helix, 15 %  $\beta$ -sheet and 21 % rc) after decomposition, which compares favorably to circular dichroism data from Meier *et al.* [299]. On the other hand, tensed samples - with a broadened (more disordered) and blue-shifted Amide I band indicate a more  $\beta$ -sheet structure and show reduced helicity (40%  $\alpha$ -helix, 32 %  $\beta$ -sheet, 27 % rc), consistent with that from Kreplak and coworkers [33].

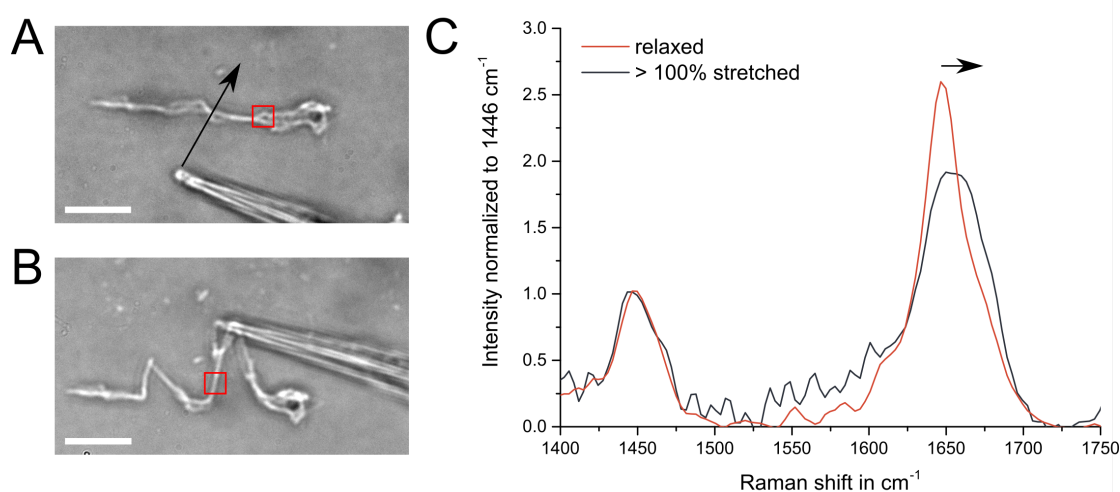


**Figure 5.1:** *In vitro* deformation experiments of Vimentin hydrogels show protein unfolding. A) Bright field microscopy image of a polymerized IF filament bundle settled on a cover slip surface. A glass capillary mounted on a micromanipulator is threaded below the filament and moved along the plane as indicated by the arrow for pulling. B) The filament bundle stretches out and stays under tension also visible by bending of the capillary tip. Scale bars in both images represent  $10\text{ }\mu\text{m}$  and the filament bundle diameter was found to be  $\sim 0.5\text{ }\mu\text{m}$ . The filament region probed by BCARS is indicated as red square. C) RL spectra of relaxed and more than 100 % strained vimentin filaments showing clear changes in the Amide I region ( $1600\text{--}1680\text{ cm}^{-1}$ ) from a narrow band at  $1640\text{ cm}^{-1}$  (assigned to  $\alpha$ -helical structure) to a red-shifted and broadened band indicating the presence of additional  $\beta$ -sheet and rc structure under load. Spectra were normalized to the  $\text{CH}_2$  deformation mode at  $1446\text{ cm}^{-1}$ .

While the changes in the Amide I band in purified, reconstituted vimentin IF networks can be unequivocally attributed to changes in vimentin structure under strain, attributing a particular Amide I spectral change as coming from a specific protein within a cell is very difficult. Cells are full of thousands of different proteins with a total protein concentration of  $\sim 200\text{ mg/mL}$  [12], and each protein contains very similar (and overlapping) vibrational moieties. Thus, the spectra from any location inside a cell will consist of the sum of all proteins within our excitation volume ( $0.4 \times 0.4 \times 5\text{ }\mu\text{m}^3$ ), making it nearly impossible to produce vibrational fingerprints from a specific protein in the cell. It is therefore necessary to separate the contribution from the target protein, in this case vimentin, and the remaining cellular background. A convenient way to create spectral contrast with minimal perturbation is stable isotope substitution such as when hydrogen ( $^1\text{H}$ ) is replaced by deuterium ( $^2\text{H}$ ), as is commonly done in NMR spectroscopy.

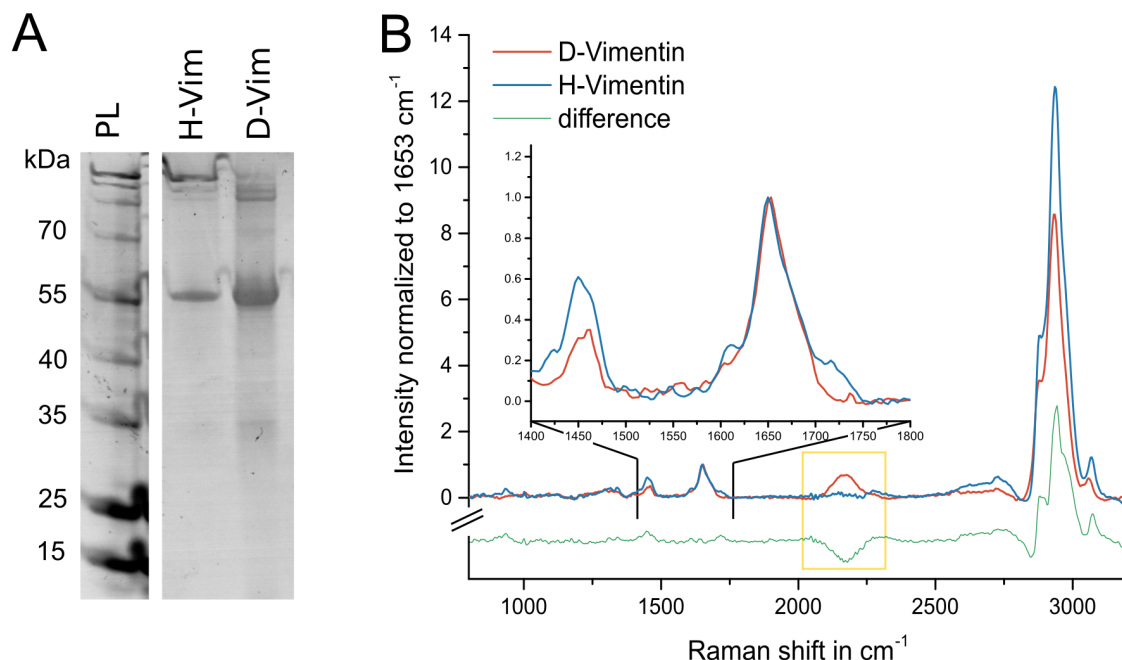


**Figure 5.2:** Characterization of deuterated Vimentin. A) Coomassie-stained SDS-PAGE gel of native vimentin (Vim) and vimentin produced from deuterated acetate (d-Vim) showing similar molecular weight at 54 kDa. The first lane shows the prestained protein ladder. B) RL spectra of native vimentin and d-Vim. The spectra are normalized to the peak intensity at  $1653\text{ cm}^{-1}$ , assumed to be independent of the deuteration. For d-Vim the RL spectra shows an additional vibrational band centered at  $2150\text{ cm}^{-1}$  originating from the CD modes. At the same time, the CH band ( $2800\text{--}3100\text{ cm}^{-1}$ ) and the  $\text{CH}_2$  deformation mode at  $1450\text{ cm}^{-1}$  appear with a reduced intensity compared to native vimentin as indicated in the difference spectrum. The Amide I band, reflecting the protein  $\text{C}=\text{O}$  backbone vibration, is identical for both proteins.

We produced a recombinant, isotopically-substituted vimentin in bacteria that were grown in M9 medium containing deuterated sugar as the carbon source (see Methods). This resulted in partial deuterium-hydrogen exchange for all amino acids in the protein as confirmed by mass spectrometry (see SI, Fig.5.7). The molecular weight of the deuterated vimentin was only slightly increased (by at most 3.7 kDa in case of 100 % D-H exchange) compared to the native human vimentin protein (54 kDa), which was undetectable via SDS-PAGE (see Fig.5.2A and SI Fig.5.11). The functionality of the protein was confirmed by successful *in vivo* polymerization (see SI Fig.5.10). Figure 5.2B shows the RL spectra of normal vimentin (Vim) and deuterated vimentin (d-Vim) in polymerized vimentin fibers. The additional peak at  $2150\text{ cm}^{-1}$  in d-Vim shows the unique carbon-deuterium (CD) spectral feature in the so-called vibrational quiescent region, which - as will be shown below - allows for uniquely identifying signals coming from d-Vim compared to the intracellular cytosolic protein pool due to low natural abundance of deuterium. Moreover, the Amide I region ( $1550\text{--}1700\text{ cm}^{-1}$ ) appears to be almost identical for d-Vim and Vim, indicating: 1) that hydrogen-deuterium exchange on NH groups in peptide bonds was minimal or rapidly exchanged in our hydrogen-based buffers and 2) the secondary structure of d-Vim was the same as Vim. We note that even though d-Vim was produced recombinantly from a nearly 100 % deuterated carbon source as described by Paliy [205], deuterium incorporation into the protein was clearly not 100 %. Strong CH signals from the protein were still observed in the RL spectrum of d-Vim (Fig.5.2B, red). The observed carbon-hydrogen bonds in d-Vim likely result from hydrogen-deuterium exchange during protein production since we used  $\text{H}_2\text{O}$ -based M9 medium and  $\text{H}_2\text{O}$ -based buffers after purification [300]. To investigate spectral features of vimentin intermediate filaments in cells, we successfully incorporated recombinantly produced d-Vim into HeLa cells following the protocol illustrated in figure



5.3A-D. First, the native IF network was depolymerized by addition of cycloheximide (see methods and SI Fig.5.8 and 5.9) [126]. Then, recombinantly produced d-Vim monomers were microinjected into the cells (d-Vim = 2 mg/mL) [301], and re-formation of IF network was induced by changing back to cycloheximide-free medium. After 12 hours of incubation in normal growth medium, the IF network recovered, and d-Vim showed successful copolymerization into the cellular vimentin IF network (see SI, Fig.5.10). Following this protocol should result in a cellular vimentin network containing d-Vim and Vim and show a CD vibration in the silent region of the RL spectra, which can, in principle, be used to localize d-Vim in the cell. A similar approach using CD isotope localization has been used to identify newly synthesized protein in cells [270,271] and for tracking cell penetrating peptides in cells [18,183]. As expected, we observed the unique CD vibration (at  $\sim 2200\text{ cm}^{-1}$ ) from d-Vim when it was sufficiently concentrated in fibers in injected cells (Fig.5.3E). This signal could be used to create contrast showing the concentration of d-Vim throughout the cell, which is clearly different than the distribution of all proteins in the cell (Fig.5.3 F and G).

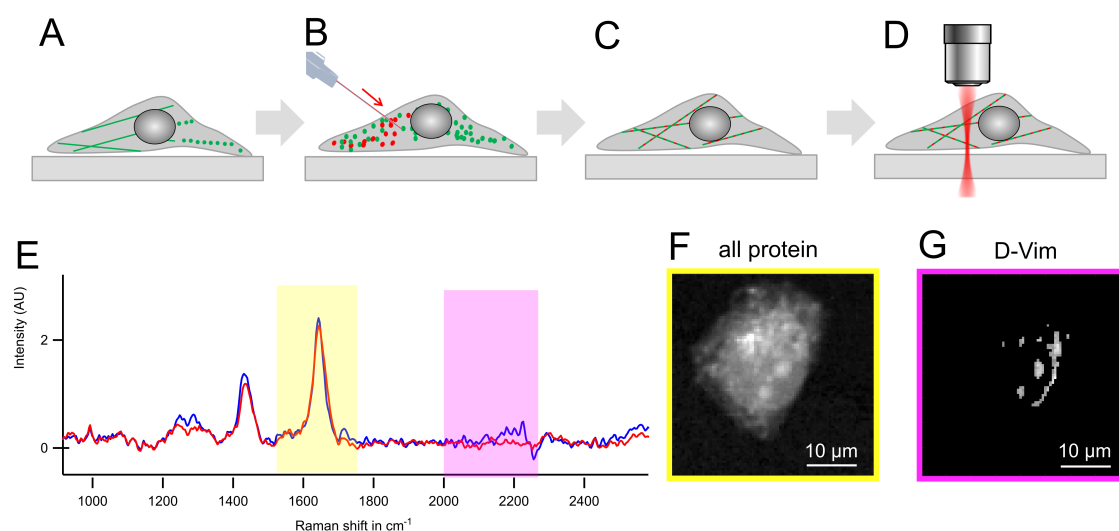


**Figure 5.3:** Deuterated vimentin creates label-free contrast within cells. The native IF network of adherent HeLa cells (depicted in green) is depolymerized by treatment with cycloheximide (A) and deuterated vimentin of high concentration (1.8 mg/ml, red) is injected (B). After incubating overnight, d-Vim is incorporated in the reformed IF network (C) and cells were fixed. Cell samples were then imaged by hyperspectral BCARS microscopy to obtain local chemical information (D). E) RL spectra obtained from two different cell locations show differences in the silent region resulting from additional molecular vibrations from the CD bonds of d-Vim. F) The total protein distribution within a cell measured by the integrated intensity of Amide I band (yellow region in E) in each spatial pixel. G) The d-Vim distribution for the same cells in F integrated over CD region (purple region in E) in each spatial pixel. The scale bars are 10  $\mu\text{m}$ .

With a method to incorporate d-Vim into the cellular IF network, combined with our previously developed analysis protocol to isolate the spectral response of isotope-labelled proteins in cells [18], we can proceed with our primary goal of determining if mechanical perturbations alter intracellular vimentin secondary structure. To that end, we manipulated the mechanical state of d-Vim-injected HeLa cells both physically and biochemically by culturing cells on soft substrates and with drug treatments that interfere with cell-generated tension, respectively. Mesenchymal cells grown on glass substrates, which can be assumed as infinitely rigid, are known to be in a tensed equilibrium between adhesion

and traction forces [93, 302]. Confocal microscopy of HeLa cells grown on collagen-coated glass expressing GFP-tagged vimentin revealed that the IF network was laterally sprawling and occupied a large area, and cells showed a typical fried egg-like appearance (Fig. 5.4A and B). Vimentin filaments formed a perinuclear cage and spread out toward the cell periphery.

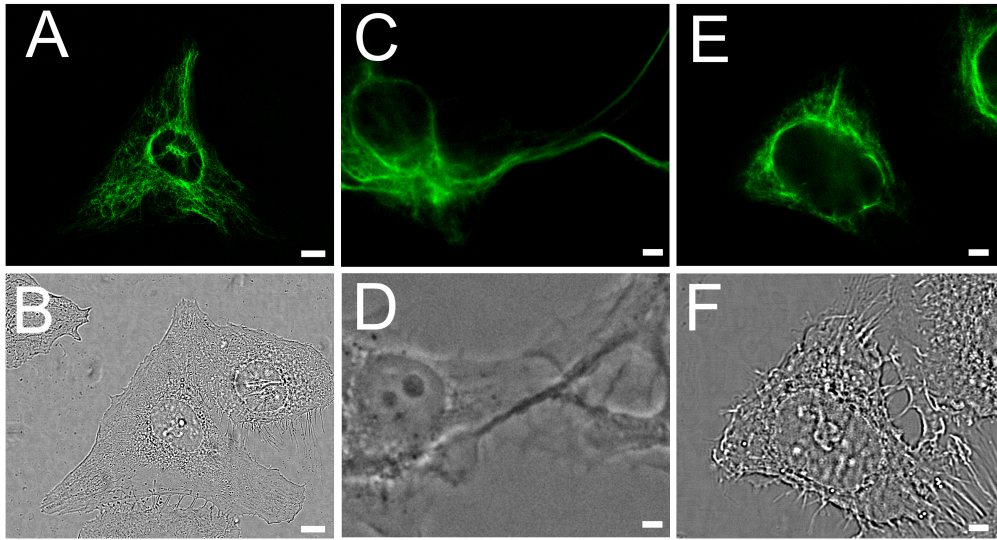


**Figure 5.4:** Architecture of the IF network is altered by substrate stiffness and drug treatment. Confocal microscopy images of GFP-tagged vimentin (A,C,E) expressing HeLa cells and brightfield images showing cell morphology (B,D,F). A,B) Control cells on collagen-coated glass substrates are well spread with a broad vimentin network. C D) Blebbistatin treatment of cells on collagen-coated glass causes cells to round up and shrink, and the vimentin IF network becomes less sprawling and more bundled. E,F) Cells grown on a collagen-coated soft substrate (0.1 kPa polyacrylamide) are rounded up compared to control cells on glass and showed a collapsed vimentin IFs as a perinuclear bundled network. All images were taken from imaging planes below the nucleus. Scale bars are 10  $\mu\text{m}$ .

In two-dimensional cell culture, intracellular tension is produced by myosin-based contraction of actin stress fibers. To investigate relaxed vimentin IFs, we treated cells grown on collagen-coated glass with blebbistatin, a non-muscle myosin II inhibitor. The drug inhibits ATP hydrolysis and thereby blocks myosin contraction [123], resulting in relaxation of cell-generated tension. Figures 5.4C and 5.4D show HeLa cells grown on glass substrates treated with blebbistatin. Treated cells partially rounded up, a hallmark of non-muscle myosin II contraction inhibition, compared to those without blebbistatin; the vimentin IFs (Fig. 5.4C) appeared wavy and less sprawled than before the treatment but still spanned large distances within the cytosol. From previous studies, it is also known that substrate stiffness regulates cellular tension [1, 303]. As an alternative to chemically reducing the tension, we cultured cells on collagen-coated soft substrates (0.1 kPa polyacrylamide gels) to again reduce the cell-exerted tensile forces. HeLa cells on soft substrates exhibited an altered morphology with a more perinuclear vimentin network and compact shape (Fig. 5.4E and F) compared to the cells grown on glass (Fig. 5.4A and B).

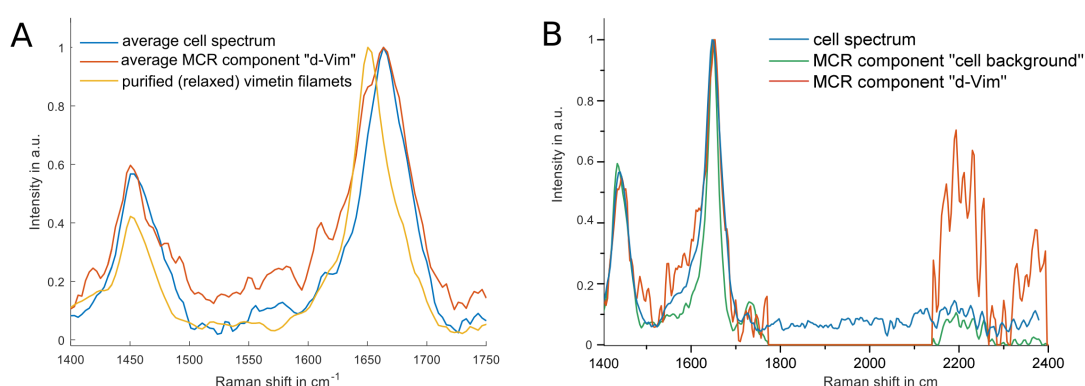


**Figure 5.5:** Separation of the vimentin component by multivariate curve resolution. A) Spectra showing the Amide I region of the entire cell (blue) and the MCR derived d-Vim component averaged over the group of cells grown on glass without further treatment (red). For comparison, the average spectrum from pure vimentin polymerized *in vitro* (yellow) is depicted. B) Representative average cell spectrum (blue) and derived MCR components assigned to the cell background (green) and d-Vim (red) from a single cell grown on glass.

Having multiple ways to affect cell mechanics, we investigated the influence of cellular tension on vimentin secondary structure by comparing the shape of the Amide I vibration in the derived d-Vim RL-spectra from cells that were grown on glass and cells being physically or chemically relaxed as described above. For each group, we acquired hyperspectral BCARS images of individual cells. Each data set covered an area of  $40 \times 40 \mu\text{m}$  and at most one cell with a step size of  $0.5 \mu\text{m}$  per spatial pixel. After retrieval of the RL spectra, the data was thresholded to retain pixels showing sufficient CD intensity, and the component spectrum of d-Vim was derived via multivariate curve resolution (MCR) in the same method that we previously established (see methods and the previous chapter 4 for detailed explanation). Exemplary spectra from this process and the d-Vim and cell background component spectra can be found in the supplementary information (see SI Fig.5.14, 5.15, 5.16, 5.17). The spectra in figure 5.5A show the Amide I spectrum averaged over all cells and the average MCR-derived d-Vim component both from all control cells on collagen-coated glass along with the spectrum from purified, (relaxed) *in vitro* polymerized vimentin fibers. Figure 5.5B shows single cell spectra for the MCR-derived d-Vim component, the MCR-derived cell background component, and the spectrum averaged over the entire cell. The CD band ( $\sim 2200\text{-}2400 \text{ cm}^{-1}$ ) is much larger in the MCR-reconstructed spectrum for d-Vim (Fig.5.5B, red) compared to the cell background or cell average spectrum, as expected. Complete average spectra for each MCR-derived component for each cell group (control, soft gel, and blebbistatin-treated) are shown in the SI (Fig.5.15, 5.16, 5.17), and all clearly show a dominant CD vibration in the d-Vim component (or lack thereof in the cell background component), demonstrating specificity / accuracy of the spectral reconstruction. The d-Vim component spectrum for cells grown on glass (Fig.5.5A, red) shows a different spectral pattern compared to purified, *in vitro* vimentin polymerized into filaments (Fig.5.5A, yellow). While the  $\text{CH}_2$  stretching vibration at  $1450 \text{ cm}^{-1}$  is conserved in the same location and width for both cases, the shape and maximum of Amide I band was altered in cells grown on glass. Changes in the Amide I band shape of the MCR-derived d-Vim component show different structural compositions of d-Vim. The peak maximum for the Amide I band was shifted from  $1650 \text{ cm}^{-1}$  for *in vitro* vimentin to  $1663 \text{ cm}^{-1}$  for the intracellular d-Vim MCR-derived component spectrum, indicating that the protein was more unfolded into  $\beta$ -sheets. The peak maximum of the Amide I region for the average cell spectrum (Fig.5.5A, blue) coincided with that of the d-Vim component; however, the Amide I band of this spectrum was to some degree narrower

than the d-Vim component, indicating a greater heterogeneity in vimentin compared to the average protein composition of the cytosol in the same voxels.

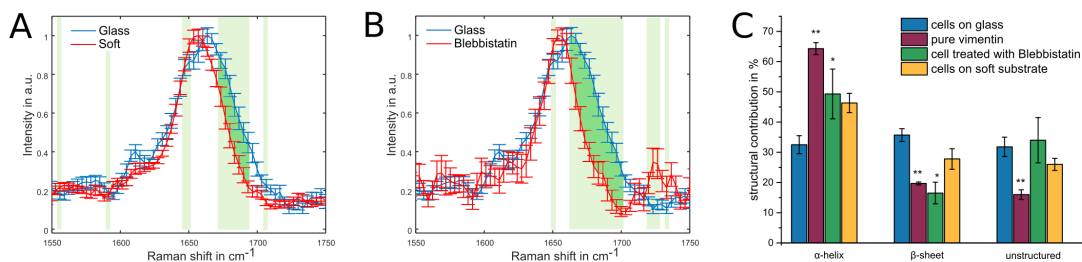


**Figure 5.6:** Vimentin structure is affected by cellular tension. Spectral analysis of cell groups of different intracellular stress shows changes in the Amide I region indicating differences in structural composition. A) Average of the Amide I bands from MCR-derived d-Vim spectra of cells grown on glass substrates (blue,  $n=14$ ), and after blebbistatin treatment (red,  $n=7$ ). B) Average of the Amide I bands from MCR-derived d-Vim spectra of cells grown on glass substrates (blue), and cells grown on soft substrates (red,  $n=17$ ). Error bars are standard error of the mean (SEM) for each spectral point in B and C. Statistically significant differences groups in B and C are shown by light green boxes. Dark green shades depict reductions in  $\beta$ -sheet and random coil contributions. C) Secondary structure content of vimentin from spectral decomposition of the Amide I band (either from pure vimentin filaments or the MCR-derived component). Error bars are standard deviation from the stated number of samples. Statistically significant differences between cells on glass and other groups from two sample t-tests are indicated as (\*) for  $P \leq 0.05$  and (\*\*) for  $P \leq 0.01$ .

To determine if cellular tension affected the structure of intracellular vimentin, we compared the average MCR-derived d-Vim Amide I spectrum from cells cultured on collagen-coated glass and treated with blebbistatin to control cells grown on the same substrates in normal medium (Fig.5.19 and 5.20). Treatment with blebbistatin resulted in a red-shifted, narrower Amide I band that was centered at  $1652 \text{ cm}^{-1}$  (Fig.6A), indicative of a greater  $\alpha$ -helical (native) structure and significantly lower contributions from the  $\beta$ -sheet structures compared to control cells on glass. In addition, the d-Vim component spectrum from cells treated with blebbistatin had a narrower Amide I region compared to the d-Vim peak from cells on glass (Fig.5.6A), similar to the purified vimentin spectrum in figure 5.5A (yellow). Similar to cells treated with blebbistatin, cells cultured on soft substrates, also coated with collagen, showed a weaker intensity at the blue shoulder (high wavenumber side) of the Amide I band, with significantly lower peak intensities from  $1660\text{--}1680 \text{ cm}^{-1}$  with respect to control cells on glass and an Amide I center frequency of  $1654 \text{ cm}^{-1}$  (Fig.5.6B). These changes again indicate that vimentin is more natively (helically) structured when tension was reduced. Comparing the MCR-derived d-Vim component spectra for cells from each sample group, we find statistically significant differences ( $P < 0.05$ ) when comparing cells with reduced tension (either with blebbistatin or cultured on soft substrates) against those grown on glass with 'native' cytoskeletal tension. Statistically significant differences for each spectral position by two-sample t-tests are shown in figure 5.6A and B with light green boxes. In order to quantify the altered Amide I line shape and relate these changes with d-Vim protein structure, we decomposed the MCR-derived d-Vim Amide I band from each cell. Figure 5.6C shows the resulting average contributions (and standard deviations) of  $\alpha$ -helical,  $\beta$ -sheet and random coil structure for all groups, as well as for pure vimentin. The spectral decomposition can be found in the supplementary information 5.19 and 5.20). While *in vitro* polymerized vimentin is found to be predominantly  $\alpha$ -helical (64 %), consistent with previous results [299] and our own circular dichroism (see SI Fig.5.21), the amount of helix structure is only 33 % for intracellular vimentin from cells grown on glass. With a lowering of the helical content in cells, the calculated contribution for  $\beta$ -sheet showed the opposite trend - being 36 % for cells on glass compared to 20% for

pure vimentin. Both chemical and physical relaxation of cells resulted in an intracellular structure of vimentin that was more helical (and less unfolded into  $\beta$ -sheets), similar to pure vimentin. We found that for cells treated with blebbistatin, vimentin is on average 49 %  $\alpha$ -helical and 17 %  $\beta$ -sheet structure while for cells grown soft substrates the structural composition is 46 %  $\alpha$ -helix and 27 %  $\beta$ -sheet. The content of unstructured vimentin was found to be similar for all groups of cells, indicating that the relaxation of cell tension did not affect random coil segments of vimentin. However, the amount calculated for cytosolic vimentin was significant higher than for *in vitro* polymerized vimentin.

### 5.3 Discussion

In this work, we demonstrated *in situ* measurements of intracellular vimentin molecular structure in HeLa cells under different cellular tensions. Microscopic pulling on purified vimentin filaments adhered to a coverslip resulted in a clear change in its Raman signature, showing a conformational change under load. This is consistent with previous results from MD simulations [7, 30, 37] and force-strain experiments [33, 39]. Because unfolding has been purported to start at  $\sim 20\%$  strain [30], the applied strain of more than 100% of the initial filament length likely caused most vimentin molecules in the stretched bundle to undergo a transition from  $\alpha$ -helical to  $\beta$ -sheet (and even into a random coil) structure. The influence of cell-generated mechanical tension on vimentin secondary structure was measured by modulating the mechanical state of cells chemically or physically and using BCARS vibrational imaging of recombinantly produced, and microinjected, deuterated vimentin (d-Vim) that incorporated into the cellular vimentin network. We used the BCARS hyperspectral datasets to derive cell-averaged spectra of d-Vim that was incorporated (and sufficiently concentrated) in intracellular vimentin IFs from cells under different tensile states. Employing our developed chemometric spectral analysis protocol not only yielded a unique d-Vim component [18], but also a 'cellular background' component of non-d-Vim proteins from the same spatial pixels in each cell. We found the average cellular spectrum (Fig.5.14) and the cellular background (non-d-Vim) component for cells under all conditions were largely statistically identical - most importantly in the Amide I region - indicating that the d-Vim component we extracted accurately reflects the d-Vim spectral fingerprint. Nevertheless, given the nature of vibrational spectroscopy and the data processing route used here, we cannot exclude the possibility that proteins which are highly spatially correlated - i.e. always bound to d-Vim such as native vimentin, also contribute to the extracted d-Vim spectral component. From our spectral decomposition of the extracted d-Vim component we found that control cells grown on collagen-coated (rigid) glass substrates, and therefore highly tensed, exhibited a d-Vim component that was structurally perturbed compared to polymerized, (relaxed) vimentin *in vitro* (Fig.5.5A). Furthermore, our data show that a reduction of cellular tension by either reducing the substrate stiffness or deactivating traction force generation through blebbistatin inhibition of acto-myosin contraction led to a more native ( $\alpha$ -helical) d-Vim component spectrum (Fig.5.6A and B). While other studies have demonstrated that IF filaments undergo an  $\alpha$ -to- $\beta$  transition *in vitro* [6, 33], our study directly shows that unfolding of vimentin's  $\alpha$ -helical structures under force occurs within cells. Intracellular vimentin in cells treated with blebbistatin was previously found to have higher accessibility to Cys-selective labels compared to tensed cells [295]. Our findings are loosely consistent with those from Johnson *et al.* in that we also observe that vimentin undergoes a conformational change in tensed versus relaxed cells; however, in contrast to what they showed, we find vimentin secondary structural transitions ( $\alpha$ -to- $\beta$ ) occur to a lesser degree - not greater degree - under tension-reducing blebbistatin treatment. The results from Johnson *et al.* state the reason for increased signal in the Cys-shotgun approach was

due to blebbistatin-induced depolymerization of vimentin IFs. Our results from GFP-fluorescence vimentin imaging do not indicate vimentin IF depolymerization in cells after treatment with blebbistatin at 50  $\mu\text{M}$  concentration for 12 hours (Fig.5.4E). Moreover, experiments done with *in vitro* polymerized vimentin fiber bundles also showed no effect of blebbistatin on vimentin morphology (see SI 5.21) nor on their vibrational spectrum, particularly in the Amide I region. Taken together, our findings are in line with previous studies that use blebbistatin as a selective drug only inhibiting myosin but not affecting IF or microtubules [304,305]. Importantly, our result showing more helical (natively folded) vimentin structure in blebbistatin-treated cells was further underscored by a similar finding when culturing cells on soft substrates, which is also well known to reduce traction forces in adherent cells [118].

The consistency of these results points to the idea that cell-generated tension puts intracellular vimentin IFs under large, finite forces that results in changes to the secondary structure of the protein in the IF network. Unfolding of coiled-coil regimes of proteins is believed to be a fundamental force-response mechanism in nature [28,32]. Such a mechanism endows a material with tunable elasticity of being soft at low tensions, which are presumably more frequent, while becoming nonlinearly stiffer at larger tensile forces (at large deformations). Previous work on fibrin, the blood clot forming protein with similar features to vimentin: an elongated molecule with coiled-coil motifs ( $\sim 45$  nm long [9,283]) that takes an initial helical structure and unfolds into sheets under tension, has suggested that the conformational changes effectively delay nonlinear stiffening to larger strains in order to retain structural integrity [9]. For vimentin IF, a similar role as the flexible part of the cytoskeleton that strain hardens at very large strains has also been proposed [27,38]. In addition to endowing vimentin IF with larger extensibility, IF protein unfolding in cells may play a role in mechanosensing. Early work by Fudge *et al.* on hagfish slime led to the initial suggestion that formation of  $\beta$ -sheets within IFs might act as a sensor for local tension. Such a conformational change in consequence of load was proposed to possibly start a binary signaling cascade for cytoskeletal repair or apoptosis [6]. Mechanical tension, and the resulting conformational changes, are known to inhibit phosphorylation of the intermediate filament protein lamin-A in the nuclear envelope [296]. Taking the structural similarities between lamin-A and vimentin into account, we suggest that a similar mechanism could take place within the cytoplasmic vimentin IF network. The results shown here indicate that vimentin in IFs, when cellular tension is high, is partially unfolded. This could lead to reduced vimentin phosphorylation and reduced IF disassembly [306,307]. Evidence for phosphorylation-influenced vimentin IF stability was shown by increased assembly from vimentin monomers into IF under dephosphorylated conditions in cultured cells [307]. In this model, only IF filaments that bear no tensional loads would be phosphorylated, depolymerized, and recycled elsewhere whereas tensed vimentin fibers would be protected from degradation as they are required to maintain mechanical integrity of the cell. This mechanism supports the 'use-it-or-loose-it' module proposed by Dingal and Discher for filamentous coiled-coil proteins [308]. Efforts are underway in our lab to observe spatially-resolved structural changes in vimentin as this could reveal intracellular mechano-chemical coupling at the molecular level.

## 5.4 Conclusion

The impact of cellular tension on intracellular vimentin IF secondary structure was investigated by quantitative, protein-specific vibrational microscopy. We used isotope-substitution combined with multivariate data analysis to isolate the unique isotope-substituted spectral fingerprint of deuterated vimentin from the background cellular protein signal and accurately reconstructed the vibrational spectrum of intracellular, deuterated vimentin.



These spectra contained information on the secondary structure of vimentin within cells, and by changing the intracellular tension either pharmacologically or by growing cells on soft substrates, we found that high cellular tension showed substantially more unfolded vimentin IFs from native  $\alpha$ -helices into  $\beta$ -sheets. Our findings show that the  $\alpha$ -to- $\beta$  transition of IF occurs within cells and such a transition could allow vimentin to potentially act as a local force sensor in the cytoskeleton.

## 5.5 Methods

### Protein expression and purification

A plasmid for human Vimentin containing a C-terminal His-tag (EX-D0114-B31, tebu-bio, Germany) was transformed into chemical competent *E. coli* BL21-Gold cells. To produce deuterated vimentin, we used deuterated sodium acetate-d<sub>3</sub> (Sigma-Aldrich) as the only carbon source while expressing in M9 minimal medium. For non-deuterated vimentin, LB medium was used for expression with no further changes to the following steps. Bacteria were grown as a pre-culture overnight in ampicillin (100  $\mu$ g/ml) containing LB-Medium and washed several times in M9 medium before inoculating the production culture 1:40. The growth medium contained 4 g/L deuterated sodium acetate in M9 minimal medium and ampicillin (100  $\mu$ g/ml). After an optical density at 600 nm (OD) of 0.8 was reached, the protein expression was induced by addition of 500  $\mu$ M IPTG followed by incubation overnight. Cells were harvested the next day by centrifugation (6000 g, 10 min, 4 °C). The pellet resulting from 1 L expression culture was resuspended in 40 mL resuspension buffer (50 mM Phosphate, 300 mM NaCl, 10% glycerol, pH = 8.0). Cells were disrupted on ice by sonication (Omni Sonic Ruptor 400, Omni) and inclusion bodies were separated by centrifugation (30 min, 6000 g, 4 °C). Next, the inclusion bodies were solubilized in lysis buffer (100 mM NaH<sub>2</sub>PO<sub>4</sub>, 10 mM Tris-HCl, 8 M Urea, 150 mM NaCl, pH = 8.0) for 3 h at room temperature. Cell residues were removed by centrifugation (15 min, 6000 g, 20 °C) and the supernatant was incubated overnight with 1 mL Ni-NTA agarose suspension at 4 °C. The solution was centrifuged (3 min, 800 rpm, 20 °C) and the pellet resuspended in 5 mL of the supernatant and loaded onto an empty column. The Ni-NTA-agarose was then washed four times using 5 mL wash buffer (100 mM NaH<sub>2</sub>PO<sub>4</sub>, 10 mM Tris-HCl, 8 M Urea, 150 mM NaCl, pH = 8) with increasing imidazole concentration (0, 5, 10, 15 mM). Vimentin was eluted twice from the column with 1 mL 400 mM imidazole in 100 mM NaH<sub>2</sub>PO<sub>4</sub>, 10 mM Tris-HCl, 8 M Urea, 150 mM NaCl, pH = 8.0. The fraction containing the target protein was dialyzed against a series of buffers with decreasing urea concentrations (6, 4, 2 M urea in 5 mM Tris-HCl, 1 mM DTT, pH = 8.4) at 4 °C for 1 h each, followed by an additional dialysis against fresh buffer (5 mM Tris-HCl, 1 mM DTT, pH = 8.4), which did not contain any urea, overnight at 4 °C. The final solution was checked by SDS-PAGE and Coomassie-staining showing only a protein band at 54 kDa as indicated by a protein ladder (PageRuler Prestained, Thermo Scientific).

### *In vitro* stretching of IF

Vimentin IFs were polymerized *in vitro* by addition of 170 mM final concentration NaCl into vimentin monomer solution (1.2 mg/ml) [309]. Filaments were formed within 2 h at 37 °C. The IF containing solution was pipetted onto a cover slip and filaments (and bundles) were allowed to settle onto the glass surface. Next, attached filaments were deformed by gently pulling with a glass capillary (Femtotip, Eppendorf) mounted to a micromanipulator (Injectman II, Eppendorf).

## Cell culture

HeLa-GFPvim cells, expressing vimentin with a GFP tag were produced by lentiviral transfection (LentiBrite GFP-Vimentin Lentiviral Biosensor, Merck Millipore) of HeLa cells. To establish a strain with sufficient high (>60% of cells) expression rate of GFP, the cells were sorted by fluorescence-activated cell sorting. For all microscopy imaging experiments, HeLa-GFPvim were grown in collagen-coated glass bottom dishes (MatTek) and in culture medium (Dulbecco's Modified Eagle's Medium + 10% fetal calf serum, Dulbecco) containing 100 U/ml Penicilium and 100  $\mu$ g/ml Streptomycin (Gibco).

## Disruption of native IF cytoskeleton

To achieve a homogenous incorporation of deuterated vimentin, the native IF network was depolymerized by cycloheximide prior to microinjecting. This treatment is known to alter only the IF network while actin stress fibers and microtubuli remain unaffected [46]. Cyclohexamide (ready made solution in DMSO, Sigma Aldrich) was diluted in DMEM containing 10% FCS to a final concentration of 10  $\mu$ g/ml and cells were let incubate in for 6 h at 37°C, 5 % CO<sub>2</sub> and 95 % relative humidity. The IF depolymerization is reversible within 12 h after changing back to normal conditions. Successful disruption was checked by fluorescence microscopy (see SI 5.9).

## D-Vim microinjection

For microinjection, the cell medium was changed to 4°C cold Leibovitz's L-15 CO<sub>2</sub> independent medium (Gibco). Concentrated vimentin monomer solution (4 mg/ml) was centrifuged at 13000 rpm for 5 min to prevent clotting of the capillary due to protein aggregates prior to microinjection. The protein solution was injected into adherent HeLa-GFPvim by a microinjection system (Injectman II and Femtojet, Eppendorf) and injection parameters were 100 Pa injection pressure, 0.5 s injection time and 50 Pa compensation pressure. After injection, the medium was changed back to normal culture medium and cells were left to incubate for 12 h.

## Alteration of cellular tension

The tension of the cytoskeleton was changed either the chemical agent blebbistatin or physical modifications of the cell substrate. Blebbistatin (Abcam), a small molecule known to inhibit myosin-II in actin stress fibers [123], was added to culture medium containing 10% FCS with a final concentration of 50  $\mu$ M. For chemically induced relaxation, HeLaGFPvim cells containing isotopically labelled d-Vim and grown on rigid collagen-coated glass substrate were incubated in the blebbistatin containing medium for 8 h. In a second series of experiments, cells were grown during all treatment steps (depolymerization, microinjection, repolymerization) on substrates of low stiffness instead of glass. Cells were therefore incubated on collagen-coated softwell hydrogel of 0.1 kPa elastic modulus (Softview, Matrigen). The surface functionalization was thereby similar to the rigid glass bottom dishes used in other experiments. In each experiment, cells were prepared for BCARS by washing the cells with PBS followed by fixation for 30 min (4 % Paraformaldehyde in PBS, pH 7.4). The cell samples were stored in PBS at 4°C and used for BCARS experiments within 3 days. Morphological changes of the IF network were visualized by confocal microscopy (see Supplementary Methods for details).



## BCARS Microspectroscopy

Fixed cell samples were analyzed with a home-built broadband anti-Stokes Raman Scattering (BCARS) spectroscopy setup that has been extensively described elsewhere [241]. A brief description of the experimental setup can be found in the supplementary information (5.22). Using this setup, a region of interest, usually covering a single cell, was raster scanned and a BCARS spectrum was recorded at each pixel. As the acquired BCARS signal consists of both non-resonant and resonant contributions from the sample and the surrounding medium, a phase retrieval procedure was performed to isolate Raman-like spectra for quantitative analysis [298]. The method described by Liu *et al.* using a time-domain Kramers-Kronig transform with a causality constraint was employed to produce the resonant contribution from each BCARS spectrum with a non-resonant spectrum acquired from nearby medium [156, 161]. However, due to these imperfect reference, the slowly altering error from the phase had to be corrected. This was achieved by subtracting a spectral baseline which was calculated by an iterative fit with a fifth-order polynomial [310]. The entire spectral processing to obtain Raman-like spectra was performed by self-written scripts in Igor Pro 6.37 (WaveMetrics). Representative hyperspectral data can be found in the Supplementary Information (SI Fig.5.12 and 5.13).

## Separation of spectral contribution from isotopically labelled protein

To separate the Raman signal of deuterated vimentin IF from all other protein contribution, we employed multivariate curve resolution using an alternating least squares algorithm (MCR-ALS) [186] on every BCARS dataset covering a single cell. The processing was done with the MCR-ALS GUI 2.0 toolbox for Matlab (R2015, MathWorks) by Tauler and coworkers [195]. A similar approach was established to isolate the spectrum of a deuterated peptide within cells by our group in an earlier study [18]. In a first step, every RL-dataset was filtered against a threshold set for the CH band intensity ( $2935\text{ cm}^{-1}$ ) to exclude pixel outside the target cell. From the remaining pixels, an average spectrum was calculated. Next, the spectral data was reduced further to spectra showing at least some traces of d-Vim as evaluated by presence of the  $\text{CD}_2$  vibration. As our interest here only was on the secondary structure and the spectral labeling in the CD region, the spectra range was narrowed the following regions:  $1400\text{ cm}^{-1}$ - $1780\text{ cm}^{-1}$  and  $2130\text{ cm}^{-1}$ - $2400\text{ cm}^{-1}$ . Thereby, extraneous spectral features as well as intrinsic noise in the quiescent region were filtered out and the prepared spectra were bundled into a single data matrix per cell. Next, MCR-ALS was used to find the optimal pure spectral components and respective loadings to represent the entire dataset. A maximum of three spectral components (for cell background, d-Vim and non-random artifacts) was chosen together with constraints for non-negativity of loadings and spectra. The iterative process was stopped either when convergence was achieved or after 50 steps. From the calculated component spectra, the d-Vim component was selected as that having the highest signal intensity in the CD part of the spectrum. From those, an average spectrum was calculated and analyzed further to judge the secondary structural content.

## Calculation of secondary structure

Raman spectroscopy is sensitive in several vibrational modes to secondary structure motifs present in the sample volume [55, 266]. This dependency was used to calculate the structural composition from the given average RL spectra as well as from component spectra obtained by MCR analysis as described above. The amide I band ( $1570$ - $1730\text{ cm}^{-1}$ ) was decomposed via least square fitting with a Levenberg-Marquard algorithm in Matlab (Mathworks). Thereby, the Raman modes assigned to different structural motifs with known peak position, were extracted. From the resulting peak areas, the overall structural

composition was calculated for the given spectrum. As shown by Berjot *et al.*, the amide I band can be decomposed into two peaks for  $\alpha$ -helix at 1635 and 1647  $\text{cm}^{-1}$ , a peak at 1660  $\text{cm}^{-1}$  for random coils, 1667  $\text{cm}^{-1}$  for  $\beta$ -sheets and 1693  $\text{cm}^{-1}$  for  $\beta$ -turn. Ring mode from tyrosine, tryptophan and phenylalanine were included with two minor peaks at 1600  $\text{cm}^{-1}$  and 1612  $\text{cm}^{-1}$  [55]. The peaks were assumed to have Lorentzian line shape, defined by a line width and center frequency both being allowed floating within a defined range. The major fitting parameter, the peak amplitude, was constrained to only positive values.

## 5.6 Appendix III - Supplementary Information

### Supplementary data

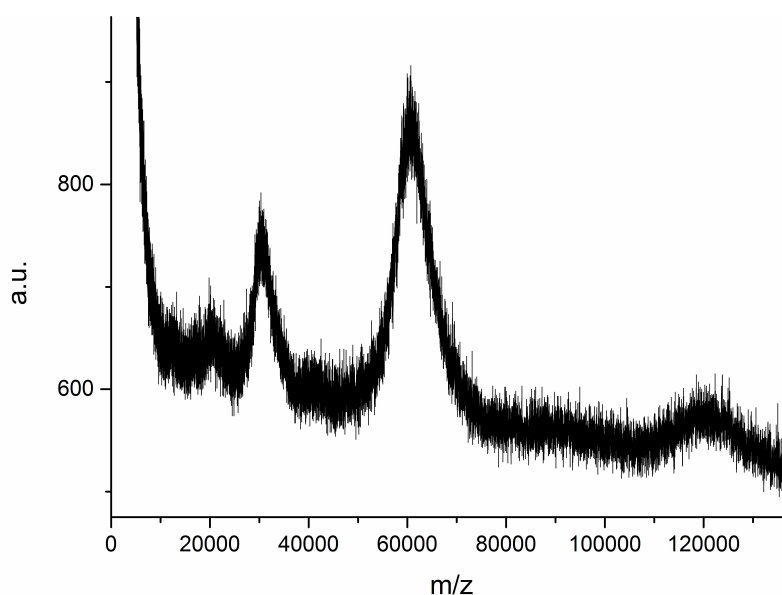


**Figure 5.7:** Maldi-TOF spectrum of recombinantly produced deuterated vimentin showing maxima at 60654.45  $m/z$  and 30243.68  $m/z$  indicating almost full isotopic exchange.

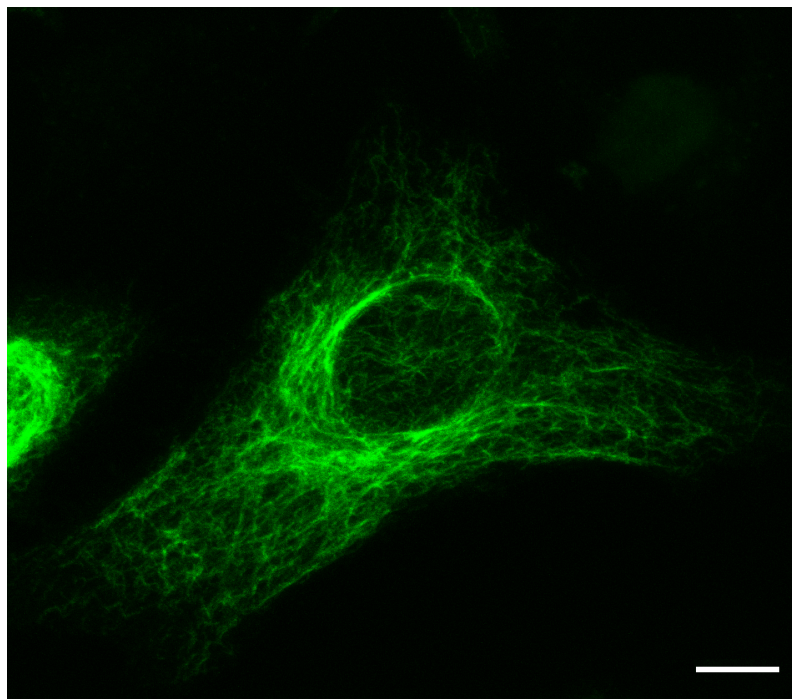


**Figure 5.8:** Confocal microscopy image of HeLa cells grown on collagen-coated rigid glass surface co-expressing Vimentin and GFP (strain Hela-GFPvim). The IF network is filamentous and spread out into the entire cytosol and being most dense in close proximity to the nucleus. The scale bar represents 10  $\mu\text{m}$ .

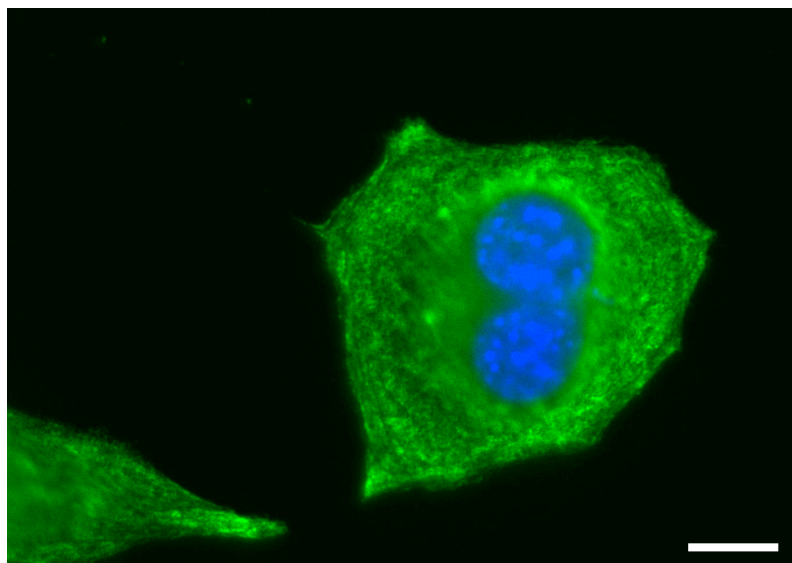


**Figure 5.9:** Merged widefield microscopy image showing the disassembled GFP-labelled (green channel) vimentin IF network in HeLa cells after 5 h of treatment with cycloheximide. The nuclei are labelled by DAPI in blue. The scale bar indicates 10  $\mu\text{m}$ .

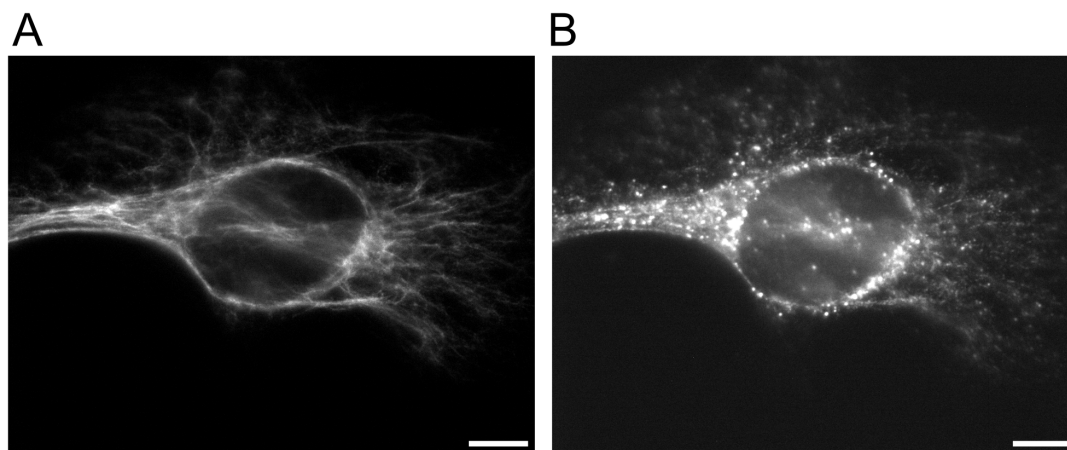


**Figure 5.10:** Incorporation of microinjected vimentin into the native IF network. (A) Fluorescence microscopy image of GFP-labelled native IF in HeLa after  $\sim 8$  h recovery from depolymerization with cycloheximide. (B) Injected, rhodamine-labelled vimentin resembling the same pattern as the intrinsic vimentin. The bright dots are caused by dye aggregates. Scale bars indicate  $10 \mu\text{m}$ .

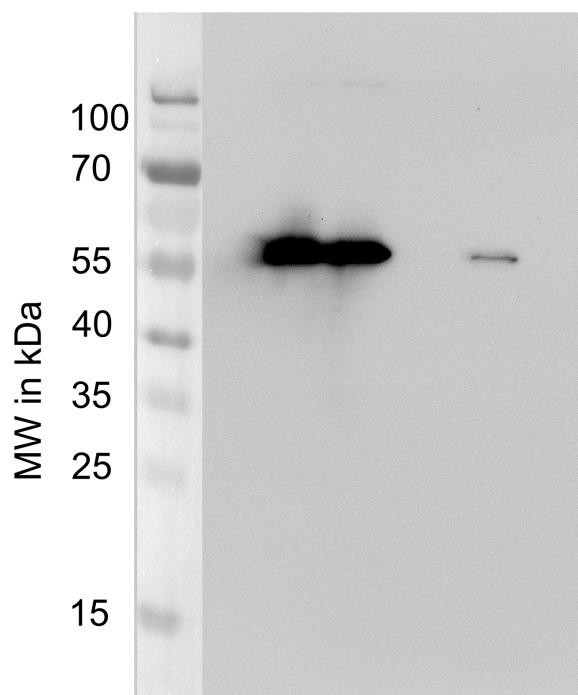


**Figure 5.11:** Western Blot showing vimentin of high (first two lanes) and low concentration (fourth lane) by an anti-his fluorophore at the expected MW of 54 kDa.

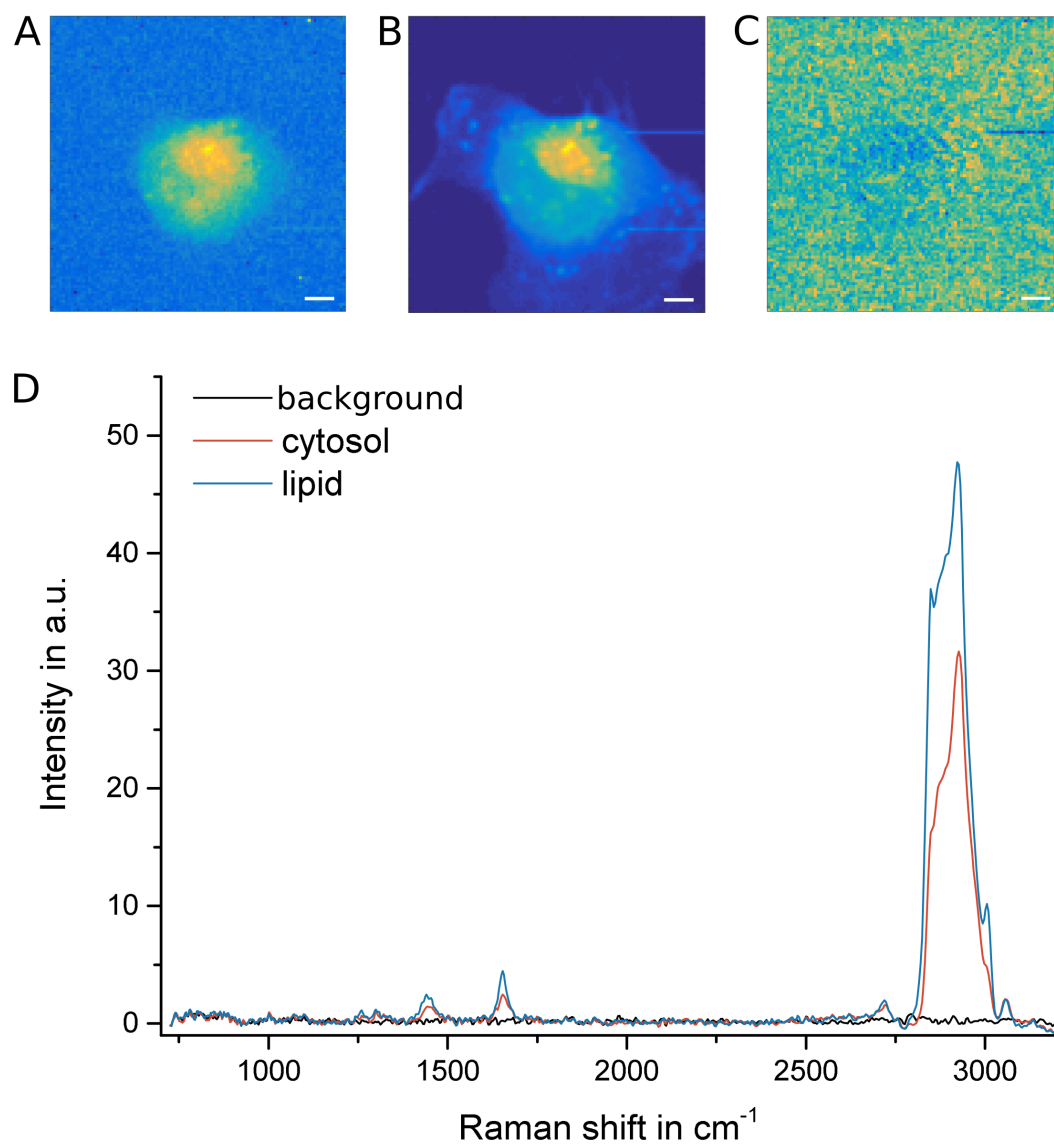


**Figure 5.12:** Broadband CARS data of a cell without the signature of deuterated vimentin. Hyperspectral maps of A) the Amide I band, B) CH band between 2800 and 3200  $\text{cm}^{-1}$  and C) CD band between 2100 and 2250  $\text{cm}^{-1}$ . D) Representative spectra from outside the cell, only showing spectral background from the medium, from the cytosol and a lipid droplet. No Raman signal appears in the silent region between 1700 and 2600  $\text{cm}^{-1}$ . Scale bars indicate 5  $\mu\text{m}$ .

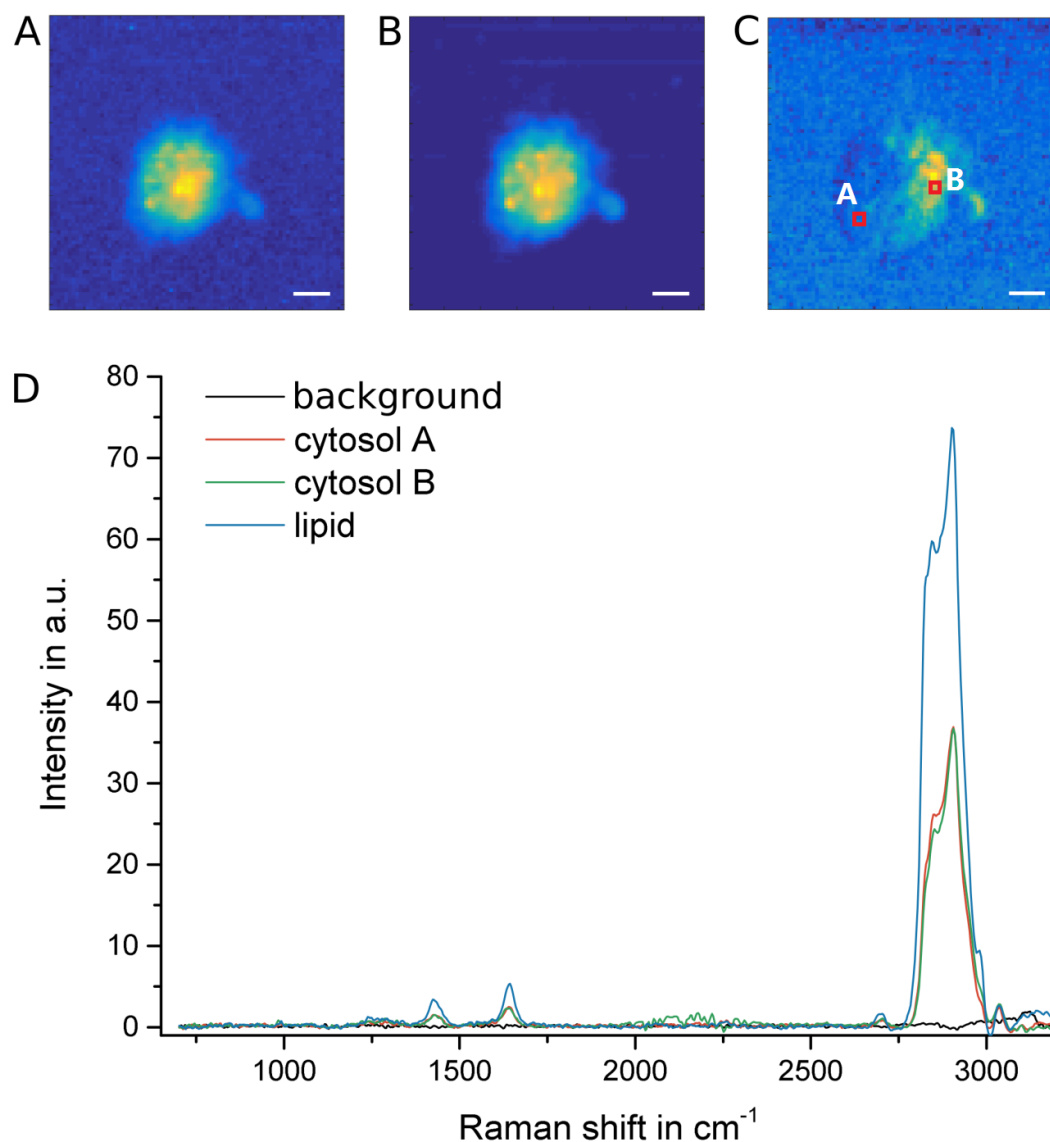


**Figure 5.13:** Cell containing deuterated vimentin. Hyperspectral maps of A) the Amide I band, B) CH band between 2800 and 3200  $\text{cm}^{-1}$  and C) CD band between 2100 and 2250  $\text{cm}^{-1}$ . D) Representative spectra from outside the cell, only showing spectral background from the medium, from two different positions in the cytosol, one without d-Vim another rich in d-Vim, and a lipid droplet. The additional signature of the CD mode appears in the silent region around 2150  $\text{cm}^{-1}$ . Scale bars indicate 5  $\mu\text{m}$ .

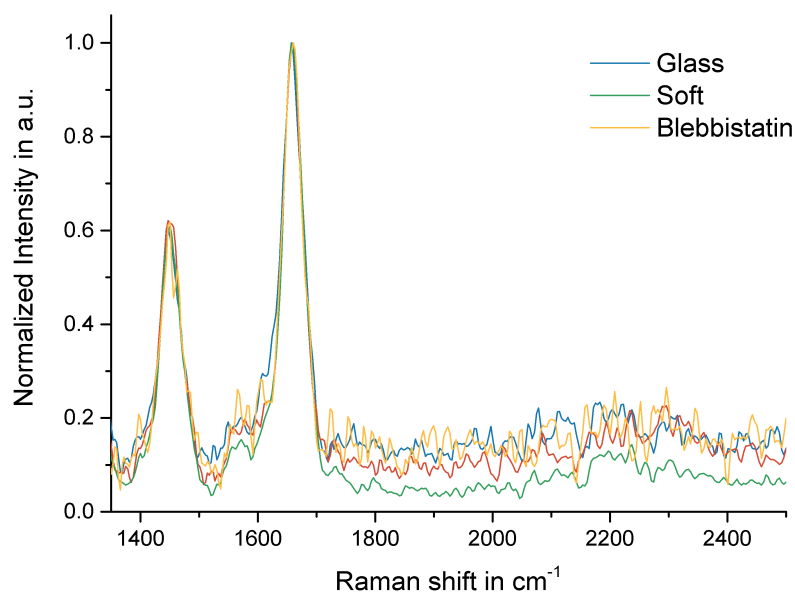


**Figure 5.14:** Normalized average cell spectrum for each group showing a constant Amide I region. The spectra per group show were calculated by pooling all spectra originating from cell-containing pixels from each cell for each group and taking the global average.

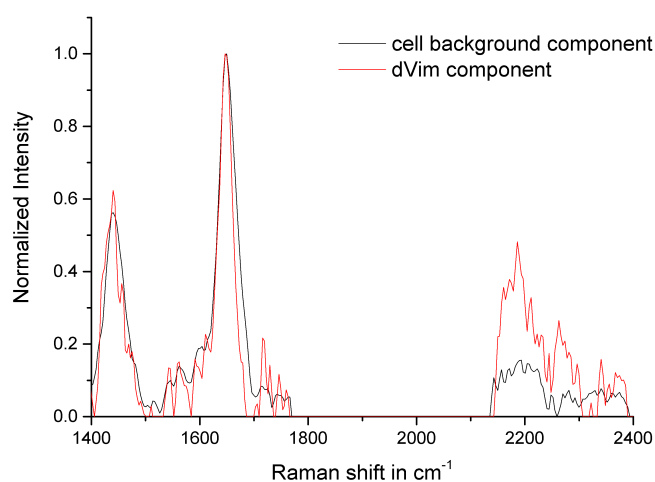


**Figure 5.15:** Average of the MCR components obtained from CD containing pixels of cells that were grown on glass substrates and treated with blebbistatin. The two components differ mostly in their intensity of the CD region with some changes in the Amide I and CH region. The component with the strongest CD region intensities was assigned to the deuterated protein while the remaining component represents any non-deuterated protein.

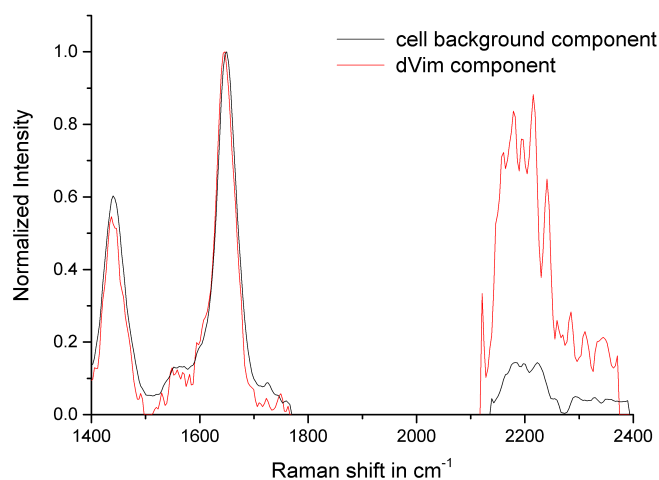


**Figure 5.16:** Average of the MCR components obtained from CD containing pixels of cells that were grown on soft substrate. The two components differ mostly in their intensity of the CD region with minor changes in the Amide I and CH region. The component of strong CD intensities was assigned to the deuterated protein while the remaining component represents any non-deuterated protein.

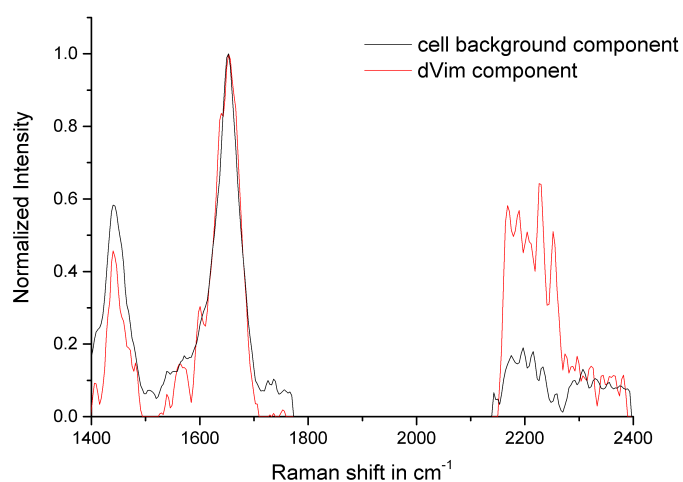


**Figure 5.17:** Average of the MCR components obtained from CD containing pixels of cells that were grown on glass substrates. The two components differ mostly in their intensity of the CD region with some changes in the Amide I and CH region. The component of strong CD intensities was assigned to the deuterated protein while the remaining component represents any non-deuterated protein.



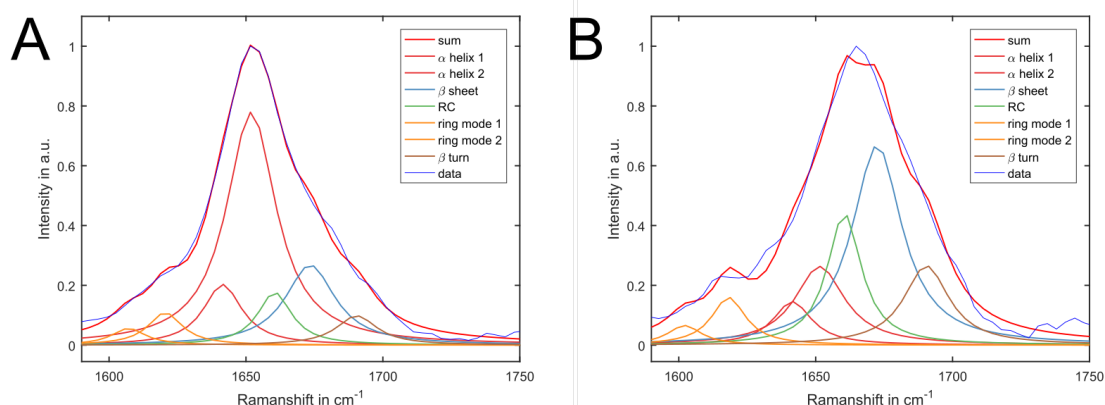


**Figure 5.18:** Amide fit on the average spectral data from pure vimentin (A) and as average over an entire cell (B).

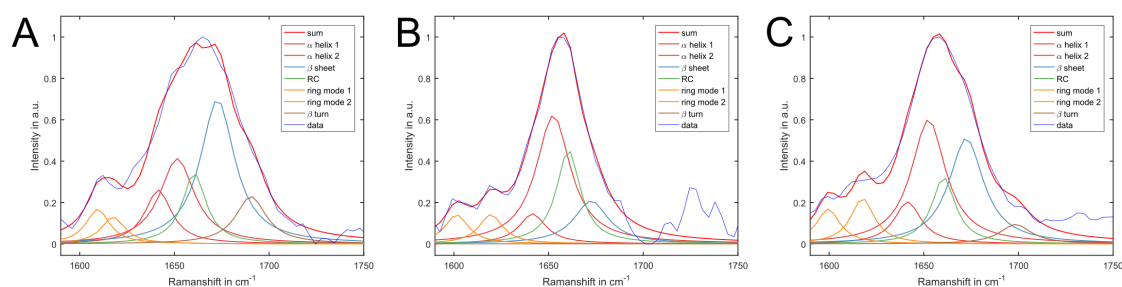


**Figure 5.19:** Amide fit on the average MCR components assigned to d-vimentin from cells grown on glass (A), treated with blebbistatin (B) and grown on soft substrate (C).

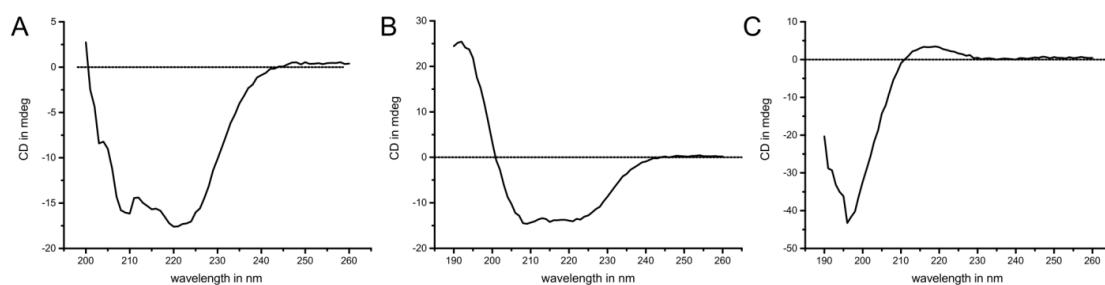


**Figure 5.20:** Circular dichroism spectroscopy of vimentin monomers in PBS showing the dominantly  $\alpha$ -helical structure of the protein.

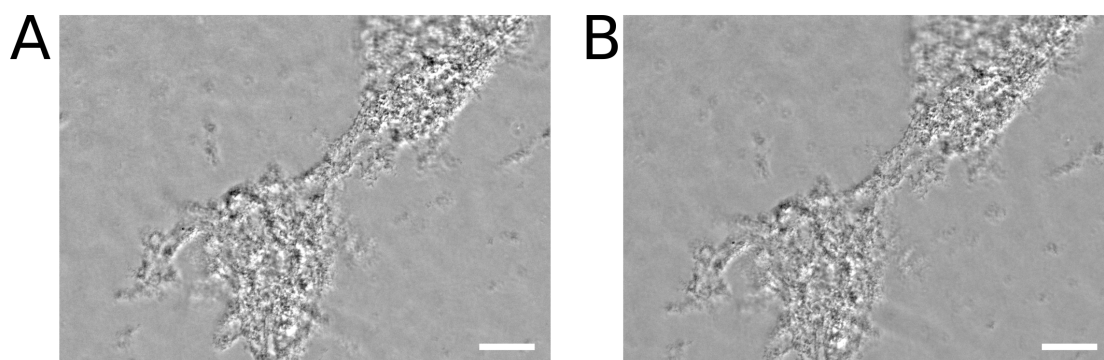


**Figure 5.21:** Phase contrast microscopy images of vimentin filaments formed in vitro before (A) and after 12 h blebbistatin treatment (B) show very similar appearance. Scale bars indicate 50  $\mu\text{m}$  and a gradient background was subtracted from both images.

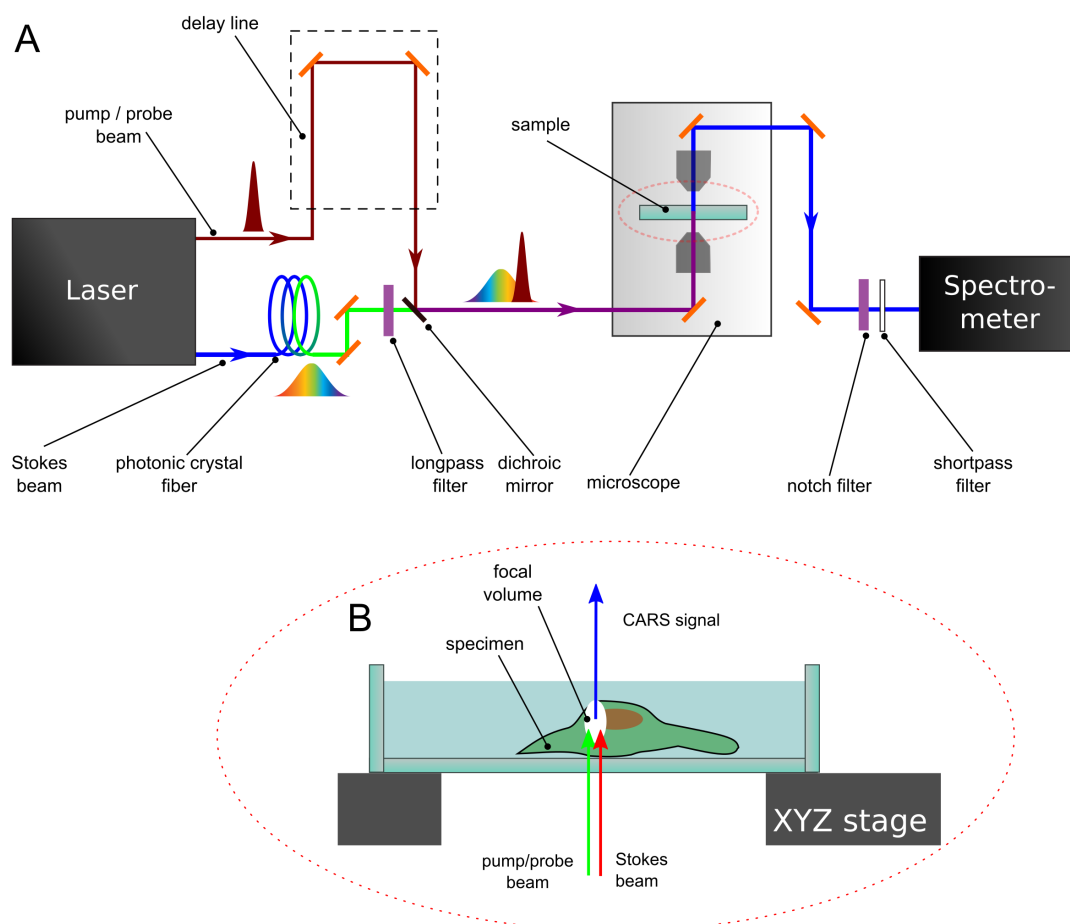


**Figure 5.22:** Illustration of the broadband CARS setup used in this work. A) Optical beam path for creating and detecting BCARS signal. B) Zoom-in showing the sample area where the Stokes beam is spatially and temporally overlapped with the pump/probe beam to create the forward-detected CARS signal.

## Supplementary Methods

### Confocal microscopy

Confocal microscopy was used to visualize the spatial distribution of vimentin IF in HeLaGFP-Vim cells under different conditions. Measurements were performed on a TCS SP5 confocal microscope (Leica, Germany) with laser excitation at 405 nm (GFP) and a 63x, 1.2 NA water immersion objective lens. The image contrast was adjusted and a smoothened background was removed in ImageJ.

### Widefield fluorescence microscopy

To determine the intracellular distribution of native IF under different treatments as well as microinjected vimentin, widefield fluorescence microscopy was used. Measurements were done on an Olympus Ti-81 microscope with 20x or 100x magnification with appropriate filters.

### Circular dichroism spectroscopy

Secondary structure of vimentin monomers was analyzed with circular dichroism spectroscopy in the range from 190 to 260 nm in 1 nm steps. Experiments were performed on a J-815 spectrometer (JASCO Inc, Easton, USA) under nitrogen atmosphere and by using quartz cuvettes of 1 mm path length. Protein was dissolved in phosphate buffer at pH 7.4 with final concentration of 2.5  $\mu$ M. For each sample, 3 spectra were taken and averaged.

### CARS microspectroscopy

Intracellular protein structure was analyzed by broadband CARS microspectroscopy setup as depicted in figure 5.22. A commercial ns-pulsed laser source (Leukos-CARS, Leukos) provides a spectrally narrow pump/probe beam ( $\lambda = 1064$  nm) from which  $\sim 50\%$  is coupled into a photonic crystal fiber to obtain a spectrally broad Stokes beam ( $\lambda = 400$ -2400 nm). To match both Stokes and pump/probe beam pulses in the sample focus temporally, the later one is guided through a delay line of several meters length. The spectral range of the Stokes beam is cut by a longpass filter and a Glan-Thompson polarizer to a bandwidth from 1100-1600 nm. The final spectral power density of the Stokes beam is more than 100  $\mu$ W nm $^{-1}$ . Both Stokes and pump/probe beam are combined by a dichroic mirror and directed to an inverted microscope (Eclipse Ti-U, Nikon) where they are focused into the sample with an objective lens (100x, NA:0.85, Zeiss) as shown in figure 5.22B. The total average laser power within the focal volume is 30 mW. To allow hyperspectral imaging, the sample is mounted on a xyz piezo stage (Nano-PDQ 375 HS, Mad City Labs) allowing sub-micrometer step size. The CARS signal is collected in forward direction with a second objective lens (10x, NA: 0.25, Zeiss) and sent to a spectrometer. To block the intense pump/probe and Stokes beams, a notch-filter (NF03-532/1064E-25, Semrock) and a short-pass filter (FES1000, Thorlabs) are placed before the entrance slit. The CARS signal is analyzed by a Czerny-Turner spectrograph (Shamrock 303i, Andor) with attached cooled CCD camera (Newport DU920P-BR-DD, Andor) resulting in a spectral range from 500 cm $^{-1}$  to 4000 cm $^{-1}$  with a spectral pitch of  $\sim 4$  cm $^{-1}$ . All components in the setup are controlled with software written in LabView (National Instruments). Further details of this BCARS experiment can be found elsewhere [18, 241].

## Chapter 6

# Outlook and Summary

### 6.1 Future directions

Research is an infinite story and the projects discussed in this work only scratch the surface of the true nature of structural changes in biomaterials and cells. The bulk of the literature on structural biochemistry exists for purified systems or crystals where signals are relatively easier to attribute to specific molecular entities in macromolecules. This is in stark contrast to the work presented here in dirty, 'soft' biomaterials and within cells. Throughout the course of working on the projects presented in the previous chapters, plenty of interesting ideas for experiments came up, for which I will briefly discuss the most promising avenues below.

#### 6.1.1 Local hydrogel deformation

Rheology experiments probe the bulk properties of a material and shear or tensile tests are based on the assumption that the sample in itself is homogeneous. As we have shown in chapter 3, this is an oversimplified picture for fibrin hydrogels [17] and most probably for other biopolymer networks, too. A crucial aspect in measuring the sample response to a deformation is the application of stress at a well-defined location. When the spatial distribution of load in a sample matters, such as in hydrogel networks [311] or when studying force distribution within the extracellular matrix [312], the usual shear (and tensile) geometries might not be appropriate. For microspectroscopy of fibrin (but other hydrogel samples as well) I therefore suggest testing the following experimental configuration: A thin sample is prepared by casting between glass slides as described before. However, a fiber or wire of small diameter ( $<100\text{ }\mu\text{m}$ ) and with elasticity greater than the test material is embedded in the sample during polymerization (see Fig.6.1). The fiber surface will act as a nucleation site for the biopolymer formation and thereby couple the fiber to the protein gel. One could for example use a piece of (stripped) optical fiber, a nanowire or simply hair. The loose end of the fiber can be attached to a micro stage or stepper motor while the hydrogel sample is fixed. Pulling on the string will then create a controlled one-dimensional shear force locally in the sample resulting in a stress distribution as shown in Fig.6.1B. Such an experiment would mimic physiological relevant scenarios like deformation of at a wound site by platelets or shear forces from blood flow (up to 38 Pa, 10000 /s [313]). The local sample deformation can be tracked by embedded microbeads especially as the shear strain has a lateral gradient in this configuration. It would be interesting to relate the shear force to local secondary structure measured by BCARS in fibrin hydrogels of different concentration and cross-linking.

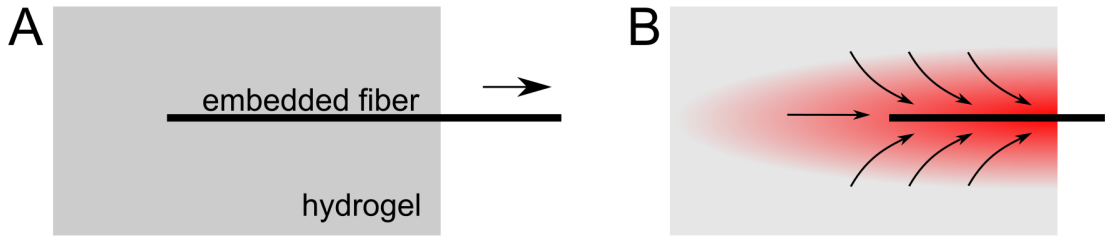


**Figure 6.1:** A) Schematic for one-dimensional shear force application on a hydrogel sample. A rigid fiber is embedded in the hydrogel sample and then pulled. B) Artist's rendition of the strain profile in the material with darker red corresponding to more strain.

### 6.1.2 Design of a cell stretching device for large deformations

The Holy Grail for intermediate filament mechanics is to quantify and understand their response to large strains within cells. IF are assumed to be the safety belts' of cells, that ensure structural integrity under extreme deformations [38]. This is achieved by their somewhat unique strain-hardening and structural properties, which have been partially shown *in vitro* [66] and in theory [6, 30]. While the experiments presented in this work indicate structural unfolding also *in vivo*, it would be even more relevant to test the response to active deformation instead of relying on the intrinsic cell-generated pre-tension [62]. BCARS microspectroscopy of deuterated vimentin IF together combined with fluorescence microscopy of GFP-vimentin under load would reveal the degree of structural transitions and the maximum strain rates occurring *in vivo* as well as the network response to such large mechanical deformations. As the relevant structural transitions in IF start around 10 % strain [39] and network rearrangement will compensate for small deformations, the cell stretching setup must allow deformations to much higher strains. Common cell stretching devices based on elastic PDMS chambers [111, 114] as well as commercial available systems only allow small deformations up to  $\sim 20\%$  and are not applicable in the constrained setup geometry of the BCARS setup. The experiments should be carried out on live cells and experimental procedures and preparations require several hours. This makes full-time coverage with cell growth medium necessary. For BCARS imaging, the specimen must be placed within the working distance of the excitation objective lens, usually 1-2 mm, and the entire sample should have the least absorption possible. Furthermore, the sample region must be accessible for the objective lens from below as well as for the collection objective lens from the top (water immersion) also having a small working distance of only 3-5 mm. To meet all those requirements, a prototype cell stretching device was developed and built with help from Mark-Jan van Zadel and Florian Gericke. Figure 6.2 shows the design and the final in-built device in the BCARS setup. The cell stretching device is based on the macroscopic deformation of a highly elastic membrane on which the cells are cultured. As membranes, we chose biologically inert and optically transparent PDMS thin films (P/N PF-30-X0, TELTEC GmbH), which have only few molecular vibrations in the fingerprint region. However, pretests showed that the CARS signal from PDMS overwhelmed any protein signal from cells seeded directly on top. We therefore added a spectral less interfering gelatin hydrogel layer of  $5\ \mu\text{m}$  thickness through spin coating to move the focal volume away from the PDMS. This reduced the now out of focus signal from PDMS sufficiently to obtain a useful signal from the seeded cells. To improve cell attachment, the substrates were coated with fibronectin solution [ $50\ \mu\text{g}/\text{ml}$ , 1 h at  $37^\circ\text{C}$ ]. The prepared membrane is clamped to two height-adjustable hooks that are mounted to stepper motors (NEMA11, Haydon Kerk). A controller board (IKS-31-303, Mocontronic Systems GmbH) allows the communication to both motors via a Labview interface and stretching of the sample is done by synchronous motion of the motors. The

minimum length for the membrane is set by the diameter of the upper objective lens ( $\sim 40$  mm), which must fit in between the clamps. This makes a respective diameter of a standard Petri dish necessary for supporting the sample liquid and a displacement stroke of 40-60 mm within the microscopy setup. For imaging, a glass bottom Petri dish was self-built where the glass slide was glued to the inside of the dish to make the sample optimal accessible (see Fig.6.2B).

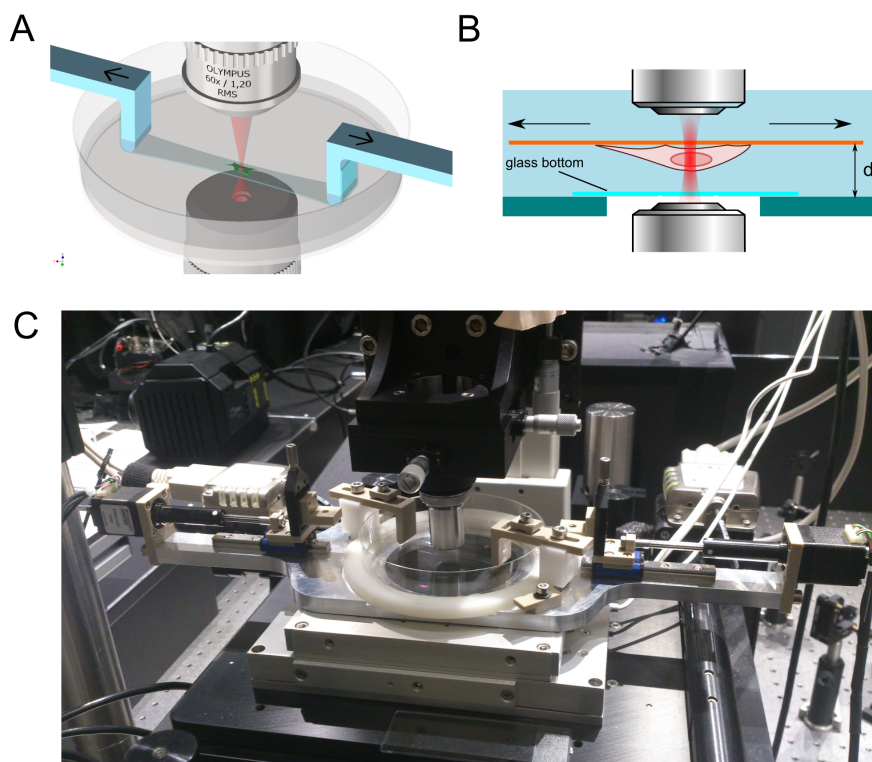


**Figure 6.2:** Design and final setup for cell stretching experiments. (A) Design study showing the idea and dimensions to scale. (B) Detail of the sample geometry. The cell specimen is grown on an elastic membrane and positioned bottom up for the experiment to be within the working distance of the high-NA excitation objective below. (C) Final cell stretcher with attached hooks that clamp the elastic membrane mounted in the BCARS setup.

To test the cell stretching device, a first experiment was performed with HeLa cells where the vimentin intermediate filaments are expressed with a GFP tag and visible in fluorescence microscopy. Cells were cultured at low density on PDMS membranes placed in six-well plates for two days under standard conditions (see methods section of chapter 4 and 5). Next, the membrane was gently peeled off and clamped to the stretcher hooks so that the adherent cells are on the bottom side as depicted in Fig.6.2B. The cell culture was kept surrounded by medium or PBS to prevent cells from drying out. Afterwards, the parts were assembled in the stretching device and the membrane submerged in serum-free,  $\text{CO}_2$ -independent medium (L-15, Gibco). For fluorescence imaging, the stretching device was mounted on a wide-field microscope (IX-81, Olympus) and images were acquired for different strains as shown in Fig.6.3. Uniaxial stretching of the elastic membrane leads to a proportional local strain that deforms the adherent cells along the load direction. Fluorescence images indicate that the intermediate filament network follows the substrate deformation without rupture up to the maximal applied strain of 50 % as depicted in Fig.6.3C. Releasing the strain leads to a relaxation of the IF network that distributes

	0 %	25 %	50 %	0 %
Cell A (x)	100	80	67	81
Cell A (y)	100	92	102	86
Cell B (x)	100	112	142	94
Cell B (y)	100	80	76	102

**Table 6.1:** Extension of IF network for two cells along the x and y axis as indicated in Fig.6.3 under different deformations. The measured length was always normalized to the initial 0% value.

similar to the initial IF arrangement (see Fig.6.3D). Quantification by measuring the extension of the IF geometry for the x- and y-axis is given in table ?? and indicates that the IF network of cells that are initially aligned along the direction of load nicely follow the deformation.

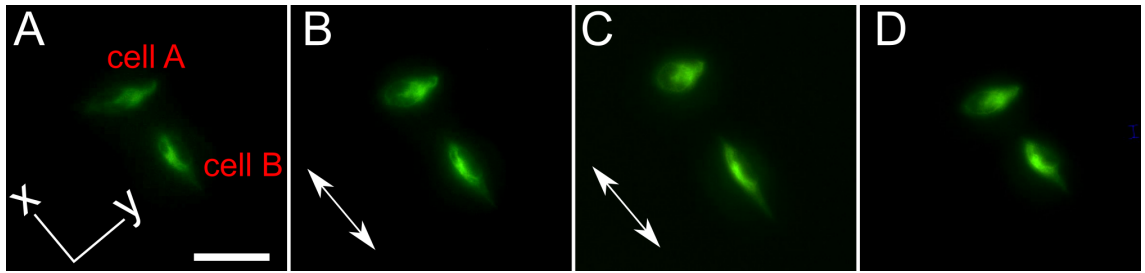


**Figure 6.3:** Fluorescence microscopy of HeLa cells under different mechanical loads: initially relaxed cells (A), 25 % strain (B), 50 % strain (C) and again relaxed (D). The direction of load is indicated by the arrows and the scale bar represents 50  $\mu\text{m}$  for all images.

Based on these preliminary results that demonstrate the suitability of the cell-stretching device - at least for fluorescence, it would be interesting to investigate the following questions in more detail:

- What is the maximum strain that can be compensated by the IF network before FA detachment or even rupture?
- How does the IF network rearrange at time-scales of minutes to hours when being deformed to different strains?
- How does this force affect other cytoskeletal networks?
- How does the secondary structure of IF change under high loads?

### 6.1.3 Reconstructing the non-resonant CARS contribution with MCR-ALS

Broadband CARS experiments suffer from the necessity to acquire a spectrum that contains only the non-resonant background (NRB) component. Usually, this reference spectrum is taken either from the glass substrate or in the medium next to a (biological) specimen. In the phase-retrieval processing (described above in chapter 1.4), the reference is then used to separate the resonant from the non-resonant CARS signal and to obtain a quantitative, Raman-like spectrum. The NRB is predominantly comprised of electronic signal contributions from other nonlinear optical phenomena that are less chemically specific [163]. The measurement of the NRB on a pixel-by-pixel basis is a nontrivial task; thus, often a single reference NRB from glass or water is acquired which then results in a local error between the actual and estimated amplitude and phase. Recently, the Langbein group proposed NaCl crystals as a universal reference material to obtain a constant NRB



over changing positions and even experiments [314].

Both techniques, however, rely upon an accurate measurement of the NRB, which also incorporates the system excitation profile and spectral response. To date, no convenient approach has been found to measure the exact NRB, so retrieved spectra in general contain phase and amplitude errors. A possible alternative to obtain the NRB spectrum without additional measurements beside the actual hyperspectral image could be principal component or MCR-ALS analysis. For MCR-ALS, a similar approach was demonstrated for removing a fluorescent background from spontaneous Raman data [272].

Every raw CARS spectrum in a hyperspectral images contains a pure NRB component, the resonant component that varies with the oscillators present in the probed volume, and the mixed term containing both contributions. As discussed earlier, the NRB term should be independent of the sample itself and therefore similar in all pixels. When ignoring the fact that the resonant signal might not follow a linear concentration dependency and only aiming for the NRB spectrum as a reference, the MCR approach should produce a meaningful component spectrum that reflects the optimal NRB signal for the entire data set that could serve as a pseudo-reference spectrum for the phase-retrieval processing.

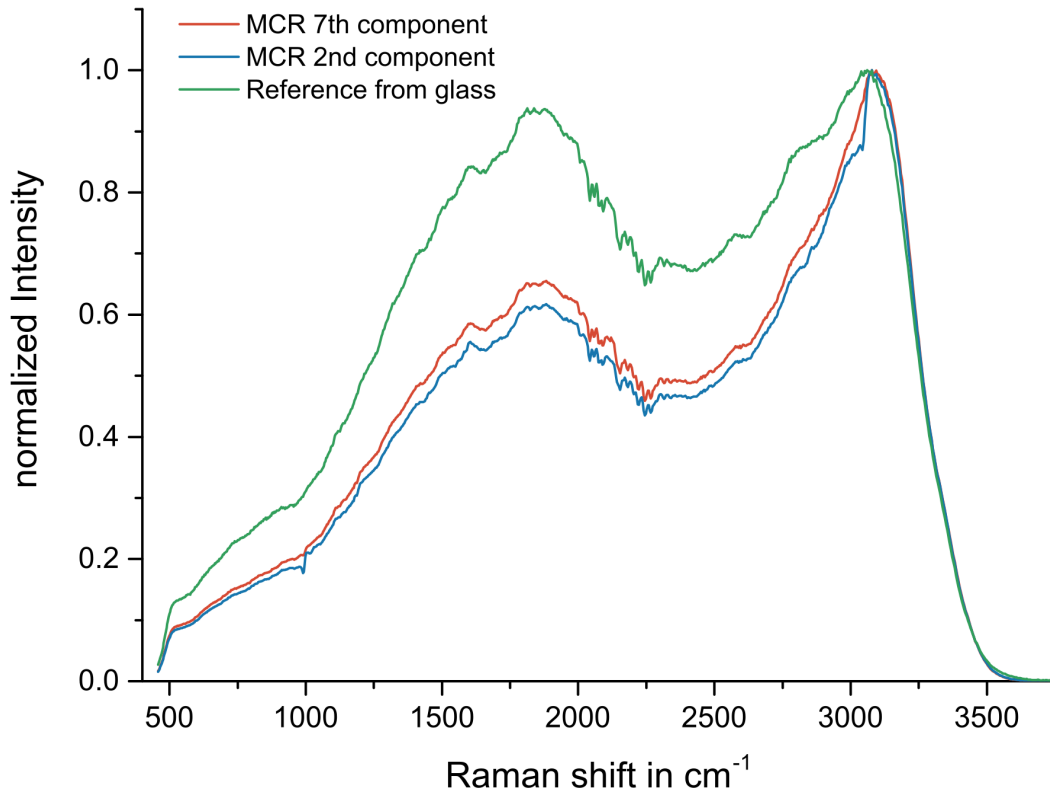


**Figure 6.4:** non-resonant background spectra from glass and from MCR processing. All spectra were normalized to their maximum value.

The proposed procedure works as follows: First, the collected raw BCARS data is imported into Matlab and unfolded into a two-dimensional matrix of (spectra x position). This data is then processed in the MCR-ALS toolbox with a sufficiently large number of allowed components (e.g. 5-8 depending on the heterogeneity of the sample) to calculate the resulting set of component spectra and loadings. From these spectra, the smoothest



one is selected manually as reference spectrum and used in the Igor Pro GUI while the further spectra and concentrations are discarded. Usually, the component with the lowest eigenvalue will represent the NRB at the best. It might be necessary to multiply the component spectrum by a constant factor so that it covers the same numerical range as the BCARS spectra. Based on such a reference, the normal BCARS data processing can be done as described in the methods chapter.

This approach was tested with a sample consisting of polystyrene beads surrounded by water and hyperspectral BCARS images were acquired with  $41 \times 41$  pixels. This data was then unfolded and processed in MCR-ALS with 7 allowed components. Figure 6.4 shows the non-resonant background obtained from glass as well as the second and seventh component obtained by the MCR procedure. While the second MCR component contains unwanted spectral features, like the sharp dip around  $3200 \text{ cm}^{-1}$ , the lower-ranked component only shows the expected NRB pattern modulated by some slowly varying background. By using those artificial spectra, the phase retrieval process can be carried out and meaningful Raman-like spectra can be achieved as shown in Fig.6.5.

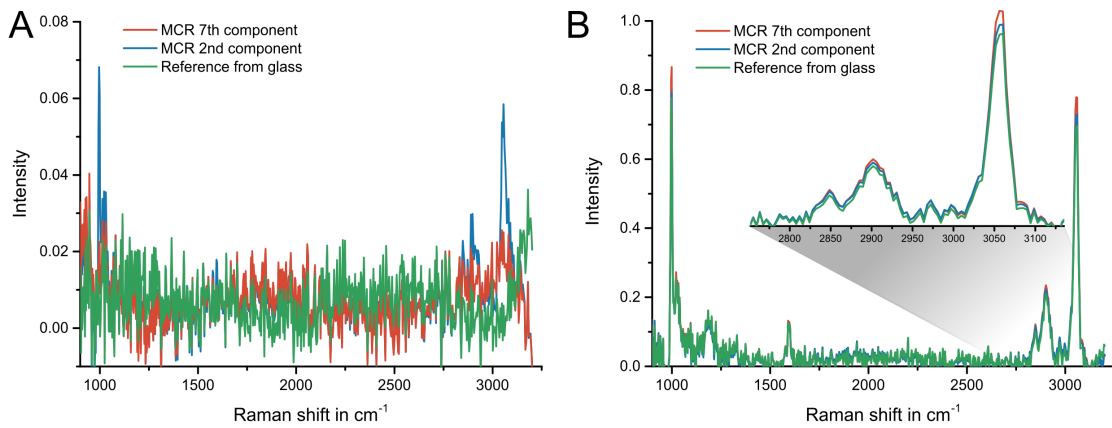


**Figure 6.5:** Raman-like spectra after phase-retrieval using different references. The spectra from an empty pixel show incorrect peaks when the 2<sup>nd</sup> MCR component was used as a reference while in case of the 7<sup>th</sup> MCR component this artifact is almost vanished (A). For polystyrene beads, the RL-spectrum is accurately for all three references with minor variation in the overall peak intensity (B).

For most samples, this approach should provide a reference spectrum that is as usable as one taken from an 'empty' pixel that contains only the surrounding medium. However, the procedure presented here might be superior to such a manual picking of a reference spectrum as the MCR algorithm successfully filters out random noise that would have influence on every single retrieved spectrum. Yet, a more systematic analysis covering different sample types and a better understanding on how efficient the resonant contribution is suppressed in the 'NRB' component is necessary to fully evaluate this idea.

## 6.2 Summary

My PhD research summarized in this thesis focused on applying molecular spectroscopy to investigate the mechanical processes in biological systems. The interdisciplinary work was done in Sapun Parekh's lab at the Max Planck Institute for Polymer Research in collaboration with the Institute of Pharmacy and Biochemistry, Johannes-Gutenberg University Mainz. Only by the support from both research groups was it possible to realize the challenging ideas of investigating isotopically labelled proteins within cells by broadband CARS microspectroscopy.

Protein secondary structure and its dynamic changes are a key mechanism to understand biomechanics both in hydrogel systems such as fibrin as well as in intracellular protein networks. In the projects presented in this dissertation, I show the capability of coherent Raman scattering as a tool to determine protein structure *in situ* and first steps towards applying this technique in cell biology.

For my research I had to heavily simplify and streamline the systems that were studied and even with this approach and the available experimental methods, I could still only reveal partial aspects of the underlying mechanisms. In approaching the research this way, proteins were to be assumed mechanical building blocks that might switch their state when under load rather than considering the plethora of biochemical properties, reactions and, especially in the cell systems, the infinite number of possible interactions with other proteins. Elsewise, I would have been lost in all the details.

In chapter 3 we investigated how the fibrin, the blood clotting protein, forms elastic network structures that become stiff and can resist large deformations while staying soft under minor strains. By BCARS microspectroscopy of fibrin hydrogels under different strains, we detected that the secondary structure of the initially predominantly  $\alpha$ -helical protein unfolds to  $\beta$ -sheet structure. Furthermore, we show by a localized calculation of the structural motifs (resulting in structural maps) that this transition appears to be heterogeneous and thereby the assumption of a 'bulk material' is insufficient to describe these hydrogel networks. The structural changes in these supramolecular features could help to locally prevent the degradation (fibrinolysis) at such load-bearing fiber strands - a first hint (from our work) towards the 'use it or lose it' principle [308]. Besides those findings, the fibrin project demonstrated that BCARS can be employed to measure protein structure *in situ*.

Next, a method had to be evaluated to find a specific isotopically labelled protein within the intracellular environment (that contains more than 200 mg/mL protein on average [269]) and to filter out the specific Raman signal of such a target molecule from the cytosolic background. Chapter 4 describes the work done on the cell penetrating peptide 'penetratin' to test the separation capabilities of chemometric data analysis on deuterated proteins from data within the cytosol. Penetratin was tagged with six deuterated glycine molecules to create a unique spectral feature and then added to cell cultures. As a CPP, the peptide translocated into the adherent cells and accumulated within the cytosol and, after some incubation time, also in the nucleus. Based on the work from Ye and coworkers [183], we localized the deuterated penetratin with both BCARS spectroscopy and confocal microscopy and determined its secondary structure in different cellular compartments. The easy to produce isotopically labeled peptide helped us to develop the data analysis methods by the chemometric toolbox MCR-ALS together with subsequent peak fitting of the amide I band to extract the structural composition.

In chapter 5 we combined the results and experience collected in chapters 3 and 4 to study the intracellular IF protein vimentin under different tensional states in HeLa cells.

The Holy Grail for my research was to determine how intermediate filaments are influenced by mechanical forces that act upon the cytoskeleton. Therefore, an experimental process of combining stable isotope labelling with MCR-ALS analysis to separate the spectral component of a target protein had to be established. Even with using the imaging method of broadband CARS microspectroscopy, the obtained spatial information had to be sacrificed in order to make the chemometric filtering of the component spectrum possible. Our results reveal that the overall structural composition of vimentin in cells grown on glass tends towards more  $\beta$ -sheet structure indicating that unfolded vimentin is present under this culture condition. On the other hand, we showed that cells that were either physically or chemically relaxed contained higher contributions of  $\alpha$ -helix structure and thereby more like *in vitro* vimentin. While we still can't create structural maps that would illustrate a spatially resolved distribution of unfolded IF, we got a first indication that unfolding of IF takes place *in vivo*. This implies that vimentin and probably also other IF forming proteins of very similar structure could act as force sensors within the cytoskeleton. If the strain becomes high at a location in the network, the involved protein molecules respond by a transition from  $\alpha$ -helix to  $\beta$ -sheet. Thereby not only each affected molecule is extended and the structural integrity is maintained while a chemical signaling cascade might have been triggered. In consequence, the IF at such a site might be protected from degradation or even be reinforced with cross-linking proteins. Such a feedback would, first of all, enable the cell to adapt continuously to varying external loads without wasting IF protein at unstressed sites. In addition, such force sensing could be involved in further adaptations or even differentiation on longer time scales and therefore our results might help to understand the role of IF beyond its structural purpose in the cytoskeleton.

Given the constraints of the experimental setup, the MCR data processing and time, my dissertation only provides a first lead how the true IF mechanics are in living cells. Further research is needed to answer all the obvious next questions such as

- How does the IF network react to active deformation?
- Is the structural transition reversible?
- Over which time scales remain unfolded segments stable and could this create some sort of memory?
- Is the structural composition different between epithelial and mesenchymal cells?

To which extent BCARS microspectroscopy can help with such next steps should be considered open and unbiased. The results of chapter 5 clearly show the limits and detection thresholds of BCARS at its current configuration. Having more effective isotopic labelling or combined measurements that exploit fluorescent tags might result in better separation of the IF signal and could allow a semi-localized imaging.

# Acknowledgements

This thesis would not have been possible without the help from many people at the MPIP and the university of Mainz. Call it support, supervision or collaboration - interdisciplinary research is not done by just sitting in the lab alone. Having this in mind, I would like to thank all co-authors and colleagues for their efforts, critical comments and constructive input.

I would like to thank Sapun for almost five years of training and guidance. It was a pleasure to watch you rightfully destroying almost aligned optics that were off just a bit or just not tight enough. You motivated me to work hard on innovative science, high risk projects and always provided smart ideas when I was stuck in a dead end. Thank you for the fair, patient and inspiring supervision during my PhD.

I wish to thank Mischa Bonn for fruitful discussions, steering of the projects and support over the entire time at the institute. Dirk Schneider I would like to thank for being an open-minded, straightforward and always helpful supervisor in the realm of biochemistry. Many thanks go to all members of the CARS group! It was a great time and we had a lot of fun together while dissecting results, discussing and drinking. Sabine I would like to thank for always being helpful and the only true lab wizardess of the MPIP. Your superb taste of music sweetened long hours in the lab and your infinite support with growing cells, producing proteins and sharing cookies is a keystone of my PhD. Xiao, you changed a lot during the last years, which always encouraged me. I thank you for all the talking and open feedback. It was good times and good food (even so I still doubt that coca cola chicken is a traditional Chinese recipe). Samet, being the elder student, you taught me a lot about the science business and how to survive at the institute. Thanks a lot for sharing your ideas on the influence of particle size on chain anisotropy I still hope for some collaborative projects where the rubber meets the skin. Yujen, you truly helped me a lot by scanning odd fibrin, vimentin, or whatever samples or repairing nasty setups. Thank you for your patient support! Also my thanks go to Yelena, Alexandra, Miriam and Sachin for all the support in the CARS or cell lab and valuable input while having a coffee together. Also, I have to acknowledge the influence of Mischa D. Schwendy to my work and career. Mischa, you were the first one to go to in case of acute frustration or creative flashes of inspirations. Thank you for all the honest and funny discussions about science, life, the universe and everything!

I am grateful to Laurie Gangloff for help with all the formalities and administrative work during my time at the MPIP. By myself I only would have reached 23 Millilaurie effectiveness here. Also I have to acknowledge Henrick Mueller for endless email communication about really important stuff.

With respect to the colleagues from good old rm. 1.504 I would like to express my gratitude. I really enjoyed the relaxed and nice atmosphere in our office. Dr. Wang, it was a pleasure to chat with you over science and life. Francesco, thanks for the advices during the early part of my PhD and how to stay motivated over some desperate times. Gabi, you encouraged me in being more extroverted on the phone and during four years I really improved. Marc-Jan, thank you for engineering all kind of objects I could use in my 'LASER'

setup or for torturing cells. To quote C.V. Raman from your favourite Bollywood movie: *Live long and prosper*. The same goes for Florian, who provided an awesome fast-track development of sample stages etc. and helped with all kinds of technical issues I had to fight with.

I would like to thank Noreen Klein for teaching me the fundamentals of biochemical lab work and for sharing her wisdom and tricks in producing proteins. My thanks also go to Hans-Dieter Bauer and Silvia Mittler who both encouraged me to do a PhD in the first place.

With respect to the work presented in chapter 3, I am very grateful to Joe Baio, Alan Liu, Gijse Koenderink, Daniel Bonn, Kaloian Koynov, Kurt Kremer, Kostas Daoulas, and Johannes Hunger for helpful and critical discussions; Vasilis Balos for initial protocols for fibrinogen cleavage. Florian Gericke and Andreas Hanewald provided excellent technical support for setup construction and rheological measurements, respectively.

Regarding chapter 4, I am very grateful to Dirk Schneider, Staffan Lindberg and Johannes Hunger for helpful and critical discussions. Anke Kaltbeitzel (MPIP), Maria Hanulova and Sandra Ritz (Institute for Molecular Biology, Mainz) provided excellent support for confocal microscopy and image processing. Stephan Türk provided MALDI measurements for peptide analysis. I would like to thank Stefanie Pannwitt and Dirk Schneider for their help with circular dichroism spectroscopy.

For the work presented in chapter 5, I also would like thank Stefanie Pannwitt and Margareta Trefz for help with protein production and sample characterization. Sabine Pütz provided invaluable support with cell culture and Mischa Schwendy with confocal microscopy. Marc-Jan van Zadel and Florian Gericke provided excellent technical support for setup construction. My thanks go to Ina Schäfer from the Core Facility Flow Cytometry, Institute for Molecular Biology Mainz, for sorting of GFP-transfected cells.

Finally, I would like to thank my family and non-scientific friends who supported me during my entire studies. For now, there will be no more weekends where I hide from you in the lab.

# Bibliography

- [1] A. J. Engler, S. Sen, H. L. Sweeney, and D. E. Discher, “Matrix elasticity directs stem cell lineage specification.,” *Cell*, vol. 126, pp. 677–689, Aug. 2006.
- [2] M. J. Paszek, N. Zahir, K. R. Johnson, J. N. Lakins, G. I. Rozenberg, A. Gefen, C. A. Reinhart-King, S. S. Margulies, M. Dembo, D. Boettiger, D. A. Hammer, and V. M. Weaver, “Tensional homeostasis and the malignant phenotype.,” *Cancer cell*, vol. 8, pp. 241–254, Sept. 2005.
- [3] D. E. Ingber, “Can cancer be reversed by engineering the tumor microenvironment?,” *Seminars in Cancer Biology*, vol. 18, no. 5, pp. 356 – 364, 2008. The Role of the Microenvironment in Tumor Biology.
- [4] M. Rief, M. Gautel, A. Schemmel, and H. E. Gaub, “The mechanical stability of immunoglobulin and fibronectin iii domains in the muscle protein titin measured by atomic force microscopy.,” *Biophysical Journal*, vol. 75, pp. 3008–3014, Dec. 1998.
- [5] M. I. Kokkinos, R. Wafai, M. K. Wong, D. F. Newgreen, E. W. Thompson, and M. Waltham, “Vimentin and epithelial-mesenchymal transition in human breast cancer—observations in vitro and in vivo.,” *Cells, tissues, organs*, vol. 185, pp. 191–203, 2007.
- [6] D. S. Fudge, K. H. Gardner, V. T. Forsyth, C. Riekel, and J. M. Gosline, “The mechanical properties of hydrated intermediate filaments: insights from hagfish slime threads,” *Biophysical journal*, vol. 85, no. 3, pp. 2015–2027, 2003.
- [7] Z. Qin, L. Kreplak, and M. J. Buehler, “Hierarchical structure controls nanomechanical properties of vimentin intermediate filaments,” *PloS one*, vol. 4, no. 10, p. e7294, 2009.
- [8] M. G. Mendez, S.-I. Kojima, and R. D. Goldman, “Vimentin induces changes in cell shape, motility, and adhesion during the epithelial to mesenchymal transition.,” *FASEB journal : official publication of the Federation of American Societies for Experimental Biology*, vol. 24, pp. 1838–1851, June 2010.
- [9] R. I. Litvinov, D. A. Faizullin, Y. F. Zuev, and J. W. Weisel, “The  $\alpha$ -helix to  $\beta$ -sheet transition in stretched and compressed hydrated fibrin clots,” *Biophysical journal*, vol. 103, no. 5, pp. 1020–1027, 2012.
- [10] M. E. Lindgren, M. M. HLlbrink, A. M. Elmquist, and I. Langel, “Passage of cell-penetrating peptides across a human epithelial cell layer in vitro,” *Biochemical Journal*, vol. 377, no. 1, pp. 69–76, 2004.
- [11] P. Lundberg and I. Langel, “Uptake mechanisms of cell-penetrating peptides derived from the alzheimers disease associated gamma-secretase complex,” *International Journal of Peptide Research and Therapeutics*, vol. 12, no. 2, pp. 105–114, 2006.

- 
- [12] R. Milo, "What is the total number of protein molecules per cell volume? a call to rethink some published values," *BioEssays*, vol. 35, no. 12, pp. 1050–1055, 2013.
- [13] L. Banci, L. Barbieri, I. Bertini, E. Luchinat, E. Secci, Y. Zhao, and A. R. Aricescu, "Atomic-resolution monitoring of protein maturation in live human cells by nmr," *Nature chemical biology*, vol. 9, pp. 297–299, Mar. 2013.
- [14] J. M. Plitzko, B. Schuler, and P. Selenko, "Structural biology outside the boxinside the cell," *Current Opinion in Structural Biology*, vol. 46, pp. 110 – 121, 2017. Cryo electron microscopy: exciting advances in CryoEM herald a new era in structural biology Biophysical methods: behind the scenes of the cryo-EM revolution.
- [15] F. R. PIEPER, F. A. VAN DE KLUNDERT, J. M. RAATS, J. B. HENDERIK, G. SCHAART, F. C. RAMAEKERS, and H. BLOEMENDAL, "Regulation of vimentin expression in cultured epithelial cells," *European Journal of Biochemistry*, vol. 210, no. 2, pp. 509–519, 1992.
- [16] J. Wehland and K. Weber, "Distribution of fluorescently labeled actin and tropomyosin after microinjection in living tissue culture cells as observed with tv image intensification," *Experimental Cell Research*, vol. 127, no. 2, pp. 397 – 408, 1980.
- [17] F. Fleissner, M. Bonn, and S. H. Parekh, "Microscale spatial heterogeneity of protein structural transitions in fibrin matrices," *Science Advances*, vol. 2, no. 7, p. e1501778, 2016.
- [18] F. Fleissner, S. Ptz, M. Schwendy, M. Bonn, and S. H. Parekh, "Measuring intracellular secondary structure of a cell-penetrating peptide in situ," *Anal Chem*, vol. 89, no. 21, pp. 11310–11317, 2017.
- [19] H. J. Fromm and M. Hargrove, *Essentials of biochemistry*. Springer Science & Business Media, 2012.
- [20] E. Buxbaum, *Fundamentals of protein structure and function*, vol. 31. Springer, 2007.
- [21] E. Hamed and S. Ketten, "Hierarchical cascades of instability govern the mechanics of coiled coils: helix unfolding precedes coil unzipping," *Biophysical journal*, vol. 107, no. 2, pp. 477–484, 2014.
- [22] T. McKee and J. R. McKee, *Biochemistry: the molecular basis of life*. Oxford University Press Oxford, 2012.
- [23] G. D. Rose, *Encyclopedia of Biological Chemistry*,. Academic Press, 2013.
- [24] D. Shortle, "The denatured state (the other half of the folding equation) and its role in protein stability.," *FASEB journal : official publication of the Federation of American Societies for Experimental Biology*, vol. 10, pp. 27–34, Jan. 1996.
- [25] L. J. Smith, K. M. Fiebig, H. Schwalbe, and C. M. Dobson, "The concept of a random coil: Residual structure in peptides and denatured proteins," *Folding and Design*, vol. 1, no. 5, pp. R95–R106, 1996.
- [26] I. Schwaiger, C. Sattler, D. R. Hostetter, and M. Rief, "The myosin coiled-coil is a truly elastic protein structure," *Nature materials*, vol. 1, no. 4, p. 232, 2002.

- [27] J. W. Weisel, "The mechanical properties of fibrin for basic scientists and clinicians," *Biophysical chemistry*, vol. 112, no. 2, pp. 267–276, 2004.
- [28] S. M. Kreuzer and R. Elber, "Coiled-coil response to mechanical force: global stability and local cracking," *Biophysical journal*, vol. 105, pp. 951–961, Aug. 2013.
- [29] G. I. Bell *et al.*, "Models for the specific adhesion of cells to cells," *Science*, vol. 200, no. 4342, pp. 618–627, 1978.
- [30] T. Ackbarow and M. J. Buehler, "Superelasticity, energy dissipation and strain hardening of vimentin coiled-coil intermediate filaments: atomistic and continuum studies," *Journal of Materials Science*, vol. 42, no. 21, pp. 8771–8787, 2007.
- [31] Y. Taniguchi, A. Kobayashi, and M. Kawakami, "Mechanical unfolding studies of protein molecules," *Biophysics*, vol. 8, pp. 51–58, 2012.
- [32] T. Ackbarow, D. Sen, C. Thaulow, and M. J. Buehler, "Alpha-helical protein networks are self-protective and flaw-tolerant," *PLoS One*, vol. 4, no. 6, p. e6015, 2009.
- [33] L. Kreplak, H. Herrmann, and U. Aebi, "Tensile properties of single desmin intermediate filaments," *Biophysical journal*, vol. 94, no. 7, pp. 2790–2799, 2008.
- [34] M. Sotomayor and K. Schulten, "Single-molecule experiments in vitro and in silico," *Science*, vol. 316, no. 5828, pp. 1144–1148, 2007.
- [35] A. Zhmurov, O. Kononova, R. I. Litvinov, R. I. Dima, V. Barsegov, and J. W. Weisel, "Mechanical transition from  $\alpha$ -helical coiled coils to  $\beta$ -sheets in fibrin (ogen)," *Journal of the American Chemical Society*, vol. 134, no. 50, pp. 20396–20402, 2012.
- [36] Z. Qin and M. J. Buehler, "Molecular dynamics simulation of the  $\alpha$ -helix to  $\beta$ -sheet transition in coiled protein filaments: Evidence for a critical filament length scale," *Physical Review Letters*, vol. 104, no. 19, p. 198304, 2010.
- [37] M. Arslan, Z. Qin, and M. J. Buehler, "Coiled-coil intermediate filament stutter instability and molecular unfolding," *Computer methods in biomechanics and biomedical engineering*, vol. 14, no. 05, pp. 483–489, 2011.
- [38] H. Herrmann, H. Bär, L. Kreplak, S. V. Strelkov, and U. Aebi, "Intermediate filaments: from cell architecture to nanomechanics," *Nature Reviews Molecular Cell Biology*, vol. 8, no. 7, pp. 562–573, 2007.
- [39] J. Block, H. Witt, A. Candelli, E. J. Peterman, G. J. Wuite, A. Janshoff, and S. Köster, "Nonlinear loading-rate-dependent force response of individual vimentin intermediate filaments to applied strain," *Physical Review Letters*, vol. 118, no. 4, p. 048101, 2017.
- [40] I. K. Piechocka, R. G. Bacabac, M. Potters, F. C. MacKintosh, and G. H. Koenenkerink, "Structural hierarchy governs fibrin gel mechanics," *Biophysical journal*, vol. 98, no. 10, pp. 2281–2289, 2010.
- [41] A. E. Brown, R. I. Litvinov, D. E. Discher, P. K. Purohit, and J. W. Weisel, "Multiscale mechanics of fibrin polymer: gel stretching with protein unfolding and loss of water," *science*, vol. 325, no. 5941, pp. 741–744, 2009.
- [42] W. W. Parson, *Modern optical spectroscopy*. Springer, 2007.
- [43] W. Demtröder, *Laser spectroscopy*, vol. 1. Springer, 2008.



- 
- [44] B. Schrader, *Infrared and Raman spectroscopy: methods and applications*. John Wiley & Sons, 2008.
- [45] G. J. Thomas, “Raman spectroscopy of protein and nucleic acid assemblies,” *Annual review of biophysics and biomolecular structure*, vol. 28, pp. 1–27, 1999.
- [46] Z. Movasaghi, S. Rehman, and I. U. Rehman, “Raman spectroscopy of biological tissues,” *Applied Spectroscopy Reviews*, vol. 42, no. 5, pp. 493–541, 2007.
- [47] M. C. Chen and R. C. Lord, “Laser-excited raman spectroscopy of biomolecules. 9. laser raman spectroscopic studies of the thermal unfolding of ribonuclease a,” *Biochemistry*, vol. 15, no. 9, pp. 1889–1897, 1976.
- [48] W. K. Surewicz, H. H. Mantsch, and D. Chapman, “Determination of protein secondary structure by fourier transform infrared spectroscopy: a critical assessment,” *Biochemistry*, vol. 32, no. 2, pp. 389–394, 1993.
- [49] T. Miyazawa, “Perturbation treatment of the characteristic vibrations of polypeptide chains in various configurations,” *The Journal of Chemical Physics*, vol. 32, no. 6, pp. 1647–1652, 1960.
- [50] R. Tuma, “Raman spectroscopy of proteins: from peptides to large assemblies,” *Journal of Raman Spectroscopy*, vol. 36, no. 4, pp. 307–319, 2005.
- [51] A. Rygula, K. Majzner, K. M. Marzec, A. Kaczor, M. Pilarczyk, and M. Baranska, “Raman spectroscopy of proteins: a review,” *Journal of Raman Spectroscopy*, vol. 44, no. 8, pp. 1061–1076, 2013.
- [52] H. Schulz and M. Baranska, “Identification and quantification of valuable plant substances by ir and raman spectroscopy,” *Vibrational Spectroscopy*, vol. 43, no. 1, pp. 13–25, 2007.
- [53] A. Barth and C. Zscherp, “What vibrations tell about proteins,” *Quarterly reviews of biophysics*, vol. 35, no. 4, pp. 369–430, 2002.
- [54] P. Hamm and M. Zanni, *Concepts and methods of 2D infrared spectroscopy*. Cambridge University Press, 2011.
- [55] M. Berjot, J. Marx, and A. Alix, “Determination of the secondary structure of proteins from the raman amide i band: the reference intensity profiles method,” *Journal of Raman spectroscopy*, vol. 18, no. 4, pp. 289–300, 1987.
- [56] S. Krimm and J. Bandekar, “Vibrational spectroscopy and conformation of peptides, polypeptides, and proteins,” *Advances in protein chemistry*, vol. 38, pp. 181–364, 1986.
- [57] M. Murrell, P. W. Oakes, M. Lenz, and M. L. Gardel, “Forcing cells into shape: the mechanics of actomyosin contractility,” *Nature reviews. Molecular cell biology*, vol. 16, pp. 486–498, Aug. 2015.
- [58] A. Mogilner and G. Oster, “Force generation by actin polymerization ii: the elastic ratchet and tethered filaments,” *Biophysical journal*, vol. 84, pp. 1591–1605, Mar. 2003.
- [59] K. J. Gooch and C. J. Tennant, *Mechanical Forces: Their Effects on Cells and Tissues*. Springer, 2012.

- [60] M. C. Raadsheer, T. M. G. J. Van Eijden, F. C. Van Ginkel, and B. Prahl-Andersen, "Human jaw muscle strength and size in relation to limb muscle strength and size.," *European journal of oral sciences*, vol. 112, pp. 398–405, Oct. 2004.
- [61] D. A. Fletcher and R. D. Mullins, "Cell mechanics and the cytoskeleton.," *Nature*, vol. 463, pp. 485–492, Jan. 2010.
- [62] D. E. Ingber, N. Wang, and D. Stamenovic, "Tensegrity, cellular biophysics, and the mechanics of living systems.," *Reports on progress in physics. Physical Society (Great Britain)*, vol. 77, p. 046603, Apr. 2014.
- [63] R. Dominguez and K. C. Holmes, "Actin structure and function.," *Annual review of biophysics*, vol. 40, pp. 169–186, 2011.
- [64] S. Deguchi, T. Ohashi, and M. Sato, "Tensile properties of single stress fibers isolated from cultured vascular smooth muscle cells.," *Journal of biomechanics*, vol. 39, pp. 2603–2610, 2006.
- [65] X. Liu and G. H. Pollack, "Mechanics of f-actin characterized with microfabricated cantilevers.," *Biophysical journal*, vol. 83, pp. 2705–2715, Nov. 2002.
- [66] P. A. Janmey, U. Euteneuer, P. Traub, and M. Schliwa, "Viscoelastic properties of vimentin compared with other filamentous biopolymer networks.," *The Journal of cell biology*, vol. 113, pp. 155–160, Apr. 1991.
- [67] F. Gittes, B. Mickey, J. Nettleton, and J. Howard, "Flexural rigidity of microtubules and actin filaments measured from thermal fluctuations in shape.," *The Journal of cell biology*, vol. 120, pp. 923–934, Feb. 1993.
- [68] M. A. Jordan and L. Wilson, "Microtubules as a target for anticancer drugs.," *Nature reviews. Cancer*, vol. 4, pp. 253–265, Apr. 2004.
- [69] H. Herrmann and U. Aebi, "Intermediate filaments: molecular structure, assembly mechanism, and integration into functionally distinct intracellular scaffolds.," *Annual review of biochemistry*, vol. 73, pp. 749–789, 2004.
- [70] N. Wang and D. Stamenovi, "Contribution of intermediate filaments to cell stiffness, stiffening, and growth.," *American journal of physiology. Cell physiology*, vol. 279, pp. C188–C194, July 2000.
- [71] E. W. Flitney, E. R. Kuczmarski, S. A. Adam, and R. D. Goldman, "Insights into the mechanical properties of epithelial cells: the effects of shear stress on the assembly and remodeling of keratin intermediate filaments.," *FASEB journal : official publication of the Federation of American Societies for Experimental Biology*, vol. 23, pp. 2110–2119, July 2009.
- [72] R. O. Hynes, "Integrins: bidirectional, allosteric signaling machines.," *Cell*, vol. 110, pp. 673–687, Sept. 2002.
- [73] A. J. Maniotis, C. S. Chen, and D. E. Ingber, "Demonstration of mechanical connections between integrins, cytoskeletal filaments, and nucleoplasm that stabilize nuclear structure.," *Proceedings of the National Academy of Sciences of the United States of America*, vol. 94, pp. 849–854, Feb. 1997.
- [74] C. Grashoff, B. D. Hoffman, M. D. Brenner, R. Zhou, M. Parsons, M. T. Yang, M. A. McLean, S. G. Sligar, C. S. Chen, T. Ha, and M. A. Schwartz, "Measuring mechanical tension across vinculin reveals regulation of focal adhesion dynamics.," *Nature*, vol. 466, pp. 263–266, July 2010.

- 
- [75] C. M. Nelson, D. M. Pirone, J. L. Tan, and C. S. Chen, "Vascular endothelial-cadherin regulates cytoskeletal tension, cell spreading, and focal adhesions by stimulating rhoa.," *Molecular biology of the cell*, vol. 15, pp. 2943–2953, June 2004.
- [76] W. F. Liu, C. M. Nelson, J. L. Tan, and C. S. Chen, "Cadherins, rhoa, and rac1 are differentially required for stretch-mediated proliferation in endothelial versus smooth muscle cells.," *Circulation research*, vol. 101, pp. e44–e52, Aug. 2007.
- [77] G. Wiche, "Role of plectin in cytoskeleton organization and dynamics.," *Journal of cell science*, vol. 111 ( Pt 17), pp. 2477–2486, Sept. 1998.
- [78] E. Fuchs and I. Karakesisoglou, "Bridging cytoskeletal intersections.," *Genes & development*, vol. 15, pp. 1–14, Jan. 2001.
- [79] D. Stamenovi and N. Wang, "Stress transmission within the cell.," *Comprehensive Physiology*, vol. 1, pp. 499–524, Jan. 2011.
- [80] D. E. Ingber, J. A. Madri, and J. D. Jamieson, "Role of basal lamina in neoplastic disorganization of tissue architecture.," *Proceedings of the National Academy of Sciences of the United States of America*, vol. 78, pp. 3901–3905, June 1981.
- [81] R. B. Fuller, "Tensegrity," *Portfolio and Art News Annual*, 1961.
- [82] S. Kumar, I. Z. Maxwell, A. Heisterkamp, T. R. Polte, T. P. Lele, M. Salanga, E. Mazur, and D. E. Ingber, "Viscoelastic retraction of single living stress fibers and its impact on cell shape, cytoskeletal organization, and extracellular matrix mechanics.," *Biophysical journal*, vol. 90, pp. 3762–3773, May 2006.
- [83] C. P. Brangwynne, F. C. MacKintosh, S. Kumar, N. A. Geisse, J. Talbot, L. Mahadevan, K. K. Parker, D. E. Ingber, and D. A. Weitz, "Microtubules can bear enhanced compressive loads in living cells because of lateral reinforcement.," *The Journal of cell biology*, vol. 173, pp. 733–741, June 2006.
- [84] C. Sultan, D. Stamenovi, and D. E. Ingber, "A computational tensegrity model predicts dynamic rheological behaviors in living cells.," *Annals of biomedical engineering*, vol. 32, pp. 520–530, Apr. 2004. Grant numbers: NASA NAG-2-1501.
- [85] K. Y. Volokh, "On tensegrity in cell mechanics.," *Molecular & cellular biomechanics : MCB*, vol. 8, pp. 195–214, Sept. 2011.
- [86] R. Kamm, *Cytoskeletal Mechanics*. CAMBRIDGE UNIVERSITY PRESS, 2006.
- [87] B. L. Ricca, G. Venugopalan, and D. A. Fletcher, "To pull or be pulled: parsing the multiple modes of mechanotransduction.," *Current opinion in cell biology*, vol. 25, pp. 558–564, Oct. 2013.
- [88] T. Iskratsch, H. Wolfenson, and M. P. Sheetz, "Appreciating force and shape: the rise of mechanotransduction in cell biology.," *Nature reviews. Molecular cell biology*, vol. 15, pp. 825–833, Dec. 2014.
- [89] B. D. Hoffman, C. Grashoff, and M. A. Schwartz, "Dynamic molecular processes mediate cellular mechanotransduction.," *Nature*, vol. 475, pp. 316–323, July 2011.
- [90] A. W. Orr, B. P. Helmke, B. R. Blackman, and M. A. Schwartz, "Mechanisms of mechanotransduction.," *Developmental cell*, vol. 10, pp. 11–20, Jan. 2006.

- [91] A. J. Engler, M. A. Griffin, S. Sen, C. G. Bnnemann, H. L. Sweeney, and D. E. Discher, "Myotubes differentiate optimally on substrates with tissue-like stiffness: pathological implications for soft or stiff microenvironments," *The Journal of cell biology*, vol. 166, pp. 877–887, Sept. 2004.
- [92] F. M. Watt and W. T. S. Huck, "Role of the extracellular matrix in regulating stem cell fate.," *Nature reviews. Molecular cell biology*, vol. 14, pp. 467–473, Aug. 2013.
- [93] D. E. Discher, P. Janmey, and Y.-L. Wang, "Tissue cells feel and respond to the stiffness of their substrate.," *Science (New York, N.Y.)*, vol. 310, pp. 1139–1143, Nov. 2005.
- [94] C. S. Chen, "Mechanotransduction - a field pulling together?," *Journal of cell science*, vol. 121, pp. 3285–3292, Oct. 2008.
- [95] M. Thery, V. Racine, A. Pepin, M. Piel, Y. Chen, J.-B. Sibarita, and M. Bornens, "The extracellular matrix guides the orientation of the cell division axis.," *Nature cell biology*, vol. 7, pp. 947–953, Oct. 2005.
- [96] V. Lecaudey and D. Gilmour, "Organizing moving groups during morphogenesis.," *Current opinion in cell biology*, vol. 18, pp. 102–107, Feb. 2006.
- [97] P. Martin and S. M. Parkhurst, "Parallels between tissue repair and embryo morphogenesis.," *Development (Cambridge, England)*, vol. 131, pp. 3021–3034, July 2004.
- [98] X. Trepac, M. R. Wasserman, T. E. Angelini, E. Millet, D. A. Weitz, J. P. Butler, and J. J. Fredberg, "Physical forces during collective cell migration," 2009.
- [99] S. Sukharev, M. Betanzos, C. S. Chiang, and H. R. Guy, "The gating mechanism of the large mechanosensitive channel mscL.," *Nature*, vol. 409, pp. 720–724, Feb. 2001.
- [100] A. del Rio, R. Perez-Jimenez, R. Liu, P. Roca-Cusachs, J. M. Fernandez, and M. P. Sheetz, "Stretching single talin rod molecules activates vinculin binding.," *Science (New York, N.Y.)*, vol. 323, pp. 638–641, Jan. 2009.
- [101] J. Arnadttir and M. Chalfie, "Eukaryotic mechanosensitive channels.," *Annual review of biophysics*, vol. 39, pp. 111–137, 2010.
- [102] Y. Sawada, M. Tamada, B. J. Dubin-Thaler, O. Cherniavskaya, R. Sakai, S. Tanaka, and M. P. Sheetz, "Force sensing by mechanical extension of the src family kinase substrate p130cas.," *Cell*, vol. 127, pp. 1015–1026, Dec. 2006.
- [103] J. L. Bos, J. de Rooij, and K. A. Reedquist, "Rap1 signalling: adhering to new models.," *Nature reviews. Molecular cell biology*, vol. 2, pp. 369–377, May 2001.
- [104] V. I. Risca, E. B. Wang, O. Chaudhuri, J. J. Chia, P. L. Geissler, and D. A. Fletcher, "Actin filament curvature biases branching direction.," *Proceedings of the National Academy of Sciences of the United States of America*, vol. 109, pp. 2913–2918, Feb. 2012.
- [105] A. R. Harris and G. T. Charras, "Experimental validation of atomic force microscopy-based cell elasticity measurements.," *Nanotechnology*, vol. 22, p. 345102, Aug. 2011.
- [106] H. Qiu, Y. Zhu, Z. Sun, J. P. Trzeciakowski, M. Gansner, C. Depre, R. R. G. Resuello, F. F. Natividad, W. C. Hunter, G. M. Genin, E. L. Elson, D. E. Vatner, G. A. Meininger, and S. F. Vatner, "Short communication: vascular smooth muscle

- cell stiffness as a mechanism for increased aortic stiffness with aging.,” *Circulation research*, vol. 107, pp. 615–619, Sept. 2010.
- [107] F. M. Hochmuth, J. Y. Shao, J. Dai, and M. P. Sheetz, “Deformation and flow of membrane into tethers extracted from neuronal growth cones.,” *Biophysical journal*, vol. 70, pp. 358–369, Jan. 1996.
  - [108] D. Raucher, T. Stauffer, W. Chen, K. Shen, S. Guo, J. D. York, M. P. Sheetz, and T. Meyer, “Phosphatidylinositol 4,5-bisphosphate functions as a second messenger that regulates cytoskeleton-plasma membrane adhesion.,” *Cell*, vol. 100, pp. 221–228, Jan. 2000.
  - [109] F. Bordeleau, J. Bessard, N. Marceau, and Y. Sheng, “Measuring integrated cellular mechanical stress response at focal adhesions by optical tweezers.,” *Journal of biomedical optics*, vol. 16, p. 095005, Sept. 2011.
  - [110] A. C. De Luca, G. Volpe, A. M. Drets, M. I. Geli, G. Pesce, G. Rusciano, A. Sasso, and D. Petrov, “Real-time actin-cytoskeleton depolymerization detection in a single cell using optical tweezers.,” *Optics express*, vol. 15, pp. 7922–7932, June 2007.
  - [111] N. Bonakdar, J. Luczak, L. Lautscham, M. Czonstke, T. M. Koch, A. Mainka, T. Jungbauer, W. H. Goldmann, R. Schrder, and B. Fabry, “Biomechanical characterization of a desminopathy in primary human myoblasts.,” *Biochemical and biophysical research communications*, vol. 419, pp. 703–707, Mar. 2012.
  - [112] R. M. Hochmuth, “Micropipette aspiration of living cells.,” *Journal of biomechanics*, vol. 33, pp. 15–22, Jan. 2000.
  - [113] L. M. Lee and A. P. Liu, “The application of micropipette aspiration in molecular mechanics of single cells.,” *Journal of nanotechnology in engineering and medicine*, vol. 5, pp. 0408011–0408016, Nov. 2014.
  - [114] D. Tremblay, S. Chagnon-Lessard, M. Mirzaei, A. E. Pelling, and M. Godin, “A microscale anisotropic biaxial cell stretching device for applications in mechanobiology.,” *Biotechnology letters*, vol. 36, pp. 657–665, Mar. 2014.
  - [115] Y. Shao, X. Tan, R. Novitski, M. Muqaddam, P. List, L. Williamson, J. Fu, and A. P. Liu, “Uniaxial cell stretching device for live-cell imaging of mechanosensitive cellular functions.,” *The Review of scientific instruments*, vol. 84, p. 114304, Nov. 2013.
  - [116] Y. Huang, N.-T. Nguyen, K. S. Lok, P. P. F. Lee, M. Su, M. Wu, L. Kocgozlu, and B. Ladoux, “Multiarray cell stretching platform for high-magnification real-time imaging.,” *Nanomedicine (London, England)*, vol. 8, pp. 543–553, Apr. 2013.
  - [117] T. Dey, M. C. Mann, and W. H. Goldmann, “Comparing mechano-transduction in fibroblasts deficient of focal adhesion proteins.,” *Biochemical and biophysical research communications*, vol. 413, pp. 541–544, Oct. 2011.
  - [118] P. A. Janmey, J. P. Winer, M. E. Murray, and Q. Wen, “The hard life of soft cells.,” *Cell motility and the cytoskeleton*, vol. 66, pp. 597–605, Aug. 2009.
  - [119] E. Moeendarbary and A. R. Harris, “Cell mechanics: principles, practices, and prospects.,” *Wiley interdisciplinary reviews. Systems biology and medicine*, vol. 6, pp. 371–388, 2014.

- [120] P. C. Georges and P. A. Janmey, "Cell type-specific response to growth on soft materials.," *Journal of applied physiology (Bethesda, Md. : 1985)*, vol. 98, pp. 1547–1553, Apr. 2005.
- [121] I. Spector, N. R. Shochet, Y. Kashman, and A. Groweiss, "Latrunculins: novel marine toxins that disrupt microfilament organization in cultured cells.," *Science (New York, N.Y.)*, vol. 219, pp. 493–495, Feb. 1983.
- [122] K. Seltsmann, A. W. Fritsch, J. A. Ks, and T. M. Magin, "Keratins significantly contribute to cell stiffness and impact invasive behavior.," *Proceedings of the National Academy of Sciences of the United States of America*, vol. 110, pp. 18507–18512, Nov. 2013.
- [123] A. F. Straight, A. Cheung, J. Limouze, I. Chen, N. J. Westwood, J. R. Sellers, and T. J. Mitchison, "Dissecting temporal and spatial control of cytokinesis with a myosin ii inhibitor.," *Science (New York, N.Y.)*, vol. 299, pp. 1743–1747, Mar. 2003.
- [124] R. L. Margolis and L. Wilson, "Addition of colchicine–tubulin complex to microtubule ends: the mechanism of substoichiometric colchicine poisoning.," *Proceedings of the National Academy of Sciences of the United States of America*, vol. 74, pp. 3466–3470, Aug. 1977.
- [125] R. A. Stanton, K. M. Gernert, J. H. Nettles, and R. Aneja, "Drugs that target dynamic microtubules: a new molecular perspective.," *Medicinal research reviews*, vol. 31, pp. 443–481, May 2011.
- [126] A. H. Sharpe, L. B. Chen, J. R. Murphy, and B. N. Fields, "Specific disruption of vimentin filament organization in monkey kidney cv-1 cells by diphtheria toxin, exotoxin a, and cycloheximide.," *Proceedings of the National Academy of Sciences of the United States of America*, vol. 77, pp. 7267–7271, Dec. 1980.
- [127] A. Zhmurov, A. D. Protopopova, R. I. Litvinov, P. Zhukov, A. R. Mukhitov, J. W. Weisel, and V. Barsegov, "Structural basis of interfacial flexibility in fibrin oligomers.," *Structure (London, England : 1993)*, vol. 24, pp. 1907–1917, Nov. 2016.
- [128] A. Undas and R. A. S. Arins, "Fibrin clot structure and function: a role in the pathophysiology of arterial and venous thromboembolic diseases.," *Arteriosclerosis, thrombosis, and vascular biology*, vol. 31, pp. e88–e99, Dec. 2011.
- [129] M. W. Mosesson, K. R. Siebenlist, and D. A. Meh, "The structure and biological features of fibrinogen and fibrin.," *Annals of the New York Academy of Sciences*, vol. 936, no. 1, pp. 11–30, 2001.
- [130] E. A. Ryan, L. F. Mockros, J. W. Weisel, and L. Lorand, "Structural origins of fibrin clot rheology.," *Biophysical journal*, vol. 77, no. 5, pp. 2813–2826, 1999.
- [131] P. K. Purohit, R. I. Litvinov, A. E. Brown, D. E. Discher, and J. W. Weisel, "Protein unfolding accounts for the unusual mechanical behavior of fibrin networks.," *Acta biomaterialia*, vol. 7, no. 6, pp. 2374–2383, 2011.
- [132] A. A. Chernyatina, S. Nicolet, U. Aebi, H. Herrmann, and S. V. Strelkov, "Atomic structure of the vimentin central-helical domain and its implications for intermediate filament assembly.," *Proceedings of the National Academy of Sciences of the United States of America*, vol. 109, pp. 13620–13625, Aug. 2012.

- 
- [133] H. Herrmann, M. Hner, M. Brettel, S. A. Mller, K. N. Goldie, B. Fedtke, A. Lustig, W. W. Franke, and U. Aebi, "Structure and assembly properties of the intermediate filament protein vimentin: the role of its head, rod and tail domains.," *Journal of molecular biology*, vol. 264, pp. 933–953, Dec. 1996.
- [134] C. G. Lopez, O. Saldanha, K. Huber, and S. Kster, "Lateral association and elongation of vimentin intermediate filament proteins: A time-resolved light-scattering study.," *Proceedings of the National Academy of Sciences of the United States of America*, vol. 113, pp. 11152–11157, Oct. 2016.
- [135] S. Nafeey, I. Martin, T. Felder, P. Walther, and E. Felder, "Branching of keratin intermediate filaments," *Journal of structural biology*, vol. 194, no. 3, pp. 415–422, 2016.
- [136] S. Koester, Y.-C. Lin, H. Herrmann, and D. A. Weitz, "Nanomechanics of vimentin intermediate filament networks," *Soft Matter*, vol. 6, no. 9, pp. 1910–1914, 2010.
- [137] Z. Qin and M. J. Buehler, "Structure and dynamics of human vimentin intermediate filament dimer and tetramer in explicit and implicit solvent models.," *Journal of molecular modeling*, vol. 17, pp. 37–48, Jan. 2011.
- [138] Y. B. Yu, "Coiled-coils: stability, specificity, and drug delivery potential," *Advanced drug delivery reviews*, vol. 54, no. 8, pp. 1113–1129, 2002.
- [139] J. Xu, Y. Tseng, and D. Wirtz, "Strain hardening of actin filament networks. regulation by the dynamic cross-linking protein alpha-actinin.," *The Journal of biological chemistry*, vol. 275, pp. 35886–35892, Nov. 2000.
- [140] N. Wang, J. P. Butler, and D. E. Ingber, "Mechanotransduction across the cell surface and through the cytoskeleton.," *Science (New York, N.Y.)*, vol. 260, pp. 1124–1127, May 1993.
- [141] M. J. Buehler, "Rupture mechanics of vimentin intermediate filament tetramers," *Journal of Engineering Mechanics*, vol. 135, no. 5, 2009.
- [142] J. J. Barrett and A. Weber, "Pure-rotational raman scattering in a co 2 electric discharge," *JOSA*, vol. 60, no. 1, pp. 70–76, 1970.
- [143] E. Smith and G. Dent, *Modern Raman Spectroscopy*. John Wiley and Sons Ltd, 2004.
- [144] M. Procházka, "Surface-enhanced raman spectroscopy," *Biological and Medical Physics, Biomedical Engineering*, 2016.
- [145] K. H. Kneipp Katrin, Moskovits Martin, ed., *Surface-Enhanced Raman Scattering*. Springer, 2006.
- [146] N. W. Woodbury EJ, "Ruby laser operation in the near ir," *Proc. IRE*, vol. 50, p. 23472348., 1962.
- [147] P. Maker and R. Terhune, "Study of optical effects due to an induced polarization third order in the electric field strength," *Phys. Rev.*, vol. 137, 1965.
- [148] C. L. Evans and X. S. Xie, "Coherent anti-stokes raman scattering microscopy: chemical imaging for biology and medicine.," *Annual review of analytical chemistry (Palo Alto, Calif.)*, vol. 1, pp. 883–909, 2008.

- [149] X. S. X. Andreas Zumbusch, Gary R. Holtom, “Three-dimensional vibrational imaging by coherent anti-stokes raman scattering,” *Physical Review Letter*, vol. 82, 1999.
- [150] C. H. Camp Jr and M. T. Cicerone, “Chemically sensitive bioimaging with coherent raman scattering,” *Nature Photonics*, vol. 9, no. 5, pp. 295–305, 2015.
- [151] J. X. Cheng and X. S. Xie, “Vibrational spectroscopic imaging of living systems: An emerging platform for biology and medicine,” *Science*, vol. 350, no. 6264, pp. aaa8870–aaa8870, 2015.
- [152] C. W. Freudiger, W. Yang, G. R. Holtom, N. Peyghambarian, X. S. Xie, and K. Q. Kieu, “Stimulated raman scattering microscopy with a robust fibre laser source,” *Nature photonics*, vol. 8, no. 2, p. 153, 2014.
- [153] R. C. Prince, R. R. Frontiera, and E. O. Potma, “Stimulated raman scattering: from bulk to nano,” *Chemical reviews*, vol. 117, no. 7, pp. 5070–5094, 2016.
- [154] R. W. Boyd, *Nonlinear Optics*. Elsevier LTD, Oxford, 2008.
- [155] E. O. Potma and S. Mukamel, *Coherent Raman scattering microscopy*. CRC press, 2016.
- [156] S. H. Parekh, Y. J. Lee, K. A. Aamer, and M. T. Cicerone, “Label-free cellular imaging by broadband coherent anti-stokes raman scattering microscopy,” *Biophysical journal*, vol. 99, no. 8, pp. 2695–2704, 2010.
- [157] J.-X. Cheng and X. S. Xie, “Coherent anti-stokes raman scattering microscopy: instrumentation, theory, and applications,” 2004.
- [158] E. M. Vartiainen, H. A. Rinia, M. Mller, and M. Bonn, “Direct extraction of raman line-shapes from congested cars spectra.,” *Optics express*, vol. 14, pp. 3622–3630, Apr. 2006.
- [159] M. T. Cicerone, K. A. Aamer, Y. J. Lee, and E. Vartiainen, “Maximum entropy and time-domain kramers-kronig phase retrieval approaches are functionally equivalent for cars microspectroscopy,” *Journal of Raman Spectroscopy*, vol. 43, no. 5, pp. 637–643, 2012.
- [160] E. M. Vartiainen, “Phase retrieval approach for coherent anti-stokes raman scattering spectrum analysis,” *J. Opt. Soc. Am. B*, vol. 9, no. 8, pp. 1209–1214, 1992.
- [161] Y. Liu, Y. J. Lee, and M. T. Cicerone, “Broadband cars spectral phase retrieval using a time-domain kramers-kronig transform.,” *Optics letters*, vol. 34, pp. 1363–1365, May 2009.
- [162] Y. Liu, Y. J. Lee, and M. T. Cicerone, “Fast extraction of resonant vibrational response from cars spectra with arbitrary nonresonant background,” *Journal of Raman Spectroscopy*, vol. 40, no. 7, pp. 726–731, 2009,.
- [163] M. Müller and A. Zumbusch, “Coherent anti-stokes raman scattering microscopy,” *ChemPhysChem*, vol. 8, no. 15, pp. 2156–2170, 2007.
- [164] C. P. Broedersz, K. E. Kasza, L. M. Jawerth, S. Munster, D. A. Weitz, and F. C. MacKintosh, “Measurement of nonlinear rheology of cross-linked biopolymer gels,” *Soft Matter*, vol. 6, no. 17, pp. 4120–4127, 2010.
- [165] . R. W. H. J W Goodwin, *Rheology for Chemists: An Introduction*. Royal Society of Chemistry, 2008.



- 
- [166] C. W. Macosko, ed., *Rheology: Principles, Measurements, and Applications*. Wiley-VCH, 1994.
- [167] M. Gardel, J. Shin, F. MacKintosh, L. Mahadevan, P. Matsudaira, and D. Weitz, “Elastic behavior of cross-linked and bundled actin networks,” *Science*, vol. 304, no. 5675, pp. 1301–1305, 2004.
- [168] M. L. Gardel, F. Nakamura, J. H. Hartwig, J. C. Crocker, T. P. Stossel, and D. A. Weitz, “Prestressed f-actin networks cross-linked by hinged filamins replicate mechanical properties of cells,” *Proc Natl Acad Sci U S A*, vol. 103, no. 6, pp. 1762–7, 2006.
- [169] T. F. Tadros, *Rheology of Dispersions: Principles and Applications*. Wiley, 2010.
- [170] M. T. J. Duncan M D, Reintjes J, “Imaging biological compounds using the coherent anti-stokes raman scattering microscope,” *Optical Engineering*, vol. 24, no. 2, p. pp. 352, 1985.
- [171] E. O. Potma, W. P. de Boeij, and D. A. Wiersma, “Nonlinear coherent four-wave mixing in optical microscopy,” *Journal of the Optical Society of America B*, vol. 17, no. 10, pp. 1678–1684, 2000.
- [172] R. L. McCreery, *Raman Spectroscopy for Chemical Analysis*. Wiley, 2005.
- [173] W. M. Tolles, J. Nibler, J. McDonald, and A. Harvey, “A review of the theory and application of coherent anti-stokes raman spectroscopy (cars),” *Applied Spectroscopy*, vol. 31, no. 4, pp. 253–271, 1977.
- [174] M. Cui, B. R. Bachler, and J. P. Ogilvie, “Comparing coherent and spontaneous raman scattering under biological imaging conditions,” *Opt Lett*, vol. 34, no. 6, pp. 773–5, 2009.
- [175] M. Okuno, H. Kano, P. Leproux, V. Couderc, and H. O. Hamaguchi, “Ultrabroadband multiplex cars microspectroscopy and imaging using a subnanosecond supercontinuum light source in the deep near infrared,” *Opt Lett*, vol. 33, no. 9, pp. 923–5, 2008.
- [176] M. Okuno, H. Kano, P. Leproux, V. Couderc, J. P. Day, M. Bonn, and H.-o. Hamaguchi, “Quantitative cars molecular fingerprinting of single living cells with the use of the maximum entropy method,” *Angewandte Chemie International Edition*, vol. 49, no. 38, pp. 6773–6777, 2010.
- [177] C. A. Schneider, W. S. Rasband, and K. W. Eliceiri, “Nih image to imagej: 25 years of image analysis,” *Nat Methods*, vol. 9, no. 7, pp. 671–5, 2012.
- [178] J. Jonkman and C. M. Brown, “Any way you slice ita comparison of confocal microscopy techniques,” *Journal of Biomolecular Techniques : JBT*, vol. 26, no. 2, pp. 54–65, 2015.
- [179] B. D. Beier and A. J. Berger, “Method for automated background subtraction from raman spectra containing known contaminants,” *Analyst*, vol. 134, no. 6, pp. 1198–202, 2009.
- [180] W. M. Sears, J. L. Hunt, and J. R. Stevens, “Raman scattering from polymerizing styrene. i. vibrational mode analysis,” *The Journal of Chemical Physics*, vol. 75, no. 4, pp. 1589–1598, 1981.

- [181] N. C. Holmes, W. J. Nellis, W. B. Graham, and G. E. Walrafen, "Spontaneous raman scattering from shocked water," *Physical Review Letters*, vol. 55, no. 22, pp. 2433–2436, 1985.
- [182] I. Jolliffe, *Principal Component Analysis*. Springer, 2002.
- [183] J. Ye, S. A. Fox, M. Cudic, E. M. Rezler, J. L. Lauer, G. B. Fields, and A. C. Terentis, "Determination of penetratin secondary structure in live cells with raman microscopy," *J Am Chem Soc*, vol. 132, no. 3, pp. 980–8, 2010.
- [184] G. Bergner, C. R. Albert, M. Schiller, G. Bringmann, T. Schirmeister, B. Dietzek, S. Niebling, S. Schlcker, and J. Popp, "Quantitative detection of c-deuterated drugs by cars microscopy and raman microspectroscopy," *Analyst*, vol. 136, no. 18, pp. 3686–93, 2011.
- [185] R. Tauler, "Multivariate curve resolution applied to second order data," *Chemometrics and Intelligent Laboratory Systems*, vol. 30, no. 1, pp. 133–146, 1995.
- [186] C. Ruckebusch and L. Blanchet, "Multivariate curve resolution: A review of advanced and tailored applications and challenges," *Analytica Chimica Acta*, vol. 765, pp. 28–36, 2013.
- [187] D. L. Massart, ed., *Handbook of Chemometrics and Qualimetrics, Volume 20A*. Elsevier Science, 1997.
- [188] J. Mendieta, M. S. Daz-Cruz, M. Esteban, and R. Tauler, "Multivariate curve resolution: a possible tool in the detection of intermediate structures in protein folding," *Biophys J*, vol. 74, no. 6, pp. 2876–88, 1998.
- [189] P. Geladi, "Notes on the history and nature of partial least squares (pls) modelling," *Journal of Chemometrics*, vol. 2, no. 4, pp. 231–246, 1988.
- [190] R. Vong, P. Geladi, S. Wold, and K. Esbensen, "Source contributions to ambient aerosol calculated by discriminat partial least squares regression (pls)," *Journal of Chemometrics*, vol. 2, no. 4, pp. 281–296, 1988.
- [191] H. Gampp, M. Maeder, C. J. Meyer, and A. D. Zuberbuehler, "Quantification of a known component in an unknown mixture," *Analytica Chimica Acta*, vol. 193, pp. 287–293, 1987.
- [192] . D. R. K. E. Ward Cheney, *Numerical Mathematics and Computing*. Brooks Cole Pub Co, 2012.
- [193] R. Tauler and E. Casassas, "Principal component analysis applied to the study of successive complex formation data in cu(ii)ethanolamine systems," *Journal of Chemometrics*, vol. 3, no. S1, pp. 151–161, 1989.
- [194] M. Vosough, C. Mason, R. Tauler, M. Jalali-Heravi, and M. Maeder, "On rotational ambiguity in model-free analyses of multivariate data," *Journal of Chemometrics*, vol. 20, no. 6-7, pp. 302–310, 2006.
- [195] J. Jaumot, A. de Juan, and R. Tauler, "Mcr-als gui 2.0: New features and applications," *Chemometrics and Intelligent Laboratory Systems*, vol. 140, pp. 1–12, 2015.
- [196] E. Hecht, "Optics, 4th," *International edition, Addison-Wesley, San Francisco*, vol. 3, 2002.

- 
- [197] D. Coling and B. Kachar, *Theory and Application of Fluorescence Microscopy*, book section 2, p. 2.1.12.1.11. John Wiley & Sons, Inc., 2001.
- [198] J. W. Lichtman and J.-A. Conchello, “Fluorescence microscopy,” *Nature Methods*, vol. 2, p. 910, 2005.
- [199] C. A. Combs, “Fluorescence microscopy: a concise guide to current imaging methods,” *Curr Protoc Neurosci*, vol. Chapter 2, p. Unit2.1, 2010.
- [200] A. Ettinger and T. Wittmann, “Fluorescence live cell imaging,” *Methods in cell biology*, vol. 123, pp. 77–94, 2014.
- [201] S. Weisenburger and V. Sandoghdar, “Light microscopy: an ongoing contemporary revolution,” *Contemporary Physics*, vol. 56, no. 2, pp. 123–143, 2015.
- [202] T. Wilson, “Resolution and optical sectioning in the confocal microscope,” *Journal of Microscopy*, vol. 244, no. 2, pp. 113–121, 2011.
- [203] J. Schindelin, I. Arganda-Carreras, E. Frise, V. Kaynig, M. Longair, T. Pietzsch, S. Preibisch, C. Rueden, S. Saalfeld, B. Schmid, *et al.*, “Fiji: an open-source platform for biological-image analysis,” *Nature methods*, vol. 9, no. 7, p. 676, 2012.
- [204] C. T. Chung, S. L. Niemela, and R. H. Miller, “One-step preparation of competent escherichia coli: transformation and storage of bacterial cells in the same solution,” *Proc Natl Acad Sci U S A*, 1989.
- [205] O. Paliy and T. S. Gunasekera, “Growth of e. coli bl21 in minimal media with different gluconeogenic carbon sources and salt contents,” *Applied microbiology and biotechnology*, vol. 73, pp. 1169–1172, Jan. 2007.
- [206] D. Wirth, “Expression, reinigung und charakterisierung von humanem vimentin,” Master’s thesis, Johannes Gutenberg-Universitt Mainz, 2015.
- [207] J. Anderl, K. Huryn-Selvar, H. Liu, K. Su, M. Santos, M. Hsu, J. Ma, and L. Armstrong, “Lentibrite lentiviral biosensors for fluorescent cellular imaging: Analysis of autophagosome formation,” *Application Note EMD Millipore Bioscience*, 2012.
- [208] N.-S. Xia, W.-X. Luo, J. Zhang, X.-Y. Xie, H.-J. Yang, S.-W. Li, M. Chen, and M.-H. Ng, “Bioluminescence of aequorea macrodactyla, a common jellyfish species in the east china sea,” *Marine Biotechnology*, vol. 4, p. 155, Mar. 2002.
- [209] J. V. Shah and P. A. Janmey, “Strain hardening of fibrin gels and plasma clots,” *Rheologica Acta*, vol. 36, no. 3, pp. 262–268, 1997.
- [210] A. S. Adhikari, A. H. Mekhdjian, and A. R. Dunn, “Strain tunes proteolytic degradation and diffusive transport in fibrin networks,” *Biomacromolecules*, vol. 13, no. 2, pp. 499–506, 2012.
- [211] W. Fowler, R. Hantgan, J. Hermans, and H. Erickson, “Structure of the fibrin protofibril,” *Proceedings of the National Academy of Sciences*, vol. 78, no. 8, pp. 4872–4876, 1981.
- [212] B. B. Lim, E. H. Lee, M. Sotomayor, and K. Schulten, “Molecular basis of fibrin clot elasticity,” *Structure*, vol. 16, no. 3, pp. 449–459, 2008.
- [213] E. Bramanti, E. Benedetti, A. Sagripanti, F. Papineschi, and E. Benedetti, “Determination of secondary structure of normal fibrin from human peripheral blood,” *Biopolymers*, vol. 41, no. 5, pp. 545–553, 1997.

- [214] C. A. Jones, M. Cibula, J. Feng, E. A. Krnacik, D. H. McIntyre, H. Levine, and B. Sun, "Micromechanics of cellularized biopolymer networks," *Proceedings of the National Academy of Sciences*, vol. 112, no. 37, pp. E5117–E5122, 2015.
- [215] S. Münster, L. Jawerth, B. Fabry, and D. Weitz, "Structure and mechanics of fibrin clots formed under mechanical perturbation," *Journal of Thrombosis and Haemostasis*, vol. 11, no. 3, pp. 557–560, 2013.
- [216] A. Downes and A. Elfick, "Raman spectroscopy and related techniques in biomedicine," *Sensors*, vol. 10, no. 3, pp. 1871–1889, 2010.
- [217] M. J. Harrington, S. S. Wasko, A. Masic, F. D. Fischer, H. S. Gupta, and P. Fratzl, "Pseudoelastic behaviour of a natural material is achieved via reversible changes in protein backbone conformation," *Journal of The Royal Society Interface*, vol. 9, no. 76, pp. 2911–2922, 2012.
- [218] R. Paquin and P. Colomban, "Nanomechanics of single keratin fibres: A raman study of the  $\alpha$ -helix  $\beta$ -sheet transition and the effect of water," *Journal of Raman Spectroscopy*, vol. 38, no. 5, pp. 504–514, 2007.
- [219] L. Galvis, J. W. Dunlop, G. Duda, P. Fratzl, and A. Masic, "Polarized raman anisotropic response of collagen in tendon: towards 3d orientation mapping of collagen in tissues," *PloS one*, vol. 8, no. 5, p. e63518, 2013.
- [220] E. O. Potma and X. S. Xie, "Detection of single lipid bilayers with coherent anti-stokes raman scattering (cars) microscopy," *Journal of Raman spectroscopy*, vol. 34, no. 9, pp. 642–650, 2003.
- [221] J. P. Day, G. Rago, K. F. Domke, K. P. Velikov, and M. Bonn, "Label-free imaging of lipophilic bioactive molecules during lipid digestion by multiplex coherent anti-stokes raman scattering microspectroscopy," *Journal of the American Chemical Society*, vol. 132, no. 24, pp. 8433–8439, 2010.
- [222] C. Otto, A. Voroshilov, S. Kruglik, and J. Greve, "Vibrational bands of luminescent zinc (ii)-octaethylporphyrin using a polarization-sensitive microscopic multiplex cars technique," *Journal of Raman Spectroscopy*, vol. 32, no. 6-7, pp. 495–501, 2001.
- [223] J.-x. Cheng, A. Volkmer, L. D. Book, and X. S. Xie, "Multiplex coherent anti-stokes raman scattering microspectroscopy and study of lipid vesicles," *The Journal of Physical Chemistry B*, vol. 106, no. 34, pp. 8493–8498, 2002.
- [224] M. Gardel, J. Shin, F. MacKintosh, L. Mahadevan, P. Matsudaira, and D. Weitz, "Scaling of f-actin network rheology to probe single filament elasticity and dynamics," *Physical review letters*, vol. 93, no. 18, p. 188102, 2004.
- [225] N. Kurniawan, J. Grimbergen, J. Koopman, and G. Koenderink, "Factor xiii stiffens fibrin clots by causing fiber compaction," *Journal of Thrombosis and Haemostasis*, vol. 12, no. 10, pp. 1687–1696, 2014.
- [226] H. Duong, B. Wu, and B. Tawil, "Modulation of 3d fibrin matrix stiffness by intrinsic fibrinogen–thrombin compositions and by extrinsic cellular activity," *Tissue Engineering Part A*, vol. 15, no. 7, pp. 1865–1876, 2009.
- [227] J.-P. Collet, J. L. Moen, Y. I. Veklich, O. V. Gorkun, S. T. Lord, G. Montalescot, and J. W. Weisel, "The  $\alpha$ c domains of fibrinogen affect the structure of the fibrin clot, its physical properties, and its susceptibility to fibrinolysis," *Blood*, vol. 106, no. 12, pp. 3824–3830, 2005.

- 
- [228] G. W. Nelb, C. Gerth, J. D. Ferry, and L. Lorand, "Rheology of fibrin clots: Iii. shear creep and creep recovery of fine ligated and coarse unligated clots," *Biophysical chemistry*, vol. 5, no. 3, pp. 377–387, 1976.
- [229] L. Pauling and R. B. Corey, "The pleated sheet, a new layer configuration of polypeptide chains," *Proceedings of the National Academy of Sciences*, vol. 37, no. 5, pp. 251–256, 1951.
- [230] J. H. Brown, N. Volkmann, G. Jun, A. H. Henschen-Edman, and C. Cohen, "The crystal structure of modified bovine fibrinogen," *Proceedings of the National Academy of Sciences*, vol. 97, no. 1, pp. 85–90, 2000.
- [231] R. F. Doolittle, "Structural basis of the fibrinogen–fibrin transformation: contributions from x-ray crystallography," *Blood reviews*, vol. 17, no. 1, pp. 33–41, 2003.
- [232] I. Azpiazu and D. Chapman, "Spectroscopic studies of fibrinogen and its plasmin-derived fragments," *Biochimica et Biophysica Acta (BBA)-Protein Structure and Molecular Enzymology*, vol. 1119, no. 3, pp. 268–274, 1992.
- [233] R. A. Ariëns, T.-S. Lai, J. W. Weisel, C. S. Greenberg, and P. J. Grant, "Role of factor xiii in fibrin clot formation and effects of genetic polymorphisms," *Blood*, vol. 100, no. 3, pp. 743–754, 2002.
- [234] C. C. Helms, R. A. Ariëns, S. U. De Willige, K. F. Standeven, and M. Guthold, " $\alpha$ - $\alpha$  cross-links increase fibrin fiber elasticity and stiffness," *Biophysical journal*, vol. 102, no. 1, pp. 168–175, 2012.
- [235] M. A. Kotlarchyk, S. G. Shreim, M. B. Alvarez-Elizondo, L. C. Estrada, R. Singh, L. Valdevit, E. Kniazeva, E. Gratton, A. J. Putnam, and E. L. Botvinick, "Concentration independent modulation of local micromechanics in a fibrin gel," *PloS one*, vol. 6, no. 5, p. e20201, 2011.
- [236] C. Storm, J. J. Pastore, F. C. MacKintosh, T. C. Lubensky, and P. A. Janmey, "Nonlinear elasticity in biological gels," *Nature*, vol. 435, no. 7039, pp. 191–194, 2005.
- [237] K. M. Weigandt, D. C. Pozzo, and L. Porcar, "Structure of high density fibrin networks probed with neutron scattering and rheology," *Soft Matter*, vol. 5, no. 21, pp. 4321–4330, 2009.
- [238] J. Weisel and R. Litvinov, "The biochemical and physical process of fibrinolysis and effects of clot structure and stability on the lysis rate," *Cardiovascular & Hematological Agents in Medicinal Chemistry (Formerly Current Medicinal Chemistry-Cardiovascular & Hematological Agents)*, vol. 6, no. 3, pp. 161–180, 2008.
- [239] I. Varjú, P. Sótónyi, R. Machovich, L. Szabó, K. Tenekedjiev, M. Silva, C. Longstaff, and K. Kolev, "Hindered dissolution of fibrin formed under mechanical stress," *Journal of Thrombosis and Haemostasis*, vol. 9, no. 5, pp. 979–986, 2011.
- [240] E. Potier, J. Noailly, C. M. Sprecher, and K. Ito, "Influencing biophysical properties of fibrin with buffer solutions," *Journal of materials science*, vol. 45, no. 9, pp. 2494–2503, 2010.
- [241] N. Billecke, G. Rago, M. Bosma, G. Eijkel, A. Gemmink, P. Leproux, G. Huss, P. Schrauwen, M. K. Hesselink, M. Bonn, *et al.*, "Chemical imaging of lipid droplets in muscle tissues using hyperspectral coherent raman microscopy," *Histochemistry and cell biology*, vol. 141, no. 3, pp. 263–273, 2014.

- [242] W. Liu, C. Carlisle, E. Sparks, and M. Guthold, "The mechanical properties of single fibrin fibers," *Journal of Thrombosis and Haemostasis*, vol. 8, no. 5, pp. 1030–1036, 2010.
- [243] D. M. Copolovici, K. Langel, E. Eriste, and U. Langel, "Cell-penetrating peptides: Design, synthesis, and applications," *Acs Nano*, vol. 8, no. 3, pp. 1972–1994, 2014.
- [244] G. P. Dietz and M. Bahr, "Delivery of bioactive molecules into the cell: the trojan horse approach," *Mol Cell Neurosci*, vol. 27, no. 2, pp. 85–131, 2004.
- [245] C. Bechara and S. Sagan, "Cell-penetrating peptides: 20 years later, where do we stand?," *FEBS Lett*, vol. 587, no. 12, pp. 1693–702, 2013.
- [246] D. Derossi, A. H. Joliot, G. Chassaing, and A. Prochiantz, "The third helix of the antennapedia homeodomain translocates through biological membranes," *J Biol Chem*, vol. 269, no. 14, pp. 10444–50, 1994.
- [247] C. Y. Jiao, D. Delaroche, F. Burlina, I. D. Alves, G. Chassaing, and S. Sagan, "Translocation and endocytosis for cell-penetrating peptide internalization," *J Biol Chem*, vol. 284, no. 49, pp. 33957–65, 2009.
- [248] T. Letoha, S. Gaal, C. Somlai, Z. Venkei, H. Glavinas, E. Kusz, E. Duda, A. Czajlik, F. Petak, and B. Penke, "Investigation of penetratin peptides. part 2. in vitro uptake of penetratin and two of its derivatives," *J Pept Sci*, vol. 11, no. 12, pp. 805–11, 2005.
- [249] O. M. Zamotaiev, V. Y. Postupalenko, V. V. Shvadchak, V. G. Pivovarenko, A. S. Klymchenko, and Y. Mely, "Monitoring penetratin interactions with lipid membranes and cell internalization using a new hydration-sensitive fluorescent probe," *Org Biomol Chem*, vol. 12, no. 36, pp. 7036–44, 2014.
- [250] P. E. G. Thorn, D. Persson, P. Isakson, M. Goksr, A. nfelt, and B. Nordn, "Uptake of analogs of penetratin, tat(4860) and oligoarginine in live cells," *Biochemical and Biophysical Research Communications*, vol. 307, no. 1, pp. 100–107, 2003.
- [251] T. Letoha, A. Keller-Pinter, E. Kusz, C. Kolozsi, Z. Bozso, G. Toth, C. Vizler, Z. Olah, and L. Szilak, "Cell-penetrating peptide exploited syndecans," *Biochim Biophys Acta*, vol. 1798, no. 12, pp. 2258–65, 2010.
- [252] S. Deshayes, M. Decaffmeyer, R. Brasseur, and A. Thomas, "Structural polymorphism of two cpp: an important parameter of activity," *Biochim Biophys Acta*, vol. 1778, no. 5, pp. 1197–205, 2008.
- [253] Y. Su, R. Mani, T. Doherty, A. J. Waring, and M. Hong, "Reversible sheet-turn conformational change of a cell-penetrating peptide in lipid bilayers studied by solid-state nmr," *J Mol Biol*, vol. 381, no. 5, pp. 1133–44, 2008.
- [254] M. Magzoub, L. E. Eriksson, and A. Graslund, "Conformational states of the cell-penetrating peptide penetratin when interacting with phospholipid vesicles: effects of surface charge and peptide concentration," *Biochim Biophys Acta*, vol. 1563, no. 1-2, pp. 53–63, 2002.
- [255] M. Lindberg, H. Biversthl, A. Grslund, and L. Mler, "Structure and positioning comparison of two variants of penetratin in two different membrane mimicking systems by nmr," *European Journal of Biochemistry*, vol. 270, no. 14, pp. 3055–3063, 2003.

- 
- [256] B. Christiaens, J. Grooten, M. Reusens, A. Joliot, M. Goethals, J. Vandekerckhove, A. Prochiantz, and M. Rosseneu, "Membrane interaction and cellular internalization of penetratin peptides," *European Journal of Biochemistry*, vol. 271, no. 6, pp. 1187–1197, 2004.
- [257] O. Maniti, I. Alves, G. Trugnan, and J. Ayala-Sanmartin, "Distinct behaviour of the homeodomain derived cell penetrating peptide penetratin in interaction with different phospholipids," *PLoS One*, vol. 5, no. 12, p. e15819, 2010.
- [258] E. Eiríksdóttir, K. Konate, U. Langel, G. Divita, and S. Deshayes, "Secondary structure of cell-penetrating peptides controls membrane interaction and insertion," *Biochim Biophys Acta*, vol. 1798, no. 6, pp. 1119–28, 2010.
- [259] C. E. B. Caesar, E. K. Esbjorner, P. Lincoln, and B. Norden, "Membrane interactions of cell-penetrating peptides probed by tryptophan fluorescence and dichroism techniques: Correlations of structure to cellular uptake," *Biochemistry*, vol. 45, no. 24, pp. 7682–7692, 2006.
- [260] C. E. B. Brattwall, P. Lincoln, and B. Norden, "Orientation and conformation of cell-penetrating peptide penetratin in phospholipid vesicle membranes determined by polarized-light spectroscopy," *Journal of the American Chemical Society*, vol. 125, no. 47, pp. 14214–14215, 2003.
- [261] C. C. Lee, Y. Sun, and H. W. Huang, "Membrane-mediated peptide conformation change from alpha-monomers to beta-aggregates," *Biophys J*, vol. 98, no. 10, pp. 2236–45, 2010.
- [262] C. Bechara, M. Pallerla, F. Burlina, F. Illien, S. Cribier, and S. Sagan, "Massive glycosaminoglycan-dependent entry of trp-containing cell-penetrating peptides induced by exogenous sphingomyelinase or cholesterol depletion," *Cellular and Molecular Life Sciences*, vol. 72, no. 4, pp. 809–820, 2014.
- [263] A. Hansen, I. Schafer, D. Knappe, P. Seibel, and R. Hoffmann, "Intracellular toxicity of proline-rich antimicrobial peptides shuttled into mammalian cells by the cell-penetrating peptide penetratin," *Antimicrob Agents Chemother*, vol. 56, no. 10, pp. 5194–201, 2012.
- [264] S. Jones, M. Lukanowska, J. Suhorutsenko, S. Oxenham, C. Barratt, S. Publicover, D. M. Copolovici, U. Langel, and J. Howl, "Intracellular translocation and differential accumulation of cell-penetrating peptides in bovine spermatozoa: evaluation of efficient delivery vectors that do not compromise human sperm motility," *Hum Reprod*, vol. 28, no. 7, pp. 1874–89, 2013.
- [265] D. Derossi, S. Calvet, A. Trembleau, A. Brunissen, G. Chassaing, and A. Prochiantz, "Cell internalization of the third helix of the antennapedia homeodomain is receptor-independent," *J Biol Chem*, vol. 271, no. 30, pp. 18188–93, 1996.
- [266] S. U. Sane, S. M. Cramer, and T. M. Przybycien, "A holistic approach to protein secondary structure characterization using amide i band raman spectroscopy," *Analytical biochemistry*, vol. 269, no. 2, pp. 255–272, 1999.
- [267] N. C. Maiti, M. M. Apetri, M. G. Zagorski, P. R. Carey, and V. E. Anderson, "Raman spectroscopic characterization of secondary structure in natively unfolded proteins: alpha-synuclein," *J Am Chem Soc*, vol. 126, no. 8, pp. 2399–408, 2004.

- [268] C. H. Camp, Y. J. Lee, and M. T. Cicerone, “Quantitative, comparable coherent anti-stokes raman scattering (cars) spectroscopy: correcting errors in phase retrieval,” *Journal of Raman Spectroscopy*, vol. 47, no. 4, pp. 408–415, 2016.
- [269] K. Bito, M. Okuno, H. Kano, S. Tokuhara, S. Naito, Y. Masukawa, P. Leproux, V. Couderc, and H.-o. Hamaguchi, “Protein secondary structure imaging with ultrabroadband multiplex coherent anti-stokes raman scattering (cars) microspectroscopy,” *The Journal of Physical Chemistry B*, vol. 116, no. 4, pp. 1452–1457, 2012.
- [270] H.-J. van Manen, A. Lenferink, and C. Otto, “Noninvasive imaging of protein metabolic labeling in single human cells using stable isotopes and raman microscopy,” *Analytical Chemistry*, vol. 80, no. 24, pp. 9576–9582, 2008.
- [271] L. Wei, Y. Yu, Y. Shen, M. C. Wang, and W. Min, “Vibrational imaging of newly synthesized proteins in live cells by stimulated raman scattering microscopy,” *Proceedings of the National Academy of Sciences of the United States of America*, vol. 110, pp. 11226–11231, July 2013.
- [272] S. Piqueras, L. Duponchel, R. Tauler, and A. de Juan, “Resolution and segmentation of hyperspectral biomedical images by multivariate curve resolution-alternating least squares,” *Anal Chim Acta*, vol. 705, no. 1-2, pp. 182–92, 2011.
- [273] G. Dom, “Cellular uptake of antennapedia penetratin peptides is a two-step process in which phase transfer precedes a tryptophan-dependent translocation,” *Nucleic Acids Research*, vol. 31, no. 2, pp. 556–561, 2003.
- [274] I. D. Alves, C. Y. Jiao, S. Aubry, B. Aussedat, F. Burlina, G. Chassaing, and S. Sagan, “Cell biology meets biophysics to unveil the different mechanisms of penetratin internalization in cells,” *Biochim Biophys Acta*, vol. 1798, no. 12, pp. 2231–9, 2010.
- [275] C. Palm, M. Jayamanne, M. Kjellander, and M. Hallbrink, “Peptide degradation is a critical determinant for cell-penetrating peptide uptake,” *Biochim Biophys Acta*, vol. 1768, no. 7, pp. 1769–76, 2007.
- [276] I. M. Kaplan, J. S. Wadia, and S. F. Dowdy, “Cationic tat peptide transduction domain enters cells by macropinocytosis,” *Journal of Controlled Release*, vol. 102, no. 1, pp. 247–253, 2005.
- [277] L. Whitmore and B. A. Wallace, “Protein secondary structure analyses from circular dichroism spectroscopy: Methods and reference databases,” *Biopolymers*, vol. 89, no. 5, pp. 392–400, 2008.
- [278] A. C. Terentis and J. Ye, “Peptide detection and structure determination in live cells using confocal raman microscopy,” *Methods Mol Biol*, vol. 1081, pp. 211–36, 2013.
- [279] N. Sreerama and R. W. Woody, “Estimation of protein secondary structure from circular dichroism spectra: Comparison of contin, selcon, and cdsstr methods with an expanded reference set,” *Analytical Biochemistry*, vol. 287, no. 2, pp. 252–260, 2000.
- [280] A. Mogilner and K. Keren, “The shape of motile cells,” *Curr Biol*, vol. 19, no. 17, pp. R762–71, 2009.



- 
- [281] J. E. Eriksson, T. Dechat, B. Grin, B. Helfand, M. Mendez, H. M. Pallari, and R. D. Goldman, "Introducing intermediate filaments: from discovery to disease," *J Clin Invest*, vol. 119, no. 7, pp. 1763–71, 2009.
- [282] P. Benes, V. Maceckov, Z. Zdrhal, H. Konecn, E. Zahradnckov, J. Muzk, and J. Smarda, "Role of vimentin in regulation of monocyte/macrophage differentiation," *Differentiation*, vol. 74, no. 6, pp. 265–76, 2006.
- [283] N. Mcke, L. Kreplak, R. Kirmse, T. Wedig, H. Herrmann, U. Aebi, and J. Langowski, "Assessing the flexibility of intermediate filaments by atomic force microscopy," *J Mol Biol*, vol. 335, no. 5, pp. 1241–50, 2004.
- [284] Y. E. Quax-Jeuken, W. J. Quax, and H. Bloemendal, "Primary and secondary structure of hamster vimentin predicted from the nucleotide sequence," *Proc Natl Acad Sci U S A*, vol. 80, no. 12, pp. 3548–52, 1983.
- [285] R. E. Leube, M. Moch, and R. Windoffer, "Intermediate filaments and the regulation of focal adhesion.," *Current opinion in cell biology*, vol. 32, pp. 13–20, Feb. 2015.
- [286] J. Ivaska, H.-M. Pallari, J. Nevo, and J. E. Eriksson, "Novel functions of vimentin in cell adhesion, migration, and signaling.," *Experimental cell research*, vol. 313, pp. 2050–2062, June 2007.
- [287] C. Gilles, M. Polette, M. Mestdagt, B. Nawrocki-Raby, P. Ruggeri, P. Birembaut, and J.-M. Foidart, "Transactivation of vimentin by beta-catenin in human breast cancer cells.," *Cancer research*, vol. 63, pp. 2658–2664, May 2003.
- [288] J. Lowery, E. R. Kuczmarski, H. Herrmann, and R. D. Goldman, "Intermediate filaments play a pivotal role in regulating cell architecture and function.," *The Journal of biological chemistry*, vol. 290, pp. 17145–17153, July 2015.
- [289] N. Pinto, F.-C. Yang, A. Negishi, M. C. Rheinstdter, T. E. Gillis, and D. S. Fudge, "Self-assembly enhances the strength of fibers made from vimentin intermediate filament proteins.," *Biomacromolecules*, vol. 15, pp. 574–581, Feb. 2014.
- [290] L. Kreplak, J. Doucet, P. Dumas, and F. Briki, "New aspects of the alpha-helix to beta-sheet transition in stretched hard alpha-keratin fibers.," *Biophysical journal*, vol. 87, pp. 640–647, July 2004.
- [291] C. P. Brangwynne, F. MacKintosh, and D. A. Weitz, "Force fluctuations and polymerization dynamics of intracellular microtubules," *Proceedings of the National Academy of Sciences*, vol. 104, no. 41, pp. 16128–16133, 2007.
- [292] F. Meng, T. M. Suchyna, E. Lazakovitch, R. M. Gronostajski, and F. Sachs, "Real time fret based detection of mechanical stress in cytoskeletal and extracellular matrix proteins.," *Cellular and molecular bioengineering*, vol. 4, pp. 148–159, June 2011.
- [293] K. Okamoto, T. Nagai, A. Miyawaki, and Y. Hayashi, "Rapid and persistent modulation of actin dynamics regulates postsynaptic reorganization underlying bidirectional plasticity," *Nat Neurosci*, vol. 7, no. 10, pp. 1104–12, 2004.
- [294] H. D. Vishwasrao, P. Trifilieff, and E. R. Kandel, "In vivo imaging of the actin polymerization state with two-photon fluorescence anisotropy," *Biophys J*, vol. 102, no. 5, pp. 1204–14, 2012.
- [295] C. P. Johnson, H.-Y. Tang, C. Carag, D. W. Speicher, and D. E. Discher, "Forced unfolding of proteins within cells," *Science*, vol. 317, no. 5838, pp. 663–666, 2007.

- [296] J. Swift, I. L. Ivanovska, A. Buxboim, T. Harada, P. C. Dingal, J. Pinter, J. D. Pajerowski, K. R. Spinler, J. W. Shin, M. Tewari, F. Rehfeldt, D. W. Speicher, and D. E. Discher, "Nuclear lamin-a scales with tissue stiffness and enhances matrix-directed differentiation," *Science*, vol. 341, no. 6149, p. 1240104, 2013.
- [297] R. W. Williams and A. K. Dunker, "Determination of the secondary structure of proteins from the amide i band of the laser raman spectrum," *Journal of Molecular Biology*, vol. 152, no. 4, pp. 783–813, 1981.
- [298] J. P. Day, K. F. Domke, G. Rago, H. Kano, H. O. Hamaguchi, E. M. Vartiainen, and M. Bonn, "Quantitative coherent anti-stokes raman scattering (cars) microscopy," *J Phys Chem B*, vol. 115, no. 24, pp. 7713–25, 2011.
- [299] M. Meier, G. P. Padilla, H. Herrmann, T. Wedig, M. Hergt, T. R. Patel, J. Stetefeld, U. Aebi, and P. Burkhard, "Vimentin coil 1a-a molecular switch involved in the initiation of filament elongation," *J Mol Biol*, vol. 390, no. 2, pp. 245–61, 2009.
- [300] B. T. Walters, A. Ricciuti, L. Mayne, and S. W. Englander, "Minimizing back exchange in the hydrogen exchange-mass spectrometry experiment.," *Journal of the American Society for Mass Spectrometry*, vol. 23, pp. 2132–2139, Dec. 2012.
- [301] K. L. Vikstrom, G. G. Borisy, and R. D. Goldman, "Dynamic aspects of intermediate filament networks in bhk-21 cells.," *Proceedings of the National Academy of Sciences of the United States of America*, vol. 86, pp. 549–553, Jan. 1989.
- [302] D. E. Ingber, "Cellular tensegrity: defining new rules of biological design that govern the cytoskeleton.," *Journal of cell science*, vol. 104 ( Pt 3), pp. 613–627, Mar. 1993.
- [303] R. J. Pelham and Y. Wang, "Cell locomotion and focal adhesions are regulated by substrate flexibility," *Proc Natl Acad Sci U S A*, vol. 94, no. 25, pp. 13661–5, 1997.
- [304] Z. M. Goeckeler, P. C. Bridgman, and R. B. Wysolmerski, "Nonmuscle myosin ii is responsible for maintaining endothelial cell basal tone and stress fiber integrity," *Am J Physiol Cell Physiol*, vol. 295, no. 4, pp. C994–1006, 2008.
- [305] Y. Kumar and R. H. Valdivia, "Actin and intermediate filaments stabilize the chlamydia trachomatis vacuole by forming dynamic structural scaffolds," *Cell Host Microbe*, vol. 4, no. 2, pp. 159–69, 2008.
- [306] B. T. Helfand, M. G. Mendez, S. N. Murthy, D. K. Shumaker, B. Grin, S. Mahammad, U. Aebi, T. Wedig, Y. I. Wu, K. M. Hahn, M. Inagaki, H. Herrmann, and R. D. Goldman, "Vimentin organization modulates the formation of lamellipodia," *Mol Biol Cell*, vol. 22, no. 8, pp. 1274–89, 2011.
- [307] J. E. Eriksson, T. He, A. V. Trejo-Skalli, A. S. Hrml-Braskn, J. Hellman, Y. H. Chou, and R. D. Goldman, "Specific in vivo phosphorylation sites determine the assembly dynamics of vimentin intermediate filaments," *J Cell Sci*, vol. 117, no. Pt 6, pp. 919–32, 2004.
- [308] P. C. D. P. Dingal and D. E. Discher, "Systems mechanobiology: tension-inhibited protein turnover is sufficient to physically control gene circuits.," *Biophysical journal*, vol. 107, pp. 2734–2743, Dec. 2014.
- [309] R. V. Zackroff and R. D. Goldman, "In vitro assembly of intermediate filaments from baby hamster kidney (bhk-21) cells," *Proc Natl Acad Sci U S A*, vol. 76, no. 12, pp. 6226–30, 1979.

- 
- [310] J. Zhao, H. Lui, D. I. McLean, and H. Zeng, “Automated autofluorescence background subtraction algorithm for biomedical raman spectroscopy,” *Appl Spectrosc*, vol. 61, no. 11, pp. 1225–32, 2007.
  - [311] X. Hong, J. P. Stegemann, and C. X. Deng, “Microscale characterization of the viscoelastic properties of hydrogel biomaterials using dual-mode ultrasound elastography,” *Biomaterials*, vol. 88, pp. 12–24, 2016.
  - [312] J. Y. Sim, J. Moeller, K. C. Hart, D. Ramallo, V. Vogel, A. R. Dunn, W. J. Nelson, and B. L. Pruitt, “A highlights from mboc selection: Spatial distribution of cell–cell and cell–ecm adhesions regulates force balance while maintaining e-cadherin molecular tension in cell pairs,” *Molecular Biology of the Cell*, vol. 26, no. 13, p. 2456, 2015.
  - [313] M. H. Kroll, J. D. Hellums, L. McIntire, A. Schafer, and J. Moake, “Platelets and shear stress,” *Blood*, vol. 88, no. 5, pp. 1525–1541, 1996.
  - [314] A. Karuna, F. Masia, P. Borri, and W. Langbein, “Hyperspectral volumetric coherent anti-stokes raman scattering microscopy: quantitative volume determination and nacl as non-resonant standard,” *Journal of Raman Spectroscopy*, vol. 47, no. 9, pp. 1167–1173, 2016.